THE UNIVERSITY
OF ADELAIDE
AUSTRALIA

Palaeo- to Mesoproterozoic Evolution of the Gawler Craton, Australia: Geochronological, geochemical and isotopic constraints

Justin L. Payne, B.Sc (Hons)

Geology and Geophysics
School of Earth and Environmental Sciences
The University of Adelaide

This thesis is submitted in fulfilment of the
requirements for the degree of Doctor of Philosophy
in the Faculty of Science, University of Adelaide

January 2008

Table of Contents

List of Figures

Abstract

The Gawler Craton, South Australia, consists of late Archaean to early Mesoproterozoic igneous and supracrustal lithologies which preserve a deformation history lasting the duration of the Palaeoproterozoic. Understanding the evolution of the Gawler Craton is of significance in global supercontient reconstructions as it preserves evidence for earliest Palaeoproterozoic collisional orogenesis (*c*. 2460-2430 Ma) and, in conjunction with the North Australian Craton and Antarctica, has often been correlated to the western margin of Laurentia. In addition, the Gawler Craton is also host to the world-class Olympic Dam Fe-oxide-Cu-Au-U type-deposit (world's fourth-largest Cu and largest U deposit) and related Fe-oxide-Cu-Au-U and Cu-Au mineralising systems. Despite the various geologically and economically important characteristics of the Gawler Craton there has traditionally been a poor understanding of the tectonothermal evolution of the Gawler Craton, in particular for the Palaeoproterozoic. This study addresses and refines the Palaeo- to Mesoproterozoic tectonothermal evolution of the Gawler Craton. This is done using geochemical, geochronological and isotopic analytical techniques to better understand selected supracrustal and igneous lithologies in the Gawler Craton and the orogenic events which have affected them.

Largely unexposed metasedimentary lithologies of the northern Gawler Craton record multiple deformation events but have previously been virtually unconstrained with respect to their timing of protolith deposition and the age of deformation/metamorphism. New geochronological data demonstrate these metasedimentary lithologies were deposited during the time period ~1750-1730 Ma before being metamorphosed and deformed during the Kimban (1730-1690 Ma) and Kararan (1570-1545 Ma) Orogenies. Detrital zircon geochronology and isotopic and geochemical characteristics of the sampled metasedimentary lithologies suggest a relatively similar protolith sedimentary succession was deposited across a large extent of the northern Gawler Craton. Detritus for the sedimentary protolith does not appear to have been sourced from the Gawler Craton. Instead the protolith it is more consistent with a North Australian Craton provenance suggesting a proximity between the northern Gawler Craton and North Australian Craton at the time of protolith deposition.

The newly defined presence of the Palaeoproterozoic Kimban Orogeny in the northern Gawler Craton demonstrates the Kimban Orogeny to be a major, high-grade, craton-wide orogenic event. This finding contradicts previous suggestions that the northern Gawler Craton was accreted to the proto-Gawler Craton during the later Mesoproterozoic Kararan Orogeny. In addition, previous reconstruction models for the Palaeo- to early Mesoproterozoic often cite the felsic Tunkillia Suite (1690-1670 Ma), western and central Gawler Craton, as representing arc magmatism prior to the subsequent amalgamation of the Gawler Craton during the Kararan Orogeny. New geochemical and isotopic data for the Tunkillia Suite have allowed for re-examination of the tectonic setting for the petrogenesis of the Tunkillia Suite. Contrary to previous suggestions (based upon discrimination diagrams), the mineralogy, geochemistry and isotopic characteristics of the Tunkillia Suite are not consistent with arc-magmatism. Instead the Tunkillia Suite is interpreted to represent a late- to post-tectonic magmatic suite generated during the waning stages of the Kimban Orogeny. This petrogenesis further highlights the importance of the Kimban Orogeny as a fundamental tectonothermal event in the evolution of the Gawler Craton.

Subsequent to the Kimban Orogeny, the Gawler Craton was thought to undergo a period of subduction-related magmatism (St Peter Suite) prior to the anorogenic magmatism of the voluminous felsic Gawler Range Volcanic (GRV) and Hiltaba Suite magmatism (1595-1575 Ma). New geochronological data for the ms-bi-gt-bearing peraluminous Munjeela Suite (1590-1580 Ma) have demonstrated the Hiltaba/GRV event was accompanied by significant crustal anatexis not associated with the Hiltaba/GRV magmatism. The Munjeela Suite and metasedimentary enclaves within it demonstrate that the Gawler Craton was likely to be undergoing compressive deformation and crustal thickening sometime during the petrogenesis of the Hiltaba/GRV magmatism. This suggests the Hiltaba/GRV magmatism did not occur in an anorogenic setting as previously proposed.

The findings of this study are incorporated into a revised tectonothermal evolution of the Gawler Craton. This is used to discuss previous reconstruction models for Proterozoic Australia and provide a new reconstruction model of Australia and Antarctica during the Palaeoproterozoic. Important facets of the proposed model are links to the Archaean-Early Palaeoproterozoic Sask Craton in the Trans-Hudson Orogen, Laurentia, and the joint evolution of the North Australian and Gawler Cratons throughout the entire Palaeoproterozoic.

Acknowledgements

First and foremost I would like to thank my supervisors, Karin and Martin. Both have been the providers of excellent supervision. I may still have ended up at this point without the Gawler LP but I doubt the process would have been anywhere near as enjoyable and enlightening. I think the level of enjoyment myself and the other PhDers have had is a reflection of the fantastic culture they have created within the research group.

I think an honourable mention is befitting for Anthony Reid and Angus Netting of the PIRSA and Adelaide Microscopy worlds, respectively. Anthony has acted in many ways as a third supervisor, especially with the final epic, but mainly has provided enjoyable discussions and wisdom on many things Gawler-related and a few other things too. Angus has had the pleasure of setting up a LA-ICP-MS (and letting Ben and I watch and play too), numerous weekend phone calls and more than a couple late carbon-coats. His good humour has made the many long hours in the med. school basement more bearable.

Pete Kinny is thanked for guidance and expertise with the SHRIMP geochronology conducted at Curtin University of Technology.

My self-appointed mentor Ben Wade who has provided many hours of entertainment, lurid laser, zircon and monazite talk and even some useful advice on the world of geochemistry and geochronology. I probably didn't pay enough attention to be a worthy protégé but somehow Karin's lab geeks worked out how to do stuff. The fellow CERGers of the recent past and present for providing all forms of conversations on most of the topics worth covering and many not over the last three and a half years (actually three quarters). Rian Dutch (a co-starter), Chris Clark (an unofficial Honours supervisor), Lachie Rutherford and Mike Szpunar (the grumpy old men), Greg Swain (Gawler tour leader and proud ute-owner), Dave E. Kelsey (a late musical addition at a higher, non-student level) and Ailsa Schwarz (food orderer extraordinaire).

My family has managed to put up with and support me for over twenty-five years now which I think is a very fine effort. A thesis dedication should go to Mum and Dad for all of their support and work in producing a family I'm more than proud to be a part of. My younger sister, Natalie, who like all young siblings has picked up most of my bad traits and added a few more, which have made sharing a house for the last couple of years a pleasure, most of the time. And although more absent in the last few years, my older sister, Emily, has been able to put up with the rubbish talked between Natalie and I, and more recently her husband, Richard (the only other real doctor in the family).

Outside of PhD life, Shane, Hannah, Aaron and Tim have been the best of friends and hopefully I don't have to say "I'm at uni" quite so much when I answer the phone in the future. And for the excitement of bi-monthly chess, Jessie.

Most importantly I would like to thank Dr. Kate. I often tell her she has never known me outside of a PhD, so of course I'll be a much better person when I'm done. Hopefully this proves to be the case. Regardless, I would like to thank her for all the reading, the long, seemingly unending and sometimes unwanted barrage of geology conversations, all the more normal conversations and for letting me do a PhD the way I have, even though you knew it didn't have to be done that way.

'you might have to think
of how you got started
sitting in your little room'

Publications and Selected Conference Abstracts

Peer Reviewed Journal Articles

Payne, J.L., Hand, M., Barovich, K.M. and Reid, A., *In review*. A Global context for the Paleoproterozoic evolution of the Mawson Continent. IGCP 509 'Palaeoproterozoic Earth' Special Issue, Geological Society of London Special Publication.

Payne, J.L., Hand, M., Barovich, K.M. and Wade, B.P., 2008. Temporal constraints on the timing of high-grade metamorphism in the northern Gawler Craton: implications for the construction of the Australian Proterozoic. Australian Journal of Earth Sciences, 55, in press.

Wade, B.P., **Payne, J.L.**, Hand, M., Barovich, K.M., 2007. Petrogenesis of the ca. 1.50 Ga granitic gneiss of the Coompana Block: filling the 'magmatic gap' of Mesoproterozoic Australia. Australian Journal of Earth Sciences, 54: 1089-1102. *(Provided in Supplementary Appendix Two)*

Payne, J.L., Barovich, K.M. and Hand, M., 2006.Provenance of metasedimentary rocks in the northern Gawler Craton, Australia: Implications for palaeoproterozoic reconstructions. Precambrian Research, 148 (3-4): 275-291.

Reid, A., **Payne, J.L.**, Wade, B.P., 2006. A new geochronological capability for South Australia - U-Pb zircon dating via LA-ICP-MS. MESA Journal, 42, 27-31. *(Provided in Supplementary Appendix Two)*

Selected Conference Abstracts

Payne, J.L., Hand, M. and Barovich, K.M., 2007. The role of Palaeoproterozoic tectonism in understanding the global evolution of the Gawler-Adelie Craton. 'Deformation in theDesert' SGTSG 2007 conference, Alice Springs, Geological Society of Australia Abstracts.

Payne, J.L., Wade, B.P., Hand, M., Barovich, K. and Clark, C., 2006. Optimising the spatial resolution, fractionation and temporal precision of monazite U-Pb LA-ICP-MS geochronology. Goldschmidt 2007, Geochimica et ActaSupplement, vol. 70, 18, pg. 476.

Payne, J.L., Barovich, K.M. and Hand, M., 2006. On the tectonic setting of the magmatic suite previously known as the 'arc-like Tunkillia/Ifould'. In: Denham, D., Australian Earth Sciences Convention 2006, Melbourne, Geological Society of Australia Abstracts.

Payne, J.L., Barovich, K.M. and Hand, M., 2006. The Gawler through time - Archaean to 1.54 Ga: Terrane mapping and geochronology of Australia's least understood craton. In: Denham, D. (Ed.) 2006, Australian Earth Sciences Convention 2006, Melbourne, Geological Society of Australia Abstracts.

Payne, J.L., Barovich, K.M., Hand, M., 2005. Provenance of sequences in the northern Gawler Craton: Re-assembling Proterozoic Australia and dispersing the Gawler Craton. Wingate, M.T.D. and Pisarevsky, S.A. (Editors) 2005. Supercontinents and Earth Evolution Symposium 2005, Geological Society of Australia Abstracts, 81.

Declaration

This thesis contains no material which has been accepted for the award of any other degree or diploma in any university or other tertiary institution and, to the best of my knowledge and belief, contains no material previously published or written by any other person, except where due reference has been made in the text.

I give consent to this copy of my thesis, when deposited in the University Library, being available for loan and photocopying.

_____

Justin L. Payne

Chapter 1

Introduction

Palaeo- to Mesoproterozoic Evolution of the Gawler Craton, Australia

The Palaeoproterozoic Era (2.5-1.6 Ga) is widely thought to be a critical time period in Earth evolution during which lateral crustal accretion (plate tectonics) overtook vertical, plume-driven accretion of the Archaean as the primary mechanism of crustal growth and recycling. Brown (2007) has described a 'Proterozoic plate tectonics' regime which was active from the Neoarchaean until some time during the Neoproterozoic. This is based upon the duality of metamorphic thermal regimes associated with subduction (eclogite high pressure - EHP) and back-arc basins (ultra high temperature - UHT). Direct evidence of plate tectonics, such as eclogite-facies metamorphism and ophiolite incorporated within accretionary/collisional orogens, does not appear to extend past *c.* 2.0 Ga (eg. *c.* 2.0 Ga Usagaran eclogites, Tanzania, Moller et al., 1995; Collins et al., 2004; Purtiniq Ophiolite, Trans-Hudson Orogen, Scott et al., 1992; Scott et al., 1999). However, evidence exists, largely provided by geochemical methods, that subduction processes and oceanic crustal accretion via spreading operated throughout the Palaeoproterozoic and Neoarchaean and at least part of the Mesoarchaean (eg. Nutman et al., 2002; Hickman, 2004; Moyen et al., 2006; Smithies et al., 2007). Recently, a sheeted-dike complex in the Isua Supracrustal Belt, Greenland, has been interpreted as an ophiolite, suggesting sea-floor spreading was active as early as ~3.8 Ga (Furnes et al., 2007).

While it is somewhat fashionable to produce evidence that plate tectonics-like processes operated in the ancient Earth, fundamental changes have occured over time in the Earth's lithosphere and atmosphere. These changes include differing geothermal gradients, the lack of ancient HP-UHP metamorphism, little UHT metamorphism and the preponderance of granite-greenstone belts in the Archaean indicate that although plate tectonic-like processes were active during the Archaean they were significantly different to modern-day plate tectonics (eg. Stern, 2005; Brown, 2007). These differences highlights the latest Archaean-Palaeoproterozoic as an important timeframe in the evolution of the Earth towards modern-day tectonic and climatic conditions including supercontinent formation and dispersal (Aspler and Chiarenzelli, 1998; Bleeker, 2003; Barley et al., 2005), crustal growth dominated by subduction and lateral accretion, and oxygenation of the atmosphere (Kump and Barley, 2007).

The Gawler Craton, South Australia, consists of late Archaean to Mesoproterozoic igneous and supracrustal rocks with a deformation history lasting the duration of the Palaeoproterozoic (Figures 1.1 and 1.2). Compared to many other terrains of similar age the Gawler Craton is poorly understood. This lack of knowledge is largely the result of a paucity of outcrop (only 5-10% outcrop in a region only slightly smaller than France, Figure 1.1) hampering research into the basement geology. Of the total outcrop only a small proportion consists of Palaeoproterozoic lithologies which is reflected by only 13 national and international peer-reviewed publications addressing the Palaeoproterozoic of the Gawler Craton in the 20 years prior to the initiation of this research project. In addition to the paucity of outcrop, a large degree of the research effort on the Gawler Craton has focused on the Gawler Range Volcanic (GRV) and Hiltaba Suite magmatic event linked to the giant Olympic Dam Fe-oxide-Cu-Au-U type-deposit and associated mineral systems (Creaser and White, 1991; Creaser, 1995; Johnson and Cross, 1995; Allen and McPhie, 2002; Allen et al., 2003; Budd, 2006; Direen and Lyons, in press). The result of this research bias is that the tectonothermal evolution of the Gawler Craton has historically been very poorly constrained and the tectonic setting of the Gawler Craton leading up to the GRV/Hiltaba magmatism is virtually unknown.

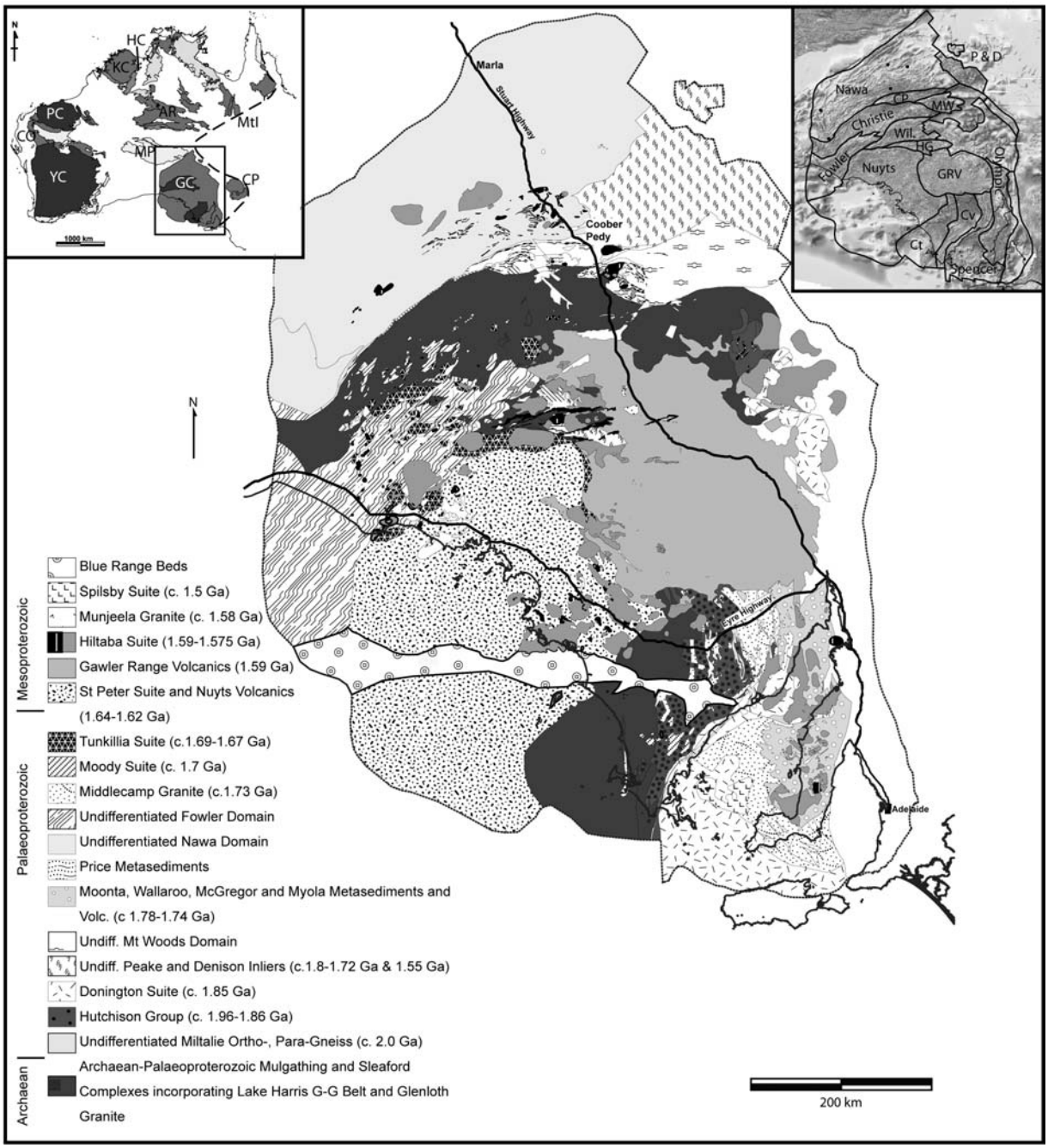

Figure 1.1 - Interpreted basement geology of the Gawler Craton after Fairclough et al. (2004). Inset Top Left: Pre-1070 Ma geological provinces of Australia after Betts et al. (2002) and Payne et al (2007) showing location of Gawler Craton. Abbreviations are: AR - Arunta Region, CO - Capricorn Orogen, CP - Curnamona Province, GC - Gawler Craton, HC - Halls Creek Orogen, KC - Kimberley Craton, MP - Musgrave Province, Mtl - Mount Isa Inlier, PC - Pilbara Craton, YC - Yilgarn Craton. Inset Top Right: Total Magnetic Intensity (TMI) image of the Gawler Craton with interpreted domains. Abbreviations are: CP - Coober Pedy Domain, Ct - Coulta Domain, Cv - Cleve Domain, GRV - Gawler Range Volcanics, HG - Harris Greenston Belt, MW - Mount Woods Domain, P & D - Peake and Denison, Wil. - Wilgena Domain.

The aim of this project is to improve understanding of the tectonothermal evolution of the Gawler Craton during the Palaeoproterozoic. Given the many pre-existing gaps in knowledge of the geology of the Gawler Craton, a large portion of the research undertaken is to provide a 'first-pass' framework of previously uncharacterised regions and to refine understanding of the tectonic setting of magmatic suites important in understanding the tectonothermal evolution of the Gawler Craton. As a result of this project and other research efforts in the last four years, there have been dramatic changes in our understanding of the evolution of the Gawler Craton, most notably in the tectonothermal events of the late Palaeoproterozoic. Detailing all previous geological interpretations

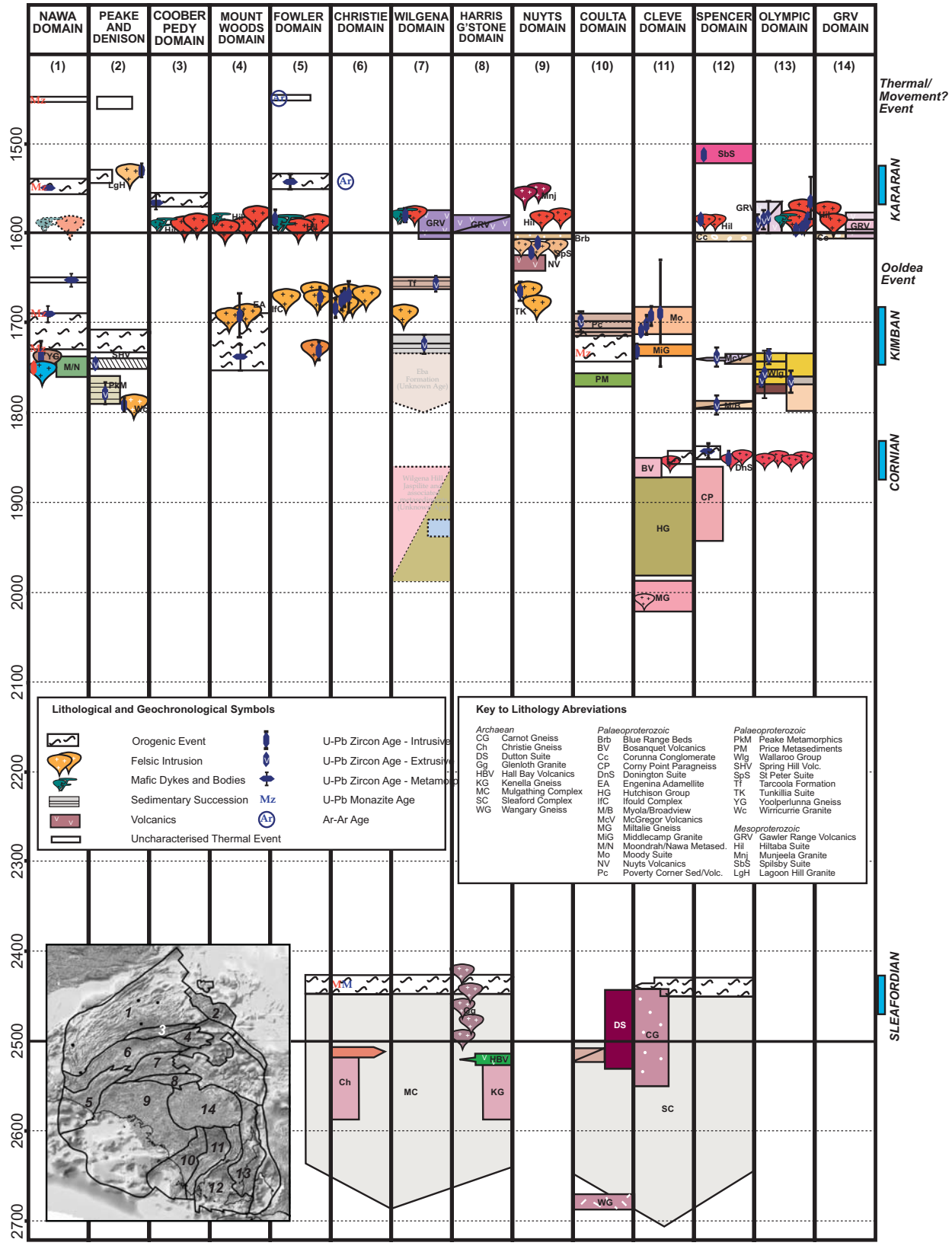

Figure 1.2 - Current Time-Space diagram for Gawler Craton and Terre Adélie Craton. Regions of the Gawler Craton correspond to domains as numbered and represented in inset map. Domains are: 1 - Nawa Domain, 2 - Peake and Denison Inliers, 3 - Coober Pedy Ridge Domain, 4 - Fowler Domain, 5 - Christie Domain, 6 - Wilgena Domain, 7 - Lake Harris Greenstone Domain, 8 - Mount Woods Domain, 9 - Nuyts Domain, 10 - Gawler Range Domain, 11 - Coulta Domain, 12 - Cleve Domain, 13 - Spencer Domain, 14 - Olympic Domain. T-S plot for Gawler Craton modified after Ferris et al. (2002) with additional data from Peucat et al. (1999; 2002), Holm (2004), Jagodzinski et al. (2006), Fraser and Lyons (2006), Payne et al. (2006), Howard et al. (2007) and Hand et al. (in press). Data sources for remainder of T-S plots are as discussed in text.

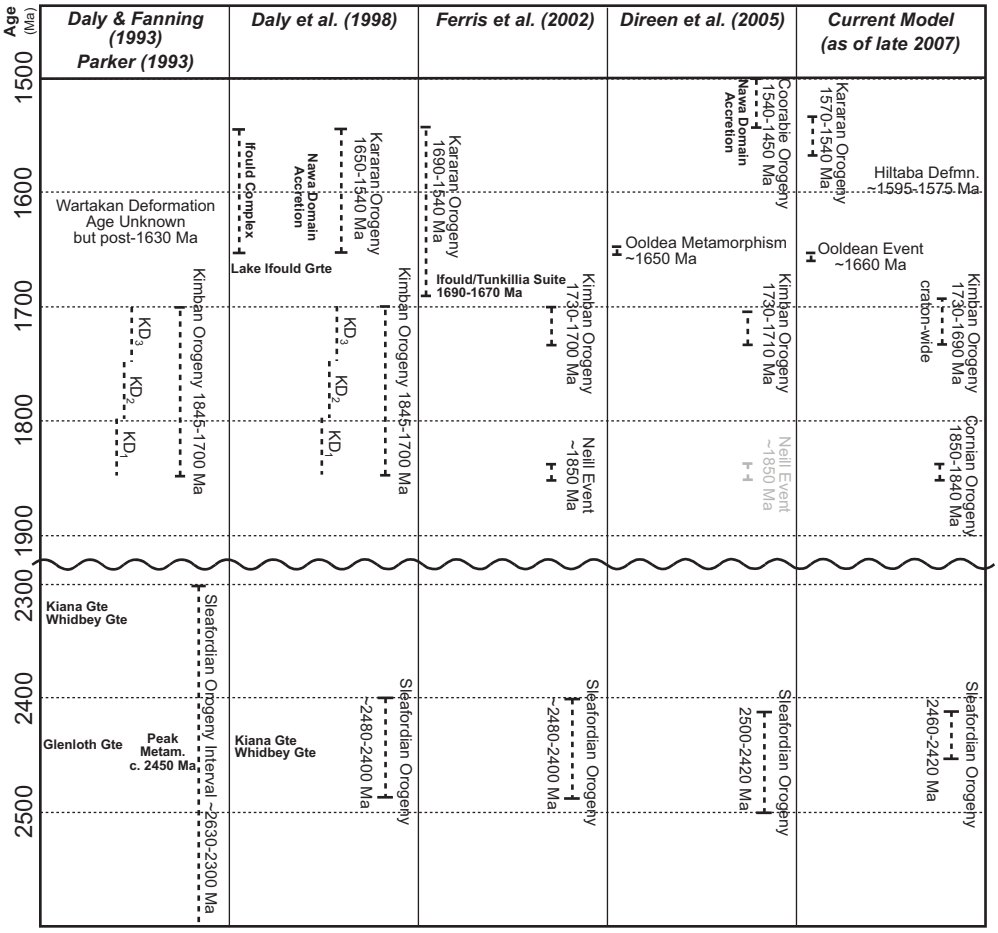

Figure 1.3 - Summary of tectonothermal events in the Gawler Craton that have undergone significant re-interpretation during the duration of this project. See discussion in text and Chapter 7 for further details.Current model for evolution of the Gawler Craton is discussed in Chapter 7 and Hand et al. (in press) and references therein.

would not add significantly to this thesis (see summaries of Daly et al., 1998; Ferris et al., 2002; Hand et al., in press; Chapter 7 of this thesis). Instead, outlined below are timelines notable for the interpretation of the evolution of the Gawler Craton and timelines which have been significantly reinterpreted as part of this project (Figure 1.3).

The oldest preserved lithologies in the Gawler Craton are the Mulgathing and Sleaford Complexes which consist of Devil's Playground and Hall Bay Volcanics (*c.* 2560-2520 Ma), Mulgathing and Carnot Gneisses (*c.* 2535-2500 Ma), Glenloth Granite and Coulta Granodiorite (*c.* 2520-2500 Ma) and Harris Greenstone Belt (*c.* 2520-2510 Ma, Daly et al., 1998; Swain et al., 2005). Detrital zircons within the metasedimentary lithologies of these units range in age from *c.* 2600-3000 Ma. No source rocks (and presumably basement to the Gawler Craton) for these detrital zircons are known in the Gawler Craton and, although some speculations have been made recently for an Antarctic source, an accepted source has not previously been nominated (see Chapter 7 for discussion). The late Archaean lithologies of the Gawler Craton were deformed during the 2460-2420 Ma Sleafordian Orogeny (Tomkins et al., 2004; Swain et al., 2005; McFarlane, 2006). The metamorphic grade of the Sleafordian Orogeny varies from sub-greenschist to granulite facies and is interpreted to represent a collisional orogeny. The Sleafordian Orogeny is globally significant as it represents the final orogenic event before an extended period (*c.* 2500-2200 Ma) of continental rifting or supercontinent/supercraton stability. Potential global correlations for the basement to the Gawler Craton and equivalent orogenesis to the Sleafordian Orogeny are discussed in Chapter 7.

The Miltalie Event at *c.* 2.0 Ga is the first event following the Sleafordian Orogeny and is represented by limited magmatism. This event has previously been suggested to represent the onset of rifting after approximately 400 Myrs of tectonic

quiescence (Daly et al., 1998; Hand et al., in press). The Miltalie Event remains effectively uncharacterised but provides a highly useful event timing for correlations with other Palaeoproterozoic terrains (Chapter 7).

Preserved within the late Palaeoproterozoic lithologies of the Gawler Craton (1850-1600 Ma) is a complex sequence of sedimentary, magmatic and orogenic events. The period from 1850-1600 Ma has undergone the most revision over the duration of this project. The review of Daly et al. (1998) outlined a sequence of events beginning with the Kimban Orogeny at 1845 - 1700 Ma. This orogeny was interpreted to consist of three events: KD_1 - 1845-1795 Ma, which produced layer parallel foliation; KD_2 - 1795-1745 Ma, which produced amphibolite to granulite grade metamorphism and upright, tight folding; KD_3 - 1745-1700 Ma, which produced regional, upright, open to tight folds and extensive mylonite development. Later deformation and metamorphism was collectively termed the Kararan Orogeny, which is interpreted to last from 1650-1540 Ma incorporating 'several younger, high-grade granulite facies events'. The Kararan Orogeny was interpreted to represent the collision of the northern Gawler Craton (Nawa Domain) with the Archaean core of the proto-Gawler Craton along the Karari Fault Zone. The term 'Ifould Complex' was coined to delineate any syn-Kararan, deformed intrusive bodies. The Ifould Complex was reassigned to the early Kararan Orogeny and, combined with the Tunkillia Suite, was proposed as a magmatic arc in the work of Ferris (2001) and Ferris et al. (2002).

Ferris et al. (2002) divided the Kimban Orogeny into the Neill Event (~1850 Ma) and the Kimban Orogeny (1730-1700 Ma). Ferris et al. (2002) agreed with the suggestion of Hoek and Schaefer (1998), that, given the *c.* 150 Myr gap between them, the two events were unlikely to be related. This is particularly the case given the extensive sediment deposition, volcanism and crustal extension that occurred between the two events. Ferris et al. (2002) retained the Kararan Orogeny nomenclature but extended the duration to 1690-1540 Ma to include metamorphism present in the Ooldea 2 drillhole and the Tunkillia and Ifould Suite intrusions. Since the review of Ferris et al. (2002) each of the late Palaeoproterozoic to Mesoproterozoic tectonic events in the Gawler Craton have been refined and re-interpreted. These changes are outlined and discussed in the majority of chapters in this thesis.

The motivation in outlining a Palaeoproterozoic tectonothermal evolution of the Gawler Craton is three-fold. Firstly, to allow for development of constraints on the tectonic setting leading up to the ensuing felsic large igneous province/event (GRV/Hiltaba) and the associated economically important mineralisation event. Secondly, to provide a sound basis for discussions on the evolution of the Palaeoproterozoic crust of Australia and recently proposed reconstruction models for this time period (Karlstrom et al., 2001; Betts et al., 2002; Dawson et al., 2002; Giles et al., 2002; Giles et al., 2004; Betts and Giles, 2006). Thirdly, to provide a basis for global correlations and reconstruction models of the Gawler Craton and Australia with other Palaeoproterozoic crust, in particular Antarctica and Laurentia. It is hoped that subsequent to this work, future discussions of Earth evolution during the late Archaean and early Proterozoic can better incorporate the information provided by the southern Australian Palaeoproterozoic.

Thesis Outline

This thesis has been written in the form of individual manuscripts addressing specific aspects of the Palaeoproterozoic evolution of the Gawler Craton culminating in the final chapter addressing the Palaeoproterozoic evolution of the Gawler Craton. The manuscripts have largely been left in their original state to allow the reader to follow the progression of the working model for the Palaeoproterozoic evolution of the Gawler Craton. This leads to some repetition but highlights the contribution of this research project to the current understanding of Proterozoic Australia and also demonstrates the significant changes in understanding of the Gawler Craton evolution.

Chapter 2 reports a series of experimental procedures for LA-ICP-MS U-Pb monazite geochronology. The author of this thesis, in association with Benjamin Wade (eg. Wade et al. 2007), undertook a large proportion of the setup of the LA-ICP-MS facility at the University of Adelaide. This chapter focuses on fractionation characteristics of the U-Pb isotope system in a monazite matrix and gives examples of comparative monazite geochronology from the Arunta Region of the North Australian Craton.

Chapter 3 investigates the temporal, geochemical and isotopic constraints on a series of previously uncharacterised Palaeoproterozoic metasedimentary lithologies from the northern Gawler Craton. This chapter is published as 'Provenance of metasedimentary rocks in the northern Gawler Craton, Australia: Implications for Palaeoproterozoic reconstructions', Payne, J.L., Barovich, K.M. and Hand, M., 2006, Precambrian Research 148, pp. 275-291. Geochronological data on an additional sample (Manya 4) is included as an appendix to the thesis chapter.

Chapter 4 investigates the timing of high-grade metamorphism in the northern Gawler Craton. This metamorphism was largely unconstrained in age. The work presented in Chapter 4 demonstrates conclusively the craton-wide nature of the Kimban Orogeny. This chapter has been accepted for publication as 'Temporal constraints on the timing of high-grade metamorphism in the northern Gawler Craton: implications for assembly of the Australian Proterozoic', Payne, J.L., Hand, M., Barovich, K.M. and Wade, B.P., 2007, Australian Journal of Earth Sciences.

Chapter 5 addresses the petrogenesis of the Tunkillia Suite magmatism using whole-rock isotope and geochemistry techniques. Previous classification as a subduction-related magmatic arc has led to its use as a plate-boundary constraint in a number of reconstruction models for Proterozoic Australia and Laurentia. However, these models have been based on a virtual absence of geochemical and isotopic data fo the Tunkillia Suite. The tectonic setting of the Tunkillia Suite is refined in light of new geochemical and isotopic data and the implications for the evolution of the Gawler Craton and for Proterozoic Australia are assessed.

Chapter 6 addresses the age and petrogenesis of the gt-ms-bi-bearing Munjeela Granite in the south-western Gawler Craton and examines the detrital zircon signature and provenance of metasedimentary enclaves within the granite.This work establishes the presence of a previously unrecognised metasedimentary sequence and highlights a metamorphic and deformational event in the period ~1620-1585 Ma. The granite is demonstrated to be generated through crustal anatexis and is co-eval with the voluminous 1595-1575 Ma Hiltaba Suite magmatism and represents crustally-derived melt. The presence of crustal thickening during the period 1620-1585 Ma is the first conclusive evidence for crustal thickening during this time period.

Chapter 7 provides a review of the evolution of the Gawler Craton in the context of the Mawson Continent that links the Gawler Craton with equivalent terrains in Terre Adelie Land and wider East Antarctica correlations. From the refined tectonothermal evolution of the Mawson Continent a new reconstruction model is proposed highlighting the apparently continuous relationship between the North Australian Craton and the Mawson Continent until their separation at *c.* 1.55 Ga. Correlations between the Mawson/NAC crust and the Sask Craton of the Trans-Hudson Orogen, Laurentia, and the North Korean peninsula are made, demonstrating the requirement for further consideration of the late Archaean-early Palaeoproterozoic history of the Earth. This chapter is currently under review for the IGCP 509 'Palaeoproterozoic Earth' Geological Society of London Special Publication.

In addition to the manuscripts listed, additional articles which I have co-authored are published in peer-reviewed journals. These manuscripts are listed in the introductory section of this thesis. Throughout this project results have been presented in conference abstracts which are also listed in the introductory section.

Supplementary Appendices are provided which include a case study of monazite geochronology from the Harts Ranges, central Australia, and copies of two co-authored peer-reviewed publications.

References

Allen, S.R. and McPhie, J., 2002. The Eucarro Rhyolite, Gawler Range Volcanics, South Australia: A > 675 km^3, compositionally zoned lava of Meso-proterozoic age. Geological Society of America Bulletin, 114(12): 1592-1609.

Allen, S.R., Simpson, C.J., McPhie, J. and Daly, S.J., 2003. Stratigraphy, distribution and geochemistry of widespread felsic volcanic units in the Mesoproterozoic Gawler Range Volcanics, South

Australia. Australian Journal of Earth Sciences, 50(1): 97-112.

Aspler, L.B. and Chiarenzelli, J.R., 1998. Two neoarchean supercontinents? Evidence from the paleoproterozoic. Sedimentary Geology, 120(1-4): 75-104.

Barley, M.E., Bekker, A. and Krapez, B., 2005. Late Archean to Early Paleoproterozoic global tectonics, environmental change and the rise of atmospheric oxygen. Earth and Planetary Science Letters, 238(1-2): 156-171.

Betts, P.G. and Giles, D., 2006. The 1800-1100 Ma tectonic evolution of Australia. Precambrian Research, 144(1-2): 92-125.

Betts, P.G., Giles, D., Lister, G.S. and Frick, L.R., 2002. Evolution of the Australian lithosphere. Australian Journal of Earth Sciences, 49(4): 661-695.

Bleeker, W., 2003. The late Archean record: a puzzle in ca. 35 pieces. Lithos, 71(2-4): 99-134.

Brown, M., 2007. Metamorphic conditions in orogenic belts: A record of secular change. International Geology Review, 49(3): 193-234.

Budd, A., 2006. The Tarcoola Goldfield of the Central Gawler Gold Province, and the Hiltaba association Granites, Gawler Craton, South Australia. Ph.D. Thesis, Australian National University, 365 pp.

Collins, A.S., Reddy, S.M., Buchan, C. and Mruma, A., 2004. Temporal constraints on Palaeoproterozoic eclogite formation and exhumation (Usagaran Orogen, Tanzania). Earth and Planetary Science Letters, 224(1-2): 175-192.

Creaser, R.A., 1995. Neodymium Isotopic Constraints for the Origin of Mesoproterozoic Felsic Magmatism, Gawler-Craton, South Australia. Canadian Journal of Earth Sciences, 32(4): 460-471.

Creaser, R.A. and White, A.J.R., 1991. Yardea Dacite - Large-Volume, High-Temperature Felsic Volcanism from the Middle Proterozoic of South-Australia. Geology, 19(1): 48-51.

Daly, S.J. and Fanning, C.M., 1993. Archaean. In: J.F. Drexel, W.V. Preiss and A.J. Parker (Editors), The geology of South Australia - The Precambrian, Bulletin 54. Mines and Energy, South Australia, Adelaide, pp. 242.

Daly, S.J., Fanning, C.M. and Fairclough, M.C., 1998. Tectonic evolution and exploration potential of the Gawler Craton, South Australia. In: I. Hodgson and B. Hince (Editors), Geology and mineral potential of major Australian mineral provinces. AGSO Journal of Australian Geology and Geophysics, pp. 145-168.

Dawson, G.C., Krapez, B., Fletcher, I.R., McNaughton, N.J. and Rasmussen, B., 2002. Did late Palaeoproterozoic assembly of proto-Australia involve collision between the Pilbara, Yilgarn and Gawler cratons? Geochronological evidence from the Mount Barren Group in the Albany-Fraser Orogen of Western Australia. Precambrian Research, 118(3-4): 195-220.

Direen, N.G., Cadd, A.G., Lyons, P. and Teasdale, J., 2005. Architecture of Proterozoic shear zones in the Christie Domain, western Gawler Craton, Australia: Geophysical appraisal of a poorly exposed orogenic terrane. Precambrian Research, 142: 28-44.

Direen, N.G. and Lyons, P., in press. Crustal setting of iron-oxide Cu-Au mineral systems of the Olympic dam region, South Australia: insights from potential fields data. Economic Geology.

Fairclough, M.C., Schwarz, M. and Ferris, G.J., 2004. Interpreted crystalline basement geology of the Gawler Craton, South Australia. In: J. Mcphie and P. McGoldrick (Editors), 17th Australian Geological Conference. Geological Society of Australia, Hobart.

Ferris, G.J., 2001. The geology and geochemistry of granitoids in the CHILDARA region, western Gawler Craton, South Australia: implications for the Proterozoic tectonic history of the western Gawler Craton and the development of the lode-style gold mineralisation at Tunkillia. M.Sc. Thesis, University of Tasmania.

Ferris, G., Schwarz, M. and Heithersay, P., 2002. The Geological Framework, Distribution and Controls of Fe-Oxide and Related Alteration, and Cu-Au Mineralisation in the Gawler Craton, South Australia: Part 1: Geological and Tectonic Framework. In: T. Porter (Editor), Hydrothermal Iron Oxide Copper-Gold & Related Deposits: A Global Perspective. PGC Publishing, Adelaide.

Fraser, G.L. and Lyons, P., 2006. Timing of Mesoproterozoic tectonic activity in the northwestern Gawler Craton constrained by $^{40}Ar/^{39}Ar$ geochronology. Precambrian Research, 151: 160-184.

Furnes, H., de Wit, M., Staudigel, H., Rosing, M. and Muehlenbachs, K., 2007. A vestige of Earth's oldest ophiolite. Science, 315(5819): 1704-1707.

Giles, D., Betts, P. and Lister, G., 2002. Far-field continental backarc setting for the 1.80-1.67 Ga basins of northeastern Australia. Geology, 30(9): 823-826.

Giles, D., Betts, P.G. and Lister, G.S., 2004. 1.8-1.5-Ga links between the North and South Australian Cratons and the Early-Middle Proterozoic configuration of Australia. Tectonophysics, 380: 27-41.

Hand, M., Reid, A. and Jagodzinski, E.A., in press. Tectonic framework and evolution of the Gawler Craton,

Southern Australia. Economic Geology.

Hickman, A.H., 2004. Two contrasting granite-greenstone terranes in the Pilbara Craton, Australia: evidence for vertical and horizontal tectonic regimes prior to 2900 Ma. Precambrian Research, 131(3-4): 153-172.

Hoek, J.D. and Schaefer, B.F., 1998. Palaeoproterozoic Kimban mobile belt, Eyre Peninsula: timing and significance of felsic and mafic magmatism and deformation. Australian Journal of Earth Sciences, 45(2): 305-313.

Holm, O., 2004. New geochronology of the Mount Woods Inlier and Central Gawler Gold Province, Gawler Craton - State of Play Conference, abstract volume. RB 2004/18, Primary Industries and Resources South Australia, Adelaide.

Howard, K.E., Reid, A.J., Hand, M., Barovich, K.M. and Belousova, E.A., 2007. Does the Kalinjala Shear Zone represent a palaeo-suture zone? Implications for distribution of styles of Mesoproterozoic mineralisation in the Gawler Craton. Minerals and Energy South Australia Journal, 43: 6-11.

Jagodzinski, E.A., Black, L.P., Frew, R.A., Foudoulis, C., Reid, A., Payne, J.L., Zang, W. and Schwarz, M., 2006. Compilation of SHRIMP U-Pb geochronological data, for the Gawler Craton, South Australia 2005. Geochronology Series Report Book 2005-1. Geochronology Series Report Book 2005-1, Primary Industries and Resources South Australia, Report Book 2006/20.

Johnson, J.P. and Cross, K.C., 1995. U-Pb Geochronological Constraints on the Genesis of the Olympic Dam Cu-U-Au-Ag Deposit, South Australia. Economic Geology and the Bulletin of the Society of Economic Geologists, 90(5): 1046-1063.

Karlstrom, K.E., Åhall, K.-I., Harlan, S.S., Williams, M.L., McLelland, J. and Geissman, J.W., 2001. Long-lived (1.8-1.0 Ga) convergent orogen in southern Laurentia, its extensions to Australia and Baltica, and implications for refining Rodinia. Precambrian Research, 111: 5-30.

Kump, L.R. and Barley, M.E., 2007. Increased subaerial volcanism and the rise of atmospheric oxygen 2.5 billion years ago. Nature, 448(7157): 1033-1036.

McFarlane, C.R.M., 2006. Palaeoproterozoic evolution of the Challenger Au Deposit, South Australia, from monazite geochronology. Journal of Metamorphic Geology, 24(1): 75-87.

Moller, A., Appel, P., Mezger, K. and Schenk, V., 1995. Evidence for a 2 Ga Subduction Zone - Eclogites in the Usagaran Belt of Tanzania. Geology, 23(12): 1067-1070.

Moyen, J.F., Stevens, G. and Kisters, A., 2006. Record of mid-Archaean subduction from metamorphism in the Barberton terrain, South Africa. Nature, 442(7102): 559-562.

Nutman, A.P., Friend, C.R.L. and Bennett, V.C., 2002. Evidence for 3650-3600 Ma assembly of the northern end of the Itsaq Gneiss Complex, Greenland: Implication for early Archaean tectonics. Tectonics, 21(1).

Parker, A.J., 1993. Palaeoproterozoic. In: J.F. Drexel, W.V. Preiss and A.J. Parker (Editors), The geology of South Australia - The Precambrian, Bulletin 54. Mines and Energy, South Australia, Adelaide, pp. 242.

Payne, J.L., Barovich, K. and Hand, M., 2006. Provenance of metasedimentary rocks in the northern Gawler Craton, Australia: Implications for palaeoproterozoic reconstructions. Precambrian Research, 148(3-4): 275-291. ***Chapter 3 of this thesis.***

Payne, J.L., Hand, M., Barovich, K. and Wade, B.P., 2007. Temporal constraints on the timing of high-grade metamorphism in the northern Gawler Craton: implications for construction of the Australian Proterozoic. Australian Journal of Earth Sciences, Accepted. ***Chapter 4 of this thesis.***

Peucat, J.J., Capdevila, R., Fanning, C.M., Ménot, R.P., Pecora, L. and Testut, L., 2002. 1.6 Ga felsic volcanic blocks in the moraines of the Terre Adélie craton, Antarctica: comparisons with the Gawler Range volcanics, South Australia. Australian Journal of Earth Sciences, 49: 831-845.

Peucat, J.J., Ménot, R.P., Monnier, O. and Fanning, C.M., 1999. The Terre Adélie basement in the East-Antarctica Shield: geological and isotopic evidence for a major 1.7 Ga thermal event; comparison with the Gawler Craton in South Australia. Precambrian Research, 94: 205-224.

Scott, D.J., Helmstaedt, H. and Bickle, M.J., 1992. Purtuniq Ophiolite, Cape-Smith Belt, Northern Quebec, Canada - a Reconstructed Section of Early Proterozoic Oceanic-Crust. Geology, 20(2): 173-176.

Scott, D.J., St-Onge, M.R., Lucas, S.B. and Helmstaedt, H., 1999. The 2.00 GA purtuniq ophiolite, Cape Smith Belt, Canada: Morb-like crust intruded by OIB-like magmatism. Ofioliti, 24(2): 199-215.

Smithies, R.H., Van Kranendonk, M.J. and Champion, D.C., 2007. The Mesoarchean emergence of modern-style subduction. Gondwana Research, 11(1-2): 50-68.

Stern, R.J., 2005. Evidence from ophiolites, blueschists, and ultrahigh-pressure metamorphic terranes that the modern episode of subduction tectonics began in

Neoproterozoic time. Geology, 33(7): 557-560.

Swain, G., Woodhouse, A., Hand, M., Barovich, K., Schwarz, M. and Fanning, C.M., 2005. Provenance and tectonic development of the late Archaean Gawler Craton, Australia; U-Pb zircon, geochemical and Sm-Nd isotopic implications. Precambrian Research, 141(3-4): 106-136.

Tomkins, A.G., Dunlap, W.J. and Mavrogenes, J.A., 2004. Geochronological constraints on the polymetamorphic evolution of the granulite-hosted Challenger gold deposit: implications for assembly of the northwest Gawler Craton. Australian Journal of Earth Sciences, 51: 1-14

Wade, B.P., Payne, J.L., Hand, M. and Barovich, K.M., 2007. Petrogenesis of ca 1.50 Ga granitic gneiss of the Coompana Block: filling the 'magmatic gap' of Mesoproterozoic Australia. Australian Journal of Earth Sciences, 54: 1089-1102.

Chapter 2

Optimisation of laser ablation conditions for LA-ICP-MS U-Pb monazite geochronology

Abstract

This study presents a method for optimisation of ablation conditions in Laser Ablation Inductively Coupled Plasma Mass Spectrometry (LA-ICP-MS) with the aim of obtaining accurate, precise and repeatable U-Pb isotopic analyses for monazite U-Pb geochronology. A series of laser irradiance experiments demonstrate decreased and stable U-Pb fractionation in monazite for laser irradiances above ~2.5 GW/cm^2 (λ=213nm, 15 and 30 μm spot size). Above ~2.5 GW/cm^2 fractionation during ablation of a monazite matrix is also demonstrated to be independent of pit depth/width ratios. This result, combined with pit depth measurements, indicates optimal irradiance at approximately 2.7-3.0 GW/cm^2.

Comparison of isotope ratios with count per second data for 15 and 30 μm diameter ablation pits suggests instrument loading or detector dead time corrections are not solely responsible for the observed plateau in isotope ratios above 2.5 GW/cm^2. The obtained results suggest ablation characteristics of a monazite matrix change at an irradiance of ~2.5 GW/cm^2, potentially due to the onset of extensive plasma shielding. Smaller ablated particle size or less thermal ablation is suggested to account for the lesser degree of mass bias observed at higher irradiance levels. The use of simultaneous tracer solution aspiration is required to fully resolve the mechanism for isotope fractionation stabilisation.

2.1 Introduction

Monazite ((REE)PO_5) is a useful accessory mineral for constraining the timing of amphibolite to granulite grade metamorphic events (ie. Parrish, 1990; Rubatto et al., 2001; Williams and Jercinovic, 2002). It has been demonstrated to generally contain negligible common Pb and is less susceptible to radiogenic Pb loss than zircon (Parrish, 1990; Smith and Giletti, 1997). Four techniques are commonly used for geochronological analysis of monazite: Thermal Ionisation Mass Spectrometry (TIMS), Electron Probe Microanalysis (EPMA) chemical dating, Secondary Ion Microprobe Spectrometry (SIMS or SHRIMP) and Laser Ablation Inductively Coupled Plasma Mass Spectrometry (LA-ICP-MS).

TIMS remains the benchmark technique for analysis of the U-Pb isotope system, but has traditionally been constrained by the necessity for bulk mineral separates. Recent advances in spikes and ultra-low level Pb-blanks (ie. 300-500 femtograms) have allowed for micro-sampling of individual or small numbers of grains (eg. Schoene et al., 2006). Despite these advances, TIMS analysis is still restricted by the expensive, complex and time-intensive nature of the method and its continuing lack of application to petrographically constrained samples. Secondary Ion Mass Spectrometry (SIMS or SHRIMP) is generally considered to be the second most precise method for U-Pb isotope dating but is a relatively time-consuming technique, requiring the mounting of the standard mineral with the monazites to be analysed (eg. Foster et al., 2000). EPMA chemical dating is the most successful for constraining the relationships of monazites to metamorphic mineral growth (eg. Montel et al., 1996; Williams and Jercinovic, 2002; Pyle et al., 2005) but is limited by lower precision (than TIMS or SIMS) and the lack of isotope analysis to resolve inherited Pb or Pb-loss. LA-ICP-MS is a quick, versatile and accurate technique but until recently has had relatively limited application to monazite geochronology to date (Kosler et al., 2001; Willigers et al., 2002; Horstwood et al., 2003).

All U-Pb isotope LA-ICP-MS analysis must overcome a consistent set of technical difficulties as summarised by Kosler et al. (2001), Russo et al. (2002a), Poitrasson et al. (2003) and Jackson et al. (2004). These are: 1) bias produced during the ionisation process in the ICP-MS; 2) mass bias produced after the ionisation process; 3) laser-induced elemental and isotope fractionation; and 4) difficulty in common Pb correction due to ^{204}Hg interference. Various methods to successfully account for common Pb correction have been developed (eg. Andersen, 2002; Horstwood et al., 2003; Hirata et al., 2005; Storey et al., 2006) and are not the focus of this study. Mass bias produced after ionisation (ie. space charge effects) is corrected using an external standard (eg. Hirata and Nesbitt, 1995; Jackson et al., 2004) or injection of a nebulised 'spike' or 'tracer' solution (eg. Horn et al., 2000; Kosler et al., 2001; Williger et al., 2002).

Bias and fractionation created during the ICP ionisation process is intimately linked to intrinsic fractionation (IF) and time-dependent fractionation (TDF), also referred to as laser induced elemental fractionation (LIEF) in many geological material based studies. The use of the term TDF includes time-dependent isotopic fractionation such as that reported by Jackson and Gunther (2003) created in the ablation process (Russo et al., 2002a).

IF results from the fact that for any laser pulse there will be preferential volatilisation of some elements and isotopes from the sample surface during the pulse, and preferential condensation of isotopes around the ablation pit and into varying particle sizes during and after the pulse (Jackson and Gunther, 2002; Russo et al., 2002a). TDF is the changing fractionation characteristics of the element or isotope ratio signal as the ablation progresses (generally as the ablation pit deepens: ie. Fryer et al., 1995; Longerich et al., 1996; Jackson and Gunther, 2002). Effectively, TDF is the manner in which the IF characteristics change over the duration of a single ablation. These sources of error are the most pressing and limiting factor of U-Pb geochronology LA-ICP-MS (Gunther and Hattendorf, 2005). Sufficient studies have demonstrated that ablation and ionisation fractionation can be successfully corrected for using matrix-matched external standards. However, a thorough understanding of the two sources of fractionation will lead to much greater accuracy and ultimately matrix independent analysis.

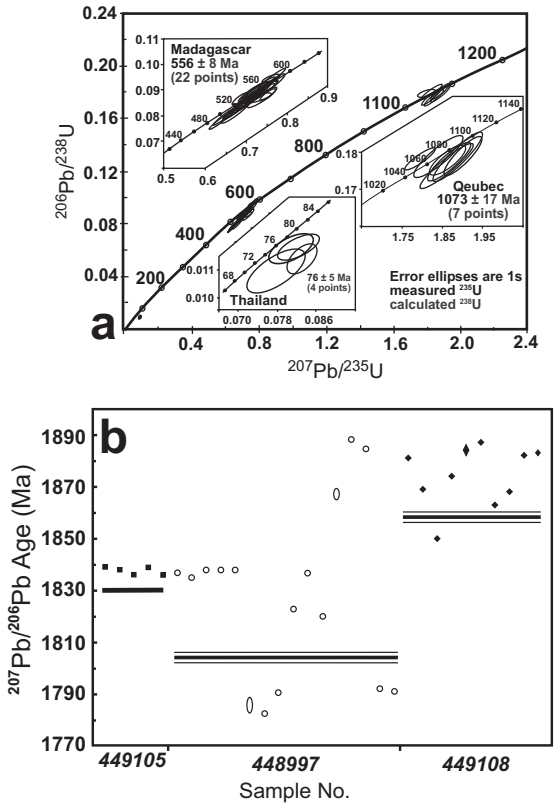

Figure 2.1 - a) Monazite LA-ICP-MS geochronology results of Kosler et al. (2001) demonstrating old ages recorded for ^{207}Pb/^{206}Pb and ^{207}Pb/^{235}U. Originally published in Geostandards Newsletter: The Journal of Geostandards and Geoanalysis (2001, Vol. 25 No. 2-3, pp. 375-386), reproduced by permission of the copyright holder - Association Scientifique pour la Geologie et ses Applications (AGSA). b) Summary of LA-MC-ICP-MS data of Williger et al (2002) and TIMS data of Williger et al (2001) for 3 monazite samples. TIMS data is represented by solid lines. 2σ error is represented by thickness of line or thin lines above and below thick line. LA-ICP-MS data is represented by points with vertical extent representing 2 S.E.

The source of fractionation within the ICP is incomplete ionisation of large particles (Jeong et al., 1999; Guillong and Gunther, 2002; Guillong et al., 2003; Jackson and Gunther, 2003). This has been demonstrated to result in elemental fractionation (ie. U-Pb, Guillong et al., 2003) and isotopic fractionation (ie. ^{65}Cu/^{63}Cu, Jackson and Gunther, 2003) but the effect can be significantly reduced and possibly removed by separation of large particles out of the transported material. The success of such methods highlights the preference of certain species to agglomerate into large particles after ablation or be enriched in large particles removed during the ablation process. However, simple particle separation does not address the

mechanisms causing the ablation fractionation and subsequent ICP mass bias. One such example is the thermal alteration of zircon to baddeleyite in the pit walls during laser ablation (resulting in the preferential removal of some elements from the matrix) and variable enrichments of differing elements in ejecta blankets (Kosler et al., 2005). Particle separation clearly does not address these phenomena. From this research, Kosler et al. (2005) pointed to the importance of matrix-matched external calibration. Further work is required to resolve the mechanisms relating to particle formation and element partitioning into particles for variable matrix compositions.

Despite the increasing usage of LA-(MC)-ICP-MS for monazite U-Pb geochronology (eg. Poitrasson et al., 2000; Foster et al., 2002; Foster et al., 2004; Gehrels et al., 2006) few publications deal directly with the procedure for U-Pb isotope geochronology of monazite. Kosler et al. (2001) produced U/Th/Pb ages using a 266nm Nd-YAG laser coupled to a single-collector quadropole ICP-MS. The method employed a tracer solution ($^{205}Tl/^{233}U$) to correct for mass bias in the ICP-MS and used laser rastering and the 'intercept method' (Sylvester and Ghaderi, 1997) to minimise and correct for laser-induced inter-element fractionation. Willigers et al. (2002) reported $^{207}Pb/^{206}Pb$ acquired using a 266 nm Nd-YAG laser and a multi-collector ICP-MS. Pb-mass bias was corrected by measuring $^{205}Tl/^{203}Tl$ in an external standard (NIST glass standard). Horstwood et al. (2003) also utilise a multi-collector ICP-MS coupled to a 266nm Nd-YAG laser but use beam rastering and tracer-solution correction method with a monazite standard to correct for ablation and ionisation fractionation. None of the above-mentioned publications use particle removal/separation devices (ie. Guillong et al., 2003).

Kosler et al. (2001) demonstrate the ability of their method to obtain accurate (within error) $^{206}Pb/^{238}U$ ages for two monazites (U-Pb TIMS ages: 72 ± 1 and 555 Ma) but U-Pb ages that are approximately 30 Myrs too old for a third monazite sample (Figure 2.1a, U-Pb concordant TIMS age: 1040 ± 2 Ma). Their data also show a systematic over-estimation of the ^{207}Pb content, which draws the data points away from concordia and results in excessively old $^{207}Pb/^{206}Pb$ ages. The authors suggest the unreliable $^{207}Pb/^{206}Pb$ ages are due to young monazites and the older age is due to sample heterogeneity. Willigers et al. (2002) report data that are not within error of the previously reported TIMS ages (Willigers et al., 2001) for the studied samples, in part due to the precise nature of their measurements (Figure 2.1b). The study highlighted the complexity of ages recorded by the investigated monazite populations (Figure 2.1b), but even for single age monazite samples the LA-MC-ICP-MS ages were older than those obtained by TIMS analysis. Horstwood et al. (2003) demonstrate monazite ages which are within error of the known TIMS ages and reproducibility typically <1% and <3% for $^{207}Pb/^{206}Pb$ and $^{206}Pb/^{238}U$ ages, respectively. They also present zircon data using monazite as an external standard with beam rastering to account for laser induced elemental fractionation, which will be discussed further in later sections.

This study presents a U-Pb dating method of monazite using a single-collector quadrupole ICP-MS and external standardisation methods and reports on a study into the optimisation of laser ablation conditions for a small beam size (15µm compared to 30-40+µm beam often employed for zircon geochronology, ie. Kosler et al., 2002; Jackson et al., 2004). The results are discussed with respect to the geochronology method and other LA-ICP-MS geochronology techniques. This study was undertaken as part of the establishment of U-Pb isotope monazite dating at the University of Adelaide which is used in later chapters of this thesis.

2.2 Instrumentation

The instrumentation used in this study consists of a Merchantek-New Wave Research UP213, 213 nm, 5 ns pulse-length UV laser. This is linked to an Agilent 7500cs quadrupole ICP-MS. A summary of operating conditions and data acquisition is provided in Table 2.1. A cell-insert that holds two 2.5cm diameter epoxy mounts was manufactured for the standard UP213 sample cell. Data reduction and presentation utilised the LA-ICP-MS data reduction program GLITTER (van Achterbergh et al., 2001) and Isoplot 3 (Ludwig, 2003). ICP-MS tuning for sensitivity was conducted upon NIST 610 silica glass to enable monitoring of oxide formation (using 248/232 = ThO/Th). Further tuning was conducted on monazite to ensure maximum sensitivity for the different monazite matrix

composition.

2.3 Methods

As monazites are often smaller than zircons and display complex compositional and growth/re-setting zoning, spatial resolution is important. Therefore this study is based upon the use of a 15 μm laser spot size focused on the monazite polished surface. Use of a small single spot optimises horizontal (x,y) spatial resolution but results in decreased vertical (z) resolution in comparison to scanned laser sampling methods (eg. Kosler et al., 2001; Foster et al., 2002). For matrix-matched methods, single spot ablation is still preferable, as research by Gonzalez et al. (2004) has demonstrated that single spot ablation has greater accuracy and precision and is less matrix dependent than scanned ablation methods (for NIST 610-616 glasses and a tuff). A set of experiments was conducted to determine the optimal laser irradiances and a comparison made with the isotopic fractionation characteristics of another matrix type (silicate glass, NIST 610). This provides some degree of independent comparison for methods which use non-matrix matched external standardisation.

Two samples are used for this section of the study. Isotopic details for each are listed in Table 2.2. The first is the monazite, MAdel. The monazite fragments come from one large grain (~3x1cm) with average Th and U concentrations of 8.98 wt% and 0.43 wt% (Appendix 2.1). TIMS analyses were conducted at Massachusetts Institute of Technology and is supplemented with in-house analysis at the University of Adelaide. The method involved is identical to that described in Schoene et al. (2006) for xenotime. In-house TIMS analysis methods follow those described for monazite in Elburg et al. (2003). TIMS analyses highlight the dual age nature of the standard MAdel, with $^{207}Pb/^{235}U$ ages of *c*. 510 Ma and *c*. 513 Ma. This age variation is well within analytical uncertainty of the LA-ICP-MS technique and is further accounted for by analysing multiple fragments within a single analysis run and assigning a 1% uncertainty to the age of the standard within GLITTER. The silicate glass analysed is NIST 610. Isotopic ratios used for this glass are those reported by Stern and Amelin (2003).

Table 2.1 - LA-ICPMS specifications and operating conditions

Laser Ablation system		
Merchantek New Wave UP 213		
Laser Type	Nd-YAG frequency quintupled	
Wavelength	213 nm	
Pulse Duration	5 ns	
Beam Cross-section	Parabolic	
Laser Irradience	Optimisation	0.4-4.4 GW/cm^2
	Analysis	~2.7 GW/cm^2
Spot Size	15 μm	
Repetition Rate	5 Hz	
Transport System		
Ablation Atmosphere	He	
Carrier Gas	Ar, ~0.9 L/min	
Tubing	Tygon ^{TM}, 3.2mm Int. Dia.	
ICP-MS		
Agilent 7500cs		
Plasma Forward Power	1300	
Plasma Gas Flow	15 L/min	
Spectrometer	Quadrupole	
Measured Masses	Optimisation - ^{204}(Hg+Pb), ^{206}Pb, ^{207}Pb, ^{235}U, ^{238}U	
	Age analysis -^{204}(Hg+Pb), ^{206}Pb, ^{207}Pb, ^{238}U	
Dwell Times	10, 15, 30 and 15 ms resp.	
Counting Mode	Pulse and Analog	

Experiments to determine the most suitable laser irradiance for monazite geochronology were conducted with a 15 μm beam diameter at 28 different power levels. These range from ~0.4 to ~4.4 GW/cm^2 as recorded by the UP213 internal power meter. This value is calculated by the UP213 software to represent the energy incident upon the sample surface (based on the assumption that the lens apparatus is clean and operating at its optimum level). Each analysis consisted of a 60 second gas blank measurement (including a 10 second laser warm-up) followed by 60 seconds of ablation. Unless otherwise described, for all U-Pb, Pb-Pb and U-U isotope measurements the signal was integrated for the interval ~10-40 seconds after the signal arrival time. Three repeats of all power levels were completed upon MAdel (Fractest 1, 2

Table 2.2 - U-Pb Isotopic composition for MAdel monazite and NIST 610

		$^{206}Pb/^{238}U$				$^{207}Pb/^{235}U$				$^{207}Pb/^{206}Pb$			
		Ratio		Age		Ratio		Age		Ratio		Age	
Sample	Method		2σ	(Ma)	2σ		2σ	(Ma)	2σ		2σ	(Ma)	2σ
Madel	TIMS[a]	0.083681	41	518.06	0.24	0.657679	434	513.19	0.27	0.057001	26	491.6	1.0
		0.083611	44	517.64	0.26	0.657445	502	513.05	0.31	0.057029	31	492.6	1.2
		0.083138	39	514.83	0.23	0.653150	453	510.42	0.28	0.056979	29	490.7	1.1
	TIMS (In-h)	0.082973	51	513.8	0.3	0.6535159	1456	510.6	0.85	0.057039	101	495.7	3.9
NIST 610	TIMS[b]	0.25664	22			97.51034*				0.9094*			

[a]TIMS analysis conducted at MIT, (In-h) = In-house TIMS analysis, [b]Data sourced from Stern and Amelin 2003,
*Ratios calculated from published data

and 3). To test the behaviour of fractionation for significantly different sample composition, a single repeat was completed upon the NIST 610 alternating with analyses of MAdel (FNIST 1 and FNMAD 1, respectively). The effects of beam diameter upon fractionation were tested by carrying out two repeats alternating between a 15 and 30 μm spot size on MAdel. To test the repeatability of isotope measurements, four repeat analyses were done at output irradiances of 0.4, 1.1, 2.3 and 3.8 GW/cm^2.

Cross-sections of selected ablation pits were constructed to enable quantification of ablation rates. This was done using a series of stereo-pair images taken in scanning electron mode on a Phillips XL30 FESEM. Repeated depth measurements on individual spots indicate a conservative accuracy estimate on the order of ~2-3 μm at a depth of 50 μm.

2.4 Optimisation Experiment Results

Basic U-Pb and Pb-Pb ratio information for the 28 power levels of ablation on monazite is represented in Figures 2 and 3. All results from optimisation experiments are reported in Appendix 2.2.

Figure 2.2a shows typical analyses (analysis run Fractest 2) for which no correction was made for ICP-MS drift. Figure 2.2b shows ratios after correction for ICP-MS drift (and by default mass bias) by using a linear fit for analyses at ~1.1 GW/cm^2 laser irradiance in consecutive runs. In

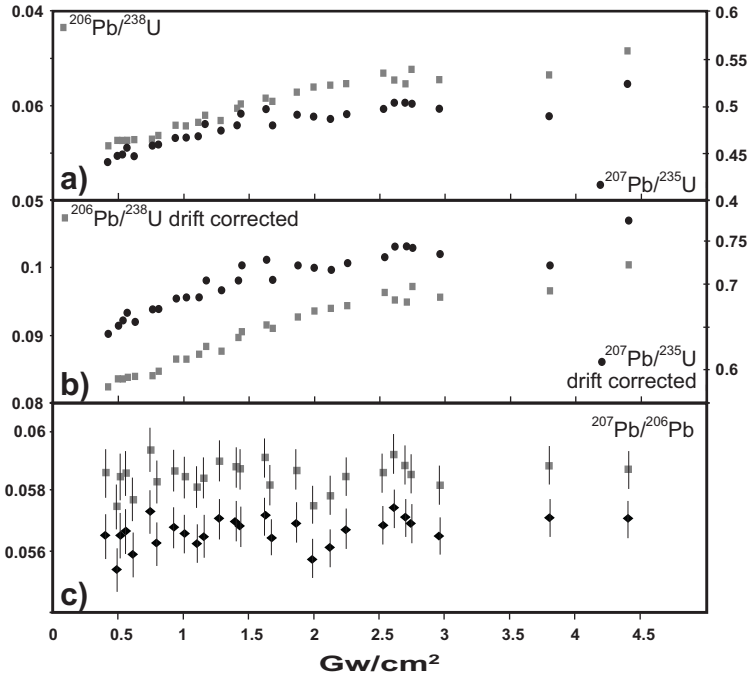

Figure 2.2 - Representative U/Pb and Pb/Pb isotope ratios obtained from integration of MAdel signal. a) Uncorrected U/Pb isotopes for analysis run Fractest 2. b) Drift (and mass bias) corrected isotope ratios of Fractest 2. $^{206}Pb/^{238}U$ is on left-hand axis, $^{207}Pb/^{235}U$ is on right-hand axis. c) Corrected (bottom set) and un-corrected $^{207}Pb/^{206}Pb$ ratios for Fractest. a) and b) demonstrate stabilisation of U/Pb ratios above ~2.5 GW/cm^2. c) demonstrates that little change is seen in $^{207}Pb/^{206}Pb$ over the irradiance range.

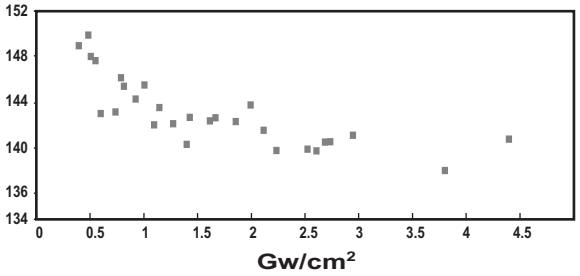

Figure 2.3 - $^{238}U/^{235}U$ ratios for MAdel demonstrating approach of ratios to actual value (137.88) at higher irradiance (Fractest 2).

all three analysis runs $^{206}Pb/^{238}U$ and $^{207}Pb/^{235}U$ ratios increase with increasing laser irradiance until ~2.2-2.5 GW/cm^2, above which ratios flatten. $^{207}Pb/^{206}Pb$ ratios for un-corrected and drift-corrected analyses are presented in Figure 2.2c. No definable trend is seen in the $^{207}Pb/^{206}Pb$ ratios across the power spectrum.

Uncorrected $^{238}U/^{235}U$ ratios are plotted in Figure 2.3 for the analysis run Fractest 2. The general trend of the isotope data is repeated in all datasets indicating it is not attributable to instrumental drift. As with the U-Pb ratios, a flattening in the isotope ratios is observed starting at approximately 2.2-2.5 GW/cm^2.

The intercept method (ie. Sylvester and Ghaderi, 1997; Kosler et al., 2001; Willigers et al., 2002) was used to calculate initial isotope ratios for 5 and 10 second intervals after the onset of ablation. The results for T_0=10 seconds are presented in Figures 2.4 and 2.5. Figure 2.4 displays the comparison between T_0 ratios and those obtained by integration of the signal. Little variation is seen between T_0 and integrated $^{207}Pb/^{206}Pb$ ratios for all irradiances. A distinct decrease is seen in the difference between the two ratios with increasing irradiance, and above ~2.5 GW/cm^2 the ratios are near identical. $^{206}Pb/^{238}U$ T_0 and integrated ratios display two notable characteristics. Below ~1 GW/cm^2 the T_0 value is greater than the integrated value. Both ratios follow a similar curvilinear trend with stabilisation of ratios above ~2.5 GW/cm^2, but T_0 ratios change by approximately half as much. Figure 2.5 displays the percent deviation of the calculated T_0 isotope ratios for NIST 610 and MAdel from their 'true' values (Table 2.2). The majority of $^{207}Pb/^{206}Pb$ analyses show that NIST ratios deviate from the true value by less than that of MAdel. For the analyses at ~3.4 and 4.2 GW/cm^2 the T_0 values are the same for both samples. The vast majority of NIST 610 Pb/U ratios deviate from their true value more than the ratios for MAdel, both of which are below the true value. Although not reported, the same trends are observed for T_0 values when calculated at T_0=5 seconds.

The mean counts per second (background subtracted) for individual isotopes and their combined total are plotted in Figure 2.6. All counts increase rapidly with increasing irradiance with the rate of increase slowing slightly at the two highest irradiance levels. Figure 2.7 displays cross-sections obtained from 8 ablation pits (irradiances ranging from 0.5-4.0 GW/cm^2) and the corresponding ablation rates. Ablation rates obtained from these pits behave in a similar manner to CPS and display a slowing in the rate of increase above ~3.0 GW/cm^2. The ablation rates do not take into account the increase in pit diameter resulting at higher irradiances.

Results of beam size comparisons are presented in Figure 2.8. Displayed are the integrated $^{206}Pb/^{238}U$ ratios obtained using a 15 and 30 μm beam diameter. Data for the 30 μm beam show a similar behaviour and stabilisation of ratios to the previously reported 15 μm beam data (Figure 2.2). When compared to the concurrent 15 μm data, the lesser degree of change in the 30 μm ratio data is evident. Above ~2.5 GW/cm^2 ratios for both beam sizes become approximately equivalent. Contrary to other test runs, a jump is seen in the 15 μm beam data prior to 2.5 GW/cm^2.

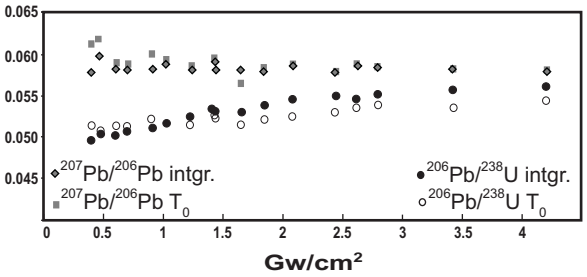

Figure 2.4 - Comparison of representative integrated and T_0 ratios demonstrating change in T_0 U/Pb ratios with irradiance.

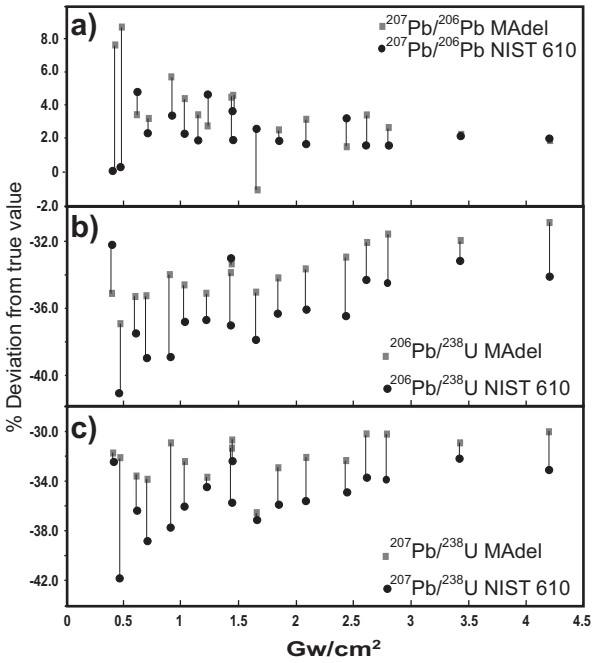

Figure 2.5 - Comparison of calculated T_0 isotope ratios for MAdel and NIST 610 demonstrating systematic difference in fractionation between the two matrix types. Axis is percent variation from actual value.

2.5 Discussion of Optimisation Experiment Results

This discussion is divided into two sections. The first addresses the results of the optimisation experiments dealing directly with the monazite analysis procedure to be utilised in later sections of the thesis. The second section deals with the implications for U-Pb dating of monazites using this and other techniques.

2.5.1 Optimisation of laser ablation for current method

Three basic factors were considered in the choice of laser power levels for the optimisation of ablation and U-Pb isotope dating of monazite: 1) the observed stabilisation of element and isotope ratios at increased laser irradiances; 2) the degree of repeatability of measurements at differing laser irradiances; and 3) the change in rate of ablation with increasing laser irradiances.

U/Pb ratios for integration of the ablation signal are observed to stabilise above ~2.2-2.5 GW/cm^2. This suggests that variation in laser intensity during analytical ablation will have less effect at irradiance levels above 2.5 GW/cm^2. This will result in an analytical signal and isotope analysis that should be not be affected by known laser instability (Tiepolo et al., 2003). Pb/U T_0 ratios (Figure 2.4) suggest the most accurate/stoichiometric ratios are observed above 2.5 GW/cm^2, where T_0 ratios display the least amount of intrinsic fractionation. This is also supported by U-U ratios (Figure 2.3) and possible Pb-Pb T_0 (Figure 2.4) stabilisation at this power level. Previous studies have reported stabilisation of Pb/U isotope ratios close to the actual value of a sample above 0.6 GW/cm^2 (Liu et al., 2000). Liu et al. reported this result for analysis of NIST 610 using 213 and 266nm laser wavelength. T_0 and integrated data from this study does not support this finding for monazite or NIST 610. It is suggested the earlier study focused on irradiance levels close to the ablation threshold and did not observe the changes in behaviour evident at higher irradiance levels.

Without simultaneous aspiration of tracer solutions it is not possible to separate changes in intrinsic laser ablation fractionation from changing ICP-MS mass bias. Potential causes for ICP-MS mass bias are increased instrument loading, detector dead time correction problems or the size and characteristics of material transported to the ICP-MS.

Two factors suggest ICP-MS mass bias due to instrument loading is not the sole explanation for the observed increase and subsequent stabilisation of Pb/U ratios. The volume of material received by the mass spectrometer (mean cps, Figure 2.6) does not follow exactly the same trend as the Pb/U ratios. A decrease in the rate of increase of mean cps is seen at ~3 GW/cm^2 but not a stabilisation as expected if ICP-MS mass bias was the sole cause for stabilisation of Pb/U ratios. Secondly, the likely candidate for ICP-MS mass bias associated with increased material volume is space-charge effects within the sample-skimmer cone region of the ICP-MS (ie. Tanner et al., 1994). If such an effect were involved, heavier isotopes (ie. ^{238}U) would be preferentially transported to the mass spectrometer, resulting in lower Pb/U ratios. This does not appear to be the case, suggesting the observed trends in Pb/U ratios are related in some manner to laser ablation.

Supporting the above observations are the 15-30 μm beam comparison data. For all but the lowest

power levels the 30 μm CPS are significantly higher than those for the 15 μm data above 2.5 GW/cm^2 (Appendix 2.2). These data suggest instrument loading is not a primary control on the fractionation stabilisation as, for equivalent volumes of ablated material, integrated isotope ratios are not equivalent. These beam comparison data also suggest detector dead time correction problems are not a primary control as isotope ratios are significantly different for equivalent counts on the most abundant mass (^{238}U).

One of the great advantages of monazite geochronology is the ability to link the growth of monazites to development of various tectonic foliations and metamorphic mineral growth (Parrish, 1990; Montel et al., 1996; Suzuki et al., 1996). For this purpose the analysis of monazites in thin-section is required. Petrographic thin-sections are generally 30-40 μm in thickness placing a maximum constraint upon ablation pit depth for the period to be integrated over (generally up to 40 sec.). Increased irradiance results in an increased rate of ablation, therefore minimising the laser irradiance while satisfying the constraints provided by the U-Pb ratio data is preferable. To this extent a laser output of ~2.6 GW/cm^2 is chosen. Such a level exceeds the 2.5 GW/cm^2 threshold for ratio stabilisation while minimising the ablation rate. The chosen level has an ablation rate of approximately 0.8 m/sec (Figure 2.7) and has been demonstrated to successfully ablate both small, mounted monazite grains (this study) and monazite grains in thin-section (Payne and Wade, unpub. data).

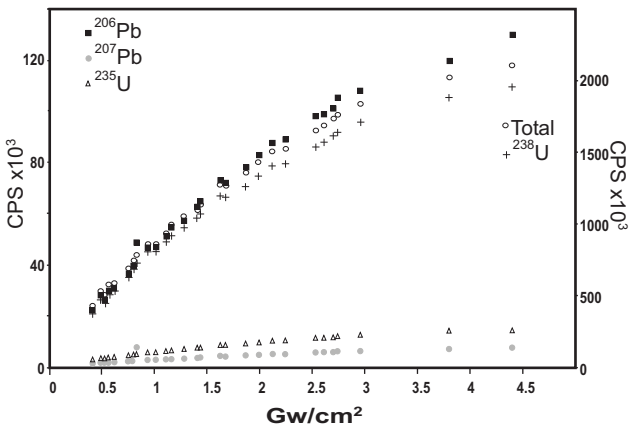

Figure 2.5 - Isotope and Total Counts Per Second for Fractest 2 analyses. Total CPS and ^{238}U CPS are on right-hand axis.

2.5.2 Implications of results for LA-ICP-MS U-Pb geochronology

This section of the discussion deals with the implications of this study for the wider field of LA-ICP-MS chemical analysis and LA-ICP-MS U-Pb monazite geochronology. Of particular note within this study is the mechanism causing isotope ratio stabilisation at ~2.5 GW/cm^2 for the wider application to producing consistent isotope measurements on geological samples, seemingly regardless of spot size. The observed difference in T_0 isotopic ratios between NIST 610 and MAdel has consequences for non-matrix matched tracer-solution method analysis of monazite.

Data obtained from integrated and T_0 ratios illustrate two modes of behaviour. The first, below ~2.5 GW/cm^2, is characterised by increasing isotope ratios and steadily increasing mean cps values (Figures 2.3 and 2.6). The second, above ~2.5 GW/cm^2, is characterised by a stabilisation of all isotope ratios, equivalence of ratios for differing beam sizes on monazite, the same ^{207}Pb/^{206}Pb ratios for NIST 610 and MAdel and a decrease in the efficiency of mass removal (typified by flattening of average cps) with irradiance (Figures 2.2, 2.5 and 2.6). This second mode is appears to also show a decrease in the extent of intrinsic fractionation (T_0 ratios closer to actual).

Increasing irradiances have been demonstrated to result in the formation of smaller particles in glass samples (Jeong et al., 1999). Increased formation of smaller ablation particles may be the mechanism causing more stoichiometric isotopic ratios for increasing irradiance in the first mode of isotope ratio behaviour. Alternatively, or more likely additionally, the slight decrease in deviation of isotopic ratios from the actual may relate to the decreasing role of thermal ablation mechanisms in monazite ablation.

The stabilisation of isotope ratios is interpreted to represent the onset of plasma shielding as indicated by the decreased efficiency of mass removal (ie. Shannon et al., 1995; Russo et al., 2002b). The occurrence of isotope fractionation stabilisation, independent of pit diameter, at the same irradiance levels is of particular interest. Further work is required to understand this phenomenon. It is suggested that the stabilisation of isotope

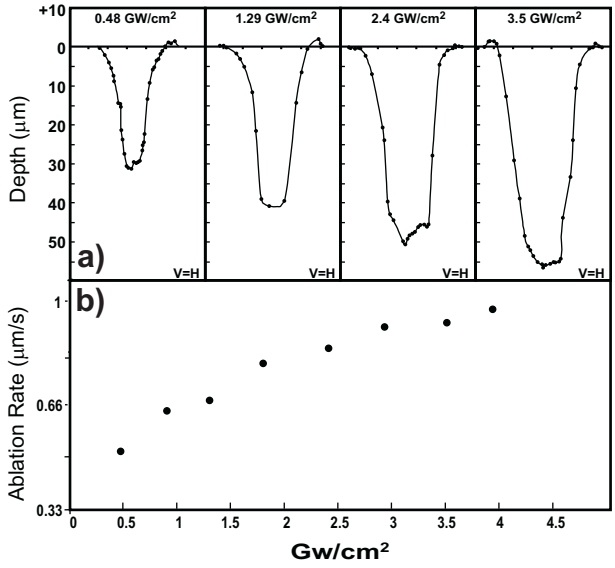

Figure 2.7 - a) Cross-sections of selected ablation pits at software measured irradiances of ~0.48, 1.29, 2.4 and 3.5 GW/cm^2. Cross-sections constructed using stereo-pair SE images. b) Ablation rates (μm/sec) for all measured pits at varying irradiances.

fractionation may represent efficient initial ablation during each laser pulse, before plasma formation shields the sample. The plasma shielding may also restrict thermal effects generated during the 5 ns laser pulse. It is hypothesised at irradiance levels in the second mode, any mass bias effects within the plasma due to incomplete ionisation are either negligible or constant, resulting in the observed isotope ratio stabilisation. The similarity in Pb-Pb T0 fractionation between monazite and NIST matrices is suggested to represent efficient ablation (possibly similar small particle sizes), and subsequently constant degrees of ICP mass bias.

The observed equivalence of integrated ratios above 2.5 GW/cm^2 for 15 μm and 30 μm beam diameters is an important outcome of this study. It indicates that TDF may not be controlled purely by the aspect ratio of ablation pits (in monazite) as surmised in previous studies (Mank and Mason, 1999; Horn et al., 2000). Investigation of this phenomena in other matrix types may provide significant information towards understanding the mechanisms of IF and TDF. Preliminary results on a NIST 610 silica glass matrix indicate integrated ratio equivalence does not occur at the same irradiance levels (Payne and Wade, unpub. data). The equivalence of ratios at different beam diameters suggests the degree to which material interacts with the laser pulse after ablation may play a dominant role in monazite analysis, as opposed to mechanisms such as pit-wall-laser interaction.

Analytical techniques using tracer solution mass bias correction and non-matrix matched standards are based upon the assumption that the initial isotopic ratios obtained by ablation are stoichiometric representations of the sample. This assumption is important as it then implies that initial ablation products of a NIST silica glass and the unknown sample share the same intrinsic fractionation effects, allowing unknowns to be corrected using NIST glass (Horn et al., 2000). Figure 2.5 demonstrates a relatively consistent variation in T_0 values for both Pb-Pb and Pb-U ratios.

Below 3 GW/cm^2 NIST 610 T_0 $^{207}Pb/^{206}Pb$ ratios are generally closer to the true value than those of MAdel. In this instance, direct correction using the NIST 610 ratios would result in a systematic under-correction/overestimation of $^{207}Pb/^{206}Pb$ ratios and ages. An unweighted average of all percent differences (excluding one anomalously low MAdel data point) results in a difference of 1.76%. Values above 3 GW/cm^2 are virtually identical suggesting that variation in Pb isotopic fractionation between different matrices may be negated at these irradiance levels.

$^{206}Pb/^{238}U$ and $^{207}Pb/^{238}U$ ratio differences show no stabilisation above 3 GW/cm^2 but some decrease in the difference is hinted at for higher laser irradiances. Unweighted averages indicate the possibility of over-correction by 2.33% and 3.27% for $^{206}Pb/^{238}U$ and $^{207}Pb/^{238}U$ ratios, respectively.

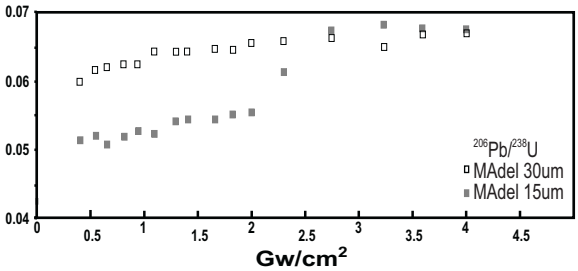

Figure 2.8 - $^{206}Pb/^{238}U$ integrated data for 15 μm and 30 μm beam diameters on monazite standard MAdel. Note approximate equivalence of data above ~2.5 GW/cm^2.

The above data highlight the potential error in the assumption that isotope ratios during the initial stages of ablation (ie. T_0) are stoichiometric. The under and over-corrections for monazite data may be evidenced by the studies of Kosler et al. (2001) and Willigers et al. (2002). Due to the lack of tracer solution data, no direct comparison can be made between the results of the current study and the age inaccuracies of the above-mentioned studies. However, the overestimation of $^{207}Pb/^{206}Pb$ ages in both studies does support our observed variation in isotopic ratios between different matrices and the concept of matrix-dependent non-stoichiometric initial ablation. In contrast to this result, is the work of investigators such as Storey et al. (2006) and Horstwood et al. (2003). In these cases non-matrix matched ablation standards are coupled with rastered or dynamic ablation conditions to negate the effects of TDF. Both studies present age data that are within error of either known ages or concordia. This suggests any consistent error in fractionation between mineral matrices is lower than the precision currently obtainable for Phanerozoic-aged samples. Horstwood et al. (2003) present monazite-corrected detrital zircon data that is within error of concordia but in many cases is above concordia, especially so for older ages. This may hint at a slight error in ratio measurements. Similar simple analysis of the data of Storey et al. (2006) is not possible due to the abundant common-Pb incorporated in titanite. Investigations into the mechanisms of fractionation may resolve the validity of such methods.

2.6 Conclusions

The majority of our conclusions above are limited by the lack of independent monitoring of ICP-MS-induced mass bias such as that provided by tracer solution aspiration. Despite this, the above findings are thought to be valid and indicate matrix-matched standards for external correction (ie. this study or Gehrels et al., 2006) or tracer-solution correction (ie. Horstwood et al., 2003) are preferable for obtaining accurate LA-ICP-MS U-Pb monazite age data. Ablation above 2.5-3 GW/cm^2 is preferable for all techniques due to the stabilisation of isotope ratios and minimisation of Pb-Pb isotope intrinsic fractionation. It is also recognised that variation between initial (T_0) isotope ratios is likely to be less when conducting zircon analysis due to the silica-based nature of both zircon and NIST 610.

References

Andersen, T., 2002. Correction of common lead in U-Pb analyses that do not report Pb-204. Chemical Geology,192(1-2): 59-79.

Elburg, M.A., Bons, P.D., Foden, J. and Brugger, J., 2003. A newly defined Late Ordovician magmatic-thermal event in the Mt Painter Province, Northern Flinders Ranges, South Australia. Australian Journal of Earth Sciences, 50(4): 611-631.

Foster, G., Gibson, H.D., Parrish, R., Horstwood, M., Fraser, J. and Tindle, A., 2002. Textural, chemical and isotopic insights into the nature and behaviour of metamorphic monazite. Chemical Geology, Chemistry and Physics of Accessory Minerals: Crystallisation, Transformation and Geochronoligical Applications, 191(1-3): 183-207.

Foster, G., Kinny, P., Vance, D., Prince, C. and Harris, N., 2000. The significance of monazite U-Th-Pb age data in metamorphic assemblages; a combined study of monazite and garnet chronometry. Earth and Planetary Science Letters, 181(3): 327-340.

Foster, G., Parrish, R.R., Horstwood, M.S.A., Chenery, S., Pyle, J. and Gibson, H.D., 2004. The generation of prograde P-T-t points and paths; a textural, compositional, and chronological study of metamorphic monazite. Earth and Planetary Science Letters, 228(1-2): 125-142.

Fryer, B.J., Jackson, S.E. and Longerich, H.P., 1995. Design, Operation and Role of the Laser-Ablation Microprobe Coupled with an Inductively-Coupled Plasma - Mass-Spectrometer (LAM-ICP-MS) in the Earth-Sciences. Canadian Mineralogist, 33: 303-312.

Gehrels, G.E., DeCellec, P.G., Ojha, T.P. and Upreti, B.N., 2006. Geologic and U-Th-Pb geochronologic evidence for early Paleozoic tectonism in the Kathmandu thrust sheet, central Nepal Himalaya. GSA Bulletin, 118(1/2): 185-198.

Gonzalez, J.J., Fernandez, A., Mao, X.L. and Russo, R.E., 2004. Scanning vs. single spot laser ablation (lambda=213 nm) inductively coupled plasma mass spectrometry. Spectrochimica Acta Part B-Atomic Spectroscopy, 59(3): 369-374.

Guillong, M. and Gunther, D., 2002. Effect of particle size distribution on ICP-induced elemental fractionation in laser ablation-inductively coupled plasma-mass spectrometry. Journal of Analytical Atomic Spectrometry, 17(8): 831-837.

Guillong, M., Kuhn, H.R. and Gunther, D., 2003. Application of a particle separation device to reduce inductively coupled plasma-enhanced elemental fractionation in laser ablation-inductively coupled plasma-mass spectrometry. Spectrochimica Acta Part B-Atomic Spectroscopy, 58(2-3): 211-220.

Gunther, D. and Hattendorf, B., 2005. Solid sample analysis using laser ablation inductively coupled plasma mass spectrometry. Trac-Trends in Analytical Chemistry, 24(3): 255-265.

Hirata, T., Iizuka, T. and Orihashi, Y., 2005. Reduction of mercury background on ICP-mass spectrometry for in situ U-Pb age determinations of zircon samples. Journal of Analytical Atomic Spectrometry, 20(8): 696-701.

Hirata, T. and Nesbitt, R.W., 1995. U-Pb Isotope Geochronology of Zircon - Evaluation of the Laser Probe-Inductively Coupled Plasma-Mass Spectrometry Technique. Geochimica Et Cosmochimica Acta, 59(12): 2491-2500.

Horn, I., Rudnick, R.L. and McDonough, W.F., 2000. Precise elemental and isotope ratio determination by simultaneous solution nebulization and laser ablation-ICP-MS: application to U-Pb geochronology. Chemical Geology, 164(3-4): 281-301.

Horstwood, M.S.A., Foster, G., Parrish, R.R., Noble, S.R. and Nowell, G.M., 2003. Common-Pb corrected in-situ U-Pb accessory mineral geochronology by LA-MC-ICP-MS. Journal of Analytical Atomic Spectrometry, 18: 837-846.

Jackson, S.E. and Gunther, D., 2002. Studies of the source of laser-induced isotopic bias in LA-MC-ICP-MS. Geochimica Et Cosmochimica Acta, 66(15A): A359-A359.

Jackson, S.E. and Gunther, D., 2003. The nature and sources of laser induced isotopic fractionation in laser ablation-multicollector-inductively coupled plasma-mass spectrometry. Journal of Analytical Atomic Spectrometry, 18(3): 205-212.

Jackson, S.E., Pearson, N.J., Griffin, W.L. and Belousova, E.A., 2004. The application of laser ablation-inductively coupled plasma-mass spectrometry to in situ U-Pb zircon geochronology. Chemical Geology, 211(1-2): 47-69.

Jeong, S.H., Borisov, O.V., Yoo, J.H., Mao, X.L. and Russo, R.E., 1999. Effects of particle size distribution on inductively coupled plasma mass spectrometry signal intensity during laser ablation of glass samples. Analytical Chemistry, 71(22): 5123-5130.

Kosler, J., Fonneland, H., Sylvester, P., Tubrett, M. and Pedersen, R.B., 2002. U-Pb dating of detrital zircons for sediment provenance studies - a comparison of laser ablation ICPMS and SIMS techniques. Chemical Geology, 182(2-4): 605-618.

Kosler, J., Tubrett, M.N. and Sylvester, P.J., 2001. Application of laser ablation ICP-MS to U-Th-Pb dating of monazite. Geostandards Newsletter-the Journal of Geostandards and Geoanalysis, 25(2-3): 375-386.

Kosler, J. et al., 2005. Chemical and phase composition of particles produced by laser ablation of silicate glass and zircon - implications for elemental fractionation during ICP-MS analysis. Journal of Analytical Atomic Spectrometry, 20(5): 402-409.

Liu, H.C., Borisov, O.V., Mao, X.L., Shuttleworth, S. and Russo, R.E., 2000. Pb/U fractionation during Nd : YAG 213 nm and 266 nm laser ablation sampling with inductively coupled plasma mass spectrometry. Applied Spectroscopy, 54(10): 1435-1442.

Longerich, H.P., Gunther, D. and Jackson, S.E., 1996. Elemental fractionation in laser ablation inductively coupled plasma mass spectrometry. Fresenius Journal of Analytical Chemistry, 355(5-6): 538-542.

Ludwig, K.R., 2003. Isoplot 3.00, A Geochronological Toolkit for Microsoft Excel. Special Publication No. 4, Berkley Geochronology Centre.

Mank, A.J.G. and Mason, P.R.D., 1999. A critical assessment of laser ablation ICP-MS as an analytical tool for depth analysis in silica-based glass samples. Journal of Analytical Atomic Spectrometry, 14(8): 1143-1153.

Montel, J.M., Foret, S., Veschambre, M., Nicollet, C. and Provost, A., 1996. Electron microprobe dating of monazite. Chemical Geology, 131: 37-53.

Parrish, R.R., 1990. U-Pb dating of monazite and its application to geological problems. Canadian Journal of Earth Sciences, 27: 1431-1450. Poitrasson, F., Chenery, S. and Shepherd, T.J., 2000. Electron microprobe and LA-ICP-MS study of monazite hydrothermal alteration: Implications for U-Th-Pb geochronology and nuclear ceramics. Geochimica Et Cosmochimica Acta, 64(19): 3283-3297.

Poitrasson, F., Mao, X.L., Mao, S.S., Freydier, R. and Russo, R.E., 2003. Comparison of ultraviolet femtosecond and nanosecond laser ablation inductively coupled plasma mass spectrometry analysis in glass, monazite, and zircon. Analytical Chemistry, 75(22): 6184-6190.

Pyle, J.M., Spear, F.S., Wark, D.A., Daniel, C.G. and Storm, L.C., 2005. Contributions to Precision and Accuracy of Chemical Ages of Monazite. American

Mineralogist, 90: 547-577.

Rubatto, D., Williams, I.S. and Buick, I.S., 2001. Zircon and monazite response to prograde metamorphism in the Reynolds Range, central Australia. Contributions to Mineralogy and Petrology, 140(4): 458-468.

Russo, R.E., Mao, X.L., Liu, H.C., Gonzalez, J. and Mao, S.S., 2002a. Laser ablation in analytical chemistry - a review. Talanta, 57(3): 425-451.

Russo, R.E., Mao, X.L. and Mao, S.S., 2002b. The physics of laser ablation in microchemical analysis. Analytical Chemistry, 74(3): 70A-77A.

Schoene, B., Crowley, J.L., Condon, D.J., Schmitz, M.D. and Bowring, S.A., 2006. Reassessing the uranium decay constants for geochronology using ID-TIMS U-Pb data. Geochimica Et Cosmochimica Acta, 70(2): 426-445.

Shannon, M.A., Mao, X.L., Fernandez, A., Chan, W.T. and Russo, R.E., 1995. Laser Ablation mass removal versus incident power density during solid sampling for Inductively Coupled Plasma Atomic Emission Spectroscopy. Analytical Chemistry, 67: 4522-4529.

Smith, H.A. and Giletti, B.J., 1997. Lead diffusion in monazite. Geochimica Et Cosmochimica Acta, 61(5): 1047-1055.

Stern, R.A. and Amelin, Y., 2003. Assessment of errors in SIMS zircon U-Pb geochronology using a natural zircon standard and NIST SRM 610 glass. Chemical Geology, 197: 111-142.

Storey, C.D., Jeffries, T.E. and Smith, M., 2006. Common lead-corrected laser ablation ICP-MS U-Pb systematics and geochronology of titanite. Chemical Geology, 227(1-2): 37-52.

Suzuki, K., Yoshida, H., Amano, K. and Yogo, S., 1996. CHIME dating of monazite from pelitic hornfels of the Kurihashi Granodiorite, Kitakami Mountains. The Journal of Earth and Planetary Sciences, Nagoya University, 43: 17-26.

Sylvester, P.J. and Ghaderi, M., 1997. Trace element analysis of scheelite by excimer laser ablation inductively coupled plasma mass spectrometry (ELA-ICP-MS) using a synthetic silicate glass standard. Chemical Geology, 141(1-2): 49-65.

Tanner, S.D., Cousins, L.M. and Douglas, D.J., 1994. Reduction of space-charge effects using a 3-aperture gas-dynamic vacuum interface for inductively-coupled plasma-mass spectrometry. Applied Spectroscopy, 48(11): 1367-1372.

Tiepolo, M., Bottazzi, P., Palenzona, M. and Vannucci, R., 2003. A laser probe coupled with ICP-double-focusing sector-field mass spectrometer for in situ analysis of geological samples and U-Pb dating of zircon. Canadian Mineralogist, 41: 259-272.

van Achterbergh, E., Ryan, C.G., Jackson, S.E. and Griffin, W.L., 2001. Data Reduction Software for LA-ICP-MS. In: P. Sylvester (Editor), Laser-Ablation-ICPMS in the Earth Sciences: Principles and Applications. Short Course Series Vol. 29. Mineralogical Association of Canada.

Williams, M.L. and Jercinovic, M.J., 2002. Microprobe monazite geochronology; putting absolute time into microstructural analysis. Journal of Structural Geology, 24: 1013-1028.

Willigers, B.J.A., Baker, J.A., Krogstad, E.J. and Peate, D.W., 2002. Precise and accurate in situ Pb-Pb dating of apatite, monazite, and sphene by laser ablation multiple-collector ICP-MS. Geochemica Et Cosmichimica Acta, 66(6): 1051-1066.

Willigers, B.J.A., Krogstad, E.J. and Wijbrans, J.R., 2001. Comparison of thermochonometers in a slowly cooled granulite terrain: Nagssugtoquidian orogen, West Greenland. Journal of Petrology, 42(9): 1729-1749.

Appendix 2.1 - Composition of MAdel monazite

Element	MAdel a (ppm)	MAdel b (ppm)	MAdel c (ppm)	Average (ppm)
Mg	0.05	0.0338	0.023	0.04
Si	12384	9760	12289	11478
Sc	0.45	0.40	0.41	0.42
Ti	18.37	19.91	17.60	18.63
Mn	0.86	0.81	0.85	0.84
Sr	1.377	0.0553	0.0727	0.50
Y	8816.1	9152.1	8579.1	8849.1
Zr	3.41	4.2	3.59	3.73
Nb	0.377	0.459	0.443	0.43
La	71474	75795	73197	73489
Ce	203895	215658	206011	208521
Pr	31226	33180	31438	31948
Nd	133777	142217	134126	136707
Sm	39599	41974	39200	40258
Eu	5.57	5.99	5.62	5.73
Gd	18331	19533	18134	18666
Tb	1284.7	1358.9	1268.6	1304.1
Dy	2483.6	2612.1	2456.5	2517.4
Ho	160.14	168.86	160.45	163.15
Er	157.48	166.20	157.35	160.34
Tm	10.62	10.91	10.32	10.62
Yb	44.95	47.03	43.27	45.08
Lu	3.65	3.69	3.36	3.57
Hf	0.36	0.38	0.37	0.37
Ta	0.05	0.06	0.06	0.06

Compositions obtained by LA-ICP-MS using Ca as internal standard

Appendix 2.2 - Data for laser optimisation tests

FracTest 1
Matrix - MAdel

Irradiance	Integrated Ratios					
(GWcm^{-2})	$^{207}Pb/^{206}Pb$	1σ	$^{206}Pb/^{238}U$	1σ	$^{207}Pb/^{235}U$	1σ
0.41	0.05881	104	0.04436	47	0.36042	693
0.43	0.05827	100	0.04557	48	0.37573	705
0.54	0.0586	93	0.04598	48	0.37887	653
0.53	0.05778	90	0.04598	48	0.38294	647
0.63	0.05715	88	0.0465	48	0.37631	631
0.74	0.05861	88	0.04648	48	0.39264	638
0.78	0.05798	86	0.04761	49	0.39264	626
0.88	0.05807	83	0.04795	49	0.40221	619
0.97	0.05767	80	0.04784	49	0.39547	592
1.01	0.05802	79	0.04967	51	0.41168	605
1.18	0.05778	80	0.04866	50	0.3988	596
1.18	0.0579	77	0.04995	51	0.41346	590
1.27	0.05825	77	0.05063	52	0.42087	599
1.38	0.05728	76	0.05084	52	0.41786	590
1.55	0.05774	75	0.05169	53	0.42074	583
1.61	0.05728	73	0.0511	52	0.4148	562
1.81	0.05864	73	0.0524	53	0.43796	579
1.84	0.05771	71	0.05282	54	0.42679	557
1.98	0.05871	72	0.05258	53	0.4352	567
2.05	0.05806	71	0.05277	53	0.42258	541
2.97	0.05749	67	0.05418	55	0.43575	535
3.80	0.0576	66	0.05468	55	0.43613	524
4.60	0.05787	66	0.05414	55	0.43577	516
2.05	0.05792	71	0.05268	53	0.42589	549
1.05	0.05678	79	0.04841	50	0.39189	584

FracTest 2
Matrix - MAdel

Irradiance	Integrated Ratios					
(GWcm^{-2})	$^{207}Pb/^{206}Pb$	1σ	$^{206}Pb/^{238}U$	1σ	$^{207}Pb/^{235}U$	1σ
0.42	0.05864	80	0.05575	58	0.44196	738
0.50	0.05751	75	0.05645	59	0.44878	705
0.53	0.0585	77	0.05642	59	0.45055	718
0.56	0.05863	75	0.05641	58	0.45727	702
0.62	0.05774	74	0.0565	58	0.44756	682
0.76	0.0594	73	0.05652	58	0.46022	667
0.80	0.05833	71	0.05696	58	0.45994	656
0.94	0.05872	70	0.05803	59	0.46774	642
1.02	0.05849	69	0.05793	59	0.46813	642
1.11	0.05816	68	0.05833	60	0.46897	633
1.16	0.05845	68	0.0591	60	0.48185	641
1.28	0.05902	68	0.05851	60	0.47445	623
1.41	0.05882	67	0.05985	61	0.48075	621
1.44	0.05873	67	0.06031	61	0.49378	636
1.63	0.05915	66	0.06089	62	0.4984	627
1.68	0.05822	66	0.06055	61	0.48067	606
1.87	0.05872	66	0.06159	62	0.49237	612
2.00	0.05755	64	0.06206	63	0.4902	605
2.12	0.05789	64	0.06227	63	0.48745	595
2.25	0.0585	65	0.06244	63	0.49307	600
2.53	0.05863	64	0.06359	64	0.49861	597
2.61	0.05924	65	0.06283	64	0.5057	606
2.74	0.0586	64	0.06398	65	0.50454	599
2.96	0.05822	63	0.06285	63	0.49877	590
3.80	0.05886	63	0.06338	64	0.48995	570
4.40	0.05874	63	0.06592	66	0.52473	607

Appendix 2.2 (cont.) - Data for laser optimisation tests

FracTest 3
Matrix - MAdel

Irradiance ($GWcm^{-2}$)	Integrated Ratios $^{207}Pb/^{206}Pb$	1σ	$^{206}Pb/^{238}U$	1σ	$^{207}Pb/^{235}U$	1σ
0.40	0.05801	87	0.05378	57	0.43451	826
0.44	0.05809	84	0.05451	58	0.44399	808
0.54	0.05865	79	0.05376	56	0.44548	738
0.62	0.05935	77	0.05404	56	0.45365	709
0.68	0.05814	77	0.05383	56	0.42764	682
0.77	0.05772	74	0.05476	57	0.43882	672
0.80	0.05713	72	0.0556	57	0.44911	673
0.87	0.05836	72	0.05621	58	0.4617	676
1.00	0.05873	72	0.05648	58	0.47119	677
1.04	0.05765	70	0.05681	58	0.45858	656
1.16	0.05784	70	0.05771	59	0.46278	648
1.23	0.05808	70	0.05814	60	0.47689	666
1.30	0.05824	69	0.05811	59	0.46927	647
1.45	0.05683	67	0.05934	61	0.45864	623
1.44	0.05847	68	0.0596	61	0.4852	651
1.61	0.05761	67	0.05998	61	0.48786	645
1.77	0.05728	66	0.05964	61	0.47797	627
1.90	0.05773	66	0.06023	61	0.48879	635
2.00	0.05866	66	0.06014	61	0.49253	628
2.17	0.05904	66	0.06056	61	0.49707	628
2.30	0.0574	64	0.06257	63	0.48986	606
2.42	0.05745	64	0.06269	63	0.49416	609
2.54	0.05737	63	0.06285	64	0.49139	600
2.72	0.05738	63	0.06286	64	0.4925	600
2.87	0.06125	67	0.06298	64	0.53125	643
3.00	0.05694	63	0.0634	64	0.49608	602
3.6	0.05686	62	0.06362	64	0.48668	581
4.4	0.05811	63	0.06356	64	0.51204	612

FracTest 2 & 3 U-isotope ratios

Irradiance FracTest 2 ($GWcm^{-2}$)	Integrated Ratios FracTest 2 $^{238}U/^{235}U$	FracTest 3 $^{238}U/^{235}U$	Irradiance FracTest 3 ($GWcm^{-2}$)
0.42	144.23	148.94	0.40
0.50	144.50	149.93	0.44
0.53	142.40	147.94	0.54
0.56	143.58	147.64	0.62
0.62	142.57	143.06	0.68
0.76	142.20	143.13	0.77
0.80	143.51	146.16	0.80
0.94	141.30	145.38	0.87
1.02	141.55	144.24	1.00
1.11	140.55	145.25	1.04
1.16	141.56	142.01	1.16
1.28	139.73	143.52	1.23
1.41	139.57	142.13	1.30
1.44	141.66	140.30	1.45
1.63	140.29	142.64	1.44
1.68	138.69	142.27	1.61
1.87	137.95	142.59	1.77
2.00	139.24	142.33	1.90
2.12	137.35	143.64	2.00
2.25	138.47	141.53	2.17
2.53	137.26	139.75	2.30
2.61	138.06	139.84	2.42
2.74	137.66	139.71	2.54
2.96	138.69	140.53	2.72
3.80	135.36	140.49	2.87
4.40	136.91	141.11	3.00
		137.94	3.6
		140.70	4.4

Appendix 2.2 (cont.) - Data for laser optimisation tests

FracNist 1- MAdel and NIST 610 glass comparison

Irradiance	Integrated Ratios						T_0 Ratios		
($GWcm^{-2}$)	$^{207}Pb/^{206}Pb$	1σ	$^{206}Pb/^{238}U$	1σ	$^{207}Pb/^{235}U$	1σ	$^{207}Pb/^{206}Pb$	$^{206}Pb/^{238}U$	$^{207}Pb/^{235}U$
Madel									
0.40	0.05702	148	0.08297	71	0.6535	217	0.06140	0.05368	0.44590
0.46	0.05868	140	0.0835	66	0.6779	206	0.06198	0.05222	0.44340
0.60	0.05676	135	0.08362	66	0.6355	193	0.05899	0.05362	0.43325
0.70	0.0567	133	0.08465	66	0.6598	198	0.05889	0.05360	0.43210
0.90	0.05667	131	0.08581	66	0.6640	196	0.06027	0.05461	0.45115
1.02	0.05734	130	0.08701	65	0.6771	196	0.05952	0.05411	0.44098
1.22	0.05678	128	0.08815	66	0.6810	196	0.05863	0.05378	0.43331
1.43	0.05749	129	0.08982	67	0.7092	204	0.05961	0.05480	0.44825
1.43	0.05662	128	0.09046	67	0.7088	204	0.05957	0.05525	0.45257
1.65	0.05663	127	0.08929	66	0.6990	200	0.05642	0.05378	0.41411
1.84	0.05673	126	0.09140	67	0.7135	203	0.05845	0.05452	0.43795
2.08	0.05705	127	0.09271	68	0.7127	202	0.05885	0.05497	0.44382
2.43	0.05691	126	0.09320	68	0.7105	201	0.05787	0.05553	0.44132
2.61	0.05724	126	0.09262	68	0.7154	201	0.05899	0.05627	0.45625
2.79	0.05699	125	0.09394	68	0.7048	198	0.05853	0.05664	0.45585
3.43	0.05646	123	0.09483	69	0.7163	200	0.05833	0.05628	0.45144
4.20	0.05646	123	0.09534	69	0.7208	201	0.05813	0.05725	0.45706
NIST 610									
0.40	0.8868	229	0.2597	23	49.04	4.69	0.89900	0.17361	21.74
0.46	0.8888	216	0.2461	18	58.05	4.91	0.91799	0.15072	18.71
0.60	0.8879	209	0.2517	16	62.13	4.75	0.92829	0.15987	20.49
0.70	0.9090	205	0.2502	14	69.08	4.65	0.92679	0.15600	19.69
0.90	0.8988	201	0.2577	13	59.52	3.38	0.92960	0.15633	20.05
1.02	0.8999	197	0.2631	13	65.87	3.61	0.93214	0.16185	20.59
1.22	0.9284	201	0.2585	12	70.51	3.73	0.94721	0.16194	21.07
1.43	0.9003	194	0.2703	12	63.58	3.12	0.91971	0.17158	21.77
1.43	0.9079	197	0.2554	12	62.16	3.06	0.93242	0.16137	20.66
1.65	0.9064	194	0.2584	11	61.16	2.79	0.92705	0.15892	20.28
1.84	0.8993	192	0.2650	11	65.70	2.8	0.94220	0.16289	20.62
2.08	0.8929	189	0.2685	10	65.94	2.59	0.92137	0.16375	20.73
2.43	0.8993	190	0.2724	10	66.02	2.45	0.94267	0.16272	20.98
2.61	0.9009	190	0.2750	10	67.58	2.46	0.92409	0.16819	21.33
2.79	0.8965	189	0.2756	10	66.02	2.37	0.93171	0.16782	21.29
3.43	0.9041	189	0.2781	10	66.59	2.3	0.93123	0.17123	21.82
4.20	0.8940	188	0.2756	10	67.56	2.31	0.92548	0.16881	21.52

Chapter 3

Provenance of metasedimentary rocks in the northern Gawler Craton, Australia: Implications for Palaeoproterozoic reconstructions

Published as: Payne, J.L., Barovich, K.M. and Hand, M., 2006. Provenance of metasedimentary rocks in the northern Gawler Craton, Australia: Implications for Palaeoproterozoic reconstructions. Precambrian Research, 148 (3-4): 275-291.

Abstract

Isotopic, geochemical and U-Pb zircon geochronological characteristics of the Nawa Domain in the South Australian Craton, Australia, have been determined to place constraints upon Palaeoproterozoic reconstruction models. U-Pb detrital zircon analysis of the Nawa Domain metasedimentary rocks indicates deposition between *c.* 1740 Ma and 1720 Ma. Sedimentary rocks are shown to be enriched in REE and sourced from evolved crust (ε_{Nd}(1.6 Ga) = -7.0 to -4.3). The combination of geochemical, Nd-isotope and U-Pb detrital zircon age data indicate the dominant source for the studied metasedimentary rocks is likely to be the Arunta region of the North Australian Craton. This indicates the Nawa Domain crustal segment was proximal to the North Australian Craton during the period *c.* 1740-1720 Ma. Provenance correlations drawn between the Nawa Domain metasedimentary rocks, lower part of the Willyama Supergroup in the Curnamona (Broken Hill) region and Maronan Supergroup in the Mount Isa region suggest contiguity of these crustal terranes during the late Palaeoproterozoic. These spatial and temporal constraints negate some reconstructions of Palaeoproterozoic Australia suggested for this period, and indicate further refinement of other models is needed. Further, the intra-continental nature and Australian sourced detritus of the lower sections of these basins limits their use as piercing points between eastern Australia and possible neighbouring continents in the Palaeo- and Mesoproterozoic.

Payne, J., Barovich, K.M. & Hand, M. (2006) Provenance of metasedimentary rocks in the northern Gawler Craton, Australia: Implications for Palaeoproterozoic reconstructions
Precambrian Research, v. 148 (3-4), pp. 275-291

Chapter 4

Temporal constraints on the timing of high-grade metamorphism in the northern Gawler Craton: implications for assembly of the Australian Proterozoic

Published as: Payne, J.L., Hand, M., Barovich, K.M. and Wade, B.P., 2008. Temporal constraints on the timing of high-grade metamorphism in the northern Gawler Craton: implications for assembly of the Australian Proterozoic. Australian Journal of Earth Sciences, 55: in press.

Abstract

LA-ICPMS U-Pb data from metamorphic monazite in upper amphibolite and granulite-grade metasedimentary rocks indicate that the Nawa Domain of the northern Gawler Craton in southern Australia underwent multiple high-grade metamorphic events in the late Palaeo- and early Meso-Proterozoic. Five of the six samples investigated here record metamorphic monazite growth during the period 1730-1690 Ma, coincident with the Kimban Orogeny which shaped the crustal architecture of the south-eastern Gawler Craton. Combined with existing detrital zircon U-Pb data, the metamorphic monazite ages constrain deposition of the northern Gawler metasedimentary protoliths to the interval *c.* 1750-1720 Ma. The new age data highlight the craton-wide nature of the 1730-1690 Ma Kimban Orogeny within the Gawler Craton.

In the Mabel Creek Ridge region of the Nawa Domain, rocks metamorphosed during the Kimban Orogeny were reworked during the Kararan Orogeny (1570-1555 Ma). The obtained Kararan Orogeny monazite ages are within uncertainty of *c.* 1590-1575 Ma zircon U-Pb metamorphic ages from the Mt Woods Domain in the central eastern Gawler Craton, which indicate that high-grade metamorphism and associated deformation was coeval with the craton-scale Hiltaba magmatic event. The timing of this deformation, and the implied compressional vector, is similar to the latter stages of the Olarian Orogeny in the adjacent Curnamona Province and appears to be part of a westward migration in the timing of deformation and metamorphism in the Southern Australian Proterozoic over the interval 1600-1545 Ma. This pattern of westward shifting tectonism is defined by the Olarian Orogeny (1600-1585 Ma, Curnamona Province); Mt Woods deformation (1590-1575 Ma); Mabel Creek Ridge deformation (1570-1550 Ma, Kararan Orogeny) and Fowler Domain deformation (1555-1545 Ma, Kararan Orogeny). This westward migration of deformation suggests the existence of a large evolving tectonic system that encompassed the emplacement of the voluminous Hiltaba Suite and associated volcanic and mineral systems.

Payne, J., Hand, M., Barovich, K.M. & Wadw, B. (2008) Temporal constraints on the timing of high-grade metamorphism in the northern Gawler Craton: implications for assembly of the Australian Proterozoic
Australian Journal of Earth Sciences, v. 55 (5), pp. 623-640

Chapter 5

A geochemical and isotopic assessment of a subduction-related petrogenesis for the Palaeoproterozoic Tunkillia Suite, Gawler Craton, Australia: implications for reconstruction models of Proterozoic Australia

Abstract

The 1690-1670 Ma felsic Tunkillia Suite, Gawler Craton, South Australia, was generated during the waning stages of the 1730-1690 Ma Kimban Orogeny. The Tunkillia Suite is typically a high-K, alkali-calcic, magnesian suite which is dominated by felsic (>70% SiO_2), moderately peraluminous granitoids. Rare earth and trace element characteristics of the Tunkillia Suite display large variations. Sr and Y concentrations range from 40-550 ppm and 4.7-41 ppm, respectively. Eu/Eu* values range from 0.2-1.6 and combined with REE patterns demonstrate the varying composition of restite associated with melt generation for the Tunkillia Suite. The majority of the Tunkillia Suite displays chemical characteristics typical of a plagioclase or hornblende dominated restite with few samples demonstrating garnet-rich restite composition.

Previous suggestions that the Tunkillia Suite was generated in a subduction-related arc setting are not supported by its lithological, geochemical and isotopic characteristics. Instead these characteristics are most consistent with a late- to post-tectonic setting for petrogenesis of the Tunkillia Suite. However, a lack of mafic material and inability to constrain the mechanisms of mantle melting precludes an unequivocal classification for a tectonic setting. Tectonic reconstruction models which use the previous subduction-related petrogenesis for the Tunkillia Suite require modification in light of the new data and classification.

5.1 Introduction

The study of Archaean and Proterozoic felsic magmatic suites is typically undertaken to establish mechanisms of petrogenesis and, from this, constrain the tectonic regime active at the time of their generation (eg. Bonin et al., 1998; Eklund et al., 1998; Griffin et al., 2000; Peterson et al., 2002; Sheppard et al., 2003; Sheppard et al., 2004; Clemens et al., 2006; Lopez et al., 2006). The tectonic setting of Precambrian magmatic suites is often largely inferred from comparisons with Phanerozoic magmatic rocks and the timing of generation with respect to other tectonic events (Foden et al., 1988; Griffin et al., 2000; Sheppard et al., 2004; Wade et al., 2006). The Palaeoproterozoic Tunkillia Suite in the Gawler Craton, South Australia, is an example of an ancient magmatic suite that has been classified using trace element tectonic discrimination diagrams. Limited geochemical data was used to suggest a subduction-related petrogenesis (Teasdale, 1997; Betts and Giles, 2006).

The basic thermodynamics of mineral reactions responsible for the generation of melt are unlikely to have changed over time, and ancient and modern-day magmatism must therefore occur under the same intensive physical parameters (ie. P-T conditions). This provides a common basis for the generation of modern and ancient felsic magmatic suites, and suggests classification of ancient magmatism through comparison with modern rock systems may be valid. However, the Earth's chemical reservoirs (ie upper and lower crust, lithospheric mantle and aesthenosphere) have evolved and undergone composition changes throughout Earth history (Taylor and McLennan, 1985; McDonough and Sun, 1995; Collerson and Kamber, 1999; Hawkesworth and Kemp, 2006). This chemical evolution is in part linked to and accompanied by the increased role of subduction in magma generation through subduction of volatile phases (namely H_2O) to depth in the mantle. The bulk chemical composition changes and increased role of subduction systems mean that tectonic

discrimination methods using element abundances need to be applied with caution to ancient magma systems. Hence, the classification of the Tunkillia Suite as subduction-related magmatism based upon limited chemical data (n=3) and trace element tectonic discrimination diagrams (Teasdale, 1997; Betts and Giles, 2006) requires reassessment if the Tunkillia Suite is to be used in tectonic reconstruction models for the Proterozoic.

The Tunkillia Suite is a felsic magmatic suite that was emplaced during the period 1690 Ma to 1670 Ma. A subduction-related classification of the Tunkillia Suite has important implications for reconstruction models of Proterozoic Australia and is used by Karlstrom et al. (2001), Betts et al. (2002), Giles et al. (2004) and Betts and Giles (2006) to infer a long-lived active margin on the southern margin of the proto-Australia during the mid-Proterozoic. Despite the apparent importance of the Tunkillia Suite in underpinning reconstruction models of the Australian Proterozoic (Karlstrom et al., 2001; Betts et al., 2002; Giles et al., 2004; Betts and Giles, 2006) virtually no work has been done on the geochemical and isotopic nature of the Tunkillia Suite. By combining new geochemical, isotope and geochronological data with mineralogical information we re-assess the previous 'subduction-related' classification of the Tunkillia Suite. The petrogenesis of the Tunkillia Suite is discussed with respect to the evolution of the Australian Proterozoic.

5.2 Geological Setting

The Gawler Craton (Figure 5.1) is composed of a central late Archaean-early Palaeoproterozoic nucleus surrounded, overlain and intruded by Palaeo- (1850-1610 Ma) and Mesoproterozoic (1590-1510 Ma) lithologies (Daly et al., 1998; Ferris et al., 2002; Hand et al., in press). Neoproterozoic and Phanerozoic sedimentary rocks and sediments overlie much of the craton. These cover sequences have greatly restricted the understanding of the crustal composition and tectonothermal evolution of the craton (Ferris et al., 2002). Tectonic domains have been interpreted using a combination of Total Magnetic Intensity (TMI) and gravity modelling (Figure 5.1, Fairclough et al., 2004).

The late Archaean nucleus of the Gawler Craton consists of *c.* 2560-2480 Ma metasedimentary, volcanic and granite-greenstone lithologies which have been extensively deformed during the *c.* 2460-2430 Ma Sleafordian Orogeny (Daly et al., 1998; Tomkins et al., 2004; Swain et al., 2005b; McFarlane, 2006; Fanning et al., 2007). This Archaean nucleus is bordered to the east by mid- to late-Palaeoproterozoic metasedimentary lithologies, the *c.* 1850 Ma Donington Granitoid suite (Daly et al., 1998; Reid et al., in press), Engenina Adamellite (~1690 Ma, Daly et al., 1998) and younger Mesoproterozoic Gawler Range Volcanics and Hiltaba Suite intrusives (1595-1575 Ma, Creaser and White, 1991; Creaser, 1995; Johnson and Cross, 1995; Allen and McPhie, 2002).

The Nuyts Domain, situated to the south and west of the Archaean nucleus of the Gawler Craton (Figure 5.1), is interpreted to consist of the Tunkillia, St Peter and Munjeela Suite intrusives (Fairclough et al., 2004). The St Peter Suite (1620-1608 Ma) is a mafic-felsic suite interpreted as forming in a subduction-related arc (Swain et al., 2005a). The Munjeela Suite consists of a small number of muscovite-garnet-bearing plutons that have previously been constrained to *c.* 1565 Ma using electron probe microanalysis (EPMA) chemical Th-U-Pb monazite geochronology (Ferris, 2001).

The Fowler Domain along the western Gawler Craton margin has little outcrop but is interpreted to consist of Palaeoproterozoic igneous and metamorphic rocks (Teasdale, 1997; Daly et al., 1998; Hand et al., in press). A mildly deformed gabbro yields an emplacement age of 1730 ± 10 Ma (Daly et al., 1998). Younger intrusive and metamorphic ages span the interval 1570-1450 Ma but have little tectonic context (Teasdale, 1997; Swain et al., 2005c; Fraser and Lyons, 2006). No constraints have yet been placed upon the maximum depositional age of metasedimentary protoliths but they have been demonstrated to have undergone metamorphism at *c*. 1720 (Teasdale, 1997).

The orogenic events that have shaped the evolution of the Gawler Craton are comparatively poorly understood. The *c.* 2460-2430 Ma Sleafordian Orogeny produced greenschist to granulite facies metamorphism and syn-tectonic magmatism (Daly and Fanning, 1993; Tomkins, 2002; Tomkins et al., 2004; Swain et al., 2005b; McFarlane, 2006). The structural and geochronological evidence of the Sleafordian Orogeny is largely overprinted by later

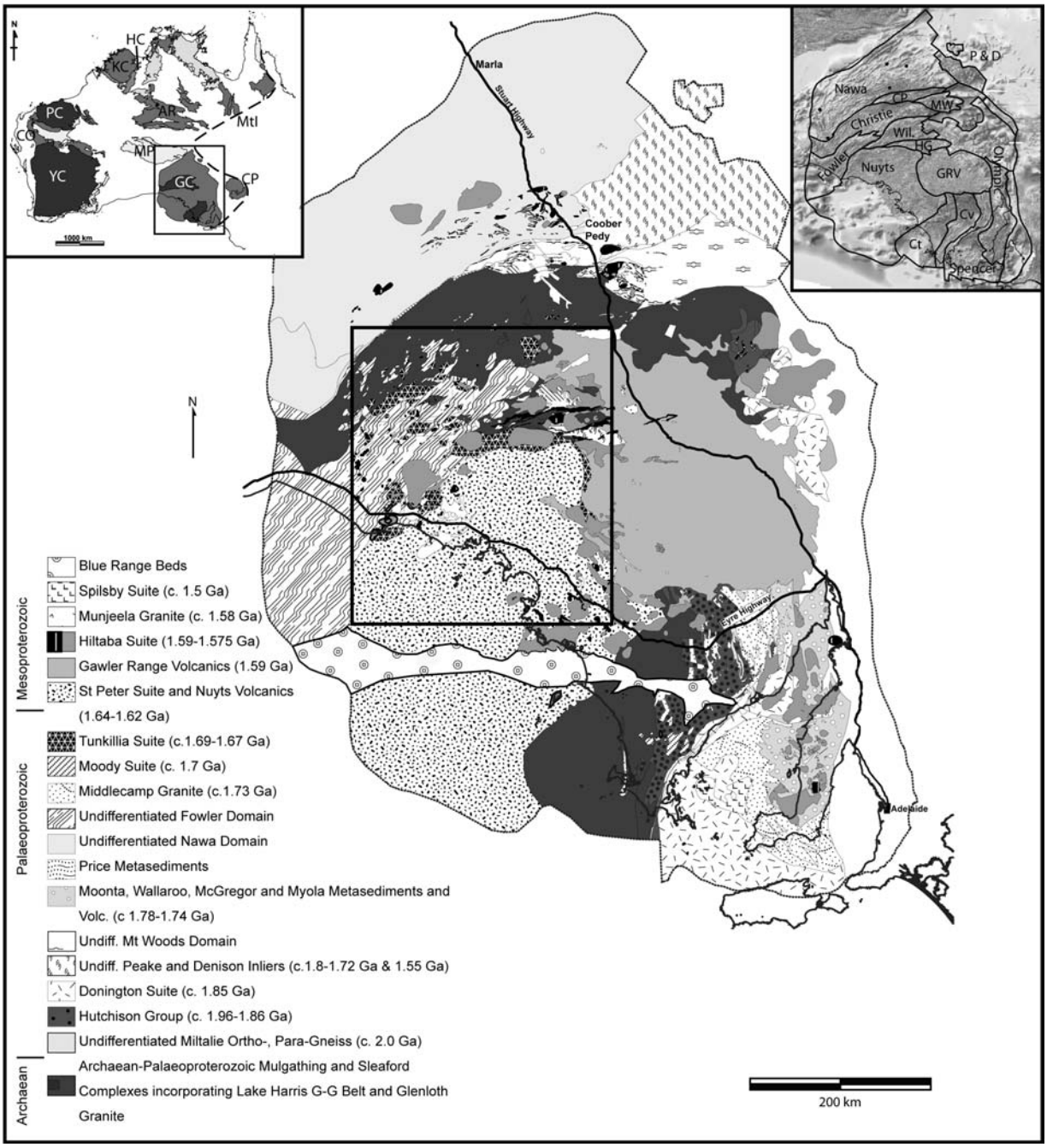

Figure 5.1 - Interpreted basement geology of the Gawler Craton after Fairclough et al. (2004). Box in main diagram represents extent of Figure 5.2. Inset Top Left: Pre-1070 Ma geological provinces of Australia after Betts et al. (2002) and Payne et al (2008) showing location of Gawler Craton. Abbreviations are: AR - Arunta Region, CO - Capricorn Orogen, CP - Curnamona Province, GC - Gawler Craton, HC - Halls Creek Orogen, KC - Kimberley Craton, MP - Musgrave Province, Mtl - Mount Isa Inlier, PC - Pilbara Craton, YC - Yilgarn Craton. Inset Top Right: Total Magnetic Intensity (TMI) image of the Gawler Craton with interpreted domains. Abbreviations are: CP - Coober Pedy Domain, Ct - Coulta Domain, Cv - Cleve Domain, GRV - Gawler Range Volcanics, HG - Harris Greenston Belt, MW - Mount Woods Domain, P & D - Peake and Denison, Wil. - Wilgena Domain.

events (eg. Direen et al., 2005; Dutch et al., 2006). The next major orogenic event, the Cornian Orogeny, is now understood to be a distinct event from ~1860-1850 Ma, which produced granulite facies metamorphism coeval with contractional and extensional deformation and the emplacement of the voluminous 1850 Ma Donington Granitoid Suite (Reid et al., in press). The proven extent of

Figure 5.2 - Detail of interpreted basement geology displaying locations, informal pluton names and ages of Tunkillia Suite Intrusives. Lithology fills as for Figure 5.1. VPF - Vermin Proof Fence. Note extent of interpreted Tunkillia Suite intrusive based upon interpretation of regional Total Magnetic Intensity (TMI) dataset (Fairclough et al., 2004).

the Cornian Orogeny is so far restricted to a small region east of the Kalinjala Shear zone in the Yorke Peninsula region. The third orogenic event is the Kimban Orogeny which is constrained temporally by early syntectonic granitoids (~1740-1726 Ma) and syn- to post-tectonic granites (~1720-1701 Ma and ~1690 Ma, Vassallo, 2001; Betts et al., 2003; Fanning et al., 2007). Newly obtained U-Pb monazite data (~1730-1690 Ma, Payne et al., 2008) record the occurrence of the Kimban Orogeny throughout the northern Gawler Craton. These data combined with the pre-existing knowledge of the extent of the Kimban Orogeny indicates it is a high-grade event (High-T, Med.-P, Daly et al., 1998; Tong et al., 2004; Dutch et al., 2006) that affected the entire Gawler Craton.

Subsequent deformation and metamorphism within the Gawler Craton is poorly constrained and understood. Significant metamorphic zircon growth occurs in the Mt Woods domain at ~1590 Ma (Skirrow et al., 2006), associated with granulite facies metamorphism (Hand et al., in press). U-Pb zircon and monazite data record a granulite facies metamorphic event at ~1560-1550 Ma in the Nawa, Coober Pedy and eastern Fowler Domains (Daly et al., 1998; Fanning et al., 2007; Payne et al., 2008).

Table 5.1 - Tunkillia Suite whole rock geochemistry with pluton names and sample locations. Locations provided in GDA 94, Zone 53.

Sample	R350424	R350426	R350427	R350428	R350429	R350431	R350433	R363434	R363435	R363436	R378933	R370928	R370929	R370932	R370934	R370935	R370936
Easting	466840	475717	475730	477797	477663	478064	481010	481130	480020	480361	477000	477656	478426	478400	477039	489996	489674
Northing	6500257	6494570	6494556	6490815	6490718	6490150	6491265	6490622	6490385	6471129	6491863	6503959	6503346	6503092	6506538	6511884	6512791
Location	Airstrip										Childara	Lake Everard					
Major (wt%)																	
SiO_2	72.00	62.90	71.80	76.40	76.80	76.30	73.70	70.50	67.70	71.60	75.60	72.90	75.60	68.90	75.30	76.00	77.10
Al_2O_3	14.90	19.30	13.50	11.50	12.00	12.30	13.20	14.70	15.60	13.70	12.20	11.90	12.80	14.00	12.90	13.10	12.00
Fe_2O_3	1.73	2.43	2.72	1.47	1.36	1.31	0.90	2.67	2.84	2.92	1.36	5.14	1.99	5.11	2.11	0.85	1.62
MnO	0.05	0.06	0.06	0.03	0.07	0.06	0.03	0.11	0.09	0.08	0.04	0.005	0.04	0.16	0.01	0.02	0.08
MgO	0.36	0.30	0.34	0.13	0.14	0.15	0.13	0.50	0.71	0.57	0.15	0.09	0.17	1.34	0.14	0.12	0.21
CaO	1.64	1.10	1.01	0.45	0.55	0.64	0.55	2.32	1.95	1.74	0.68	0.26	0.36	2.63	0.18	0.31	0.64
Na_2O	4.22	4.16	2.64	2.72	3.85	3.87	2.93	3.7	3.21	2.63	2.96	2.13	2.13	3.07	2.86	2.95	2.91
K_2O	4.15	8.24	5.84	5.41	4.42	4.50	6.69	3.70	6.05	5.16	5.30	5.23	6.58	3.70	6.36	6.00	4.73
TiO_2	0.21	0.22	0.31	0.14	0.11	0.11	0.14	0.22	0.49	0.3	0.1	0.17	0.2	0.64	0.2	0.11	0.14
P_2O_5	0.13	0.09	0.11	0.04	0.03	0.03	0.04	0.11	0.13	0.08	0.18	0.02	0.03	0.12	0.03	0.08	0.03
LOI	1.11	1.33	1.31	0.73	0.56	0.92	1.11	1.33	1.43	1.44	0.64	1.65	0.85	1.05	0.54	0.68	0.77
Total	100.50	100.13	99.64	99.02	99.89	100.19	99.42	99.86	100.20	100.22	99.21	99.50	100.75	100.72	100.63	100.22	100.23
Trace and REE (ppm)																	
La	26.0	15.0	48.0	78.0	25.5	30.0	30.5	33.0	43.0	41.0	24.0	12.0	50.0	68.0	44.0	22.0	29.5
Ce	46.5	27.0	98.0	140.0	60.0	70.0	60.0	56.0	88.0	90.0	50.0	21.0	110.0	115.0	66.0	35.5	52.0
Pr	5.5	3.4	11.5	16.0	7.5	8.5	6.5	6.5	9.5	9.5	6.0	2.3	11.5	12.5	7.5	3.7	5.0
Nd	19.0	13.0	44.5	60.0	29.5	33.5	21.5	21.5	30.5	32.0	21.0	7.5	42.0	46.5	23.0	10.5	14.5
Sm	3.2	2.5	8.5	10.5	7.0	8.0	3.3	2.8	4.3	6.0	4.7	1.5	6.5	7.0	4.0	1.6	2.2
Eu	1.1	0.8	0.8	0.6	0.4	0.4	1.2	1.9	2.6	1.3	0.6	0.5	0.6	1.2	0.7	0.4	0.4
Gd	3.1	1.9	5.5	6.5	4.8	5.0	2.5	2.4	3.5	4.9	4.6	1.6	3.8	4.4	3.1	1.3	1.7
Tb	0.5	0.4	1.1	1.3	1.1	1.2	0.3	0.3	0.5	0.8	0.7	0.3	0.6	0.7	0.5	0.2	0.3
Dy	2.9	2.6	6.5	8.0	7.5	7.5	1.7	1.7	2.4	4.4	4.3	1.8	3.8	4.6	2.5	1.3	1.6
Ho	0.6	0.5	1.1	1.4	1.4	1.4	0.3	0.3	0.4	0.8	0.9	0.4	0.6	0.8	0.5	0.3	0.4
Er	1.9	1.5	3.5	4.3	4.6	4.6	0.8	0.9	1.3	2.6	2.8	1.4	2.1	2.5	1.5	1.0	1.3
Tm	0.3	0.2	0.5	0.7	0.8	0.7	0.1	0.2	0.2	0.4	0.4	0.2	0.3	0.4	0.2	0.2	0.2
Yb	2.3	1.6	3.5	4.3	5.5	5.5	0.8	0.9	1.3	2.4	2.8	1.6	2.0	2.5	1.6	1.5	1.9
Lu	0.4	0.2	0.5	0.6	0.8	0.7	0.1	0.2	0.2	0.4	0.4	0.2	0.3	0.4	0.3	0.3	0.3
Ba	1250	600	460	270	200	220	1400	2250	2950	1100	400	600	250	700	500	220	200
Cr	3.0	7.0	6.0	4.0	3.0	3.0	2.0	3.0	4.0	6.0	bdl	13.0	6.0	6.0	3.0	bdl	2.0
Cu	15.0	18.0	8.5	6.0	5.5	5.5	6.0	52.0	150.0	9.0	7.0	7.0	52.0	14.5	36.0	15.0	34.0
Ga	17.0	26.0	20.5	19.5	19.5	22.0	13.5	17.5	18.5	17.5	17.5	15.0	17.0	19.5	16.5	15.0	16.0
Hf	2.0	3.0	2.0	3.0	3.0	3.0	3.0	3.0	6.0	3.0	5.0	4.0	3.0	5.0	4.0	3.0	3.0
Nb	8.0	14.0	13.0	11.0	23.5	26.5	6.0	6.0	8.0	10.0	12.0	12.0	8.5	11.0	10.0	14.0	14.0
Ni	bdl	3.0	bdl	3.0	bdl	bdl	bdl	bdl	bdl	3.0	2.0	bdl	4.0	3.0	bdl	bdl	bdl
Pb	22.0	26.0	33.0	29.0	36.5	33.5	26.0	22.0	36.0	20.0	34.0	28.0	34.5	26.0	28.0	26.0	22.0
Rb	120	410	300	230	250	270	145	72	110	135	220	155	250	185	200	260	240
Sr	360	58	54	35.5	43	41	145	500	470	260	62	66	40	94	105	56	110
Ta	4	4	4	4	4	4	3	3	3	3	4	11	8	8	7	7	7
Th	13.0	22.5	27.5	26.0	41.0	26.0	10.0	3.1	14.5	19.5	28.5	14.5	33.0	23.0	28.0	25.5	30.5
U	3.3	3.9	5.5	4.7	6.5	4.8	0.7	0.4	1.7	2.1	4.9	1.7	3.1	3.2	3.1	4.9	5.5
V	15.0	14.0	15.0	3.0	3.0	2.0	6.0	12.0	23.0	23.0	5.0	155.0	11.0	16.0	8.0	5.0	6.0
Y	15.0	11.0	31.5	35.0	38.5	41.0	7.0	8.0	11.5	20.5	23.0	10.5	16.5	20.0	11.0	7.5	11.0
Zn	36.0	47.0	66.0	50.0	60.0	48.5	13.0	64.0	60.0	37.0	31.0	10.0	39.0	56.0	13.0	9.0	18.0
Zr	140	160	120	140	120	130	170	180	380	180	140	170	100	220	190	80	90
La_N/Yb_N	7.64	6.54	9.27	12.26	3.13	3.69	25.76	24.78	23.25	11.54	5.79	5.07	16.89	18.38	18.58	10.25	10.49
Eu/Eu*	1.02	1.08	0.36	0.22	0.20	0.21	1.22	2.18	2.05	0.73	0.37	0.94	0.36	0.66	0.60	0.79	0.58
ASI	1.04	1.09	1.09	1.04	0.99	0.99	1.01	1.04	1.03	1.06	1.05	1.24	1.14	1.02	1.09	1.11	1.09

Table 5.1 (cont.) - Tunkillia Suite whole rock geochemistry with pluton names and sample locations. Locations provided in GDA 94, Zone 53.

Sample	444829	444830	879-47	444832	444833	444834	WGC81	WGC165	444835	R368571	R378924	R378920	R378921	R368573
Easting	-	-	-	-	-	-	360200	286130	-	484124	484352	466420	466740	472307
Northing	-	-	-	-	-	-	6619150	6612680	-	6535828	6536030	6561795	6561175	6553627
Location	Lake Ifould			Lake Tallacootra			Wynbring	Barton	Mulgathing	Vermin Proof Fence				
Major (wt%)														
SiO_2	70.65	70.04	72.1	72.83	71.39	75.711	73.1	71.9	75.90	66.7	73	72.2	74.6	72.7
Al_2O_3	14.63	15.05	13.8	12.86	14.28	13.01	12.5	14.3	13.10	14.6	14.2	15	13.5	14.3
Fe_2O_3	3.26	2.62	2.12	2.76	2.32	1.278	2.42	2.04	0.87	4.14	1.72	1.74	1.29	1.3
MnO	0.03	0.03	0.02	0.059	0.041	0.021	0.04	0.06	0.005	0.14	0.05	0.05	0.02	0.05
MgO	0.86	0.67	0.58	0.59	0.22	0.278	0.59	0.51	0.03	0.95	0.39	0.37	0.16	0.3
CaO	1.55	2.21	1.91	1.05	0.56	1.05	1.41	1.67	0.78	2.58	2.15	2.14	1.15	1.78
Na_2O	3.447	3.148	3.15	2.072	3.255	3.802	3.03	3.39	3.13	1.96	3.36	3.54	3.37	3.44
K_2O	4.57	5.54	4.46	6.52	6.53	4.4	4.77	4.7	5.57	4.98	3.95	4.21	5.26	4.43
TiO_2	0.546	0.316	0.335	0.403	0.208	0.222	0.355	0.225	0.05	0.51	0.17	0.16	0.14	0.13
P_2O_5	0.046	0.095	0.1	0.049	0.109	0.033	0.08	0.07	0.08	0.14	0.13	0.07	0.17	0.04
LOI	0.134	0.159	1.18	0.582	0.945	0.023	0.68	0.77	0.3	3.31	0.56	0.5	0.46	0.68
Total	99.71	99.87	99.76	99.77	99.86	99.83	98.98	99.64	99.82	100.01	99.68	99.98	100.12	99.15
Trace and REE (ppm)														
La	135.0	105.0	90.0	36.5	34.0	125.0	62.0	98.0	66.0	20.0	31.0	28.0	18.0	24.5
Ce	290.0	165.0	160.0	68.0	76.0	210.0	130.0	120.0	130.0	38.0	54.0	45.5	33.5	45.0
Pr	32.0	16.0	18.0	7.0	10.0	24.0	15.0	20.5	15.0	4.6	6.0	4.9	3.8	5.5
Nd	120.0	54.0	58.0	27.0	42.5	92.0	56.0	72.0	48.0	15.5	20.0	15.0	12.5	17.5
Sm	25.5	5.0	6.5	4.0	8.0	15.0	10.0	11.0	8.5	2.7	2.8	2.3	2.2	2.9
Eu	1.7	2.0	2.3	0.8	1.5	2.3	1.5	2.0	0.8	1.0	1.4	0.9	0.5	1.4
Gd	15.0	3.0	3.6	2.5	4.8	9.5	6.0	6.5	6.5	2.3	2.3	1.5	1.5	2.5
Tb	2.4	0.3	0.5	0.4	0.9	1.6	1.2	1.1	1.1	0.3	0.3	0.2	0.2	0.4
Dy	10.0	1.4	2.3	2.5	5.5	8.5	6.5	5.5	6.5	1.6	1.5	1.0	1.1	2.0
Ho	1.2	0.2	0.4	0.4	1.0	1.4	1.1	0.9	1.3	0.3	0.3	0.2	0.2	0.4
Er	2.1	0.7	1.1	1.2	3.1	3.7	2.8	2.4	4.1	0.8	0.8	0.6	0.7	1.1
Tm	0.2	0.1	0.2	0.2	0.5	0.5	0.4	0.4	0.6	0.1	0.1	0.1	0.1	0.2
Yb	0.9	0.6	1.1	0.7	3.1	2.7	2.5	2.3	4.4	0.8	0.8	0.6	0.8	1.1
Lu	0.2	0.1	0.2	0.1	0.4	0.4	0.4	0.4	0.6	0.1	0.2	0.1	0.1	0.2
Ba	1050	2450	3650	290	1050	1100	900	950	290	1000	1600	1000	210	1350
Cr	19.0	8.0	20.0	8.0	4.0	10.0	30.0	30.0	9.0	6.0	2.0	11.0	bdl	3.0
Cu	15.0	8.0	7.0	5.0	4.0	10.5	2.5	5.0	23.0	58.0	13.0	4.0	13.0	92.0
Ga	24.5	16.5	17.0	20.0	18.5	23.5	18.0	20.5	15.0	14.5	15.5	20.0	16.0	15.5
Hf	6.5	5.3	0.0	8.6	5.5	4.7	0.0	0.0	2.0	3.0	3.0	2.0	4.0	1.0
Nb	19.0	3.0	7.0	8.5	9.5	15.0	15.5	15.0	20.0	6.0	6.0	18.0	6.0	bdl
Ni	12.0	2.0	2.0	2.0	bdl	4.0	4.0	3.0	4.0	bdl	2.0	4.0	bdl	bdl
Pb	35.5	22.0	19.0	16.5	15.5	16.0	21.5	29.0	28.0	28.0	26.0	36.0	40.0	28.0
Rb	110	72	39	74	31.5	35	110	145	220	100	92	150	135	110
Sr	270	550	750	92	240	340	155	230	58	370	500	440	155	390
Ta	0.5	0.3	bdl	1.5	0.6	1.1	bdl	bdl	3	1	4	3	7	1
Th	78.0	12.0	13.0	3.1	3.1	7.5	22.0	21.0	37.5	10.0	10.0	20.0	30.5	10.5
U	2.2	0.4	0.7	1.0	0.4	0.7	2.1	3.8	6.0	1.6	0.9	2.0	1.6	1.1
V	43.0	19.0	20.0	10.0	7.0	31.0	20.0	20.0	14.0	9.0	10.0	14.0	6.0	13.0
Y	29.5	5.0	12.0	10.0	26.0	31.5	29.0	29.0	33.0	7.0	6.5	4.7	5.5	9.0
Zn	100.0	105.0	29.5	54.0	60.0	125.0	43.0	41.0	31.0	25.0	76.0	19.0	13.0	24.0
Zr	258	249	310	306	252	176	280	180	80	250	110	70	120	70
La_N/Yb_N	101.36	118.26	55.29	35.24	7.41	31.28	16.76	28.79	10.14	16.89	26.19	31.53	16.22	15.77
Eu/Eu*	0.27	1.58	1.45	0.78	0.72	0.59	0.57	0.70	0.34	1.20	1.63	1.42	0.86	1.53
ASI	1.09	1.00	1.03	1.04	1.07	1.01	0.99	1.05	1.05	1.11	1.05	1.06	1.03	1.05

5.3 Lithological character and geochronological constraints of the Tunkillia Suite

Sample locations for this study are provided in Figure 5.2 and Table 5.1. For ease of discussion, samples are grouped by location into informal pluton names (Table 5.1 and Figure 5.2). Previous U-Pb zircon geochronology has constrained crystallisation ages of the Tunkillia Suite to the period ~1690-1670 Ma (Teasdale, 1997; Ferris and Schwarz, 2004; Fanning et al., 2007). The distribution of these ages is plotted in Figure 5.2.

The Tunkillia Suite is predominantly composed of felsic intrusives that include syenite, adamellite, granodiorite and granite (Figure 5.3). Felsic intrusives are typically medium to coarse-grained with K-feldspar, plagioclase, quartz and biotite as the major primary igneous mineral phases. Zircon is the most common accessory mineral with minor titanite and apatite. Secondary minerals (including chlorite and epidote) reflect variable degrees of low-T alteration. Some plutons contain volumetrically minor mafic enclaves. The majority of intrusives occur as isolated outcrops with no country rock contacts exposed. Intrusives displaying country-rock contacts are found in the Christie and northern Fowler Domains (Figure 5.2) and in this region intrude the late-Archaean Christie Gneiss (ie. Barton South). Intrusives in the Christie Domain also contain extensive enclaves of Christie Gneiss (Teasdale, 1997). Minor mafic dykes occur as highly weathered subcrop intruding some of the eastern Tunkillia Suite outcrops. The sub-cropping nature of these dykes inhibits their classification as Tunkillia Suite-related and hence they are not included in this study.

The Tunkillia Suite is variably deformed and often occurs in outcrop as ortho-gneisses, augen-gneisses and in discrete zones (10cm-3m) as mylonite. From geophysical data and field observations, intrusives of the suite have previously been interpreted to be cut by the Yerda, Yalbrinda and Tallacootra shear zones (Teasdale, 1997; Swain et al., 2005c). The timing of deformation of the Tunkillia Suite is currently not well understood but in some instances is suggested to be approximately the same age as the Tunkillia Suite (eg. Lake Ifould pluton cut by *c.* 1680 Ma Tallacootra Shear Zone, Swain et al., 2005c).

5.4 Analytical Procedure

Samples were crushed and an aliquot was milled in a WC mill. Approximately half of the analytical pulp was used for whole-rock geochemistry, the remainder retained for isotopic analysis.

Major elements were analysed by fusion of a 0.1 g sub-sample of the analytical pulp with lithium metaborate followed by dissolution in nitric acid solution to give a "total solution" for ICP-MS analysis. Analysis of trace and REE elements is achieved by digestion of up to 0.5 g of the analytical pulp in a HF/multi acid solution and introduced into an ICP-MS for the quantification of the elements of interest.

Sm-Nd isotope analyses were conducted at the University of Adelaide. The method used is the same as that outlined in Payne et al. (2006). Samples were spiked with a $^{150}Nd/^{147}Sm$ solution and dissolution was carried out in high-pressure Teflon vessels over a 7 day period at 160°C. REEs were separated in Biorad Polyprep columns, this was then further separated in HDEHP-impregnated Teflon-powder columns to isolate Sm and Nd. Nd was analysed on a Finnigan MAT 262 Thermal Ionisation Mass Spectrometer (TIMS) with an in-house Nd standard (Johnson Matthey, $^{143}Nd/^{144}Nd$ = 0.511604 ± 0.000008) for each run. Sm was analysed on a MAT 261 TIMS. Throughout the duration of the study the standard had a measured $^{143}Nd/^{144}Nd$ value of 0.511601 ± 0.000013 (1 st. dev., n = 8), and blanks ranged from 104-296 pg Nd. Running average for La Jolla over the duration of this study is 0.511838 ± 0.000008 (1 st.dev., n = 6).

5.5 Results

Whole-rock geochemical and Sm-Nd isotopic results are reported in Tables 5.1 and 5.2, respectively.

5.5.1 Major Element Geochemistry

Samples within this study are characterised geochemically following the classification scheme of Frost et al. (2001). Major element characterisation diagrams are provided in Figure 5.4. Tunkillia Suite samples are predominantly felsic and range from 62.9 - 77.3 wt% SiO_2, with the majority above ~70

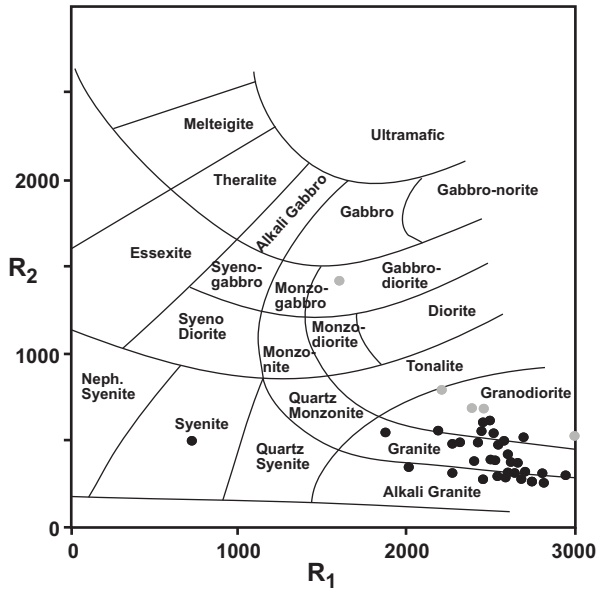

Figure 5.3 - Plutonic rock classification diagram after De la Roche et al. (1980). Tunkillia Suite samples are plotted as black dots and Low-K samples from Lake Ifould are plotted as gray dots.

wt% SiO_2. The majority of Tunkillia Suite samples plot as ferroan on Fe*-SiO_2 diagram (Figure 5.4a). Figure 5.b plots the Modified Alkali Lime Index (MALI, Frost et al., 2001). Tunkillia samples display a spread on the MALI diagram but predominantly fall within the alkalic-calcic and calc-alkalic fields. Figure 5.4c demonstrates the moderately peraluminous nature of the majority of the Tunkillia Suite samples. Plotting of samples on a K_2O-SiO_2 diagram (Figure 5.4d) shows the High-K to shoshinitic character of the Tunkillia Suite.

5.5.2 Trace and RE Element Geochemistry

REE chondrite and Primitive Mantle normalised spider plots are displayed in Figures 5.5 and 5.6, respectively. Chondrite-normalised REE patterns of the Tunkillia Suite show considerable variation in La_n/Yb_n, total concentrations and Eu anomalies (Table 5.1 , Figure 5.5). Most samples display flat HREE patterns, negative Eu* anomalies and La_n/Yb_n ratios in the range ~ 3-30. Such REE characteristics are typical of an average upper continental crust composition (Taylor and McLennan, 1985). Alternatively some samples record REE patterns with relatively consistent slopes (Figure 5.5d) or upwardly concave patterns showing no to positive Eu* anomalies (eg. Figure 5.5b and 5.f).

The majority of samples show similar trace element patterns on primitive mantle-normalised plots (Figure 5.6). Variable depletions of P, Nb and Ti are observed for all samples. Significant variations in concentration are evident for Ba, Sr, Y, and Zr.

5.5.3 Sm-Nd isotope systematics

Sm-Nd isotopic data is presented in Table 5.2 and growth curves are displayed in Figure 5.7. $\varepsilon_{Nd}(T)$ values are calculated at 1680 Ma, with their spatial distribution represented in Figure 5.8.

$\varepsilon_{Nd}(1.68\ Ga)$ values for Tunkillia suite samples ranges from -6.3 to +2.6. These values show a systematic spatial distribution, with intrusives in the western Christie and Fowler Domains which intrude Archaean crust ranging from -6.3 to -5.3 while the remainder of the samples range from -2.8 to +2.6 (Figure 5.9).

5.6 Discussion

5.6.1 Assessment of tectonic discrimination diagram data of the Tunkillia Suite

A subduction-related petrogenesis for the Tunkillia Suite has previously been based upon data from outcrop at Lake Ifould (location in Figure 5.2) reported in Teasdale (1997, sourced from unpub. Honours thesis of Taylor, 1987). Betts and Giles (2006) incorporated this data to delineate a volcanic-arc classification on a Rb v Nb+Y plot and a syn-collisional/volcanic arc classification on a Nb v Y plot (refer to Figure 5.9 in Betts and Giles, 2006). Four of the seven samples plotted in Betts and Giles (2006) display different chemical characteristics from the remainder of samples from Lake Ifould and the Tunkillia Suite in general (Table 5.1 and Appendix 5.1). Most notable is the differing major element chemistry in which the four Lake Ifould samples display low-to medium-K characteristics in comparison to the high-K nature of the Tunkillia Suite rocks. The differing major element characteristics and evolved nature (Figure 5.7 and Appendix 5.1) of the low- to medium-K Lake Ifould lithologies suggest they are not representative of the Tunkillia Suite.

Geochemical data was not obtained for the sample from Lake Ifould dated by Teasdale (1997) but sample description and location indicate it was sourced from the high-K intrusion. Reconnaissance

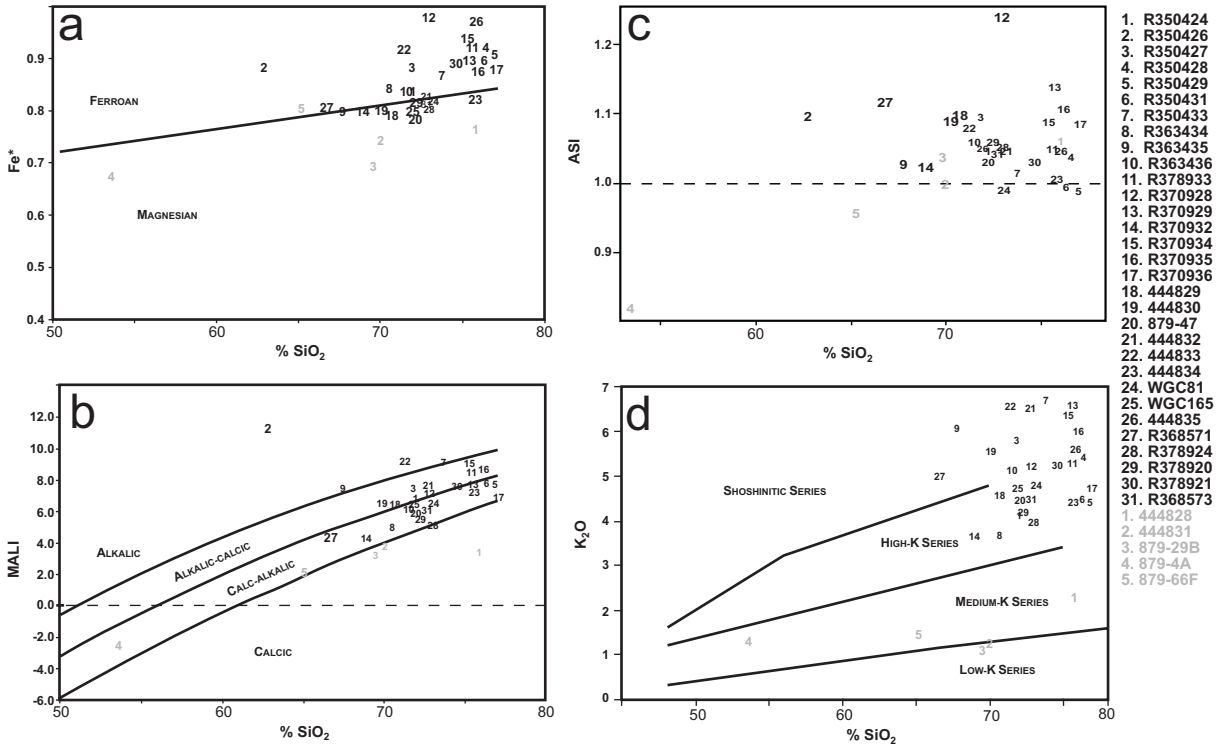

Figure 5.4 - Major element classification diagrams of Frost et al. (2001) and K_2O v SiO_2 diagram plot. a) Fe* v SiO_2, b) Modified Alkali Lime Index (MALI) v SiO_2, c) Aluminium Saturation Index (ASI) v SiO_2, d) K_2O v SiO_2. Low-K samples from Lake Ifould are plotted with gray numbers. Data for Lake Ifould low-K samples in Appendix 5.1.

U-Pb zircon geochronology from one low-K Lake Ifould sample is displayed in Figure 5.9 (Data in Appendix 5.1). Although data are limited, all analysed zircon grains provide an early Palaeoproterozoic age, which provide a statistically valid mean $^{207}Pb/^{206}Pb$ age of 2436 ± 14 Ma (n=6, MSWD=0.98). This is interpreted as the crystallisation age of the low- to medium-K lithologies from Lake Ifould. Although this zircon age may be due to zircon inheritance, the lack of any younger magmatic zircon suggests this is not the case. An early Palaeoproterozoic crystallisation age for the low- to medium-K Lake Ifould samples indicates they are not part of the 1690-1670 Ma Tunkillia Suite. This contrasts with a co-magmatic interpretation by Teasdale (1997) but is consistent with the differing geochemical characteristics and earlier mapping (Taylor, 1987) which described two separate magmatic events. The separation of the outcropping lithologies into two magmatic events was based upon an early structural fabric present in the low- to medium-K lithologies but not in the high-K intrusion (Taylor, 1987) subsequently dated by Teasdale (1997).

The re-interpretation of the extent of the Tunkillia Suite at Lake Ifould highlights the need for reassessment of the tectonic classification of the Tunkillia Suite. Trace element data from the Tunkillia Suite is plotted in Figure 5.10 and also includes the data of the low- to medium-K Lake Ifould samples. On the Nb versus Y discrimination diagram of Pearce et al. (1984) the Tunkillia Suite data plot in both the volcanic arc/syn-collisional and within-plate granite fields (Figure 5.10a). The Rb v Nb+Y plot used by Betts and Giles (2006) is not reliable for the Tunkillia Suite due to the well-documented mobility of Rb in metamorphic and deformation systems such as those that have affected Tunkillia Suite intrusions (Barovich and Patchett, 1992; Patel et al., 1999; Masters and Ague, 2005). Despite the potential mobility of Rb, the Ta:Hf ratios of Tunkillia Suite samples (Figure 5.10b) are in contrast to those expected for subduction-related granitoids using the discrimination diagram of Harris et al. (1986), which yields a dominantly late and post-collisional and within-plate classification (Figure 5.10). The variable nature of classification using discrimination diagrams, and inability to definitively assign a tectonic setting, highlights the the need for integrated mineralogical, geochemical and isotopic

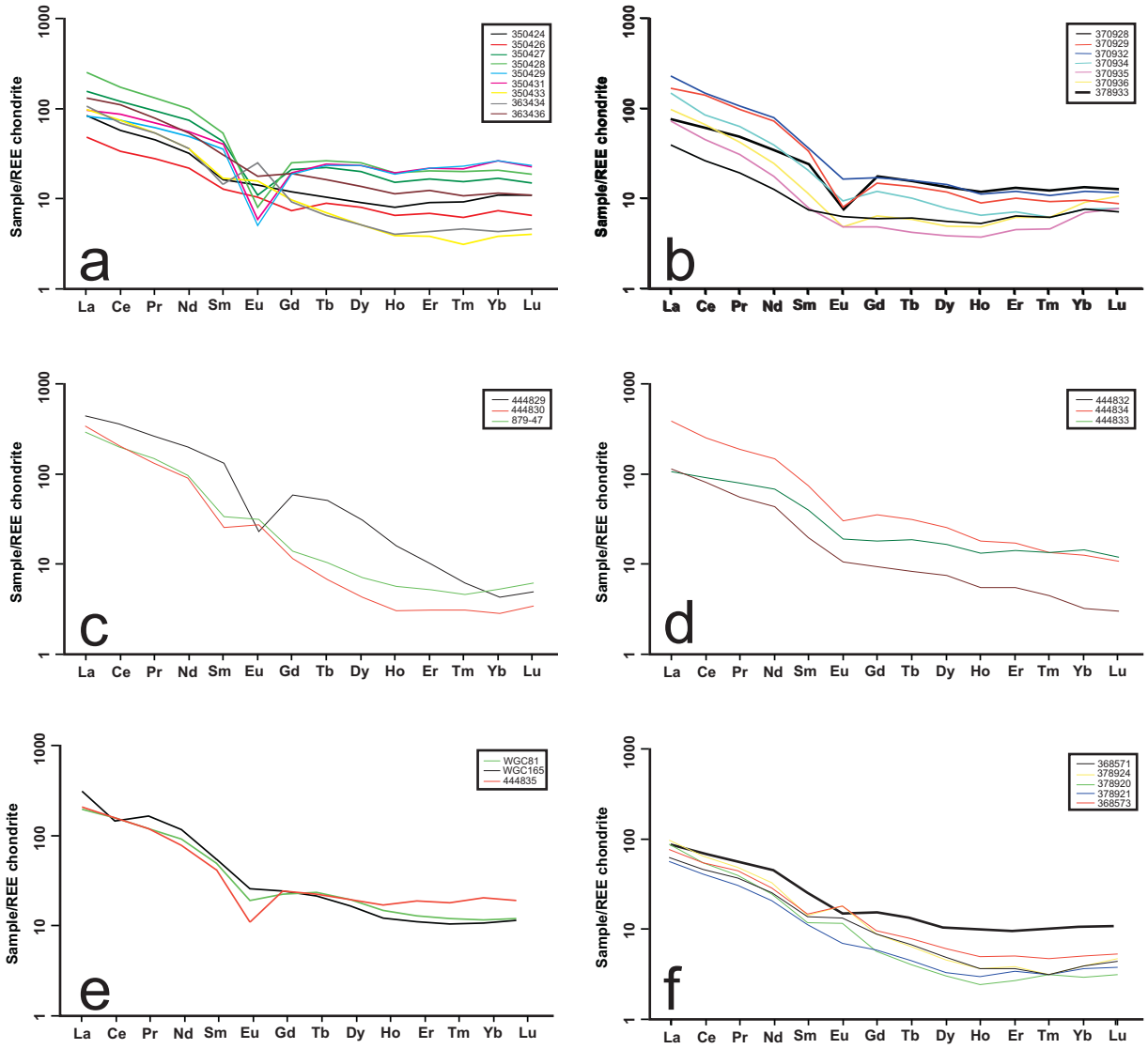

Figure 5.5 - REE Chondrite Normalised Spider Plots for samples of the Tunkillia Suite grouped by pluton. a) Airstrip, b) Childara and Lake Everard, c) Lake Ifould, d) Lake Tallacootra, e) WGC 81 - Wynbring, WGC 165 - Barton, 444835 - Mulgathing, f) Vermin Proof Fence.

studies to determine the petrogenesis of granitoid suites.

5.6.2 Geochemical, mineralogical and isotopic constraints on petrogenesis of the Tunkillia Suite

In this discussion the petrogenesis of the Tunkillia Suite is addressed by considering multiple methods used to discern the petrogenesis of granitic rocks. This includes mineralogy, major, trace and rare earth element geochemistry and Nd-isotope signature.

A first order method to assess the petrogenesis of the Tunkillia Suite is simply to consider the bulk mineralogy (eg. Barbarin, 1999) and associated major element chemistry (eg. Frost et al., 2001). To this extent, the mineralogy of quartz-feldspar-plagioclase-biotite with zircon ± apatite ± titanite best fits the high-potassium calc-alkaline granite (KCG) group defined by Barbarin (1999). Frost et al. (2001) propose a three-tiered scheme for the classification of granitic rocks based upon major element chemistry. According to this scheme the Tunkillia Suite can be considered predominantly ferroan, alkali-calcic to calc-alkalic and predominantly peraluminous. A further descriptor

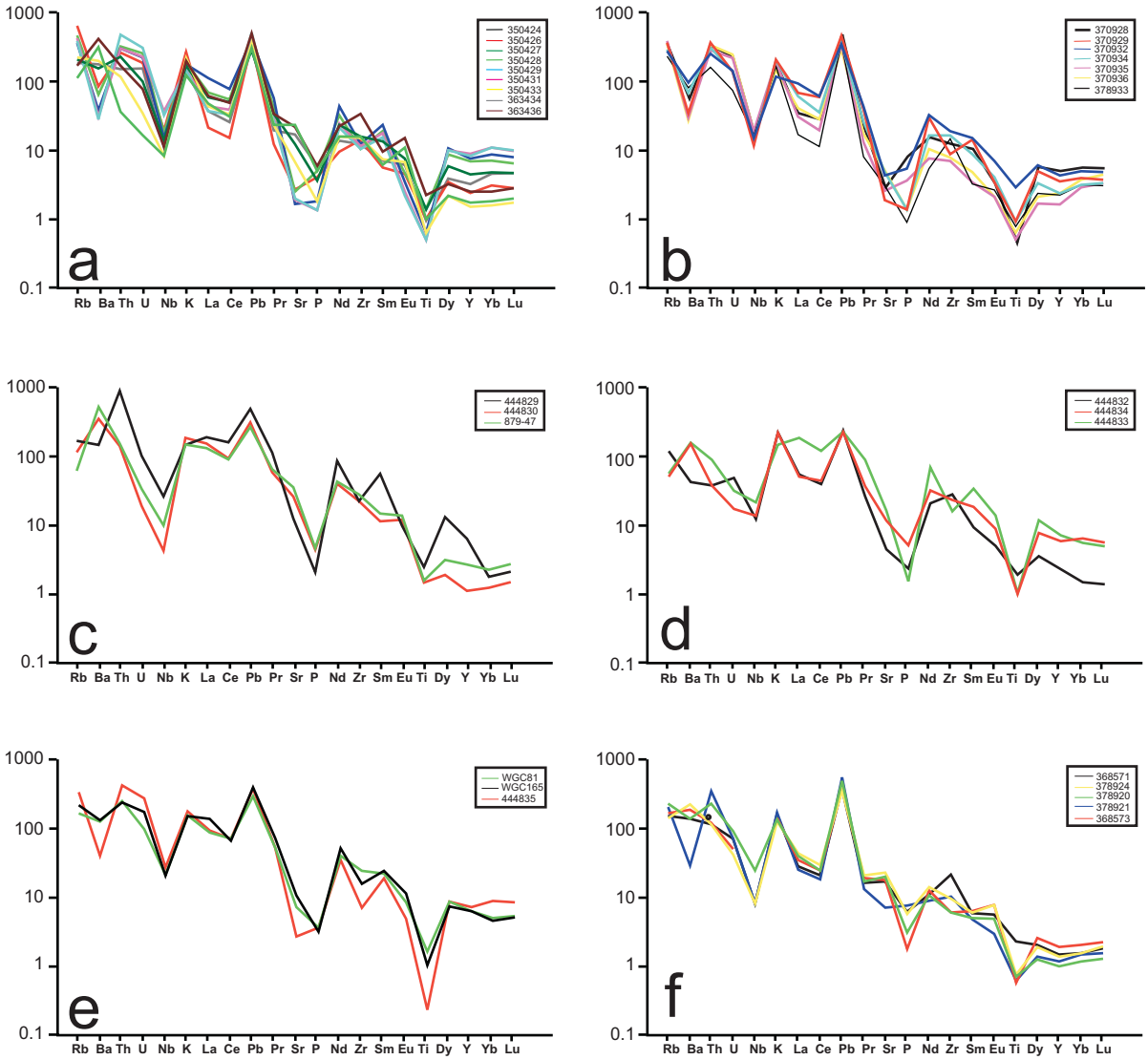

Figure 5.6 - Primitive-Mantle Normalised Spider Plots for Tunkillia Suite samples. Pluton groupings as for Figure 5.5.

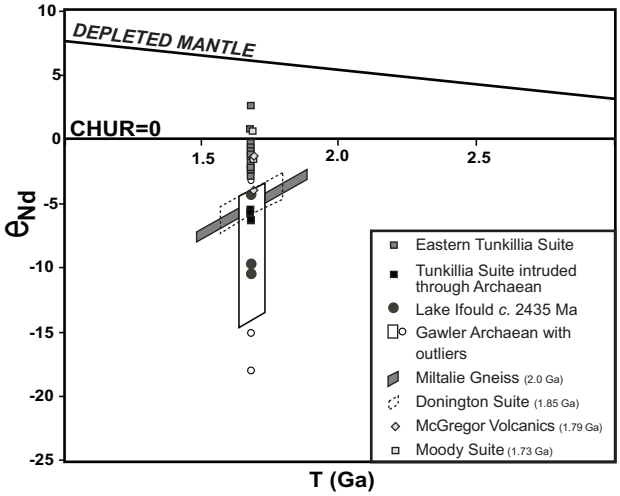

Figure 5.7 -Nd-isotope growth curves displaying Nd-isotope data at 1.68 Ga for Tunkillia Suite, low- to medium-K Lake Ifould Suite, Gawler Craton Archaean and pre-1.7 Ga magmatic lithologies of the Gawler Craton. Data for the low- to medium-K Lake Ifould samples are provided in Appendix 5.1.

not directly included in the scheme of Frost et al. (2001) is the K_2O v SiO_2 diagram of Figure 5.5d. This highlights the added characteristic that the majority of samples are classified as High-K to shoshonitic. A petrogenetic classification of the Tunkillia Suite is limited by the majority of samples containing >70 wt% SiO_2. As discussed by Frost et al. (2001), for SiO_2 values above 70 wt% granite suites transgress into the ferroan field of the Fe* diagram and spread across all fields in the MALI diagram. This requires consideration of both a ferroan and magnesian classification for the Tunkillia Suite. In the case of a ferroan classification, similarly classified granites are typically two-mica granites and occur as part of 'A-type' granite suites. The general lack of muscovite in the Tunkillia Suite rocks indicates a ferroan granite suite classification is inappropriate. Given the high-K nature of the

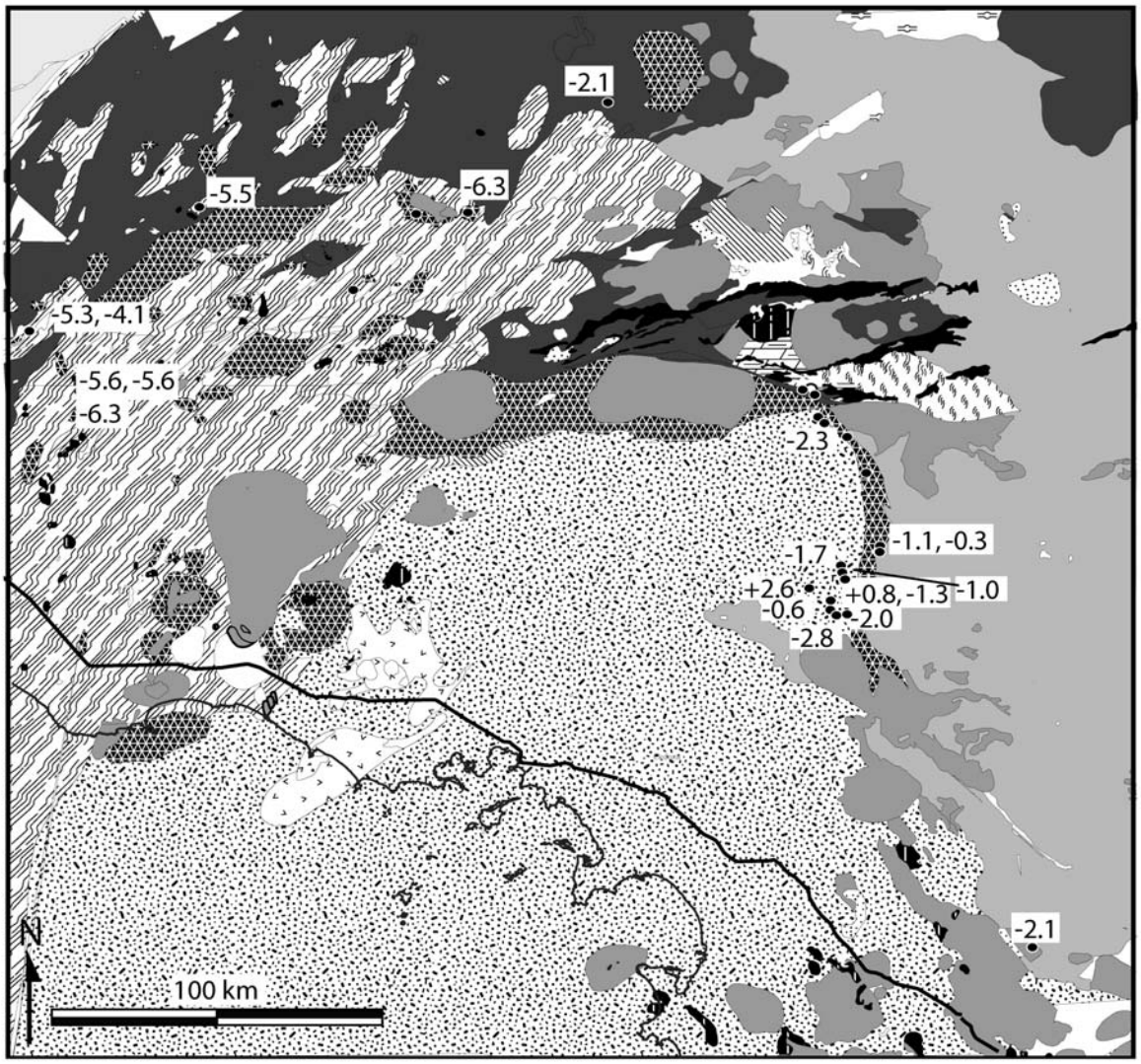

Figure 5.8 - Distribution of ε_{Nd} values for the Tunkillia Suite demonstrating the spatial variation between the eastern Tunkillia Suite and the western Tunkillia Suite.

Tunkillia Suite and similar high-K nature of magnesian, alkali-calcic granites in the classification of Frost et al. (2001), it is suggested a magnesian, alkali-calcic classification may best describe the Tunkillia Suite.

The KCG group is interpreted by Barbarin (1999) to represent a mixed contribution of mantle and crustal melt which is consistent with granite of the magnesian, alkali-calcic classification of Frost et al. (2001). The range of $\varepsilon_{Nd}(T)$ values recorded by the Tunkillia Suite (Figures 5.7 and 5.8) also indicate the involvement of both juvenile mantle melt material (+ve $\varepsilon_{Nd}(T)$) and melt from isotopically evolved, older crust (-ve $\varepsilon_{Nd}(T)$). Mantle involvement in the generation of the Tunkillia Suite, as demonstrated by Nd-isotope data, is consistent with the current interpretations suggesting the vast majority of granitoids involve mantle melting in their generation (eg. Barbarin, 1999; Patino Douce, 1999; Vigneresse, 2004). The apparent lack of juvenile, mafic and/or intermediate material associated with the Tunkillia Suite inhibits characterisation of the nature of mantle melting involved in the Tunkillia Suite petrogenesis. Additionally the small compositional range of the Tunkillia Suite (majority of SiO_2 values 70-76 wt%), and general lack of host country rock, results in an inability to define assimilation/fractional crystallisation trends in Tunkillia Suite geochemistry and hence determine model mantle melt compositions. In the absence of mafic material and modelled mantle melt compositions, discussion on trace and rare earth element geochemistry is

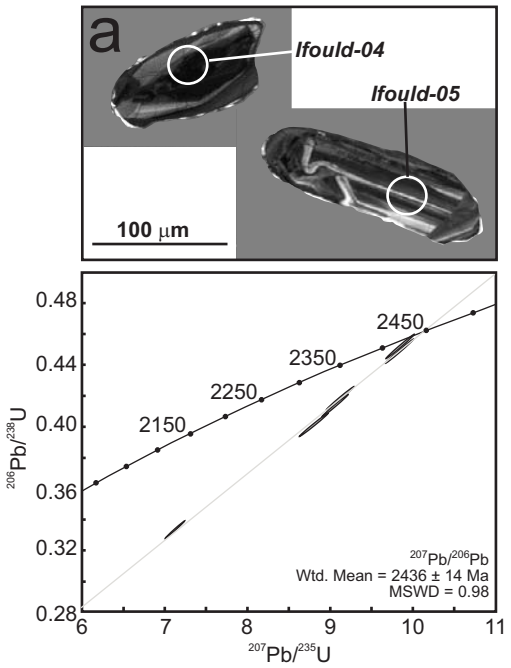

Figure 5.9 - a) Representative cathodoluminesence images of zircons analysed from Lake Ifould Low-K granite. b) Concordia diagram of reconnaisance geochronology data for Lake Ifould Low-K granite.

focused on the more juvenile felsic samples and mineral phases likely to be controlling crustal melt composition.

The Tunkillia Suite displays large within-suite REE variation (Figure 5.5) when compared to other coherent granitoid suites within Proterozoic Australia (eg. Foden et al., 1988; Griffin et al., 2000; Sheppard et al., 2001; Sheppard et al., 2004; Wade et al., 2006; Wade et al., 2007). This variation in REE composition is interpreted to represent differing contributions of mantle and crustal melt and also differing pressure and temperature conditions of crustal melting. REE patterns for Tunkillia Suite samples that display large negative Eu anomalies with enriched LREE and flat HREE patterns (Figure 5.5a and 5.5b) are similar to average upper continental crust compositions (Taylor and McLennan, 1985). Such REE patterns are interpreted to result from the presence of plagioclase as a restitic phase during crustal melting (Taylor and McLennan, 1985; Wyborn et al., 1992) which is supported for the Tunkillia Suite by the positive correlation of Sr and Eu/Eu* (Figure 5.11a) and Sr and CaO (not plotted, Wyborn et al., 1992). The positive correlation of Ba and Sr with Eu/Eu* (Figure 5.11a) and Ba and Sr (Figure 5.11b) demonstrates the control of K-feldspar over post-melting, fractional crystallisation processes within the Tunkillia Suite samples.

Tunkillia Suite samples with no or positive Eu anomalies and an upward concave REE pattern (eg. Figures 5.5a, 5.5b, and 5.5f) are not consistent with plagioclase as a restitic phase during melt generation. REE patterns with upward concave shapes are consistent with crustal melt composition, and subsequently felsic granite composition being controlled by hornblende as a restitic phase. Samples 350424 and 378924 which display upward concave REE pattern have comparably juvenile ε_{Nd}(T) values (+2.6 and -0.3) suggesting this REE pattern is the most representative of melt composition with the least crustal contamination. However, the isotopically more juvenile nature of these samples may simply represent differing composition of crustal comntaminants. Other

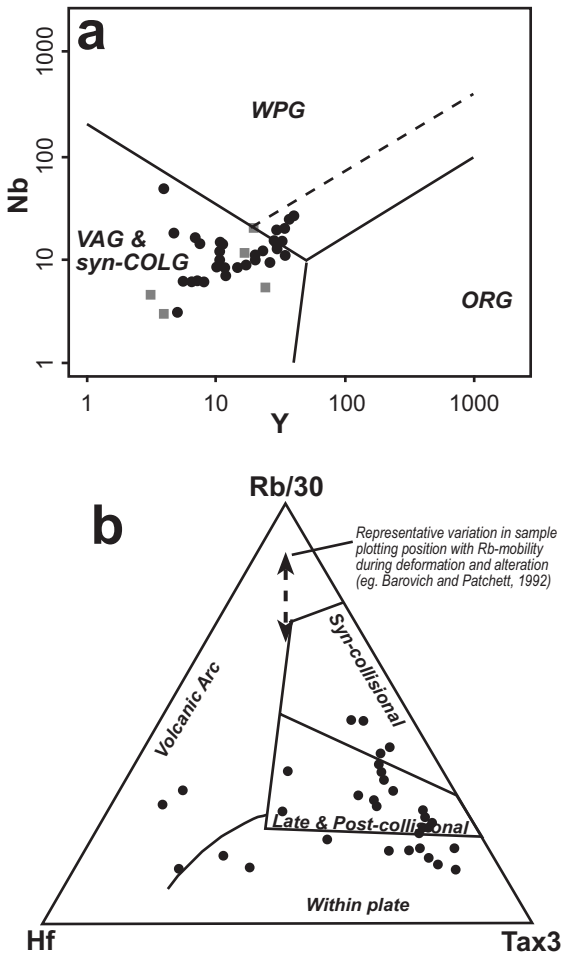

Figure 5.10 - a) Nb v Y Pearce tectonic discrimination diagram with Tunkillia Suite samples (circles) and low- to medium-K Lake Ifould samples (squares, Appendix 5.1). b) Hf-Rb-Ta tectonic discrimination diagram of Harris et al. (1986).

Table 5.2 - Nd-isotope data for Tunkillia Suite samples

Sample No.	*Pluton*	Sm (ppm)	Nd (ppm)	$^{147}Sm/^{144}Nd$	$^{143}Nd/^{144}Nd$	2 S.E.	$\varepsilon_{Nd}(0)^a$	$\varepsilon_{Nd}(T)$	T_{DM} (Ga)
350435	Airstrip	3.9	25.4	0.0922	0.511382	10	-24.5	-2.0	2.2
363436	Airstrip	5.7	33.6	0.1022	0.511452	11	-23.1	-2.8	2.30
350424	Airstrip	3.2	18.8	0.1042	0.511752	8	-17.3	2.6	1.93
350428	Airstrip	9.7	57.5	0.1023	0.511527	9	-21.7	-1.3	2.19
378933	Childara	4.3	20.1	0.1302	0.511875	12	-14.9	-0.6	2.30
370938	Childara	11.6	59.2	0.1180	0.511811	10	-16.1	0.8	2.10
370932	Lake Everard	6.7	45.0	0.0899	0.511372	8	-24.7	-1.7	2.17
370936	Lake Everard	1.9	13.5	0.0863	0.511366	9	-24.8	-1.0	2.1
879-47	Lake Ifould	6.9	57.5	0.0729	0.511001	11	-31.9	-5.3	2.30
444833	L. Tallacootra	7.2	39.2	0.1115	0.511414	6	-23.9	-5.6	2.6
444832	L. Tallacootra	3.9	27.1	0.0873	0.511111	11	-29.8	-6.3	2.4
444834	L. Tallacootra	13.8	84.6	0.0988	0.511271	8	-26.7	-5.6	2.5
WGC 81	Wynbring	9.5	55.9	0.1026	0.511281	13	-26.5	-6.3	2.53
444825	Barton	4.2	23.5	0.1080	0.511376	7	-24.6	-5.5	2.53
444835	Mulgathing	7.3	44.0	0.0997	0.511459	6	-23.0	-2.1	2.24
368571	Vermin Proof F.	3.1	17.6	0.1046	0.511568	10	-20.9	-1.1	2.19
368573	Vermin Proof F.	2.9	17.0	0.1026	0.511483	7	-22.5	-2.3	2.26
378924	Vermin Proof F.	3.8	26.0	0.0888	0.511433	8	-23.5	-0.3	2.07
444824	Pinbong	9.1	53.8	0.1025	0.511494	9	-22.3	-2.1	2.25

[a] $^{143}Nd/^{144}Nd$ CHUR(0) = 0.516638, $^{147}Sm/^{144}Nd$ CHUR = 0.1967

comparably isotopically juvenile samples display negative Eu anomalies (eg. 378933), and some samples with upward concave patterns yield evolved, negative $\varepsilon_{Nd}(T)$ values.

Samples displaying positive Eu anomalies, Sm-depletion and HREE depletion (eg. Figure 5.5c) are more typical of a melt composition dominated by garnet-rich restite. Samples with this type of REE pattern plot as a distinct group on a Sm/Nd versus Y plot (Figure 5.11d) with Sm-depletion corresponding to low Y concentrations. The correlation of Sm-depletion with low Y content is consistent with a garnet-rich restite and supports the interpretation based upon REE patterns.

Trace element compositions of Tunkillia Suite samples are relatively consistent with variation largely occurring in Ba, Sr, Y and REEs. Concentrations of Ba and Sr in magmatic rocks are largely controlled by plagioclase and K. feldspar during melting or fractional crystallisation. The observed variation of Ba and Sr is consistent with plagioclase and K. feldspar as controlling phases evidenced by correlations between Ba and Sr and also Eu/Eu* values (Figure 5.11a and 5.11b, see above). Y depletion is suggested to be due to a garnet-rich restite in samples also containing characteristic Sm-depletion (Figure 5.11d, see above). Hornblende in restite also preferentially incorporates Y resulting in Y-depleted melt but does not create the same degree of Sm-Nd fractionation in melt (partitition coefficients summarised in: Rollinson, 1993; Slagstad et al., 2005). Hence samples with Y-depletion but a lesser degree of Sm-Nd fractionation (Figure 5.11d) are likely to have Y content controlled by a hornblende-rich restite. Samples with high Y content are likely to represent a plagioclase-rich, hornblende-poor restite and/or fractional crystallisation progressively enriching Y in the melt.

Rare-earth and trace element characteristics of the Tunkillia Suite indicate melts were largely generated with hornblende or plagioclase-dominated restite material. Evidence for hornblende as a restitic phase in a large number of Tunkillia Suite samples suggests hornblende-dehydration melting reactions were not the dominant melt mechanism for Tunkillia Suite melt generation. High-K content, K/Na ratios and alkali versus ferromagnesian components of the Tunkillia Suite support the generation of melt generation primarily through biotite-dehydration melt reactions (eg. Patino Douce and Beard, 1995; Patino Douce, 1999). The limited number of samples with an

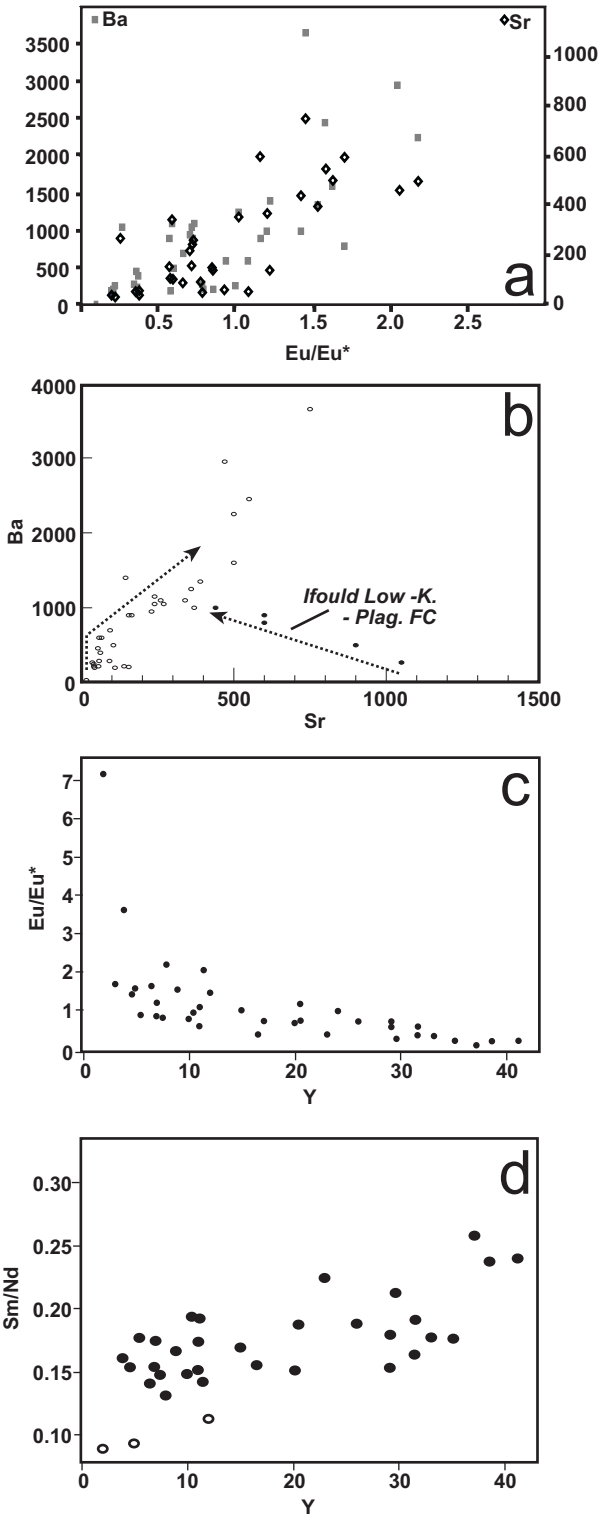

Figure 5.11 - a) Ba and Sr vs Eu/Eu* displaying rough positive correlation of Ba and Sr with Eu/Eu*, b) Ba v Sr plot displaying trend of Tunkillia Suite data which is consistent with K. Feldspar dominated fractional crystallisation. Low-K Ifould Suite is plotted for comparison demonstrating the influence of fractional crystallisation controlled by plagioclase, c) Eu/Eu* v Y plot demonstrating the low Y content for samples with positive Eu anomalies, d) Sm/Nd v Y plot displaying Sm-depletion for samples with REE and Y distributions consistent with garnet-rich restite (open circles).

interpreted garnet-rich restite indicates melting for the Tunkillia Suite largely occurred at lower P-T conditions than the garnet-in melt reaction. This places maximum P-T constraints, mainly pressure, on crustal melt conditions for generation of the Tunkillia Suite through comparison with melt experiments. Potential crustal source regions for the Tunkillia Suite are likely to have undergone metamorphism and potentially partial melting during the Sleafordian Orogeny and/or Kimban Orogeny (Daly et al., 1998; Hand et al., in press). This suggests that suitable starting materials for comparative melt experiments are biotite gneiss, amphibolite or Archaean TTG as studied by Patino Douce and Beard (1995), Wolf and Wyllie (1994) and Watkins et al. (2007), respectively. Vapour-absent experimental results for garnet-in melt reactions are plotted in Figure 5.12. Depending upon starting composition, and to a lesser degree temperature, Gt-in reactions vary from 8-12 kbar (Figure 5.12, Wolf and Wyllie, 1994; Patino Douce and Beard, 1995; Watkins et al., 2007). The apparent prevalence of biotite dehydration melting reactions in the generation of the Tunkillia Suite suggests a biotite gneiss (Patino Douce and Beard, 1995) or biotite-bearing tonalite (Watkins et al., 2007) may be the best representation of bulk source lithologies for the Tunkillia Suite. This suggests crustal melting involved in the Tunkillia Suite generation is likely to have occured with upper pressure constraints of 8-11 kbar based upon the garnet-in reactions. This places a broad P-T window of >800°C and <11kbar for crustal melting involved in the generation of the Tunkillia Suite (Figure 5.12). The general lack of compositional and P-T constraints on potential protolith material for the Tunkillia Suite limits further interpretation of crustal melting conditions.

5.6.3 Tectonic setting for the petrogenesis of the Tunkillia Suite

The previously assigned subduction-related petrogenesis of the Tunkillia Suite requires revision due to the inconclusive nature of tectonic discrimination diagrams and incorrect incorporation of early Palaeoproterozoic low-K granites into the Tunkillia Suite (Section 5.6.1). Accurate assessment of the tectonic setting for granitoid suites incorporating both mantle and crustal material is best accomplished through investigation of juvenile, mafic end-members. The lack of juvenile mafic

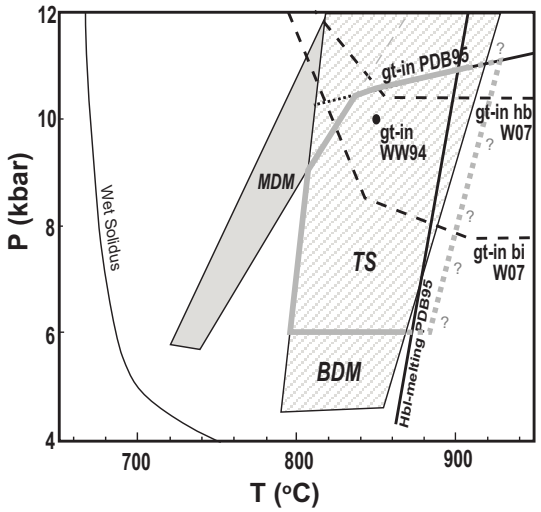

Figure 5.12 - P-T diagram with experimentally constrained muscovite and biotite dehydration melting fields (Patino Douce, 1999, and references therein) and hornblende dehydration melting reaction line (Patino Douce and Beard, 1995). Garnet-in isopleths are: gt-in bi W07 - biotite dehydration melting data of Watkins et al. (2007); gt-in hbl W07 - hornblende dehydration melting data of Watkins et al. (2007); gt-in PD95 - hornblende and biotite dehydration melting data of Patino Douce and Beard (1995); gt-in WW94 - hornblende dehydration data of Wolf and Wyllie (1994). Thick solid and dashed gray lines represent suggested field of melt generation for the Tunkillia Suite.

and intermediate phases in the Tunkillia Suite inhibits conclusive classification of the associated tectonic setting. Instead, the most appropriate tectonic setting for the Tunkillia Suite is outlined based upon the timing and style of granite petrogenesis with alternative tectonic settings also considered.

The timing of the Tunkillia Suite (1690-1670 Ma) is in a late- to post-tectonic timeframe with respect to the 1730-1690 Ma Kimban Orogeny (Daly et al., 1998; Dutch et al., 2006; Payne et al., 2007; Hand et al., in press). Geochronological constraints on shear zones such as the Tallacootra Shear Zone (Lake Tallacootra and Lake Ifould) indicate it was active (1680 ± 37 Ma) during the emplacement of the Tunkillia Suite (Swain et al., 2005c). The timing of the Tunkillia Suite with respect to orogenesis is consistent with post-tectonic magmatism in other orogens throughout the world (Liegeois et al., 1998; Altherr et al., 2000; Peterson et al., 2002; Konopelko and Eklund, 2003; Duchesne et al., 2007).

The KCG granitoids of Barbarin (1999) are considered to correlate with post-collisional tectonic regimes but are also found in limited numbers in active margin settings or during orogenic events (Barbarin, 1999). The lack of intermediate magmas, combined with major element chemistry and mineralogy, suggest the Tunkillia Suite did not form in a volcanic-arc setting. This interpretation is also supported by the comparably shallow melting level (below garnet-in) and predominance of biotite-dehydration melting which are not commonly observed in volcanic arc magmas (Calvache and Williams, 1997; Blein et al., 2003). Instead, any potential genetic relationship of the Tunkillia Suite with a subduction zone would be as an inboard expression of the arc magmatism.

A suggested Phanerozoic equivalent of the Tunkillia Suite are the Younger Granites (YG) and potentially some of the Older Granites (NS intrusions) of the late- to post-tectonic Carboniferous Vosges granites, France (Altherr et al., 2000). The YG in particular have similar mineralogy, major element chemistry and trace element characteristics to the Tunkillia Suite. Notably the YG display equivalent ranges in elements such as Y, U, Th, Ba, Rb, Sr and K_2O and display similar, but slightly less variation in REE patterns (Altherr et al., 2000). In contrast, Cordilleran interior granites display a much more restricted range of trace and major element compositions for equivalent SiO_2 values (eg. White Creek Batholith, southern Canadian Cordilleran, Brandon and Lambert, 1994) and typically display a higher proportion of mafic and intermediate lithologies and deeper melting depths (ie. D'Andrea Kapp et al., 2002; Ramo et al., 2002).

Given the timing of granite petrogenesis, mixed mantle-crust melting, highly variable trace and RE element characteristics and similarity to Phanerozoic granite suites such as the Vosges YG granites, a late- to post-tectonic setting appears to best describe the Tunkillia Suite. This tectonic classification is equivocal due to the inability to sample or model mantle melt composition and melting conditions. However, the Tunkillia Suite is unlikely to directly represent a subduction-related magmatic system as previously proposed with the use of tectonic discrimination diagrams (Teasdale, 1997; Betts and Giles, 2006). The potential for a subduction-related petrogenesis does exist, but as an inboard expression of magmatism such as

represented by Cordilleran interior granites. Given the evidence outlined above, classification as a late- to post-tectonic magmatic suite is the favoured interpretation of the authors.

5.6.4 Implications for Proterozoic Reconstruction models

The interpretation of the Tunkillia Suite as a late- to post-tectonic granite suite related to the Kimban Orogeny has implications for a number of continental reconstruction models. The previous classification of the Tunkillia Suite as a subduction-related magmatic arc was important in continental reconstruction models as it provided palaeogeographical constraints on plate-margin locations (eg. Betts et al., 2002). Removal of this plate margin constraint means there is no direct evidence for plate margin processes in the Gawler Craton between the 2460-2420 Ma Sleafordian Orogeny (Swain et al., 2005b) and 1620-1610 Ma St Peter Suite magmatism (Swain et al., 2005a). Continental reconstruction models that use the magmatic arc classification of the Tunkillia Suite require modification or in the least an added element of equivocation. This includes the models of Karlstrom et al. (2001), Betts et al. (2002), Giles et al. (2004) and Betts and Giles (2006). These models are discussed in detail in Chapter 7 of this thesis.

5.7 Conclusions

The petrogenesis of the Tunkillia Suite is dominated by crustal melting with biotite-dehydration melting reactions providing the bulk of crustal melt. Variation in trace and RE element characteristics indicate multiple modes of melt generation were involved including a limited number of samples generated with a garnet-rich restite.

New geochemical and isotopic data for the Tunkillia Suite have indicated the previous interpretation of a subduction-related petrogenesis is inappropriate. Instead a post-tectonic petrogenesis in relation to the craton-wide Kimban Orogeny is suggested. This suggests continental reconstruction models incorporating the previous subduction-related petrogenesis require revision.

References

Allen, S.R. and McPhie, J., 2002. The Eucarro Rhyolite, Gawler Range Volcanics, South Australia: A >675 km^3, compositionally zoned lava of Mesoproterozoic age. Geological Society of America Bulletin, 114(12): 1592-1609.

Altherr, R., Holl, A., Hegner, E., Langer, C. and Kreuzer, H., 2000. High-potassium, calc-alkaline I-type plutonism in the European Variscides: northern Vosges (France) and northern Schwarzwald (Germany). Lithos, 50(1-3): 51-73.

Barbarin, B., 1999. A review of the relationships between granitoid types, their origins and their geodynamic environments. Lithos, 46(3): 605-626.

Barovich, K.M. and Patchett, P.J., 1992. Behaviour of isotopic systematics during deformation and metamorphism - A Hf, Nd and Sr isotopic study of mylonitized granite. Contributions to Mineralogy and Petrology, 109(3): 386-393.

Betts, P.G. and Giles, D., 2006. The 1800-1100 Ma tectonic evolution of Australia. Precambrian Research, 144(1-2): 92-125.

Betts, P.G., Giles, D., Lister, G.S. and Frick, L.R., 2002. Evolution of the Australian lithosphere. Australian Journal of Earth Sciences, 49(4): 661-695.

Betts, P.G., Valenta, R.K. and Finlay, J., 2003. Evolution of the Mount Woods Inlier, northern Gawler Craton, southern Australia; an integrated structural and aeromagnetic analysis. Tectonophysics, 366(1-2): 83-111.

Blein, O., LaFleche, M.R. and Corriveau, L., 2003. Geochemistry of the granulitic Bondy gneiss complex: a 1.4 Ga arc in the central Metasedimentary Belt, Grenville Province, Canada. Precambrian Research, 120: 193-217.

Bonin, B.L., Azzouni-Sekkal, A., Bussy, F. and Ferrag, S., 1998. Alkali-calcic and alkaline post-orogenic (PO) granite magmatism: petrologic constraints and geodynamic settings. Lithos, 45(1-4): 45-70.

Brandon, A.D. and Lambert, R.S., 1994. Crustal Melting in the Cordilleran Interior: The Mid-Cretaceous White Creek Batholith in the Southern Canadian Cordillera. Journal of Petrology, 35(1): 239-269.

Calvache, M.L.V. and Williams, S.N., 1997. Geochemistry and petrology of the Galeras Volcanic Complex, Colombia. Journal of Volcanology and Geothermal Research, 77: 21-38.

Clemens, J.D., Yearron, L.M. and Stevens, G., 2006. Barberton (South Africa) TTG magmas: Geochemical and experimental constraints on

source-rock petrology, pressure of formation and tectonic setting. Precambrian Research, 151(1-2): 53-78.

Collerson, K.D. and Kamber, B.S., 1999. Evolution of the continents and the atmosphere inferred from Th-U-Nb systematics of the depleted mantle. Science, 283(5407): 1519-1522.

Creaser, R.A., 1995. Neodymium Isotopic Constraints for the Origin of Mesoproterozoic Felsic Magmatism, Gawler-Craton, South Australia. Canadian Journal of Earth Sciences, 32(4): 460-471.

Creaser, R.A. and White, A.J.R., 1991. Yardea Dacite - Large-Volume, High-Temperature Felsic Volcanism from the Middle Proterozoic of South-Australia. Geology, 19(1): 48-51.

Daly, S.J. and Fanning, C.M., 1993. Archaean. In: J.F. Drexel, W.V. Preiss and A.J. Parker (Editors), The geology of South Australia - The Precambrian, Bulletin 54. Mines and Energy, South Australia, Adelaide, pp. 242.

Daly, S.J., Fanning, C.M. and Fairclough, M.C., 1998. Tectonic evolution and exploration potential of the Gawler Craton, South Australia. In: I. Hodgson and B. Hince (Editors), Geology and mineral potential of major Australian mineral provinces. AGSO Journal of Australian Geology and Geophysics, pp. 145-168.

D'Andrea Kapp, J., Miller, C.F. and Miller, J.S., 2002. Ireteba Pluton, Eldorado Mountains, Nevada: Late, deep-source, peraluminous magmatism in the Cordilleran Interior. Journal of Geology, 110: 649-669.

De la Roche, H., Leterrier, J., Grandclaude, P. and Marchal, M., 1980. A classification of volcanic and plutonic rocks using R1R2-diagram and major-element analyses - Its relationships with current nomenclature. Chemical Geology, 29(1-4): 183-210.

Direen, N.G., Cadd, A.G., Lyons, P. and Teasdale, J., 2005. Architecture of Proterozoic shear zones in the Christie Domain, western Gawler Craton, Australia: Geophysical appraisal of a poorly exposed orogenic terrane. Precambrian Research, 142: 28-44.

Duchesne, J.C., Auwera, J.V., Liegeois, J.P., Barton, E.S. and Clifford, T.N., 2007. Geochemical constraints of the petrogenesis of the O'okiep Koperberg Suite and granitic plutons in Namaqualand, South Africa: A crustal source in Namaquan (Grenville) times. Precambrian Research, 153(1-2): 116-142.

Dutch, R., Hand, M. and Kinny, P.D., 2006. On the Kimban overprint: New geochronological constraints on high-grade metamorphism from Eyre Peninsula, southern Gawler Craton. In: D. Denham (Editor), Australian Earth Sciences Convention 2006. Geological Society of Australia, Melbourne.

Eklund, O., Konopelko, D., Rutanen, H., Frojdo, S. and Shebanov, A.D., 1998. 1.8 Ga Svecofennian post-collisional shoshonitic magmatism in the Fenno-scandian shield. Lithos, 45(1-4): 87-108.

Fairclough, M.C., Schwarz, M. and Ferris, G.J., 2004. Interpreted crystalline basement geology of the Gawler Craton, South Australia. In: J. Mcphie and P. McGoldrick (Editors), 17th Australian Geological Conference. Geological Society of Australia, Hobart.

Fanning, C.M., Reid, A.J. and Teale, G.S., 2007. A geochronological framework for the Gawler Craton, South Australia. Bulletin 55, Geological Survey, Primary Industries and Resources South Australia.

Ferris, G.M., Schwarz, M. and Heithersay, P., 2002. The Geological Framework, Distribution and Controls of Fe-Oxide and Related Alteration, and Cu-Au Mineralisation in the Gawler Craton, South Australia: Part 1: Geological and Tectonic Framework. In: T. Porter (Editor), Hydrothermal Iron Oxide Copper-Gold & Related Deposits: A Global Perspective. PGC Publishing, Adelaide.

Ferris, G.M., 2001. The geology and geochemistry of granitoids in the CHILDARA region, western Gawler Craton, South Australia: implications for the Proterozoic tectonic history of the western Gawler Craton and the development of the lode-style gold mineralisation at Tunkillia. M.Sc. Thesis, University of Tasmania.

Ferris, G.M. and Schwarz, M., 2004. Definition of the Tunkillia Suite, western Gawler Craton. MESA Journal, 34: 32-41.

Foden, J.D., Buick, I.S. and Mortimer, G.E., 1988. The petrology and geochemistry of granitic gneisses from the East Arunta Inlier, central Australia; implications for Proterozoic crustal development. Precambrian Research, 40-41: 233-259.

Fraser, G.L. and Lyons, P., 2006. Timing of Mesoproterozoic tectonic activity in the northwestern Gawler Craton constrained by $^{40}Ar/^{39}Ar$ geochronology. Precambrian Research, 151: 160-184.

Frost, B.R., Barnes, C.G., Collins, W.J., Arculus, R.J., Ellis, D.J. and Frost, C.D., 2001. A geochemical classification for granitic rocks. Journal of Petrology, 42(11): 2033-2048.

Giles, D., Betts, P.G. and Lister, G.S., 2004. 1.8-1.5-Ga links between the North and South Australian Cratons and the Early-Middle Proterozoic configuration of Australia. Tectonophysics, 380: 27-41.

Griffin, T.J., Page, R.W., Sheppard, S. and Tyler, I.M.,

2000. Tectonic implications of Palaeoproterozoic post-collisional, high-K felsic igneous rocks from the Kimberley region of northwestern Australia. Precambrian Research, 101(1): 1-23.

Hand, M., Reid, A. and Jagodzinski, E.A., in press. Tectonic framework and evolution of the Gawler Craton, Southern Australia. Economic Geology.

Harris, N.B.W., Pearce, J.A. and Tindle, A.G., 1986. Geochemical characteristics of collision-zone magmatism. Geological Society, London, Special Publications, 19(1): 67-81.

Hawkesworth, C.J. and Kemp, A.I.S., 2006. Evolution of the continental crust. Nature, 443(7113): 811-817.

Johnson, J.P. and Cross, K.C., 1995. U-Pb geochronological Constraints on the Genesis of the Olympic Dam Cu-U-Au-Ag Deposit, South Australia. Economic Geology and the Bulletin of the Society of Economic Geologists, 90(5): 1046-1063.

Karlstrom, K.E., Åhall, K.-I., Harlan, S.S., Williams, M.L., McLelland, J. and Geissman, J.W., 2001. Long-lived (1.8-1.0 Ga) convergent orogen in southern Laurentia, its extensions to Australia and Baltica, and implications for refining Rodinia. Precambrian Research, 111: 5-30.

Konopelko, D. and Eklund, O., 2003. Timing and geochemistry of potassic magmatism in the eastern part of the Svecofennian domain, NW Ladoga Lake Region, Russian Karelia. Precambrian Research, 120(1-2): 37-53.

Liegeois, J.P., Navez, J., Hertogen, J. and Black, R., 1998. Contrasting origin of post-collisional high-K calc-alkaline and shoshonitic versus alkaline and peralkaline granitoids. The use of sliding normalization. Lithos, 45(1-4): 1-28.

Lopez, S., Fernandez, C. and Castro, A., 2006. Evolution of the Archaean continental crust: Insights from the experimental study of Archaean granitoids. Current Science, 91(5): 607-621.

Masters, R.L. and Ague, J.J., 2005. Regional-scale fluid flow and element mobility in Barrow's metamorphic zones, Stonehaven, Scotland. Contributions to Mineralogy and Petrology, 150(1): 1-18.

McDonough, W.F. and Sun, S.-S., 1995. The composition of the Earth. Chemical Geology, 120: 223-253.

McFarlane, C.R.M., 2006. Palaeoproterozoic evolution of the Challenger Au Deposit, South Australia, from monazite geochronology. Journal of Metamorphic Geology, 24(1): 75-87.

Parker, A.J., 1993. Palaeoproterozoic. In: J.F. Drexel, W.V. Preiss and A.J. Parker (Editors), The geology of South Australia - The Precambrian, Bulletin 54. Mines and Energy, South Australia, Adelaide, pp. 242.

Patel, S.C., Frost, C.D. and Frost, B.R., 1999. Contrasting responses of Rb-Sr systematics to regional and contact metamorphism, Laramie Mountains, Wyoming, USA. Journal of Metamorphic Geology, 17(3): 259-269.

Patino Douce, A.E., 1999. What do experiments tell us about the relative contributions of crust and mantle to the origin of granitic magmas? In: A. Castro, C. Fernandez and J.L. Vigneresse (Editors), Understanding Granites: Integrating New and Classical Techniques. Geological Society, London, Special Publications, 168, pp. 55-75.

Patino Douce, A.E. and Beard, J.S., 1995. Dehydration-melting of Biotite Gneiss and Quartz Amphibolite from 3 to 15 kbar. Journal of Petrology, 36(3): 707-738.

Payne, J.L., Barovich, K.M. and Hand, M., 2006. Provenance of metasedimentary rocks in the northern Gawler Craton, Australia: Implications for palaeoproterozoic reconstructions. Precambrian Research, 148 (3-4): 275-291.

Payne, J.L., Hand, M., Barovich, K.M. and Wade, B.P., 2008. Temporal constraints on the timing of high-grade metamorphism in the northern Gawler Craton: implications for construction of the Australian Proterozoic. Australian Journal of Earth Sciences, 55, in press.

Pearce, J.A., Harris, N.B.W. and Tindle, A.G., 1984. Trace-Element Discrimination Diagrams for the Tectonic Interpretation of Granitic-Rocks. Journal of Petrology, 25(4): 956-983.

Peterson, T.D., Van Breemen, O., Sandeman, H. and Cousens, B., 2002. Proterozoic (1.85-1.75 Ga) igneous suites of the Western Churchill Province: granitoid and ultrapotassic magmatism in a reworked Archean hinterland. Precambrian Research, 119(1-4): 73-100.

Ramo, O.T., Calzia, J.P. and Kosunen, P.J., 2002. Geochemistry of Mesozoic plutons, southern Death Valley region, California: Insights into the origin of Cordilleran interior magmatism. Contributions to Mineralogy and Petrology, 143(4): 416-437.

Reid, A., Hand, M., Jagodzinski, E.A., Kelsey, D. and Pearson, N.J., in press. Palaeoproterozoic orogenesis within the southeastern Gawler Craton, South Australia. Australian Journal of Earth Sciences.

Rollinson, H.R., 1993. Using Geochemical Data: Evaluation, Presentation, Interpretation. Longman Scientific and Technical UK, 352 pp.

Sheppard, S., Griffin, T.J., Tyler, I.M. and Page, R.W., 2001. High- and low-K granites and adakites at a Palaeoproterozoic plate boundary in northwestern Australia. Journal of the Geological Society, London, 158: 547-560.

Sheppard, S., Occhipinti, S.A. and Tyler, I.M., 2003. The relationship between tectonism and composition of granitoid magmas, Yarlarweelor Gneiss Complex, Westem Australia. Lithos, 66(1-2): 133-154.

Sheppard, S., Occhipinti, S.A. and Tyler, I.M., 2004. A 2005-1970 Ma Andean-type batholith in the southern Gascoyne Complex, Western Australia. Precambrian Research, 128(3-4): 257-277.

Skirrow, R., Fairclough, M., Budd, A., Lyons, P., Raymond, O., Milligan, P., Bastrakov, E., Fraser, G., Highet, L., Holm, O. and Williams, N., 2006. Iron oxide Cu-Au (-U) potential map of the Gawler Craton, South Australia. (First Edition) 1:500 000 scale. Geoscience Australia, Canberra, ISBN: 1 920871 76 4.

Slagstad, T., Jamieson, R.A. and Culshaw, N.G., 2005. Formation, crystallisation, and migration of melt in the mid-orogenic crust: Muskoka Domain migmatites, Grenville Province, Ontario. Journal of Petrology, 46(5), 893-919.

Swain, G., Barovich, K., Hand, M. and Ferris, G.J., 2005a. Proterozoic magmatic arcs and oroclines: St Peter Suite, Gawler Craton, SA. In: M.D. Wingate and S.A. Pisarevsky (Editors), Supercontinents and Earth Evolution Symposium. Geological Society of Australia Inc. Abstracts 81, 177 p.

Swain, G., Woodhouse, A., Hand, M., Barovich, K., Schwarz, M. and Fanning, C.M., 2005b. Provenance and tectonic development of the late Archaean Gawler Craton, Australia; U-Pb zircon, geochemical and Sm-Nd isotopic implications. Precambrian Research, 141(3-4): 106-136.

Swain, G.M., Hand, M., Teasdale, J., Rutherford, L. and Clark, C., 2005c. Age constraints on terrane-scale shear zones in the Gawler Craton, southern Australia. Precambrian Research, 139(3-4): 164-180.

Taylor, M.J., 1987. The metamorphism, petrology and geochemistry of the Ooldea 2 drillcore and the Lake Ifould area. unpub. Honours Thesis, University of Adelaide, Adelaide.

Taylor, S.R. and McLennan, S.M., 1985. The Continental Crust: its composition and Evolution. Blackwell, Oxford., 312 pp.

Teasdale, J., 1997. Methods for understanding poorly exposed terranes: The interpretive geology and tectonothermal evolution of the western Gawler Craton. PhD Thesis, University of Adelaide, Adelaide, 179 pp.

Tomkins, A., 2002. Evolution of the granulite-hosted Challenger gold deposit, South Australia: implications for ore genesis. PhD Thesis, Australian National University, Canberra.

Tomkins, A.G., Dunlap, W.J. and Mavrogenes, J.A., 2004. Geochronological constraints on the poly-metamorphic evolution of the granulite-hosted Challenger gold deposit: implications for assembly of the northwest Gawler Craton. Australian Journal of Earth Sciences, 51: 1-14.

Tong L., Wilson C.J.L. and Vassallo J.J., 2004. Metamorphic evolution and reworking of the Sleaford Complex metapelites in the southern Eyre Peninsula, South Australia, Australian Journal of Earth Sciences 51 (4): 571-589.

Vassallo, J.J., 2001. Tectonic Investigation in the Gawler Craton. PhD Thesis, University of Melbourne, Melbourne, 172 pp.

Vigneresse, J.L., 2004. A new paradigm for granite generation. Transactions: Earth Sciences, 95: 11-22.

Wade, B.P., Barovich, K.M., Hand, M., Scrimgeour, I.R. and Close, D.F., 2006. Evidence for early Mesoproterozoic arc magmatism in the Musgrave Block, central Australia: Implications for Proterozoic crustal growth and tectonic reconstructions of Australia. Journal of Geology, 114(1): 43-63.

Wade, B.P., Payne, J.L., Barovich, K.M., Hand, M. and Reid, A., 2007. Petrogenesis of the 1.5 Ga magmatism in the Coompana Block - Filling the magmatic gap in Proterozoic Australia. Australian Journal of Earth Sciences, In Press.

Watkins, J.M., Clemens, J.D. and Treloar, P.J., 2007. Archaean TTGs as sources of younger granitic magmas: melting of sodic metatonalites at 0.6-1.2 GPa. Contributions to Mineralogy and Petrology, 154(1): 91-110.

Wolf, M.B. and Wyllie, P.J., 1994. Dehydration-melting of amphibolite at 10 kbar: the effects of temperature and time. Contributions to Mineralogy and Petrology, 115(4): 369-383.

Wyborn, L.A.I., Wyborn, D., Warren, R.G. and Drummond, B.J., 1992. Proterozoic granite types in Australia: implications for lower crust composition, structure and evolution. Second Hutton Symposium, Transactions of the Royal Society of Edinburgh: Earth Sciences, 83, 201-209

Appendix 5.1 - Lake Ifould geochemistry and U-Pb zircon geochronology

Low- to Medium-K lithologies at Lake Ifould are described by Teasdale (1997) as complexly deformed intrusive agmatites and migmatites and were interpreted to form gradational contacts with the Tunkillia Suite. In contrast detailed mapping by Taylor (1987) identified a structural fabric present in the low- to medium-K lithologies which is not present in the high-K granite. New geochemical and Nd-isotope analyses of samples from Taylor (1987) and Teasdale (1997) are reported in Table 5.A1.1 and 5.A1.2. This geochemical data further demonstrates the distinct geochemical nature of the here-in labelled low- to medium-K lithologies.

On the basis of the observed bulk geochemical differences between the low- to medium-K lithologies and those dated by Teasdale (1997), sample 879-66F was selected for reconnaissance U-Pb zircon geochronology. LA-ICPMS U-Pb zircon geochronology was undertaken at Adelaide Microscopy, University of Adelaide. Zircons were separated from a 79-425 μm sieved fraction using standard panning, Frantz Isodynamic magnetic and heavy liquid separation techniques. LA-ICP-MS operating procedures are similar to those described in Payne et al. (2006). U-Pb geochronology data are reported in Table 5.A1.3.

Zircons from 879-66F sample range in size from 100 - 250 m, are generally euhedral and clear to pale yellow in colour and display magmatic zoning commonly overprinted by metamictisation in CL imaging (Figure 5.9a). Figure 5.9b displays the U-Pb isotope data plotted upon a concordia diagram. An upper intercept age of 2449 ± 17 Ma (n=6, MSWD=10.8) is yielded. A weighted average of $^{207}Pb/^{206}Pb$ ages is 2436 ± 14 Ma (n=6, MSWD=0.98). As the upper intercept age has an excessively large MSWD value the $^{207}Pb/^{206}Pb$ age is used as the crystallisation age of the analysed zircon population. Relict magmatic zoning and lack of younger age analyses suggests the age obtained is representative of the magmatic crystallisation age of the low- to medium-K lithologies. Limited analyses numbers mean this can only be considered a reconnaissance age.

Table 5.A1.1 - Whole rock geochemistry

Sample	444828	444831	879-29B	879-4A	879-66F
Major (wt%)					
SiO_2	76.07	70.21	69.80	53.80	65.40
Al_2O_3	13.47	17.17	15.90	18.40	15.20
Fe_2O_3	1.74	1.80	2.17	8.53	6.26
MnO	0.04	0.02	0.03	0.15	0.06
MgO	0.55	0.62	0.95	4.13	1.45
CaO	2.43	3.00	3.10	8.00	3.87
Na_2O	3.62	5.50	5.24	4.10	4.57
K_2O	2.26	1.23	1.13	1.28	1.46
TiO_2	0.23	0.20	0.33	0.72	1.07
P_2O_5	0.08	0.02	0.11	0.17	0.23
LOI	0.67	0.02	1.67	0.80	0.61
Total	101.14	99.78	100.43	100.08	100.18
Trace and REE (ppm)					
La	80.0	6.5	48.5	45.0	54.0
Ce	135.0	10.0	86.0	92.0	105.0
Pr	15.0	1.2	9.5	11.5	12.0
Nd	54.0	4.2	32.0	49.0	47.0
Sm	8.0	0.7	3.6	9.0	8.5
Eu	1.4	0.7	1.4	2.3	2.6
Gd	4.4	0.6	1.8	5.5	5.5
Tb	0.7	0.1	0.2	1.0	0.9
Dy	4.0	0.9	0.7	5.5	4.7
Ho	0.7	0.2	0.1	1.0	0.8
Er	2.1	0.6	0.3	2.5	2.0
Tm	0.3	0.1	0.1	0.4	0.3
Yb	2.1	0.7	0.3	2.3	1.7
Lu	0.3	0.1	0.1	0.4	0.3
Ba	900	500	800	270	900
Cr	11.0	12.0	30.0	50.0	30.0
Cu	6.0	4.0	3.0	14.5	8.5
Ga	19.5	22.0	21.0	27.0	22.0
Hf	3.3	1.9	0.0	0.0	0.0
Nb	11.5	3.0	4.5	5.5	21.0
Ni	3.0	8.0	8.0	30.0	10.0
Pb	24.0	13.0	13.5	12.5	12.0
Rb	140	40	15.5	16.5	20.5
Sr	165	900	600	1050	600
Ta	0.6	0.6	bdl	bdl	bdl
Th	21.0	3.3	13.0	7.0	16.0
U	2.3	0.6	0.5	0.4	0.7
V	22.0	25.0	20.0	100.0	40.0
Y	17.0	3.9	3.1	24.0	20.5
Zn	62.0	50.0	45.0	115.0	88.0
Zr	128	76	160	100	270
La_N/Yb_N	25.74	6.76	131.10	13.22	22.12
Eu/Eu*	0.72	3.62	1.70	1.00	1.16
ASI	1.06	1.09	1.04	0.82	0.96

Table 5.A1.2 - Sm-Nd isotope data for low- to medium-K Lake Ifould granites

Sample No.	*Pluton*	Sm (ppm)	Nd (ppm)	$^{147}Sm/^{144}Nd$	$^{143}Nd/^{144}Nd$	2 S.E.	$\varepsilon_{Nd}(0)$	$\varepsilon_{Nd}(T)$	T_{DM} (Ga)
879-29B	Ifould Low-K	3.2	29.4	0.0652	0.510656	38	-38.7	-10.4	2.53
879-4A	Ifould Low-K	7.9	48.6	0.0982	0.511341	9	-25.3	-4.1	2.36
879-66F	Ifould Low-K	7.4	43.7	0.1018	0.511109	10	-29.8	-9.5	2.75

$\varepsilon_{Nd}(T)$ calculated at T=1680 Ma

Table 5.A1.3 - LA-ICP-MS U-Pb zircon geochronology data for sample 879-66F

Analysis No.	$^{207}Pb/^{206}Pb$ ratio	1σ	$^{207}Pb/^{235}U$ ratio	1σ	$^{206}Pb/^{238}U$ ratio	1σ	$^{206}Pb/^{238}U$ Age (Ma)	1σ (Ma)	$^{207}Pb/^{206}Pb$ Age (Ma)	1σ (Ma)	% Conc.
IFLD01	0.15827	0.00168	9.85173	0.11756	0.45147	0.0053	2401.8	23.6	2437.3	17.8	98.5
IFLD02	0.15507	0.00156	7.12963	0.0821	0.33349	0.00386	1855.3	18.7	2402.5	17.0	77.2
IFLD03	0.15896	0.00161	9.05174	0.10479	0.41302	0.00479	2228.7	21.8	2444.6	17.1	91.2
IFLD03B	0.15929	0.00165	8.80332	0.10314	0.40086	0.00466	2173.0	21.5	2448.1	17.4	88.8
IFLD04	0.15828	0.00159	9.12064	0.10462	0.41795	0.00482	2251.2	21.9	2437.4	16.9	92.4
IFLD05	0.15903	0.00167	9.83699	0.11614	0.44866	0.00523	2389.3	23.3	2445.4	17.6	97.7

Chapter 6

Crustal anatexis in the Gawler Craton, South Australia: Evidence for early Mesoproterozoic crustal thickening

Abstract

Intrusions belonging to the Mesoproterozoic Munjeela Suite, southwestern Gawler Craton, southern Australia, are muscovite-biotite-garnet-bearing peraluminous granites. New U-Pb SHRIMP zircon geochronology demonstrates the granites crystallised at ~1590-1580 Ma and are a coherent igneous suite. Major, trace and rare-earth element characteristics of the intrusions indicate they were generated through muscovite-dehydration melting of a metasedimentary protolith. Nd-isotope data indicate the metasedimentary protolith is likely to belong to the same sedimentary sequence as metasedimentary enclaves within the granite.

HREE enrichment and Sm-Nd disequilibrium in one intrusion (Pt James) is related to xenocrystic garnet within the granite. REE data for xenocrystic garnet indicates it could not have grown in equilibrium with granitic melt of the Munjeela Suite. The Pt James intrusion also incorporates rapakivi feldspar textures, suggesting decompression during granite crystallisation.

Metasedimentary enclaves within the granite are derived from a sedimentary sequence which does not otherwise outcrop. U-Pb LA-ICP-MS detrital zircon geochronology indicate at least part of the sedimentary sequence had a maximum depositional age of ~1625 Ma. This maximum deposition age constrains the metamorphism and deformation within the metasedimentary packages to ~1625-1590 Ma.

P-T constraints for metamorphism of the metasedimentary enclaves (7 kbar, 650°C) provides evidence for burial of >20 km sometime during the period ~1625-1590 Ma. The presence of two tectonic foliations within metasedimentary enclaves and the generation of the Munjeela Suite through muscovite-dehydration melting suggests this burial is related to crustal thickening. If this is the case then the *c.* 1595-1575 Ma Gawler Range Volcanics and Hiltaba Suite magmatic event occurred at least partly synchronous with crustal thickening. A deforming, possibly orogenic, system for the large volume, high-temperature felsic Hiltaba magmatic event is in contrast with previously proposed anorogenic settings for the magmatism.

6.1 Introduction

The Gawler Craton in southern Australia is a large, late Archaean to Mesoproterozoic crustal terrain with a complex, one billion year record of crustal re-working (Daly et al., 1998; Hand et al., in press). Early Mesoproterozoic tectonics of the Gawler Craton are dominated by the voluminous Gawler Range Volcanics (GRV) and Hiltaba Suite magmatism and associated Fe oxide-Cu-Au-U and Cu-Au mineralising systems, including the giant Olympic Dam deposit (Johnson and Cross, 1995; Johnson and McCulloch, 1995; Garner and McPhie, 1999; Morrow and McPhie, 2000; Allen and McPhie, 2002; Allen et al., 2003; Budd and Fraser, 2004). The GRV and Hiltaba Suite incorporate magmas described as I- and A-type (Creaser and White, 1991; Creaser, 1995) and were thought to be emplaced in an anorogenic tectonic setting. In contrast, recent work has suggested the Hiltaba Suite was emplaced into a crustal system undergoing high-grade metamorphism and deformation (Forbes and Giles, 2007; Direen and Lyons, in press; Hand et al., in press). This paper provides evidence that the early Mesoproterozoic of the Gawler Craton also included the melting of

young sedimentary packages to produce leucocratic garnet-muscovite-biotite-bearing granite of the Munjeela Suite.

Highly peraluminous, garnet-bearing granite, such as the Munjeela Suite, can be divided into two general types: Muscovite-biotite ± garnet granite and biotite-cordierite ± garnet granite. The differing mineralogy of these granite types is a reflection of the conditions and mineral melt reactions of their petrogenesis. Barbarin (1996) described a fluid-present melt generation ("wet" anatexis) for muscovite-biotite granites and a fluid-absent melt generation for biotite-cordierite granite (heat provided by mantle melt input into crust). However, many studies describe muscovite and/or biotite dehydration melting reactions for the majority of muscovite-biotite-bearing granite (eg. Harris and Inger, 1992; Inger and Harris, 1993; Patino Douce and Harris, 1998; Nabelek and Liu, 2004). Some small-volume leucogranites are ascribed to fluid-present melting during prograde metamorphism, but these are readily discernible by their geochemistry that is characterised by low Rb/Sr, high Ba and positive Eu anomalies representing the influence of feldspar melt reactions in the presence of fluid (Prince et al., 2001). Large-volume muscovite-biotite-bearing granites generated solely through dehydration melting are intimately linked to orogenic processes (Harris and Inger, 1992; Inger and Harris, 1993; Patino Douce and Harris, 1998; Barbarin, 1999; Patino Douce, 1999; Harris et al., 2000; Nabelek and Liu, 2004). Granite formed by muscovite and/or biotite dehydration melting occurs through primarily through prograde heating during orogenesis or decompression melting related to erosion of thickened crust (eg. Harris et al., 2000, and references therein). Relatively localised prograde heating due to shear-heating is a proposed mechanism for granite generation (eg. England et al., 1992), and has been demonstrated through thermal modelling to be a viable mechanism (England et al., 1992; Nabelek and Liu, 2004). Decompression melting is suggested to only result in muscovite-dehydration melting, as biotite-dehydration melting has a steeper (>dP/dT) melting solidus (Patino Douce and Harris, 1998). In contrast, both muscovite and biotite-dehydration melting can occur through prograde heating with the degree of melting and melt reactions involved strongly controlled by P-conditions and rate of heating (Harris et al., 2000).

In this paper, we assess the petrogenesis of peraluminous, garnet-bearing granite of the Munjeela Suite in the southern Gawler Craton, South Australia. Petrogenesis of the Munjeela Suite is constrained using geochronology, whole-rock and mineral geochemistry and Sm-Nd isotopic analysis of the granite and metasedimentary enclaves within the granite. These data provide new age constraints for generation of the Munjeela Suite and provide information on the tectonic regime during the early Mesoproterozoic of the Gawler Craton.

6.2 Geological Setting

The Gawler Craton of South Australia represents largely unexposed late Archaean to early Mesoproterozoic crust (Figure 6.1, Daly et al., 1998; Hand et al., in press). The oldest preserved crust of the Gawler Craton consists of late-Archaean magmatic and supracrustal lithologies *(c.* 2560-2460 Ma) deformed and metamorphosed during the *c.* 2460-2430 Ma Sleafordian Orogeny (Daly and Fanning, 1993; Swain et al., 2005b; McFarlane, 2006). Following the Sleafordian Orogeny the Gawler Craton underwent ~400 Myr of tectonic quiescence prior to felsic magmatism associated with the *c.* 2000 Ma Miltalie Event (Daly et al., 1998; Fanning et al., 2007; Howard et al., 2007). The tectonic setting of this event is unconstrained, but is suggested to represent anorogenic magmatism associated with the initiation of rifting on the Gawler Craton (Daly et al., 1998). This was followed by a period of sediment deposition prior to magmatism and deformation of the *c.* 1860-1850 Ma Cornian Orogeny (Jagodzinski et al., 2006; Fanning et al., 2007; Reid et al., in press). Following the Cornian Orogeny, the Gawler-Adelie Craton underwent a period of extensive sediment deposition and volcanism prior to the craton-wide 1730-1690 Ma Kimban Orogeny (Conor, 1995; Teasdale, 1997; Daly et al., 1998; Cowley et al., 2003; Dutch et al., 2006; Payne et al., 2006a; Fanning et al., 2007; Payne et al., 2007). The Kimban Orogeny included magmatism of the pre- to syn-tectonic Middle Camp and Moody Suites and the post-tectonic Tunkillia Suite (*c.* 1690-1670 Ma, Teasdale, 1997; Daly et al., 1998; Ferris and Schwarz, 2004; Payne et al., 2006b; Fanning et al., 2007). UHT metamorphism is recorded in the north-western Gawler Craton at *c.* 1660 Ma (Ooldean Event, Teasdale, 1997; Fanning et al., 2007), apparently synchronous with a period of

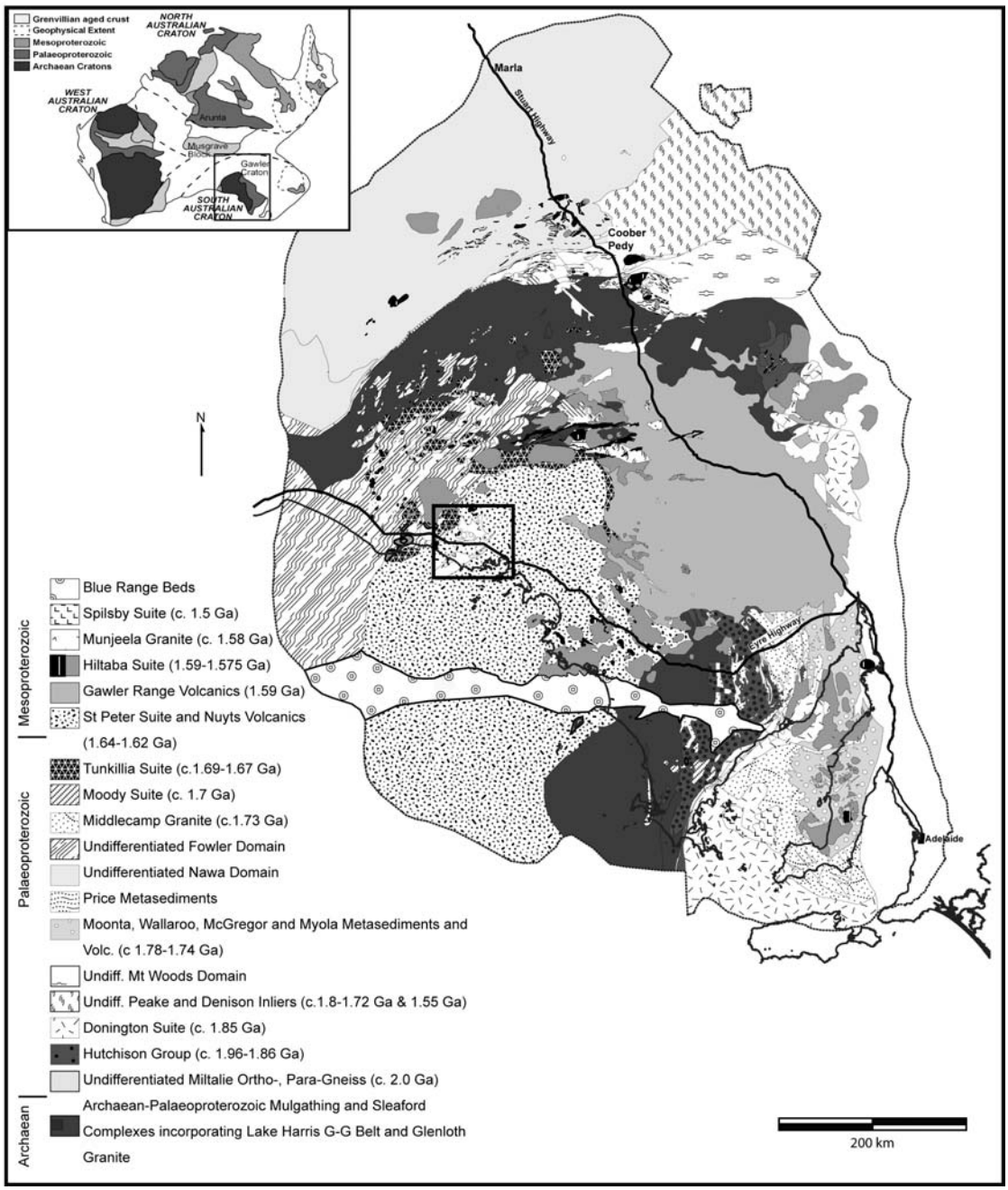

Figure 6.1 - Simplified Geology of the Gawler Craton after Fairclough et al. (2004) with box representing location of Figure 6.2. Inset: Simplified pre-1070 Ma geology of Australia after Betts et al. (2002) and Myers et al. (1996), showing location of Gawler Craton map.

graben-development and sediment deposition in the central Gawler Craton (Cowley and Martin, 1991; Fanning et al., 2007). This was followed by eruption of the Nuyts Volcanics in the southern Gawler Craton at *c.* 1630-1627 Ma (Rankin et al., 1990) and subsequent intrusion of the St Peter Suite (*c.* 1618-1608 Ma, Flint et al., 1990; Swain et al., 2005a; Fanning et al., 2007).

The Mesoproterozoic history of the Gawler Craton initiated with the Gawler Range Volcanics and Hiltaba Suite magmatism and associated Fe-oxide-Cu-Au-U and Cu-Au mineralisation (Flint, 1993; Johnson and Cross, 1995; Daly et al., 1998; Allen and McPhie, 2002; Budd, 2006; Skirrow et al., 2006; Hand et al., in press). Increasing evidence indicates that a period of deformation and metamorphism accompanied this magmatic event (Holm, 2004; Skirrow et al., 2006; Direen and Lyons, in press; Hand et al., in press). This is supported by metamorphic ages of 1587 ± 2 Ma and 1583 ± 18 Ma from granulites in the Mt Woods

Figure 6.2 - Total Magnetic Intensity map of the south-western Gawler Craton displaying locations of Munjeela Suite intrusions and field sampling localities. Intepretation of M. Hand, modified after Fairclough et al. (2004).

Domain (Figure 6.1, Holm, 2004), steeply-dipping Lower GRV overlain by the flat-lying Upper GRV, and a range of retrograde structural fabrics in the south-eastern Gawler Craton correlating with Ar-Ar and Sm-Nd isotopic ages of *c.* 1610-1580 Ma (Foster and Ehlers, 1998; Hand et al., in press). Structural effects of this deformation event are largely unconstrained but appear consistent with NW-SE directed shortening (Hand et al., in press). This magmatic and deformation event was followed shortly thereafter by the *c.* 1570-1555 Ma Kararan Orogeny in the northern and western Gawler Craton (Teasdale, 1997; Fanning et al., 2007; Hand et al., in press; Payne et al., 2008). The effects of the Kararan Orogeny are poorly constrained but include granulite facies metamorphism in the southern Nawa Domain and Fowler Domain, and is correlated to an E-W structural trend in outcrop and regional geophysical datasets (Hopper, 2001;Hand et al., in press; Payne et al., 2008). Following the Kararan Orogeny the Gawler Craton experienced minor magmatism in the Peake and Denison Domain (*c.* 1533 Ma, Lagoon Hills Granite, Hopper, 2001) and south-eastern Gawler Craton (*c.* 1500 Ma, Spilsby Suite, Jagodzinski et al., 2006; Fanning et al., 2007). Cratonisation occurred after ~1450 Ma with a final episode of shear zone reactivation recorded at *c.* 1450 Ma by Ar-Ar and metamorphic monazite ages (Swain et al., 2005c; Fraser and Lyons, 2006).

6.3 Munjeela Suite - Field Occurrence, Geophysical Characteristics and Petrography

The Munjeela Suite outcrops in a small number of isolated locations in the south-western Gawler Craton (Figures 6.1 and 6.2). These outcrops are herein referred to informally as the Rockhole, Pt Sinclair, Pt Bell and Pt James outcrops for ease of discussion. These locations are defined in the Total Magnetic Intensity (TMI) image of Figure 6.2. The Rockhole intrusion outcrops at Munjeela Rockhole on the north-western side of the Koonibba shear zone (Figure 6.2). As evident in the regional TMI data, the Pt Sinclair and Pt Bell outcrops belong to a single intrusion, Sinclair/Bell intrusion, which appears (TMI data is of limited resolution at southern end) elongate in a NE-SW direction and cut by the Koonibba shear zone (Figure 6.2). The Pt James outcrop represents a small (~5km wide)

circular intrusion that has not suffered significant post-intrusion deformation either at outcrop-scale or at regional TMI-scale. The Pt James intrusive preserves sharp intrusive contacts with granite of the 1618-1608 Ma St Peter Suite. The remainder of the Munjeela Suite intrusives occur as isolated outcrops with no preserved contacts.

The Pt Sinclair location is a granite headland that exposes approximately 1 km of outcrop length up to 200 m wide. The outcrop consists of relatively homogeneous, undeformed granite with a small number of metasedimentary enclaves. Two phases of granite are present at Pt Sinclair: a dominant Qtz-Kfs-Plg-Ms-Bi±Grt granite which contains enclaves and blebs of a slightly less peraluminous muscovite-biotite-garnet-poor phase. The ms-bi-gt-poor phase occurs as 20 cm diameter blebs up to ~2 m enclaves with biotite selvedges (Figure 6.3a). The Pt Bell outcrop is a 4 km long expanse of coastal outcrop which varies in width from 10 m to 100 m. At the Pt Bell location intrusive phases show much greater magmatic variation than at Pt Sinclair (Figure 6.3b and 6.3c), and are also variably deformed. Mineralogy is typically Qtz-Kfs-Pl-Ms-Bi-Gt-Tur. In comparison to Pt Sinclair, the granite at Pt Bell is typically more garnet-rich (up to 5 mm, Figure 6.3b). Structural fabrics within the Pt Bell outcrop range from a weakly developed foliation defined by micas, to intense S-C mylonites. Fabrics are typically subvertical (~80°) and trend 025-060° with a conjugate shear fabric formed at *c.* 115° (Figure 6.3d). Exposure at the western end of the Pt Bell outcrop is extensively deformed with S-C mylonite fabrics, offset pegmatitic veins and shear-sense indicators within proto-mylonites indicating a left-lateral (sinstral) sense of movement with gently north-east plunging mineral stretching lineations. Garnet-muscovite-bearing pegmatitic and granitic veins both cross-cut and are deformed by shear fabrics indicating deformation was synchronous with granite intrusion and crystallisation. Elsewhere foliated granitic phases are intruded by un-foliated phases.

In thin section the Sinclair/Bell intrusion is typically characterised by coarse-grained muscovite (up to 4 mm) and K-feldspar (2-4 mm) with coarse- and fine-grained quartz crystallising late in the assemblage (Figure 6.4a). These three minerals typically comprise 70-80% of the granite. Plagioclase is typically less than 2 mm across and is often rimmed by K-feldspar. Biotite is typically less than 2mm long but does occur as larger grains. Figure 6.4b shows a less peraluminous example of the granite assemblage dominated by K-feldspar (40%) and quartz (25%) with lesser amounts of muscovite, garnet and biotite. In highly deformed granite, the matrix is composed of fine-grained quartz, K-feldspar and muscovite with porphyroblasts of relict K-feldspar and muscovite (Figure 6.4c). New garnet growth occurs in the matrix of the deformed granite and is typically inclusion-free and less than 300 μm across.

The Pt James intrusive outcrops along two small wave-cut outcrops separated by a region of no outcrop. In the regional TMI dataset these outcrop locations correlate with a conspicuous circular low TMI response (Figure 6.2). Sharp intrusive contacts are preserved with the surrounding foliated ms-gt-absent St Peter Suite granite. The granite is a Qtz-Kfs-Pl-Ms-Bi ± Gt granite with a number of intermingled leucocratic phases. This includes phases which contain 1-2 cm quartz and plagioclase phenocrysts within a fine-grained matrix (<1mm) consisting pre-dominantly of quartz, plagioclase, muscovite and biotite (Figures 6.3e and 6.3f). Some biotite phenocrysts are also present ranging up to 2-3 mm in length. Garnet occurs as rare phenocrysts. The bulk of the granite ranges from coarse-grained equigranular leucogranite to porphyritic leucogranite with 4-8 mm quartz and feldspar within a medium to coarse-grained (2-3 mm) matrix. Coarse-grained lithologies from Pt James contain a higher proportion of garnet (Figure 6.4d) than fine-grained lithologies and also contain rapakivi feldspar textures (Figure 6.4e). Garnet is typically <1 mm, often present as relicts of once larger grains that appear to have undergone dissolution and occurs as inclusions within K-feldspar (Figure 6.4d). K-feldspar occurs predominantly as microcline and often forms large (7 mm), inclusion-rich phenocrysts containing plagioclase and quartz. Plagioclase occurs in three forms. Small plagioclase (<1 mm) occurs distributed throughout the rock but is relatively uncommon. Larger plagioclase grains occur as zoned crystals with zoning defined by inclusions (fluid and mineral) which are absent in the outer rim of the crystal. Plagioclase also mantles microcline forming rapakivi textures (Figure 6.4e). In the rapakivi texture the plagioclase is also fluid-inclusion rich with an outermost inclusion-free rim (Figure 6.4e). The large zoned plagioclase is interpreted to have grown at the same time as the rapakivi plagioclase

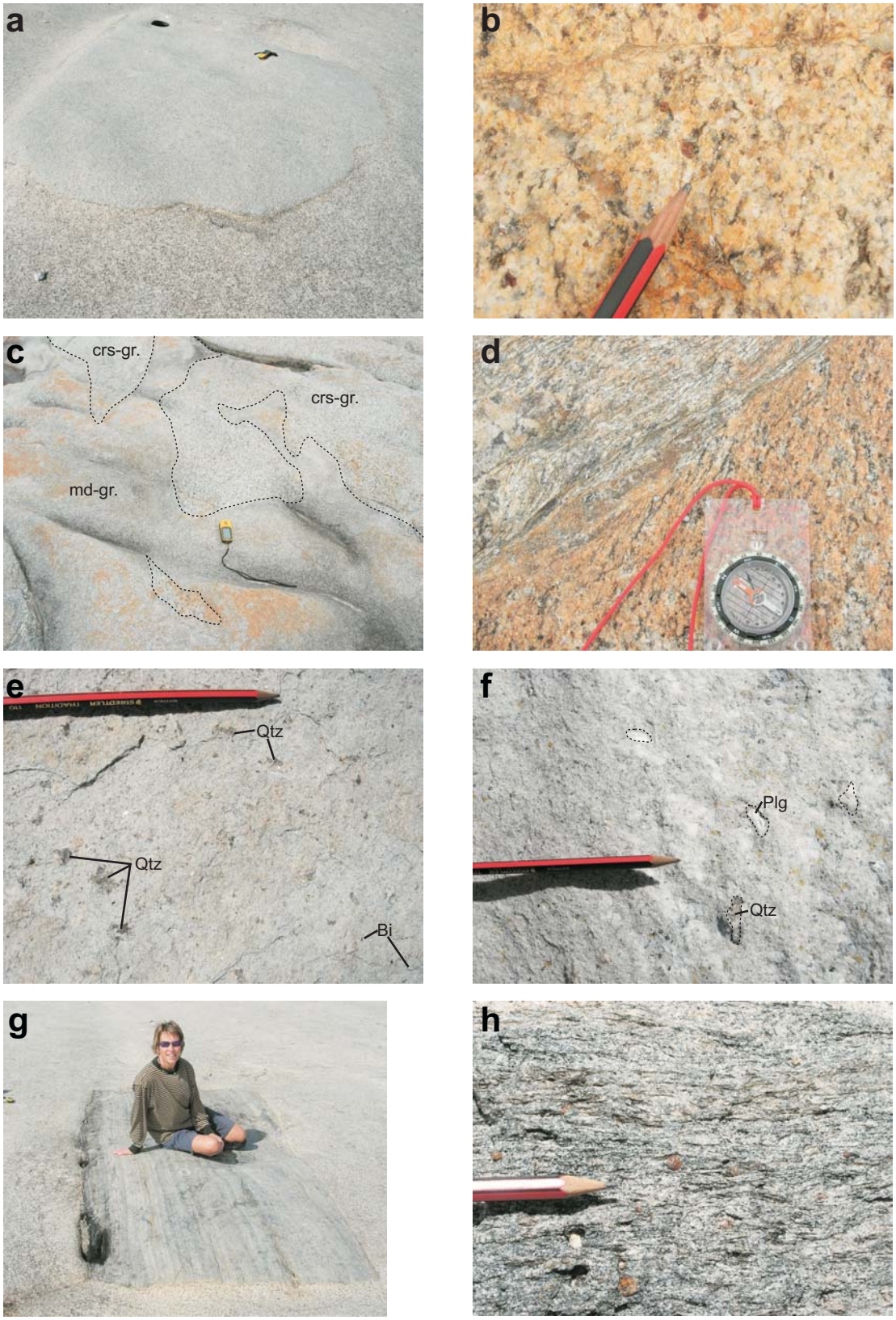

Figure 6.3 - Photographs of Munjeela Suite field localities. a) large ms-bi-gt-poor phase within Pt Sinclair granite, GPS for scale is approximately 10cm long; b) Garnet-rich ms-bi granite at Pt Bell locality; c) Pt Bell outcrop displaying mingling of coarse grained ms-bi-gt granite (crs-gr.) and medium grained ms-bi±gt granite (md-gr., foreground); d) Foliation in granite (strike-060°) entrained into conjugate dextral shear zone striking approximately 120°; e) Quartz and biotite phenocrysts within a fine-grained leucocratic matrix at Pt James; f) Plagioclase phenocrysts in fine grained matrix at Pt James; g) Large metasedimentary enclave within granite at Pt Sinclair; h) Muscovite-biotite-garnet metasedimentary enclave within Pt Sinclair granite showing garnet porphyroblasts (source of sample 06-MJMS-6).

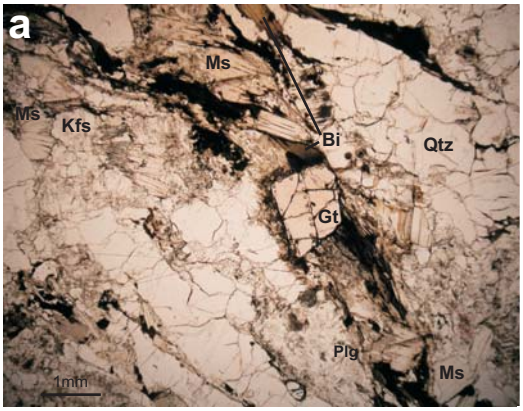
a
Ms
Ms
Kfs
Bi
Qtz
Gt
Plg
Ms
1mm

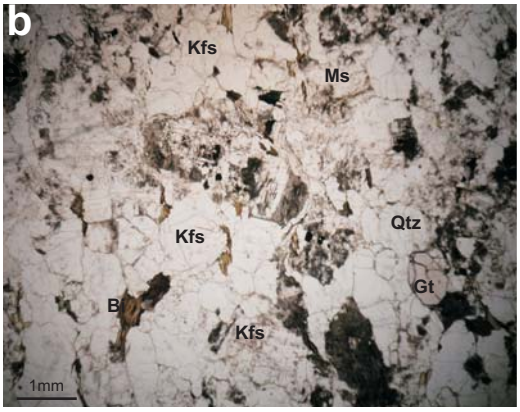
b
Kfs
Ms
Kfs
Qtz
Gt
Bi
Kfs
1mm

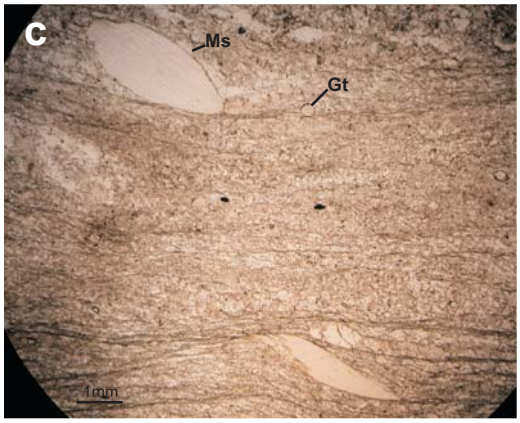
c
Ms
Gt
1mm

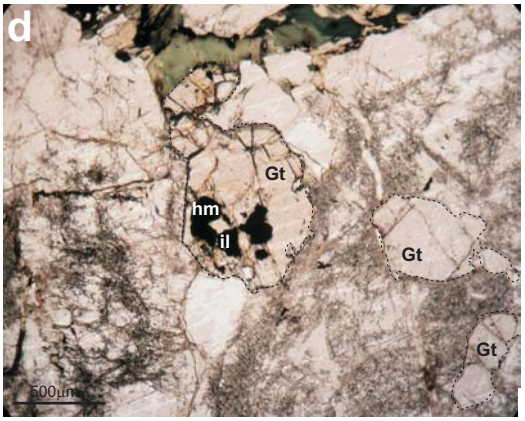
d
Gt
hm
il
Gt
Gt
500µm

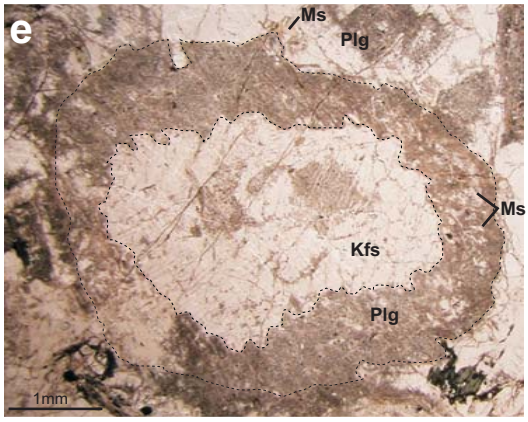
e
Ms
Plg
Ms
Kfs
Plg
1mm

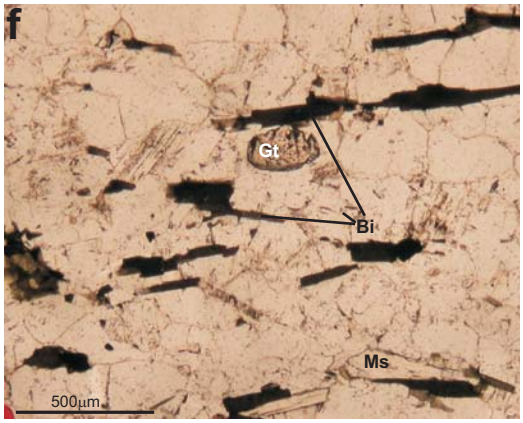
f
Gt
Bi
Ms
500µm

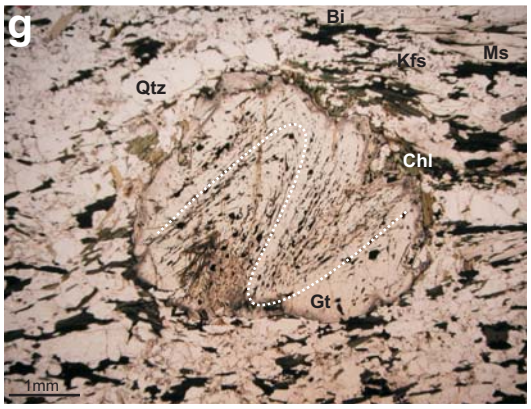
g
Bi
Kfs
Ms
Qtz
Chl
Gt
1mm

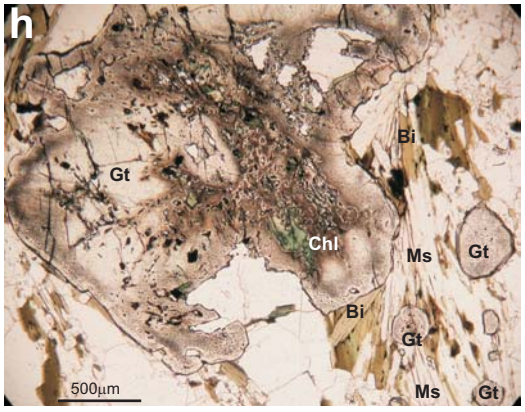
h
Bi
Gt
Chl
Ms
Gt
Bi
Gt
Ms
Gt
500µm

based upon the transition from inclusion-rich cores to inclusion-free rims. Muscovite and biotite form primary minerals dispersed throughout the rock. Metasedimentary enclaves within the Pt Sinclair intrusive are typically 5 cm to 50 cm in size but are as large as ~1.5 x 2.5 m (Figure 6.3g). Enclaves are either Qtz-Bi-Ms-Kfs ± Pl ± Grt psammo-pelites, Ms-Bi-Grt-Qtz-Pl-Kfs schists (Figure 6.3h) or Hbl-Grt mafic schists. The Hbl-Gt bearing enclaves were not sampled due to small size and smooth outcrop surface. Of the samples used in this study, enclave samples 06-MJMS-1 and 06-MJMS-3 are psammo-pelitic while 06-MJMS-4 and 06-MJMS-6 are pelitic. Psammo-pelitic lithologies are dominated by quartz (~60%) with muscovite (15%), biotite (10%) K-feldspar (7%) and plagioclase (5%) forming the bulk of the mineralogy. Garnet (3%) grew late in the mineral assemblage, occurring as grains less than 250 μm across (Figure 6.4f). A weak planar foliation is defined by muscovite and biotite. Muscovite growth is up to ~1.5 mm, often overgrown by biotite grains of less than 1mm. Pelitic lithogies are muscovite-biotite-garnet schists with quartz, K-feldspar and minor plagioclase. Sample 06-MJMS-6 preserves the coarsest mineral growth. Muscovite, chlorite, ilmenite, magnetite and epidote occur as inclusions within garnet. Inclusion trails within garnet record the presence of syn-metamorphic deformation as indicated by folded inclusion trails pictured in Figure 6.4g. Garnet is porphyroblastic with diameters ranging from 2-5mm. Fine grain muscovite occurs as inclusions within K-feldspar and plagioclase while muscovite in the matrix occurs as grains up to 2mm long. Biotite is typically less than 1mm. Minor magnetite and ilmenite occur within the matrix of sample 06-MJMS-4.

6.4 Analytical Methods

Representative samples of granite and metasedimentary enclaves were taken from outcrop at Pt Sinclair, Pt Bell and Pt James. Sample locations are provided in Table 6.1. Fresh sample material was crushed for whole rock geochemistry and U-Pb zircon geochronology. An aliquot was milled in a WC mill. Approximately half of the analytical pulp was used for whole-rock geochemistry and the remainder retained for isotopic analysis. For U-Pb zircon geochronology, crushate was sieved using disposable nylon mesh with the 79-450 μm fraction retained for mineral separation. Zircon separation was conducted using standard panning, Frantz Isodynamic and heavy liquid mineral separation techniques.

Major elements were analysed by fusion of a 0.1 g sub-sample of the analytical pulp with lithium metaborate followed by dissolution in nitric acid to give a "total solution" for ICP-MS analysis. Analysis of trace and REE elements is achieved by digestion of up to 0.5 g of the analytical pulp in a HF/multi acid solution and introduced into an ICP-MS for the quantification of the elements of interest.

Major element concentrations for minerals were obtained using a Cameca SX-51 electron microprobe at Adelaide Microscopy, University of Adelaide. In addition trace element chemistry was obtained on garnets from selected granite samples using LA-ICPMS facilities at Adelaide Microscopy. Analyses were conducted with an Agilent 7500cs ICP-MS connected to a New Wave 213nm Nd-YAG laser. A 50 μm beam diameter was used with a laser pulse rate of 5 Hz. Rare-earth element and Y concentrations of garnet in thin-section were collected using a NIST 610 glass as an internal standard. Element mass bias and fractionation were corrected using ^{43}Ca was used as an internal standard. Ca-concentrations were taken from microprobe analyses of the same spot locations.

Sm-Nd isotope analyses were conducted at the University of Adelaide. The method used is the same as that outlined in Wade et al. (2006). Samples were spiked with a ^{150}Nd/^{147}Sm solution and dissolution was carried out in high-pressure

Figure 6.4 (prev. page) - Photomicrographs of granite and metasedimentary lithologies. a) Ms-bi-gt-bearing granite (06-MNJ-11) with garnet mapped in Figure 6.11b; b) Gt-poor granite showing typical assemblage of Kfs-qtz-ms-bi with small garnet grain; c) Mylonitic granite from Pt Bell showing dynamic recrystallisation of matrix (Kfs-qtz-ms) with new garnet growth and muscovite fish displaying sinistral sense of movement; d) Typical garnet from Pt James outcrop (06-MNJ-32) showing fragmentary nature and inclusion within large K-feldspar grain. Garnet in centre is mapped in Figure 6.11c; e) Rapakivi feldspar texture (06-MNJ-32) showing relatively inclusion-free K-feldspar core with inclusion-rich plagioclase mantle; f) Psammo-pelitic lithology of 06-MJMS-1 with muscovite-biotite and small garnet; g) Ms-Bi schist (06-MJMS-6) with large garnet hosting folded inclusion trails of ilmenite-hematite-chlorite-muscovite-epidote; h) Ms-Bi schist of 06-MSMJ-4 with large garnet hosting chlorite-ilmenite-hematite-quartz inclusions and small garnet distributed through matrix.

Table 6.1 - Sample Location and Whole rock geochemistry for Munjeela Suite and metasedimentary enclave samples

Sample	06-MNJ-01	06-MNJ-02	06-MNJ-03	06-MNJ-05	06-MNJ-06	06-MNJ-09	06-MNJ-10	06-MNJ-11	06-MNJ-12	06-MNJ-13	06-MNJ-14	06-MNJ-15	06-MNJ-16	06-MNJ-17	06-MNJ-18	06-MNJ-19	06-MNJ-20
Outcrop	Pt Bell	Pt Bell	Pt Bell	Pt Bell	Pt Bell	Pt Bell	Pt Bell	Pt Bell	Pt Sinclair	Pt Sinclair	Pt Sinclair	Pt Sinclair	Pt Sinclair	Pt Bell	Pt Bell	Pt Bell	Pt Bell
Easting	325322	325322	325322	325322	325322	324489	324489	324489	309506	309427	309400	309420	309433		323787	323835	323750
Northing	6436579	6436579	6436579	6436579	6436579	6436168	6436168	6436168	6446146	6446105	6446100	6446287	6446430		6437155	6437323	6437271
SiO2	73.40	76.30	73.90	74.50	73.80	73.10	74.70	73.50	73.00	72.60	73.00	71.90	73.50	73.00	73.00	72.50	71.70
TiO2	0.10	0.09	0.08	0.09	0.09	0.10	0.15	0.10	0.15	0.11	0.13	0.15	0.12	0.14	0.15	0.16	0.21
Al2O3	14.50	13.90	14.10	14.30	14.30	14.60	13.70	14.40	14.20	14.30	14.30	14.00	14.00	14.20	13.90	14.20	14.30
Fe2O3	1.18	0.49	1.04	0.71	1.12	1.19	1.27	1.06	1.52	1.17	1.50	1.58	1.35	1.58	1.56	1.59	1.81
MnO	0.18	0.01	0.02	0.14	0.19	0.14	0.03	0.15	0.11	0.17	0.12	0.11	0.11	0.12	0.12	0.13	0.08
MgO	0.22	0.11	0.12	0.19	0.22	0.22	0.24	0.24	0.39	0.24	0.30	0.35	0.32	0.39	0.36	0.37	0.46
CaO	0.64	0.59	0.60	0.59	0.56	0.73	0.49	0.68	0.87	0.72	0.76	0.84	0.94	0.87	1.04	0.99	1.13
Na2O	3.39	3.71	3.56	3.91	3.54	3.44	3.13	3.59	3.17	3.20	3.12	3.17	3.26	3.11	3.21	3.09	3.02
K2O	4.89	4.45	4.37	4.48	4.48	4.99	5.03	4.95	5.45	5.34	5.19	5.63	5.06	5.23	4.90	5.43	5.71
P2O5	0.12	0.10	0.10	0.13	0.20	0.19	0.10	0.13	0.10	0.12	0.15	0.11	0.13	0.14	0.15	0.09	0.12
LOI	1.02	0.96	0.86	0.96	0.70	0.69	0.90	0.97	0.65	0.94	0.71	0.54	1.01	0.68	0.93	0.64	0.70
Total	99.64	100.71	98.75	100.00	99.20	99.39	99.74	99.77	99.61	98.91	99.28	98.38	99.80	99.46	99.32	99.19	99.24
REE and Trace Elements (ppm)																	
La	14.5	3.5	5.5	10.0	12.5	13.0	18.0	12.0	26.5	16.5	19.0	28.5	23.5	24.0	20.5	37.0	50.0
Ce	27.0	8.0	12.0	20.5	25.5	27.0	37.0	24.5	54.0	33.5	37.0	58.0	49.0	50.0	40.5	80.0	100.0
Pr	3.3	1.0	1.5	2.8	3.2	3.3	4.6	3.0	6.5	4.1	4.7	7.0	6.0	6.0	5.0	9.5	11.5
Nd	9.5	3.4	4.2	10.0	10.0	10.0	14.0	9.5	19.5	12.5	14.5	22.0	17.5	18.0	15.0	27.5	33.5
Sm	2.5	1.3	1.4	2.6	2.7	2.6	3.7	2.5	4.9	3.1	3.7	5.5	4.5	4.7	3.5	6.5	7.5
Eu	0.4	0.1	0.1	0.3	0.4	0.4	0.4	0.4	0.6	0.5	0.5	0.6	0.6	0.6	0.6	0.9	1.0
Gd	2.4	1.1	1.5	2.3	2.8	2.9	3.6	2.5	4.8	3.3	3.9	5.5	4.5	4.7	3.5	6.0	7.0
Tb	0.4	0.3	0.4	0.4	0.5	0.6	0.6	0.5	0.8	0.6	0.7	0.9	0.8	0.8	0.6	0.9	1.1
Dy	2.8	2.1	2.7	3.0	3.3	3.8	3.9	3.1	4.9	3.9	4.3	5.5	4.5	4.9	3.5	4.9	5.5
Ho	0.5	0.4	0.4	0.5	0.5	0.6	0.6	0.5	0.7	0.6	0.7	0.9	0.7	0.7	0.5	0.7	0.7
Er	1.7	1.2	1.5	1.5	1.8	2.1	2.0	1.9	2.5	2.2	2.2	2.9	2.2	2.5	1.7	2.3	2.1
Tm	0.3	0.2	0.3	0.3	0.3	0.3	0.3	0.3	0.4	0.4	0.3	0.4	0.3	0.4	0.3	0.3	0.3
Yb	2.1	1.6	2.0	1.8	2.2	2.2	1.9	2.3	2.4	2.4	2.3	2.7	2.2	2.5	1.8	2.3	1.8
Lu	0.3	0.2	0.2	0.2	0.3	0.3	0.2	0.3	0.3	0.3	0.3	0.3	0.3	0.3	0.2	0.3	0.2
Ba	160.0	-	30.0	-	150.0	210.0	60.0	180.0	340.0	310.0	260.0	290.0	310.0	300.0	310.0	480.0	750.0
Cs	34.5	14.0	13.0	41.5	54.0	64.0	22.0	47.0	29.0	31.5	30.0	37.5	47.5	49.5	27.0	15.0	29.5
Cu	29.0	11.0	39.5	4.5	5.5	22.0	35.5	19.5	9.5	21.5	20.0	12.0	10.0	21.5	10.0	10.0	80.0
Ga	17.5	19.0	17.0	19.0	18.0	17.0	15.5	17.5	16.0	16.5	16.0	15.5	15.5	17.0	17.0	16.0	16.5
Nb	30.5	21.5	20.5	34.0	31.0	23.5	21.0	28.5	17.5	18.5	21.0	16.5	17.0	21.5	22.0	13.0	18.5
Ni	5.0	<2	2.0	<2	<2	<2	<2	<2	3.0	<2	2.0	3.0	<2	2.0	4.0	3.0	4.0
Pb	26.0	20.5	24.0	23.5	24.5	29.0	31.0	27.5	32.5	31.5	29.5	34.0	31.5	31.5	30.0	39.0	37.5
Rb	360.0	300.0	280.0	380.0	410.0	320.0	280.0	360.0	310.0	300.0	290.0	340.0	270.0	300.0	330.0	270.0	310.0
Sc	8.0	12.0	10.0	6.0	6.0	6.0	6.0	6.0	<5	<5	6.0	6.0	<5	6.0	<5	<5	<5
Sr	180.0	115.0	130.0	185.0	280.0	84.0	180.0	185.0	60.0	56.0	50.0	46.5	56.0	54.0	58.0	88.0	98.0
Th	9.0	6.0	7.0	10.0	9.5	9.5	13.0	9.0	17.0	11.0	13.0	18.5	15.5	16.5	13.5	24.5	30.5
U	2.8	3.1	5.5	7.0	11.5	2.7	2.4	4.0	6.5	4.4	4.8	3.4	3.9	4.1	7.5	2.7	5.5
Y	14.0	10.0	12.5	14.0	16.0	19.0	17.5	16.0	23.0	19.5	20.0	25.0	20.0	22.5	16.0	21.0	21.0
Zn	27.0	8.0	14.0	26.5	36.5	24.0	22.0	40.0	39.5	26.0	33.0	40.0	35.0	38.5	36.5	33.0	45.0
Zr	50.0	30.0	40.0	40.0	40.0	50.0	70.0	50.0	90.0	60.0	60.0	90.0	70.0	80.0	80.0	110.0	150.0

Table 6.1 (cont.) - Sample Location and Whole rock geochemistry for Munjeela Suite and metasedimentary enclave samples

Sample	06-MNJ-24	06-MNJ-25	06-MNJ-27	06-MNJ-29	06-MNJ-31	06-MNJ-32	06-MNJ-33	06-MNJ-34	06-MNJ-36	06-MNJ-18M	06-MJMS-1	06-MJMS-3	06-MJMS-4	06-MJMS-6
Outcrop	Pt Bell	Pt Bell	Pt James	Pt James	Pt James	Pt James	Pt James	Pt James	Pt James	Pt Bell	Enclave	Enclave	Enclave	Enclave
Easting			348020	347914	348564	348564	348405	349829	351188		309504	309433	309441	309439
Northing			6436543	6436610	6436763	6436763	6436590	6436391	6436550		6446137	6446430	6446442	6446484
SiO2	72.80	72.00	75.60	75.10	75.70	74.70	74.80	75.20	75.20	73.10	72.00	71.90	69.60	65.30
TiO2	0.17	0.16	0.05	0.04	0.10	0.11	0.11	0.06	0.06	0.14	0.38	0.45	0.45	0.56
Al2O3	14.00	14.00	13.20	13.00	12.70	12.90	13.10	13.10	12.70	13.90	13.90	13.70	14.50	15.30
Fe2O3	1.68	2.02	1.01	0.86	1.22	1.47	1.17	0.94	1.17	1.47	3.46	3.19	4.63	5.89
MnO	0.08	0.07	0.17	0.18	0.15	0.13	0.09	0.11	0.12	0.13	0.25	0.10	0.61	0.37
MgO	0.30	0.36	0.04	0.03	0.11	0.17	0.10	0.06	0.06	0.44	0.94	0.94	1.20	2.29
CaO	0.94	1.46	0.26	0.52	0.90	0.75	0.65	0.56	0.44	0.93	0.97	1.70	1.04	1.17
Na2O	3.25	3.06	4.42	4.48	4.28	3.84	3.96	4.15	4.06	3.09	2.65	3.59	2.71	2.90
K2O	4.85	4.80	4.26	4.09	3.39	4.34	4.39	4.55	4.44	4.88	4.42	3.68	3.83	4.58
P2O5	0.11	0.08	<0.01	<0.01	0.02	<0.01	0.03	<0.01	<0.01	0.12	0.10	0.07	0.14	0.08
LOI	0.93	0.95	0.88	0.53	0.37	0.55	0.52	0.19	0.23	1.15	1.32	1.10	1.45	1.18
Total	99.11	98.96	99.89	98.83	98.94	98.96	98.92	98.92	98.48	99.35	100.39	100.42	100.16	99.62
REE and Trace Elements (ppm)														
La	24.0	60.0	2.0	7.5	24.5	18.5	20.0	15.0	17.0	23.5	54.0	49.0	44.5	46.5
Ce	48.5	98.0	3.5	18.0	52.0	38.5	43.0	35.5	36.0	49.0	105.0	92.0	98.0	92.0
Pr	5.5	11.0	0.6	2.8	6.5	5.0	6.0	5.0	4.8	6.0	13.0	12.5	11.0	11.0
Nd	16.0	29.0	1.6	10.5	20.5	17.0	20.0	18.5	16.5	18.0	45.0	45.0	40.5	39.0
Sm	3.5	5.5	0.7	5.5	6.0	5.5	6.5	7.5	7.0	4.6	8.5	8.5	7.0	7.0
Eu	0.6	1.0	0.1	0.1	0.4	0.5	0.5	0.3	0.4	0.6	1.3	1.6	1.4	1.3
Gd	3.1	4.8	1.5	9.0	7.0	7.0	8.5	11.0	11.0	4.7	6.0	6.0	5.0	5.0
Tb	0.5	0.7	0.6	2.1	1.4	1.5	1.9	2.2	2.3	0.8	0.9	0.8	0.8	0.7
Dy	2.8	3.4	6.0	17.0	9.5	10.5	13.0	15.5	17.0	4.7	4.8	4.4	4.2	3.5
Ho	0.4	0.5	1.5	3.6	1.8	2.0	2.4	2.9	3.2	0.7	0.8	0.6	0.7	0.5
Er	1.4	1.6	7.5	15.5	7.0	7.5	9.0	11.5	12.5	2.3	2.4	1.8	2.0	1.2
Tm	0.2	0.2	1.6	2.9	1.3	1.2	1.5	1.8	2.0	0.4	0.4	0.3	0.3	0.2
Yb	1.5	1.6	14.0	24.5	10.5	9.5	11.5	13.5	15.0	2.3	3.0	1.8	2.1	1.2
Lu	0.2	0.2	1.9	3.1	1.4	1.2	1.4	1.7	1.8	0.3	0.5	0.3	0.3	0.2
Ba	360.0	800.0	30.0	20.0	80.0	220.0	190.0	70.0	80.0	260.0	-	-	-	-
Cs	34.5	34.0	20.5	27.0	17.0	21.5	21.0	13.5	14.5	47.0	15.0	22.5	66.0	76.0
Cu	8.5	18.0	2.0	1.5	7.5	7.0	6.0	1.5	12.5	26.5	3.5	54.0	15.5	11.5
Ga	16.5	17.0	25.0	26.0	22.0	22.0	21.0	23.0	21.5	16.5	22.0	21.0	23.5	25.0
Nb	21.0	14.0	28.5	42.5	40.5	30.5	31.0	37.5	36.0	21.0	17.5	14.5	18.0	21.5
Ni	3.0	3.0	<2	<2	<2	2.0	<2	<2	<2	2.0	10.0	8.0	16.0	31.0
Pb	31.5	30.0	58.0	70.0	38.0	41.0	49.5	36.0	54.0	30.0	32.0	26.0	23.0	23.0
Rb	290.0	240.0	430.0	460.0	310.0	420.0	390.0	370.0	370.0	290.0	200.0	175.0	270.0	320.0
Sc	<5	<5	10.0	10.0	6.0	8.0	8.0	8.0	8.0	6.0	8.0	10.0	10.0	12.0
Sr	340.0	145.0	5.5	5.0	24.0	34.0	31.5	13.5	60.0	50.0	105.0	130.0	100.0	78.0
Th	15.0	23.0	18.0	22.0	20.0	22.5	21.5	26.5	28.5	16.0	29.5	22.5	19.5	21.5
U	2.9	2.4	3.7	7.0	7.0	6.5	11.0	6.5	6.0	4.3	3.6	6.5	3.1	1.8
Y	13.0	15.0	36.0	145.0	64.0	64.0	82.0	98.0	98.0	20.5	21.0	17.0	18.5	13.0
Zn	28.5	33.5	54.0	47.0	38.0	58.0	32.5	45.5	60.0	38.0	54.0	45.0	68.0	84.0
Zr	70.0	120.0	70.0	70.0	100.0	80.0	110.0	90.0	80.0	80.0	220.0	210.0	210.0	170.0

Teflon vessels over a 7 day period at 160°C. REEs were separated in Biorad Polyprep columns, this was then further separated in HDEHP-impregnated Teflon-powder columns to isolate Sm and Nd. Nd was analysed on a Finnigan MAT 262 Thermal Ionisation Mass Spectrometer (TIMS) with an in-house Nd standard (Johnson Matthey, $^{143}Nd/^{144}Nd$ = 0.511604 ± 0.000008) for each run. Sm was analysed on a MAT 261 TIMS. Throughout the duration of the study the standard had a measured $^{143}Nd/^{144}Nd$ value of 0.511602 ± 0.000010 (1 st. dev., n = 4), and blanks ranged from 104-299pg Nd. Running average for La Jolla over the duration of this study is 0.511828 ± 0.000012 (1 st.dev., n = 7).

SHRIMP U-Pb zircon geochronology was conducted at the John de Laeter Centre for Mass Spectrometry, Curtin University of Technology, Australia. Zircons (also detrital zircons) were imaged using a Gatan CL attached to a Phillips XL-20 SEM. Analyses were conducted on SHRIMP IIA and IIB using routine U-Pb analysis procedures as outlined in Kinny et al. (2003). Zircon standards BR-266 ($^{206}Pb/^{238}U$ = 0.09059) and CZ-3 ($^{206}Pb/^{238}U$ = 0.0914) were used as age and U concentration correction standards.

Detrital zircon U-(Th)-Pb LA-ICPMS geochronology was undertaken at Adelaide Microscopy, University of Adelaide. LA-ICP-MS operating procedures are similar to those described in Payne et al. (2006), Wade et al. (2007) and Jackson et al. (2004). U-Pb isotopic analyses were obtained using a New Wave 213nm Nd-YAG laser in a He ablation atmosphere, coupled to an Agilent 7500cs ICP-MS. A 60 second gas blank was analysed followed by 120 seconds of measurement during zircon ablation. U-Pb fractionation was corrected using the GEMOC GJ-1 zircon standard (TIMS normalisation data $^{207}Pb/^{206}Pb$= 608.3 Ma, $^{206}Pb/^{238}U$= 600.7 Ma and $^{207}Pb/^{235}U$= 602.2 Ma, Jackson et al., 2004) and accuracy was checked using an in-house Sri Lankan zircon standard (BJWP-1, *c.* 720 Ma). Common Pb is monitored during analysis (using mass ^{204}Pb(+Hg)) and if excessive and/or variable common-Pb is present the analysis is discarded. For analyses with consistent, minor common-Pb the 'Excel' plug-in 'CommPbcorr' (Andersen, 2002) is used to correct for common Pb using a 3-D Concordia method.

6.5 Results

6.5.1 U-Pb Zircon Geochronology

Granite U-Pb zircon geochronology results are presented in Figure 6.5 for representative samples from the Sinclair/Bell (06-MNJ-05 and 06-MNJ-18) and Pt James (06-MNJ-32) intrusions, respectively. SHRIMP U-Pb zircon data are reported in Table 6.2. LA-ICP-MS U-Pb detrital zircon geochronology was conducted on three metasedimentary enclaves collected from the Pt Sinclair outcrop; 06-MJMS-1, 06-MJMS-3 and 06-MJMS-6. These data are reported in Table 6.3 and displayed in Figure 6.6.

Thirteen analyses were conducted for Sinclair/Bell sample 06-MNJ-05 during two analytical sessions. Zircon from 06-MNJ-05 show varied CL responses, from dark regions with concentric magmatic zoning to bright CL responses, with zonation overprinting consistent with variable degrees of metamictisation (Figure 6.5a). In all cases zircons have a thin rim with a dark CL response and a high U and common-Pb content. Analyses attempted on these rims failed due to excessive common-Pb and discordance. U contents for analyses range from 174.8 to 9935 ppm and Th/U ratios range from 0.1 to 1.4. A weighted average of all data for 06-MNJ-05 provides a $^{207}Pb/^{206}Pb$ age of 1591 ± 11 Ma (Figure 6.5a, MSWD=0.99, n=13). Inclusion of all data in a discord yields upper and lower age intercepts of 1594 ± 13 Ma and 5 ± 14 Ma, respectively (MSWD=1.03, Figure 6.5a). Concentric zoning (Figure 6.5a) suggestive of magmatic crystallisation suggests 1591 ± 11 Ma is the age of crystallisation of the granite intrusion sampled by 06-MNJ-05.

Thirty one analyses were collected from Sinclair/Bell sample 06-MNJ-18. Zircon CL-images are similar to those for sample 06-MNJ-05, but display higher degrees of metamictisation represented by darkened CL-responses and disrupted concentric zoning (Figure 6.5b). As with sample 06-MNJ-05, zircons display variable, but often high, U concentrations and often contain significant common-Pb (Table 6.2). A number of analyses were discarded due to excessively disturbed U-Pb ratios and/or common-Pb content. A weighted average of $^{207}Pb/^{206}Pb$ data with minimal CL-evidence for metamictisation at the site of analysis yields an age of 1582 ± 7 Ma (MSWD = 1.01, n=25, Figure 6.5b). Further filtering of this data to

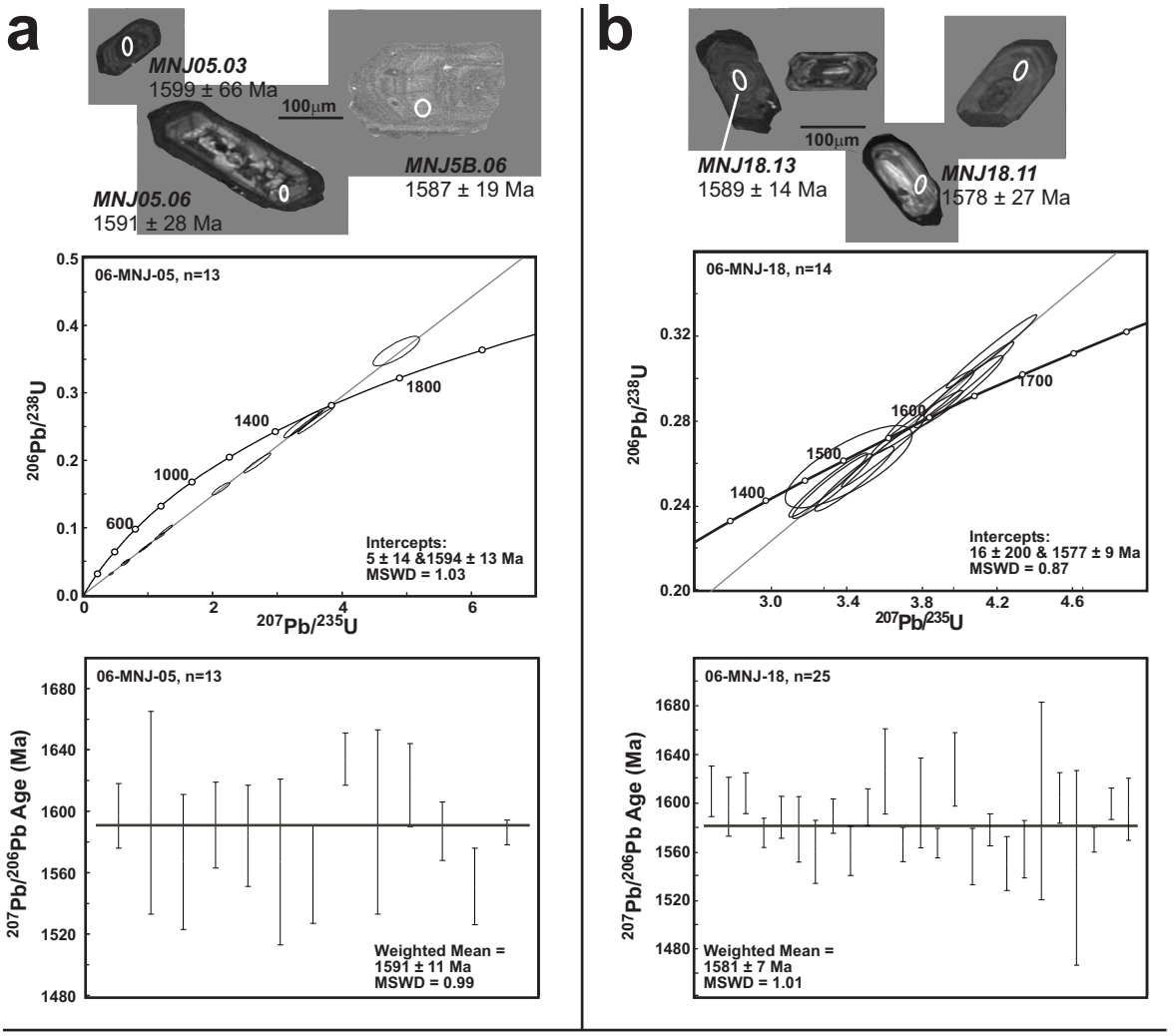

Figure 6.5 - a) Zircon CL images and U-Pb age diagrams for sample 06-MNJ-05. b) Zircon CL images and U-Pb age diagrams for sample 06-MNJ-18. c) Zircon CL images and U-Pb age diagrams for sample 06-MNJ-32. See text for discussion of crystallisation ages.

remove analyses with greater than 10% discordance yields a weighted average of 1577 ± 8.1 Ma (MSWD = 0.79, n=14). Limiting age calculations to analyses with less than 10% discordance and less than 1% ^{206}Pb contribution by common-Pb yields a weighted average age of 1577 ± 8.6 Ma (MSWD = 0.79, n = 11). A discord constructed using zircons with less than 10% discordance yields upper and lower intercept ages of 1577 ± 9 Ma and 16 ± 200 Ma, respectively (MSWD = 0.87, n = 14). The similarity of these ages suggests that the selected analyses are reliable despite the relatively poor nature of zircons from this sample for geochronology. The age considered representative of this sample is the $^{207}Pb/^{206}Pb$ weighted average of 1577 ± 9 Ma.

Zircon grains from Pt James sample 06-MNJ-32 typically show some degree of metamictisation, commonly have darkened CL-responses and often contain high U concentrations and appreciable common-Pb (Table 6.2, Figure 6.5c). A weighted average of all $^{207}Pb/^{206}Pb$ data provides an age of 1580 ± 12 Ma (MSWD = 1.8, n = 21). Removing analyses with greater than 10% discordance provides a $^{207}Pb/^{206}Pb$ weighted average age of 1580 ± 15 Ma (MSWD = 2.2, n = 13). Removing analyses with greater than 5% common-Pb ^{206}Pb from this subset results in a weighted average age of 1580 ± 22 Ma (MSWD = 3.9, n = 7). The generally high-U, metamict nature of zircon from this sample limits the reliability of geochronological constraints. However, given the consistency of calculated ages, the age of 1580 ± 15 Ma (MSWD = 2.2) is considered representative of granite crystallisation. Further geochronology is required to provide a more precise age of granite crystallisation.

Thirty seven U-Pb detrital zircon analyses were conducted for metasedimentary enclave sample 06-MJMS-1 with $^{207}Pb/^{206}Pb$ ages ranging from 1616 to 2010 Ma (Table 6.3, Figure 6.6a). Analyses with less than 10% discordance display ages in the range from 1616 to 1744 Ma, with the majority between 1620 and 1660 Ma. The youngest age obtained is 1616 ± 22 Ma. A concordia age calculated from the four youngest ages provides an age of 1623.4 ± 3.6 Ma (MSWD=0.28, Figure 6.6a) which is considered to represent the maximum age of deposition. Inclusion of the next youngest analysis decreases the reliability of the age as indicated by a MSWD of 3.3 (produces age of 1626 ± 10 Ma).

Thirty one analyses were conducted for metasedimentary enclave sample 06-MJMS-3 with $^{207}Pb/^{206}Pb$ ages in the range 1636-2024 Ma (Table 6.3, Figure 6.6b). Analyses with less than 10% discordance are in the range from 1636 to 1737 Ma. The two youngest analyses yield ages of 1636 ± 25 Ma and 1639 ± 29 Ma, which combine to yield a weighted mean of 1638 ± 33 Ma. Although within error of the next youngest analysis (1658 ± 40 Ma) the significant gap between the two age groupings (~20 Myr) suggests a distinct population at ~ 1638 Ma.

Sixty one analyses were obtained for metasedimentary enclave sample 06-MJMS-6 with $^{207}Pb/^{206}Pb$ ages in the range 1670-1988 Ma. A range of 1670 Ma to 1915 Ma is obtained from analyses with less than 10% discordance (n=38, Figure 6.6c). Within this range, the majority of ages fall within a continuum from *c.* 1670-1750 Ma with another notable peak in the age range *c.* 1800-1830 Ma. The youngest age obtained (1669.7 ± 20.6 Ma) is slightly above concordia (+3.2% discord., Figure 6.6c). The next youngest age (1673.7 ± 19 Ma) falls within error of the concordia (-0.3% discord.) and is the more reliable single grain maximum depositional age constraint. An intercept age calculated with the eight youngest ages ($^{207}Pb/^{206}Pb$ age = 1669-1689 Ma) produces an age of 1678.7 ± 7 Ma (MSWD=1.6, Figure 6.6c). This age is considered a reasonable estimate of the maximum deposition age.

6.5.2 Whole Rock Geochemistry

Twenty seven samples of granite and four metasedimentary enclave samples were analysed for whole rock major, trace and rare earth element composition. All data are reported in Table 6.1 with selected geochemical plots displayed in Figure 6.7. The analysed samples have a limited range of major element compositions. SiO_2 values fall between 71.7 and 76.3 wt% and Al_2O_3 values between 13.0 and 14.6 wt%. Figure 6.7b demonstrates the peraluminous nature of all granite samples, and highlights a bulk geochemical difference between the Sinclair/Bell and Pt James plutons. Samples from the Pt James rapakivi intrusion form a distinct group and are less peraluminous than the remainder of the Munjeela Suite samples.

Table 6.2 - SHRIMP U-Pb zircon geochronology dat for Munjeela Suite granite samples

Spot	U (ppm)	Th (ppm)	$^{232}Th/^{238}U$	$^{206}Pb^*$ (ppm)	% $^{206}Pb_c$	$^{206}Pb/^{238}U$	%	$^{207}Pb^*/^{235}U$	%	$^{207}Pb^*/^{206}Pb^*$	%	$^{206}Pb/^{238}U$ Age		$^{207}Pb/^{206}Pb$ Age		Concord. (%)
MNJ5.1	1368.2	846.3	0.6	80.4	1.0	0.0677	3.9	0.920	4.1	0.09850	1.1	422.0	16.0	1597.0	21.0	-73.6
MNJ5.3	2810.3	3283.8	1.2	84.1	9.3	0.0316	3.9	0.430	5.3	0.09870	3.5	200.4	7.8	1599.0	66.0	-87.5
MNJ5.4	9935.0	5221.8	0.5	451.0	5.0	0.0502	4.1	0.671	4.7	0.09700	2.3	315.0	13.0	1567.0	44.0	-79.9
MNJ5.6	1342.3	940.3	0.7	102.0	1.5	0.0874	4.0	1.184	4.3	0.09820	1.5	540.0	21.0	1591.0	28.0	-66.1
MNJ5.7	440.0	333.0	0.8	60.1	1.0	0.1575	3.9	2.125	4.3	0.09790	1.8	943.0	34.0	1584.0	33.0	-40.5
MNJ5.8	2604.0	276.6	0.1	935.0	13.4	0.3620	4.0	4.840	4.9	0.09700	2.9	1992.0	69.0	1567.0	54.0	27.1
MNJ5B.1	185.7	221.9	1.2	40.9	1.5	0.2530	5.1	3.370	5.3	0.09660	1.7	1453.0	66.0	1559.0	32.0	-6.8
MNJ5B.2	197.6	202.6	1.1	44.1	0.2	0.2590	5.0	3.590	5.1	0.10056	0.9	1486.0	66.0	1634.0	17.0	-9.1
MNJ5B.3	397.2	257.8	0.7	16.8	3.4	0.0476	5.6	0.646	6.4	0.09840	3.2	300.0	16.0	1593.0	60.0	-81.2
MNJ5B.4	174.8	119.2	0.7	29.6	0.6	0.1958	4.9	2.690	5.1	0.09960	1.4	1153.0	52.0	1617.0	27.0	-28.7
MNJ5B.6	1239.3	1101.0	0.9	78.0	0.8	0.0726	5.0	0.981	5.1	0.09801	0.99	452.0	22.0	1587.0	19.0	-71.5
MNJ5B.7	341.0	361.6	1.1	28.5	0.7	0.0965	5.1	1.279	5.2	0.09610	1.3	594.0	29.0	1551.0	25.0	-61.7
MNJ5B.8	1369.4	1827.7	1.4	300.0	0.1	0.2550	4.9	3.450	4.9	0.09799	0.43	1464.0	64.0	1586.3	8.0	-7.7
MNJ18B.1	513	435	0.88	119	0.37	0.2680	4.9	3.580	5.0	0.09694	0.75	1532.0	67.0	1566.0	14.0	-2.2
MNJ18B.2	365	333	0.94	73	3.41	0.2250	4.9	3.060	5.3	0.09870	2	1308.0	58.0	1600.0	37.0	-18.3
MNJ18B.4	492	210	0.44	130	0.09	0.3070	4.9	4.100	5.0	0.09700	0.63	1724.0	75.0	1567.0	12.0	10.0
MNJ18B.6	1369	820	0.62	125	7.58	0.0986	4.9	1.363	5.2	0.10020	1.6	606.0	29.0	1628.0	30.0	-62.8
MNJ18B.7	371	206	0.57	72.5	3.62	0.2190	4.9	2.800	5.5	0.09270	2.3	1277.0	57.0	1482.0	43.0	-13.8
MNJ18B.8	612	542	0.92	65.1	1.65	0.1218	4.9	1.619	5.1	0.09640	1.2	741.0	35.0	1556.0	23.0	-52.4
MNJ18B.10	247	300	1.25	55.4	0.14	0.2610	5.0	3.510	5.0	0.09759	0.71	1494.0	66.0	1578.0	13.0	-5.3
MNJ18B.11	468	596	1.31	103	1.21	0.2530	4.9	3.350	5.1	0.09610	1.2	1453.0	64.0	1550.0	22.0	-6.3
MNJ18B.12	512	505	1.02	114	0.95	0.2570	5.0	3.430	5.1	0.09670	1.3	1475.0	65.0	1562.0	24.0	-5.6
MNJ18.13	1071	442	0.43	88.5	5.08	0.0913	4.9	1.244	6.6	0.09880	4.3	563.0	27.0	1602.0	81.0	-64.9
MNJ18.14	284	350	1.27	48.5	0.78	0.1969	4.9	2.690	5.0	0.09890	1.2	1158.0	52.0	1604.0	21.0	-27.8
MNJ18.15	789	571	0.75	95.1	2.95	0.1360	4.9	1.783	5.1	0.09510	1.3	822.0	38.0	1529.0	24.0	-46.2
MNJ18.17	423	189	0.46	95.1	1.33	0.2580	5.0	3.410	6.5	0.09590	4.3	1479.0	66.0	1547.0	80.0	-4.4
mnj18.1	1240	552	0.46	207	1.15	0.1916	3.9	2.373	4.0	0.08983	1	1130.0	40.0	1422.0	19.0	-20.5
mnj18.2	655	352	0.55	142	0.20	0.2515	3.9	3.370	3.9	0.09717	0.53	1446.0	51.0	1570.0	10.0	-7.9
mnj18.3	843	601	0.74	171	0.89	0.2338	3.9	3.180	3.9	0.09870	0.68	1354.0	47.0	1600.0	13.0	-15.4
mnj18.4	384	374	1.00	99.1	2.38	0.2930	3.9	3.980	4.1	0.09850	1.3	1657.0	57.0	1595.0	25.0	3.9

Table 6.2 (cont.) - SHRIMP U-Pb zircon geochronology dat for Munjeela Suite granite samples

Spot	U (ppm)	Th (ppm)	$^{232}Th/^{238}U$	$^{206}Pb^*$ (ppm)	% $^{206}Pb_c$	$^{206}Pb/^{238}U$	%	$^{207}Pb^*/^{235}U$	%	$^{207}Pb^*/^{206}Pb^*$	%	$^{206}Pb/^{238}U$ Age		$^{207}Pb/^{206}Pb$ Age		Concord. (%)
MNJ18.5	370	191	0.53	80.8	1.10	0.2518	3.9	3.440	4.0	0.09920	1.1	1448.0	50.0	1610.0	20.0	-10.1
MNJ18.6	589	321	0.56	127	1.44	0.2470	4.0	3.360	4.2	0.09860	1.3	1423.0	52.0	1597.0	24.0	-10.9
MNJ18.7	471	545	1.19	99.6	0.95	0.2437	4.0	3.330	4.1	0.09912	0.9	1406.0	50.0	1608.0	17.0	-12.6
MNJ18.8	1837	821	0.46	300	0.21	0.1898	3.9	2.283	3.9	0.08724	0.65	1120.0	40.0	1366.0	13.0	-18.0
MNJ18.9	635	310	0.50	151	0.30	0.2760	3.9	3.710	3.9	0.09744	0.62	1570.0	54.0	1576.0	12.0	-0.4
MNJ18.10	797	223	0.29	183	1.80	0.2620	3.9	3.550	4.0	0.09809	0.92	1501.0	53.0	1588.0	17.0	-5.5
MNJ18.11	225	59	0.27	55.9	0.68	0.2870	3.9	3.860	4.2	0.09750	1.4	1627.0	56.0	1578.0	27.0	3.1
MNJ18.12	277	124	0.46	60	0.84	0.2490	4.0	3.320	4.2	0.09660	1.4	1435.0	52.0	1560.0	26.0	-8.0
MNJ18.13	532	220	0.43	137	0.47	0.2990	3.9	4.050	3.9	0.09816	0.75	1687.0	58.0	1589.0	14.0	6.2
MNJ18.14	582	450	0.80	161	0.34	0.3200	3.9	4.270	4.0	0.09670	1.1	1792.0	61.0	1561.0	20.0	14.8
MNJ18.17	349	422	1.25	79.3	0.35	0.2640	3.9	3.590	4.0	0.09857	0.8	1510.0	52.0	1597.0	15.0	-5.4
MNJ18.18	996	299	0.31	218	2.52	0.2480	3.9	3.200	4.2	0.09360	1.6	1428.0	50.0	1499.0	30.0	-4.7
MNJ18.19	479	470	1.01	91.1	0.87	0.2196	3.9	2.890	4.1	0.09550	1.2	1280.0	45.0	1537.0	22.0	-16.7
MNJ18.20	1201	433	0.37	84.2	3.91	0.0784	4.1	1.082	4.5	0.10010	1.9	487.0	19.0	1626.0	35.0	-70.0
MNJ32.1	252	276	1.13	64.8	6.90	0.2790	4.0	3.950	6.8	0.10280	5.5	1584.0	56.0	1675.0	100.0	-5.4
MNJ32.2	166	178	1.11	42.1	3.88	0.2840	3.9	3.860	5.4	0.09850	3.7	1611.0	56.0	1595.0	69.0	1.0
MNJ32.3	1371	1382	1.04	524	16.11	0.3730	4.2	5.270	4.6	0.10240	1.9	2045.0	73.0	1669.0	36.0	22.5
MNJ32.4	783	389	0.51	214	0.30	0.3170	3.9	4.400	4.0	0.10055	0.78	1777.0	60.0	1634.0	14.0	8.8
MNJ32.5	162	132	0.84	39.3	2.55	0.2750	3.9	3.790	5.5	0.09980	3.9	1568.0	55.0	1621.0	72.0	-3.3
mnj32B.1	217	159	0.76	55.5	0.67	0.2960	5.0	3.910	5.2	0.09570	1.3	1672.0	74.0	1543.0	24.0	8.4
MNJ32B.3	179	117	0.67	42.4	2.31	0.2690	4.9	3.500	5.2	0.09430	1.7	1536.0	67.0	1515.0	33.0	1.4
MNJ32B.5	293	997	3.51	65.5	9.87	0.2340	5.1	2.950	12.0	0.09130	11	1356.0	62.0	1453.0	200.0	-6.7
MNJ32B.6	425	210	0.51	31.6	15.39	0.0732	5.1	0.894	9.3	0.08850	7.8	455.0	23.0	1394.0	150.0	-67.4
MNJ32B.8	53	56	1.09	10.8	2.97	0.2310	5.0	3.110	6.6	0.09770	4.3	1341.0	61.0	1580.0	80.0	-15.1
MNJ32B.9	229	237	1.07	59.2	6.34	0.2820	4.9	3.730	5.6	0.09590	2.7	1602.0	70.0	1546.0	50.0	3.6
MNJ32.10	126	85	0.70	30	4.93	0.2630	5.0	3.360	6.5	0.09250	4.2	1507.0	67.0	1478.0	80.0	2.0
MNJ32B.13	166	753	4.69	40.6	32.15	0.1930	5.9	2.570	11.0	0.09660	9.2	1138.0	61.0	1560.0	170.0	-27.1
MNJ32B.15	296	356	1.25	78	10.80	0.2740	5.0	3.610	6.2	0.09550	3.8	1562.0	69.0	1538.0	71.0	1.6
MNJ32B.16	67	66	1.01	19	0.89	0.3260	5.0	4.260	5.9	0.09480	3.1	1819.0	80.0	1523.0	59.0	19.4

Table 6.2 (cont.)- SHRIMP U-Pb zircon geochronology dat for Munjeela Suite granite samples

Spot	U (ppm)	Th (ppm)	$^{232}Th/^{238}U$	$^{206}Pb^*$ (ppm)	% $^{206}Pb_c$	$^{206}Pb/^{238}U$	%	$^{207}Pb^*/^{235}U$	%	$^{207}Pb^*/^{206}Pb^*$	%	$^{206}Pb/^{238}U$ Age		$^{207}Pb/^{206}Pb$ Age		Concord. (%)
MNJ32B.17	96	81	0.87	27.9	1.73	0.3340	5.0	4.410	5.8	0.09580	2.9	1856.0	81.0	1544.0	55.0	20.2
MNJ32B.19	126	682	5.58	31.4	15.75	0.2440	5.4	3.040	23.0	0.09000	22	1409.0	69.0	1429.0	430.0	-1.4
MNJ32B.22	220	220	1.03	50.9	11.30	0.2380	5.0	3.170	6.6	0.09630	4.3	1378.0	63.0	1554.0	81.0	-11.3
MNJ32B.23	1787	1069	0.62	470	0.06	0.3060	4.9	4.110	4.9	0.09748	0.27	1720.0	74.0	1576.4	5.0	9.1
MNJ32B.24	89	235	2.75	24.6	7.59	0.2990	5.0	3.900	8.4	0.09460	6.8	1686.0	75.0	1520.0	130.0	10.9
MNJ32B.26	94	151	1.67	23.5	5.73	0.2740	5.0	3.540	9.0	0.09370	7.5	1561.0	69.0	1502.0	140.0	3.9

MnO shows a wide range of concentrations from 0.01 wt% to high values of 0.19 wt%. The average MnO content of 0.12 wt% is comparatively high when compared to other garnet-bearing peraluminous granites (eg. Corretge and Suarez, 1994; Kebede et al., 2001; Lackey et al., 2006), but is similar to those reported by Dahlquist et al. (2007). The granite is also characterised by relatively low $Fe_2O_{3(tot)}$ and MgO consistent with the muscovite-rich mineral assemblage (Barbarin, 1999). K_2O concentrations are shoshonitic to High-K (Figure 6.7a). Major elements show a negative trend with increasing SiO_2, with the exception of Na_2O which displays a positive trend and MnO which displays a weak positive trend (Figure 6.7a). The general decrease in most elements is consistent with element dilution with increasing quartz content, while increasing Na_2O represents increased albite content.

Primitive Mantle normalised trace element plots for data from the Sinclair/Bell pluton show similar patterns (Figure 6.7c). Notable differences are observed in the Pt James data with lower concentrations of Ba, Sr and P and higher Y and HREE concentrations (Figure 6.7c). Chondrite normalised REE-patterns show the Pt James intrusion also typically has slightly lower LREE values and a greater negative Eu anomaly (Figure 6.7d).

Major element compositions of the metasedimentary enclaves are relatively limited (Figures 6.7e and 6.7f), in part due to limited sample numbers. Psammo-pelitic samples contain SiO_2 and Al_2O_3 concentrations of 71.9-72 wt% and 13.7-13.9 wt%, respectively. Pelitic samples have SiO_2 and Al_2O_3 concentrations of 65.3-69.6 wt% and 14.5-15.3 wt%, respectively. In both cases REE patterns (Figure 6.7f) display LREE values consistent with Post-Archaean Average Shale (PAAS, Taylor and McLennan, 1985), but display slightly enriched HREE concentrations.

6.5.3 Sm-Nd Isotope Geochemistry

Thirteen granite samples and four metasedimentary enclave samples were selected for Sm-Nd isotope analysis. These data are reported in Table 6.4 and plotted in Figure 6.8. $\varepsilon_{Nd}(T)$ is calculated for T = 1585 Ma for all samples. Samples from Pt Bell and Pt Sinclair yield $^{147}Sm/^{144}Nd$ and $^{143}Nd/^{144}Nd$

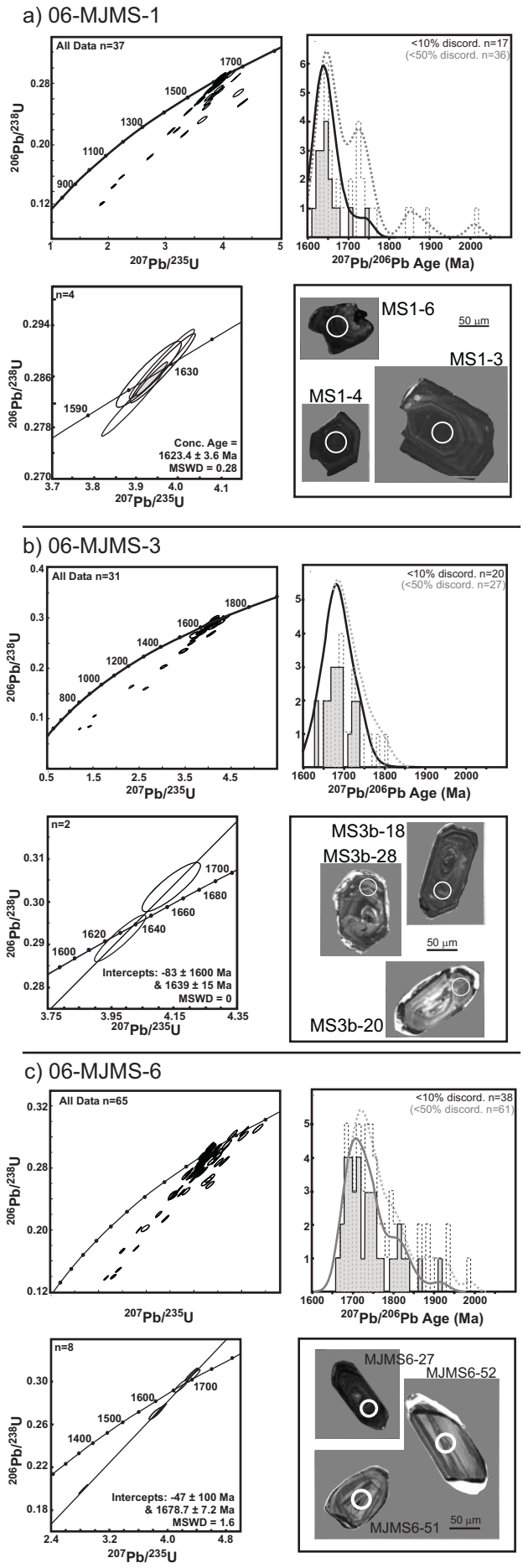

Figure 6.6 - Representative Zircon CL images and U-Pb age data for selected metasedimentary enclaves from Pt Sinclair. a) 06-MJMS-1; b) 06-MJMS-3, c) 06-MJMS-6.

ratios in the ranges 0.1009 - 0.1876 and 0.51172 - 0.51261 respectively. $\varepsilon_{Nd}(T)$ values range from -0.8 to +1.5. Samples from Pt James show elevated $^{147}Sm/^{144}Nd$ ratios in the range 0.1879 - 0.3199. $\varepsilon_{Nd}(T)$ for these samples show similar values to the Bell/Sinclair samples but have a slightly greater range of -3.2 to +2.5. Depleted mantle model ages for the Bell/Sinclair samples range from 1.9 to 2.3 Ga. Model ages are not included for Pt James samples as the elevated $^{147}Sm/^{144}Nd$ ratios result in meaningless model ages.

Sm-Nd isotope results for the metasedimentary enclaves display a range which relates to lithological variation. Psammo-pelitic samples have $\varepsilon Nd(T)$ values of -0.6 and -0.1, while the two pelitic samples yield more evolved values of -1.5 and -3.4. Similarly, depleted mantle model ages (T_{DM}) are 2.1 Ga for both psammo-pelitic samples but are slightly older at 2.2 Ga and 2.3 Ga for 06-MJMS-4 and 06-MJMS-6, respectively.

6.5.4 Mineral Composition

Major element mineral compositions were analysed in thin-section for granite and metasedimentary enclave samples. Trace element data was also analysed for garnet from selected granite samples. Major and trace element mineral compositions are reported in Table 6.5 and Table 6.6, respectively.

6.5.4.1 Granite mineral composition

Mineral composition analyses from the Sinclair/Bell pluton were analysed for samples from the Pt Bell outcrop. Analysed samples included both plagioclase-poor and plagioclase-rich assemblages, but otherwise contained similar assemblages of quartz-K-feldspar-muscovite-biotite-garnet ± ilmenite. K-feldspar in plagioclase-poor assemblages has an average composition of $Or_{0.95}Ab_{0.05}$. K-feldspar in plagioclase-rich assemblages is significantly more Na-rich with an average composition of $Or_{0.66\text{-}0.68}Ab_{0.32\text{-}0.34}$. Plagioclase has a composition range of $Ab_{0.86\text{-}0.90}An_{0.09\text{-}0.13}Or_{<0.01}$ and is comparatively Na-rich. Muscovite contains considerable FeO_T (3.42-3.86 wt%) and MgO (1.53-1.59 wt%). Based upon Mg, Na (0.25-0.5 wt% oxide) and Ti (0.5-0.8 wt% oxide) concentrations,

Table 6.3 - Detriral zircon LA-ICP-MS U-Pb geochronology data

Analysis No.	Th/U	$^{207}Pb/^{206}Pb$ ratio	1σ	$^{207}Pb/^{235}U$ ratio	1σ	$^{206}Pb/^{238}U$ ratio	1σ	$^{206}Pb/^{238}U$ Age (Ma)	1σ (Ma)	$^{207}Pb/^{206}Pb$ Age (Ma)	1σ (Ma)	% Conc.
MJMS1-2	0.89	0.11584	0.00153	4.2633	0.0605	0.26691	0.00334	1525.1	17.0	1893.0	23.5	-19.4
MJMS1-3	0.85	0.10096	0.00108	3.8433	0.0463	0.27610	0.00323	1571.7	16.3	1641.9	19.7	-4.3
MJMS1-4	0.68	0.10277	0.00117	4.1384	0.0548	0.29208	0.00366	1651.9	18.3	1674.8	21.0	-1.4
MJMS1-5	0.83	0.10100	0.00109	3.9098	0.0495	0.28078	0.00345	1595.3	17.4	1642.6	19.9	-2.9
MJMS1-6	1.15	0.10137	0.00107	3.5639	0.0440	0.25501	0.00308	1464.2	15.8	1649.3	19.5	-11.2
MJMS1-7	0.60	0.11115	0.00136	1.8939	0.0241	0.12358	0.00142	751.1	8.1	1818.2	22.0	-58.7
MJMS1-8	1.52	0.10580	0.00117	3.8670	0.0511	0.26514	0.00338	1516.1	17.3	1728.2	20.2	-12.3
MJMS1-9	1.38	0.10188	0.00130	3.9124	0.0562	0.27858	0.00362	1584.2	18.2	1658.6	23.4	-4.5
MJMS1-10	1.31	0.10136	0.00110	3.3900	0.0451	0.24257	0.00315	1400	16.3	1649.2	20.0	-15.1
MJMS1-11	0.88	0.10048	0.00109	3.7446	0.0475	0.27028	0.00332	1542.2	16.9	1633.1	20.0	-5.6
MJMS1-12	0.97	0.10412	0.00119	3.7520	0.0491	0.26136	0.00324	1496.8	16.5	1698.9	20.9	-11.9
MJMS1-13	0.94	0.10022	0.00106	3.8898	0.0469	0.28151	0.00332	1599	16.7	1628.2	19.5	-1.8
MJMS1-14	0.88	0.10324	0.00114	3.0955	0.0411	0.21750	0.00279	1268.7	14.8	1683.1	20.3	-24.6
MJMS1-15	0.44	0.12375	0.00134	4.3384	0.0582	0.25430	0.00335	1460.6	17.2	2010.9	19.1	-27.4
MJMS1-16	0.68	0.09960	0.00118	3.9305	0.0508	0.28623	0.00342	1622.7	17.1	1616.7	21.8	0.4
MJMS1-17	0.37	0.10254	0.00115	2.2340	0.0283	0.15802	0.00191	945.8	10.6	1670.5	20.6	-43.4
MJMS1-19	0.91	0.10079	0.00106	3.8960	0.0471	0.28037	0.00333	1593.2	16.8	1638.8	19.3	-2.8
MJMS1-22	0.52	0.10672	0.00109	4.2204	0.0542	0.28683	0.00368	1625.7	18.5	1744.2	18.6	-6.8
MJMS1-23	0.71	0.10239	0.00110	3.9755	0.0500	0.28161	0.00346	1599.5	17.4	1667.9	19.7	-4.1
MJMS1-25	8.00	0.10110	0.00109	3.6120	0.0454	0.25913	0.00317	1485.4	16.2	1644.3	19.8	-9.7
MJMS1-26	0.90	0.10426	0.00124	2.0941	0.0286	0.14568	0.00185	876.7	10.4	1701.3	21.7	-48.5
MJMS1-27	0.74	0.11298	0.00121	3.3289	0.0431	0.21372	0.00271	1248.6	14.4	1847.9	19.2	-32.4
MJMS1-28	1.14	0.10180	0.00112	3.8190	0.0486	0.27210	0.00334	1551.5	16.9	1657.1	20.2	-6.4
MJMS1-29	1.01	0.10583	0.00113	3.1940	0.0391	0.21892	0.00262	1276.2	13.9	1728.7	19.5	-26.2
MJMS1-30	0.96	0.09983	0.00108	3.9613	0.0508	0.28784	0.00359	1630.7	18.0	1620.8	20.0	0.6
MJMS1-31	1.43	0.10184	0.00109	3.6138	0.0463	0.25738	0.00323	1476.4	16.6	1657.9	19.7	-10.9
MJMS1-32	0.88	0.10459	0.00119	3.9204	0.0516	0.27188	0.00340	1550.4	17.2	1707.0	20.9	-9.2
MJMS1-33	1.52	0.10781	0.00121	3.7060	0.0458	0.24939	0.00292	1435.3	15.1	1762.7	20.3	-18.6
MJMS1-35	0.09	0.10543	0.00107	3.7473	0.0464	0.25778	0.00320	1478.5	16.4	1721.9	18.5	-14.1
MJMS1-36	0.80	0.10607	0.00114	3.9469	0.0449	0.26995	0.00296	1540.6	15.0	1733.0	19.6	-11.1
MJMS1-37	1.72	0.10137	0.00113	4.0530	0.0510	0.29001	0.00349	1641.6	17.5	1649.3	20.5	-0.5
MJMS1-39	0.62	0.10009	0.00110	3.9629	0.0510	0.28719	0.00357	1627.5	17.9	1625.7	20.2	0.1
MJMS1-40	1.00	0.10750	0.00119	2.7272	0.0356	0.18400	0.00232	1088.8	12.6	1757.5	20.1	-38.0
MJMS1-41	1.03	0.10084	0.00105	3.7369	0.0459	0.26876	0.00326	1534.5	16.6	1639.7	19.3	-6.4
MJMS1-42	0.91	0.10626	0.00121	3.7409	0.0505	0.25534	0.00328	1466	16.9	1736.3	20.7	-15.6
MJMS1-43	0.79	0.10536	0.00114	3.8179	0.0510	0.26287	0.00341	1504.5	17.4	1720.5	19.8	-12.6
MJMS1-44	0.78	0.11372	0.00147	3.6345	0.0541	0.23184	0.00312	1344.2	16.3	1859.7	23.2	-27.7

Table 6.3 (cont.) - Detriral zircon LA-ICP-MS U-Pb geochronology data

Analysis No.	Th/U	$^{207}Pb/^{206}Pb$ ratio	1σ	$^{207}Pb/^{235}U$ ratio	1σ	$^{206}Pb/^{238}U$ ratio	1σ	$^{206}Pb/^{238}U$ Age (Ma)	1σ (Ma)	$^{207}Pb/^{206}Pb$ Age (Ma)	1σ (Ma)	% Conc.
MJMS3-1	0.47	0.10397	0.00124	3.7019	0.0581	0.25828	0.00383	1481.0	19.6	1696.3	21.8	-12.7
MJMS3-4	0.31	0.10336	0.00126	3.9270	0.0652	0.27559	0.00433	1569.1	21.9	1685.4	22.3	-6.9
MJMS3-5	0.87	0.10280	0.00119	3.8793	0.0597	0.27373	0.00404	1559.7	20.4	1675.3	21.2	-6.9
MJMS3-6	0.41	0.11028	0.00126	4.0691	0.0625	0.26766	0.00395	1528.9	20.1	1804.0	20.7	-15.2
MJMS3-7	0.79	0.10274	0.00123	4.0254	0.0621	0.28418	0.00412	1612.4	20.7	1674.2	22.0	-3.7
MJMS3-8	0.68	0.10319	0.00116	3.9551	0.0601	0.27803	0.00409	1581.4	20.6	1682.3	20.6	-6.0
ms3B01	0.84	0.10554	0.00129	3.6345	0.0510	0.24975	0.00323	1437.2	16.7	1723.8	22.3	-16.6
ms3B03	0.40	0.10287	0.00150	4.1644	0.0668	0.29354	0.00398	1659.2	19.9	1676.6	26.8	-1.0
ms3B05	0.29	0.10184	0.00227	3.7294	0.0837	0.26570	0.00414	1518.9	21.1	1657.9	40.7	-8.4
ms3B06	0.18	0.10636	0.00153	4.2635	0.0663	0.29065	0.00383	1644.8	19.1	1737.9	26.2	-5.4
ms3B08	0.24	0.10556	0.00163	4.1094	0.0674	0.28230	0.00381	1602.9	19.1	1724.0	28.1	-7.0
MS3B09	0.36	0.10419	0.00146	2.3359	0.0353	0.16264	0.00210	971.4	11.7	1700.1	25.7	-42.9
MS3B10	0.47	0.10691	0.00144	1.5330	0.0228	0.10396	0.00136	637.6	8.0	1747.4	24.4	-63.5
MS3B11	0.72	0.10481	0.00194	4.0913	0.0780	0.28302	0.00409	1606.6	20.5	1710.9	33.6	-6.1
MS3B12	0.29	0.12466	0.00196	1.4248	0.0227	0.08288	0.00106	513.3	6.3	2024.0	27.6	-74.6
MS3B13	0.41	0.10614	0.00119	4.4031	0.0562	0.30079	0.00366	1695.2	18.2	1734.1	20.5	-2.2
MS3B14	0.92	0.10892	0.00144	3.0332	0.0443	0.20195	0.00262	1185.8	14.0	1781.3	24.0	-33.4
MS3B15	0.56	0.10375	0.00155	3.8715	0.0623	0.27053	0.00364	1543.5	18.5	1692.3	27.4	-8.8
MS3B16	0.41	0.11276	0.00153	1.2117	0.0185	0.07801	0.00106	484.2	6.4	1844.4	24.3	-73.7
MS3B17	1.19	0.12094	0.00160	2.6403	0.0373	0.15842	0.00198	948.0	11.0	1970.1	23.4	-51.9
MS3B18	0.50	0.10080	0.00122	3.9790	0.0541	0.28625	0.00359	1622.8	18.0	1638.8	22.3	-1.0
MS3B19	0.82	0.10214	0.00182	4.0532	0.0749	0.28769	0.00407	1630.0	20.4	1663.4	32.7	-2.0
MS3B20	0.71	0.10188	0.00158	4.1321	0.0683	0.29402	0.00398	1661.6	19.8	1658.7	28.5	0.2
MS3B21	1.29	0.10731	0.00162	3.4546	0.0560	0.23335	0.00316	1352.1	16.5	1754.3	27.4	-22.9
MS3B22	0.58	0.10394	0.00125	4.1103	0.0558	0.28675	0.00361	1625.3	18.1	1695.5	22.0	-4.1
MS3B24	0.69	0.10314	0.00132	3.9971	0.0574	0.28106	0.00365	1596.7	45.5	1681.4	23.4	-5.0
MS3B25	0.39	0.10368	0.00127	4.1221	0.0579	0.28816	0.00373	1632.3	18.4	1691.0	22.4	-3.5
MS3B26	0.51	0.10238	0.00138	3.8294	0.0572	0.27107	0.00356	1546.2	18.7	1667.6	24.8	-7.3
MS3B27	0.53	0.10538	0.00144	4.1793	0.0613	0.28752	0.00365	1629.1	18.0	1721.0	24.8	-5.3
MS3B28	0.55	0.10065	0.00138	4.1420	0.0614	0.29826	0.00382	1682.7	18.3	1636.2	25.2	2.8
MS3B29	1.02	0.10780	0.00154	3.4788	0.0532	0.23392	0.00305	1355.0	19.0	1762.5	25.9	-23.1
MS601	0.36	0.10699	0.00118	4.4799	0.0660	0.30381	0.00436	1710.2	21.56	1748.8	19.99	-2.2
MS602	0.74	0.11056	0.00121	4.1908	0.0614	0.27503	0.00394	1566.3	19.9	1808.6	19.77	-13.4
MS603	0.96	0.10735	0.00123	4.1355	0.0619	0.27950	0.00402	1588.8	20.24	1755	20.79	-9.5
MS604	0.63	0.11077	0.00115	4.6412	0.0662	0.30400	0.00431	1711.1	21.31	1812.1	18.81	-5.6
MS605	0.49	0.10657	0.00112	4.4585	0.0638	0.30353	0.00430	1708.8	21.26	1741.7	19.09	-1.9
MS606	0.50	0.11676	0.00128	4.6325	0.0675	0.28786	0.00410	1630.8	20.5	1907.2	19.61	-14.5
MS607	0.96	0.11877	0.00141	2.4127	0.0364	0.14738	0.00211	886.3	11.88	1937.8	21.14	-54.3

Table 6.3 (cont.) - Detriral zircon LA-ICP-MS U-Pb geochronology data

Analysis No.	Th/U	$^{207}Pb/^{206}Pb$ ratio	1σ	$^{207}Pb/^{235}U$ ratio	1σ	$^{206}Pb/^{238}U$ ratio	1σ	$^{206}Pb/^{238}U$ Age (Ma)	1σ (Ma)	$^{207}Pb/^{206}Pb$ Age (Ma)	1σ (Ma)	% Conc.
MS609	0.91	0.10881	0.00119	3.9860	0.0573	0.26575	0.00374	1519.2	19.02	1779.6	19.82	-14.6
MS610	1.22	0.11542	0.00130	3.3983	0.0496	0.21360	0.00301	1248	16	1886.4	20.22	-33.8
MS611	1.18	0.10352	0.00107	2.8377	0.0395	0.19886	0.00276	1169.2	14.86	1688.2	18.88	-30.7
MS612	0.88	0.10347	0.00104	3.8747	0.0534	0.27167	0.00376	1549.3	19.06	1687.2	18.47	-8.2
MS613	1.47	0.10669	0.00120	3.9942	0.0581	0.27157	0.00381	1548.8	19.3	1743.7	20.55	-11.2
MS614	0.70	0.11159	0.00117	4.4735	0.0625	0.29080	0.00403	1645.5	20.13	1825.5	18.85	-9.9
MS618	0.79	0.11530	0.00125	2.7844	0.0395	0.17518	0.00243	1040.6	13.35	1884.6	19.43	-44.8
MS615	0.72	0.10477	0.00117	4.1068	0.0591	0.28434	0.00396	1613.2	19.87	1710.3	20.44	-5.7
MS616	0.36	0.10511	0.00109	4.1415	0.0574	0.28581	0.00394	1620.5	19.73	1716.3	18.98	-5.6
MS619	0.63	0.10313	0.00136	3.8360	0.0598	0.26980	0.00380	1539.8	19.29	1681.1	24.07	-8.4
MS620	0.61	0.11411	0.00130	2.1570	0.0309	0.13711	0.00188	828.3	10.69	1865.8	20.46	-55.6
MS621	0.85	0.10592	0.00120	3.9270	0.0562	0.26890	0.00369	1535.2	18.75	1730.4	20.72	-11.3
MS622	1.89	0.12061	0.00166	2.3063	0.0366	0.13868	0.00197	837.2	11.12	1965.3	24.32	-57.4
MS623	0.59	0.10567	0.00108	3.5353	0.0476	0.24266	0.00327	1400.5	16.97	1725.9	18.61	-18.9
MS624	0.59	0.10649	0.00112	3.6897	0.0505	0.25130	0.00340	1445.2	17.5	1740.1	19.29	-16.9
MJMS6-25	0.61	0.11067	0.00138	4.5002	0.0585	0.29488	0.00346	1665.8	17.22	1810.4	22.41	-8.0
MJMS6-26	0.72	0.10732	0.00128	4.4074	0.0590	0.29791	0.00372	1680.9	18.47	1754.5	21.64	-4.2
MJMS6-27	0.69	0.10249	0.00115	4.3265	0.0571	0.30645	0.00390	1723.2	19.26	1669.7	20.64	3.2
MJMS6-28	0.99	0.10610	0.00119	4.2525	0.0556	0.29091	0.00368	1646.1	18.36	1733.5	20.39	-5.0
MJMS6-29	0.73	0.10397	0.00159	4.2423	0.0695	0.29618	0.00404	1672.4	20.08	1696.2	27.99	-1.4
MJMS6-31	0.84	0.10410	0.00125	4.2179	0.0563	0.29395	0.00363	1661.3	18.08	1698.4	22.03	-2.2
MJMS6-32	0.11	0.11211	0.00113	5.0494	0.0620	0.32682	0.00406	1823	19.72	1833.8	18.21	-0.6
MJMS6-34	0.82	0.10961	0.00120	3.7309	0.0480	0.24695	0.00309	1422.7	15.99	1792.9	19.88	-20.6
MJMS6-38	0.69	0.10467	0.00114	4.2087	0.0538	0.29171	0.00363	1650	18.13	1708.5	19.99	-3.4
MJMS6-39	0.88	0.10639	0.00113	4.0987	0.0510	0.27949	0.00343	1588.8	17.29	1738.4	19.31	-8.6
MJMS6-40	0.48	0.10486	0.00112	4.1281	0.0506	0.28557	0.00344	1619.3	17.23	1711.8	19.48	-5.4
MJMS6-41	0.36	0.11725	0.00140	5.3382	0.0709	0.33030	0.00408	1839.9	19.79	1914.7	21.32	-3.9
MJMS6-42	0.47	0.10441	0.00130	4.3760	0.0615	0.30403	0.00391	1711.3	19.31	1703.9	22.83	0.4
MJMS6-45	0.50	0.10571	0.00123	4.0848	0.0541	0.28034	0.00348	1593.1	21.3	1726.6	17.54	-7.7
MJMS6-46	0.62	0.10410	0.00111	4.2896	0.0516	0.29886	0.00352	1685.7	19.43	1698.6	17.45	-0.8
MJMS6-47	1.09	0.11429	0.00132	4.5184	0.0607	0.28673	0.00367	1625.2	20.7	1868.6	18.36	-13.0
MJMS6-48	0.80	0.10604	0.00183	3.5519	0.0617	0.24317	0.00324	1403.2	31.26	1732.3	16.79	-19.0
MJMS6-49	1.07	0.10955	0.00152	4.1106	0.0615	0.27224	0.00353	1552.2	25.06	1791.9	17.88	-13.4
MJMS6-51	1.59	0.10337	0.00115	3.9000	0.0518	0.27365	0.00352	1559.3	20.46	1685.4	17.83	-7.5
MJMS6-52	0.38	0.10271	0.00135	4.1844	0.0607	0.29546	0.00382	1668.8	24.02	1673.7	19.01	-0.3
MJMS6-53	0.98	0.10510	0.00132	2.4912	0.0352	0.17191	0.00221	1022.6	22.99	1716.1	12.14	-40.4
MJMS6-54	0.71	0.10418	0.00120	4.1455	0.0535	0.28866	0.00351	1634.8	21.1	1699.9	17.54	-3.8
MJMS6-55	0.41	0.10883	0.00113	4.4805	0.0541	0.29865	0.00358	1684.6	18.84	1779.9	17.79	-5.4

Table 6.3 (cont.) - Detriral zircon LA-ICP-MS U-Pb geochronology data

Analysis No.	Th/U	$^{207}Pb/^{206}Pb$ ratio	1σ	$^{207}Pb/^{235}U$ ratio	1σ	$^{206}Pb/^{238}U$ ratio	1σ	$^{206}Pb/^{238}U$ Age (Ma)	1σ (Ma)	$^{207}Pb/^{206}Pb$ Age (Ma)	1σ (Ma)	% Conc.
MJMS6-56	0.57	0.12214	0.00154	4.3318	0.0572	0.25739	0.00305	1476.5	22.27	1987.7	15.66	-25.7
MJMS6-57	0.65	0.10360	0.00124	4.3554	0.0598	0.30493	0.00393	1715.7	21.84	1689.5	19.39	1.6
MJMS6-58	0.48	0.11381	0.00137	5.0306	0.0697	0.32058	0.00416	1792.6	21.54	1861.1	20.32	-3.7
MJMS6-59	0.55	0.10968	0.00134	4.6816	0.0666	0.30963	0.00411	1738.9	22.11	1794	20.25	-3.1
MJMS6-60	0.77	0.10279	0.00112	4.3303	0.0562	0.30554	0.00387	1718.7	19.96	1675.1	19.12	2.6
MJMS6-61	0.50	0.10513	0.00117	4.1433	0.0547	0.28584	0.00365	1620.7	20.31	1716.5	18.29	-5.6
MJMS1-62	0.43	0.10898	0.00117	4.1386	0.0513	0.27551	0.00334	1568.7	19.54	1782.4	16.87	-12.0
MJMS1-63	0.10	0.10823	0.00125	4.8076	0.0663	0.32215	0.00426	1800.2	20.96	1769.7	20.78	1.7
MJMS1-64	0.76	0.10549	0.00170	3.5637	0.0605	0.24502	0.00337	1412.7	29.26	1722.9	17.47	-18.0
MJMS1-65	0.81	0.11153	0.00144	3.8299	0.0554	0.24915	0.00325	1434.1	23.3	1824.4	16.78	-21.4
MJMS1-67	1.43	0.10773	0.00130	3.2568	0.0422	0.21932	0.00260	1278.3	21.91	1761.4	13.76	-27.4
MJMS1-68	2.35	0.10732	0.00199	2.9769	0.0562	0.20121	0.00288	1181.8	33.45	1754.4	15.46	-32.6
MJMS1-69	0.48	0.10603	0.00140	4.1926	0.0627	0.28680	0.00385	1625.5	24.05	1732.2	19.29	-6.2
MJMS1-70	0.60	0.10684	0.00118	4.1011	0.0525	0.27845	0.00345	1583.6	19.97	1746.2	17.42	-9.3
MJMS1-71	0.72	0.10720	0.00117	4.3215	0.0564	0.29247	0.00373	1653.9	19.76	1752.3	18.61	-5.6
MJMS1-72	0.66	0.11838	0.00185	4.2644	0.0711	0.26169	0.00363	1498.5	27.69	1931.9	18.53	-22.4
MJMS6-73	0.16	0.11846	0.00161	4.3406	0.0634	0.26599	0.00342	1520.4	24.16	1933.2	17.43	-21.4
MJMS6-75	0.83	0.11022	0.00137	4.3779	0.0600	0.28818	0.00361	1632.4	22.49	1803	18.06	-9.5
MJMS6-77	1.04	0.10474	0.00123	4.1379	0.0569	0.28658	0.00373	1624.4	21.47	1709.8	18.71	-5.0

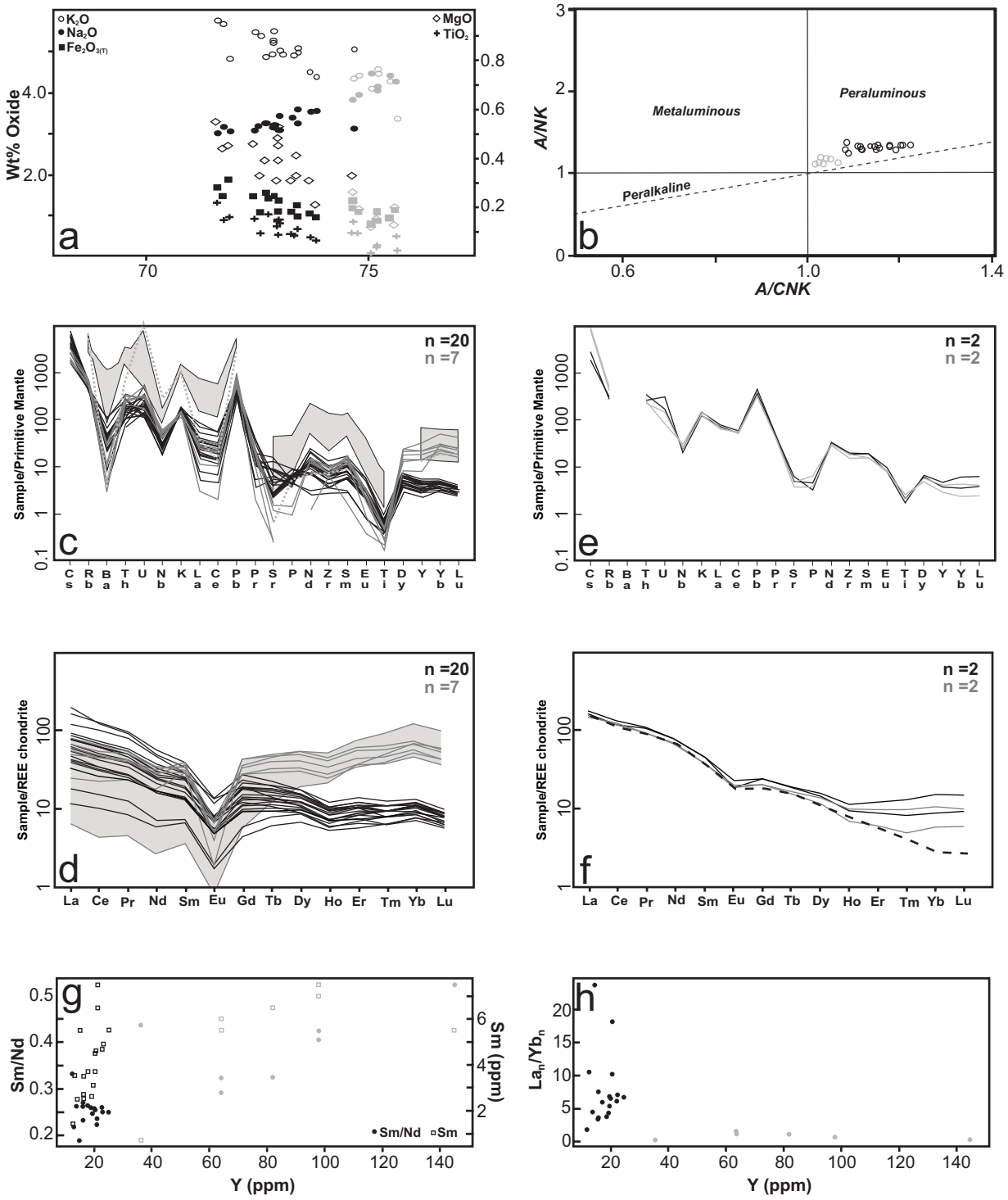

Figure 6.7 - Whole-rock geochemistry plots for studied Munjeela Suite granite and metasedimentary enclaves from Pt Sinclair. In all granite geochemistry diagrams gray symbols represent Pt James intrusion samples and black represent Sinclair/Bell intrusion samples. a) Major element trends of granite plotted against SiO_2; b) A/NK v A/CNK plot demonstrating the peraluminous nature of the granite with distinct groups for the Pt James and Sinclair/Bell intrusions; c) Primitive mantle normalised trace element data for granite (Sun and McDonough, 1989). Shaded field represents Hiltaba Suite intrusions discussed in Section 6.8 (Stewart and Foden, 2001). Dashed line represents an outlier Hiltaba Suite sample; d) Chondrite-normalised rare-earth element (REE) plot displaying M- and HREE enriched compositions of Pt James samples. Gray field shows spread of Pt James samples; e) Primitive-mantle normalised trace element data for metasedimentary enclaves from Pt Sinclair; f) Chondrite-normalised REE plot for metasedimentary enclaves. Dashed line represents Post-Archaean average shale (PAAS) composition of Taylor and McLennan (1985); g) Sm/Nd (dots) and Sm (squares) versus Y plot for granite data demonstrating the enriched and positive correlation of Sm/Nd and Sm with Y for Pt James (gray) data; h) $La_{(n)}/Yb_{(n)}$ versus Y demonstrating highly HREE enriched nature of Pt James samples.

muscovite falls in the primary magmatic field of the Mg-Na-Ti ternary diagram of Miller et al. (1981), consistent with the petrographic interpretation that it is a magmatic phase. Biotite has a composition of $Ann_{0.58-0.59}Phl_{0.41-0.42}$, assuming ideal Fe-Mg substitution. The biotite is also Mn-rich with MnO concentrations ranging from 0.98-1.04 wt%. This is consistent for biotite crystallising with Mn-rich garnet (eg. Miller and Stoddard, 1981; Dahlquist et al., 2007).

Garnet within the Sinclair/Bell intrusion is Mn-rich and has a general composition of $Alm_{0.44}Sps_{0.47}Py_{0.07}Grs_{0.01}$ to $Alm_{0.39}Sps_{0.55}Py_{0.03}Grs_{0.03}$. Garnet compositions are represented in Figure 6.9a with element maps and traverses of two garnets shown in Figure 6.10. Garnet from sample 06-MNJ-05 (Figure 6.10a), shows two compositional zones defined by Ca-zoning. The outer zone correlates to a drop in Mn then a rimwards increase with the reverse observed for Fe and Mg (Figure 6.10a). Garnet from sample 06-MNJ-11 (Figure 6.10b), shows concentric zoning with five Ca-defined compostion zones. The innermost zone shows slight enrichment of Mn and depletion of Fe and Ca compared to the second growth zone. A consistent increase in Mn and Ca and decrease in Fe and Mg is observed from the outer edge of the second growth zone to the garnet rim. This outer zoning is similar to that observed in 06-MNJ-05 (Figure 6.10a) but significantly more pronounced. Analyses in the outermost Ca-rich zone yield a composition of $Alm_{0.27}Sps_{0.52}Py_{0.01}Grs_{0.20}$.

Samples analysed from Pt James have a quartz-K-feldspar-plagioclase-muscovite-biotite-chlorite-garnet-ilmenite-hematite mineral assemblage with rapakivi feldspar textures. K-feldspar in the matrix of the granite displays a limited composition range $Or_{0.94-0.96}Ab_{0.04-0.06}$ with an average composition of $Or_{0.95}Ab_{0.05}$. K-feldspar within the rapakivi textures demonstrate a slightly more variable composition, with a range of $Or_{0.92-0.98}Ab_{0.02-0.08}$. Plagioclase occurs in three textural settings: relatively small crystals within the matrix which crystallised early; large, zoned crystals with fluid inclusions defining the crystal zoning; and as well developed, inclusion-rich rims around K-feldspar in the rapakivi texture. Large, zoned plagioclase has a composition range of $Ab_{0.88-0.98}An_{0.02-0.1}Or_{<0.01-0.02}$. Ca is enriched towards the rim of the plagioclase with a Na-rich outermost rim. Plagioclase in the rapakivi texture has a composition range of $Ab_{0.93-0.98}An_{0.02-0.07}Or_{<0.01}$ with Ca most-enriched in the inclusion free outermost-rim. Muscovite is enriched in Mn with as much as 10 times that present in muscovite from Sinclair/Bell samples. Muscovite in rapakivi feldspars contains the greatest enrichment with 0.32-0.51 wt % MnO.

The largest garnet found in thin section from Pt James retains the most euhedral shape and is mapped in Figure 6.10c. Composition of this garnet ranges from $Alm_{0.31}Sps_{0.66}Py_{0.01}Grs_{0.025}$ to $Alm_{0.26}Sps_{0.70}Py_{0.01}Grs_{0.03}$ within the Ca-poor, inner zone defined in Figure 6.11c. The outer, largely decomposed Ca-rich rim has a composition range of $Alm_{0.23}Sps_{0.65}Py_{0.005}Grs_{0.11}$ to $Alm_{0.22}Sps_{0.62}Py_{0.005}Grs_{0.16}$. Mn values for all garnet grains analysed from Pt James are higher than any observed in granite samples from the Bell/Sinclair intrusion (Figures 6.9 and 6.10). Ilmenite inclusions within the garnet (Figure 6.10c) contain significant MnO, with concentrations varying from 19.1-26.5wt% MnO.

Chondrite-normalised REE compositions of garnet from sample 06-MNJ-11 and 06-MNJ-32 are plotted in Figure 6.9b and 6.9c. Laser spot locations are displayed in Figure 6.10. The Ca-poor core of garnet analysed from sample 06-MNJ-32 (Figure 6.10c) displays highly enriched Sm and HREE values, large negative Eu anomalies and Sm-Nd ratios between 7.1 and 11.8 (Figure 6.9b). The

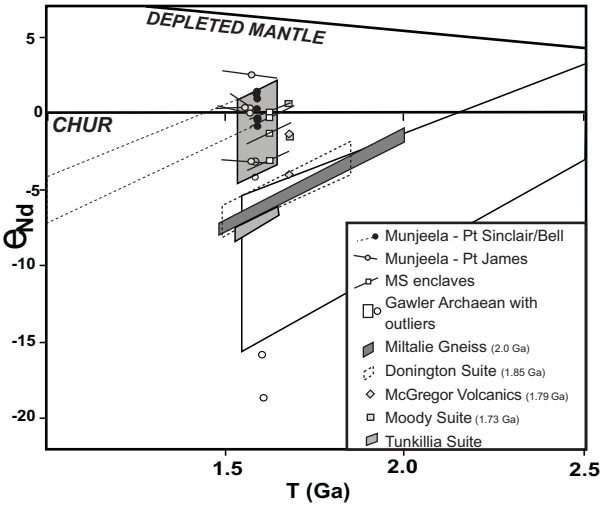

Figure 6.8 - Sm-Nd isotope growth curves for Munjeela Suite data and metasedimentary enclaves. Also plotted is selected data from pre-1.6 Ga lithologies of the Gawler Craton demonstrating the isotopic similarity between these lithologies and the metasedimentary enclaves found within the Munjeela Suite granite.

outer Ca-rich zone displays variable REE patterns but has consistently lower HREE enrichment. Representative garnet from sample 06-MNJ-11 displays highly variable HREE concentrations but relatively consistent LREE concentrations. Analyses from the outermost, thin Ca-rich zone of the garnet display MREE enrichment and in the case of analysis 11.gt.5r, also LREE enrichment. All analyses display lower HREE values than 06-MNJ-32 garnet, particularly in the case of analyses from the interior of the 06-MNJ-11 garnet.

6.5.4.2 Metasedimentary enclave mineral composition

Within psammo-pelitic samples garnet, biotite, muscovite, K-feldspar and plagioclase were analysed. Garnet is spessartine-rich with Xsps ranging from 0.60 to 0.63. Plagioclase is albite-rich with a compositional range of $Ab_{0.84-0.86}An_{0.14-0.16}$.

Pelitic mineral assemblages analysed include garnet, muscovite, biotite, chlorite, K-feldspar, plagioclase, ilmenite and magnetite. Muscovite and biotite both contain considerable MnO with *c.* 0.45 wt% and *c.* 1.1 wt%, respectively. MgO content in muscovite varies from 2-5 wt%. Garnet is either spessartine-almandine dominated ($Alm_{0.26-0.29}Sps_{0.58-0.62}$) or almandine poor with very high spessartine content ($Sps_{0.68-0.71}$). An element map of a large, spessartine-rich garnet from sample 06-MJMS-6 is shown in Figure 6.10d. Element concentrations are relatively flat in the garnet interior with Fe-

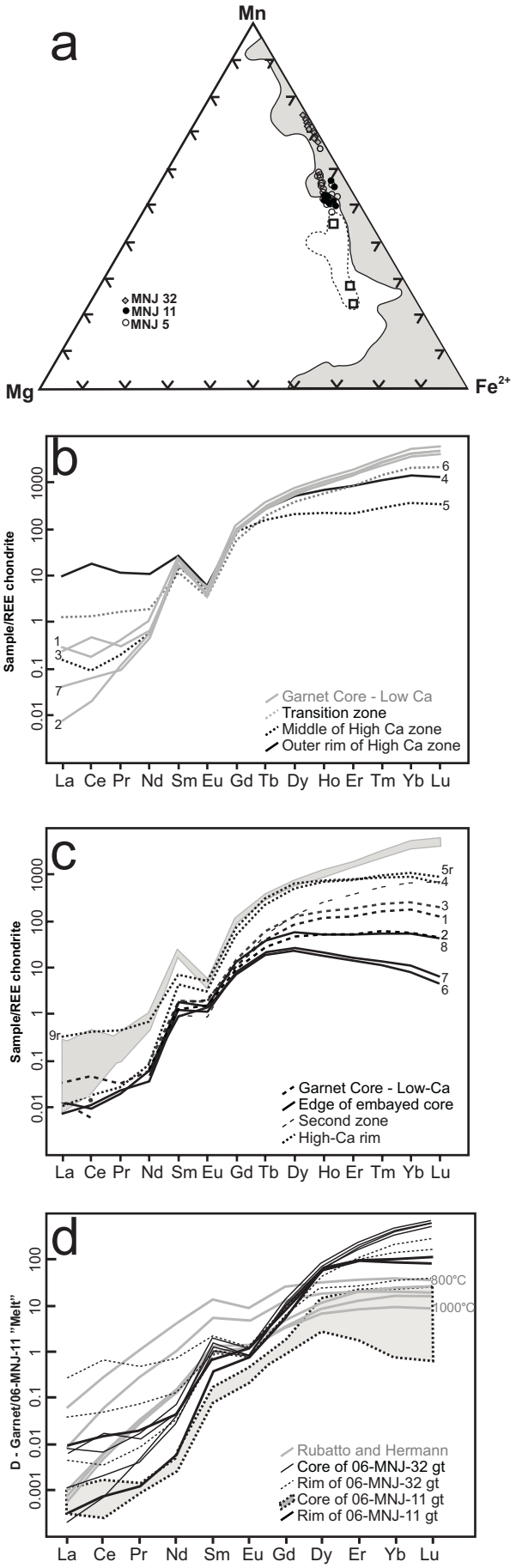

Figure 6.9 - Major and REE element information for garnet from Munjeela Suite granite. a) Mn-Mg-Fe^{2+} ternery diagram for garnet demonstrating Mn-rich nature of Pt James garnet. Shaded field represents magmatic garnet field of Miller and Stoddard (1981). Dashed line represents field of garnet composition from Dahlquist et al. (2007) with squares representing average compositions from the three studied plutons; b) Chondrite-normalised REE data for garnet from sample 06-MNJ-32 (Pt James); c) Chondrite-normalised REE data for garnet from sample 06-MNJ-11 (Pt Sinclair) with gray field representing garnet core data from 06-MNJ-32; d) REE distribution coefficients for garnet using whole-rock geochemistry of 06-MNJ-11 to estimate melt composition. Solid gray lines represent experimental data of Rubatto and Hermann (2007).

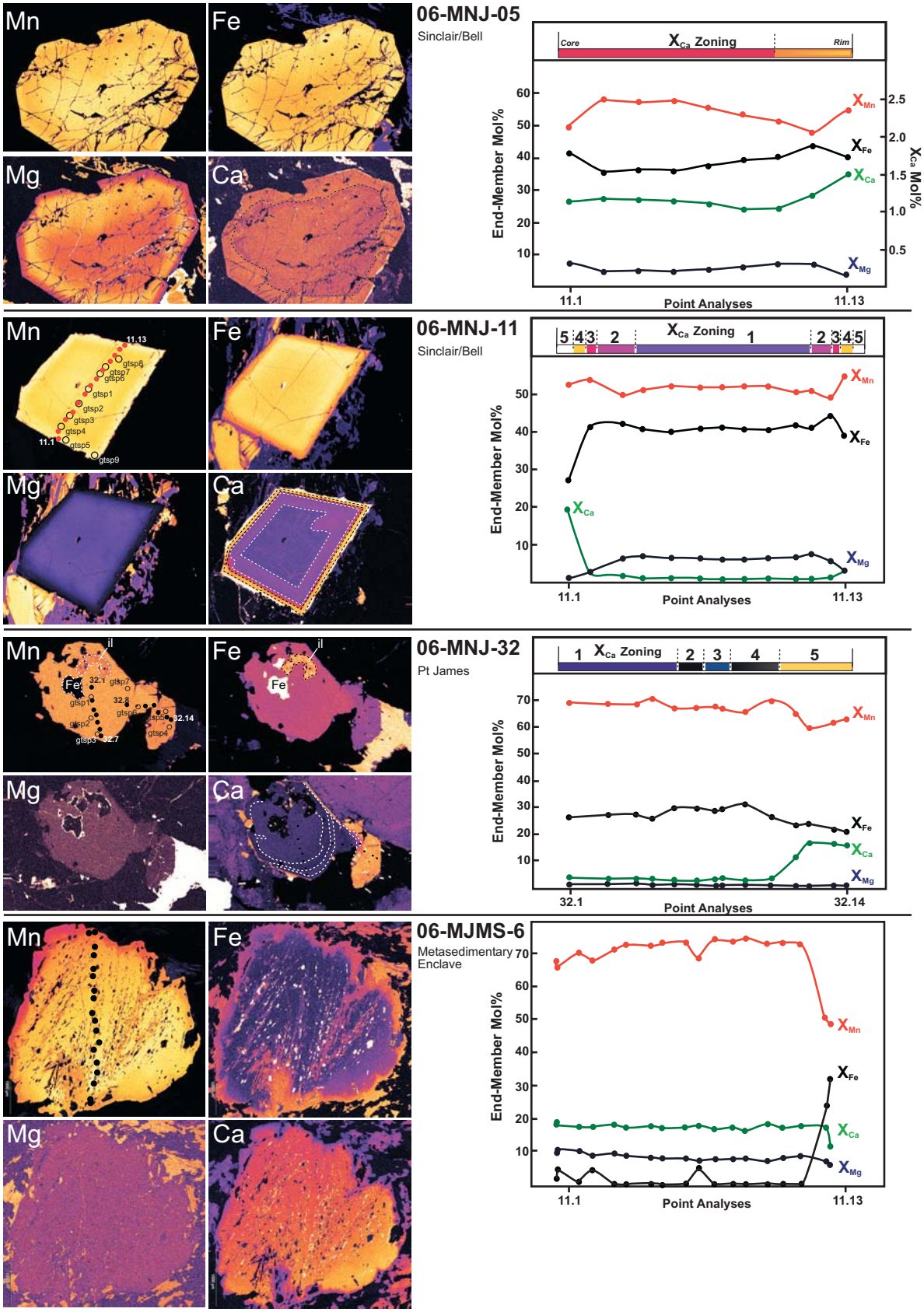

Figure 6.10 - Mn-Fe-Mg-Ca composition maps of selected granite and metasedimentary-hosted garnet with major element spot analyses traverses. Colour-coded bars above spot analyses traverses correlate to Ca zoning in garnet. Dashed lines highlight changes in compositional zoning. Traverse locations are represented by small dots and LA-ICP-MS spot analyses (Figure 6.9) are represented by circles. Spot locations for sample 06-MNJ-05 are not shown as they correspond in part to areas of the garnet which were not mapped due to beam current drop during element mapping process.

Table 6.4 - Sm-Nd isotope data for Munjeela Suite granite and metasedimentary enclave samples

Sample No.	Location	Sm (ppm)	Nd (ppm)	$^{147}Sm/^{144}Nd$	$^{143}Nd/^{144}Nd$	2 S.E.	$\varepsilon_{Nd}(0)^a$	$\varepsilon_{Nd}(T)$	T_{DM} (Ga)
06-MJMS-1	Pt Sinclair	7.3	41.7	0.1063	0.51167		-19.0	-0.6	2.1
06-MJMS-3	Pt Sinclair	8.1	42.6	0.1148	0.51178		-16.8	-0.1	2.1
06-MJMS-4	Pt Sinclair	7.5	40.4	0.1126	0.51169		-18.5	-1.5	2.2
06-MJMS-6	Pt Sinclair	7.2	39.1	0.1109	0.51157		-20.8	-3.4	2.3
06-MNJ-01	Pt Bell	2.9	12.1	0.1451	0.51215		-9.5	1.0	1.9
06-MNJ-03	Pt Bell	1.7	5.6	0.1876	0.51261		-0.5	1.4	2.2
06-MNJ-05	Pt Bell	2.8	11.0	0.1533	0.51214		-9.6	-0.8	2.1
06-MNJ-10	Pt Bell	4.4	17.8	0.1492	0.51212		-10.0	-0.4	2.1
06-MNJ-12	Pt Sinclair	6.0	25.4	0.1420	0.51205		-11.4	-0.3	2.3
06-MNJ-18	Pt Sinclair	3.9	17.7	0.1327	0.51195		-13.4	-0.4	2.2
06-MNJ-20	Pt Bell	8.1	40.5	0.1206	0.51186		-15.1	0.4	2.1
06-MNJ-25	Pt Bell	6.5	39.0	0.1009	0.51172		-17.9	1.5	1.9
06-MNJ-27	Pt James	0.9	2.7	0.2106	0.51262		-0.3	-3.2	-
06-MNJ-29	Pt James	6.8	12.8	0.3199	0.51393		25.2	0.1	-
06-MNJ-32	Pt James	6.1	19.8	0.1879	0.51257		-1.3	0.5	-
06-MNJ-34	Pt James	8.5	23.0	0.2226	0.51304		7.8	2.5	-
06-MNJ-36	Pt James	7.0	17.8	0.2357	0.51304		7.9	-0.1	-

[a] $^{143}Nd/^{144}NdCHUR(0) = 0.516638$, $^{147}Sm/^{144}NdCHUR = 0.1967$

enrichment and Mn-depletion in the outer rim. Almandine content in the Fe-rich rim is up to $Alm_{0.38}$. Fe diffusion into garnet is evident around magnetite-rich inclusion trails.

6.5.5 Thermobarometry

Mineral equilibria modelling was undertaken using the program Thermocalc 3.3.0 (Powell and Holland, 1988) using the internally consistent dataset of Holland and Powell (1998, data set tcds55, file created 01/01/2004). Construction of a P-T pseudosection was undertaken in the MnNCKFMASH system (Figure 6.11). The sources of activity-composition relationships used in calculations are: muscovite - Coggon and Holland (2002); Mn-garnet - Mahar et al. (1997), Vance and Holland (1993); binary plagioclase - Holland and Powell (1992); Mn-biotite - Powell and Holland (1999); Mn-cordierite - Holland and Powell (1998); Mn-chlorite - Stowell et al. (2001); Liquid/melt - White et al. (2001). As discussed by White et al. (2007) the use of Mn-endmember a-x models in conjunction with NCKFMASH is likely to generate unreliable results due to the use of simple ideal-mixing models in the initial calibrations of Mahar et al. (1997). As pelitic rock samples within this study are Mn-rich (06-MJMS-6 - 0.61 wt% oxide), and garnet is highly spessartine-rich, the potential errors resulting from use of Mn are considered preferable to disregarding Mn entirely.

A P-T pseudosection was calculated using the bulk chemical composition of metasedimentary enclave sample 06-MJMS-6. The calculated P-T pseudosection (Figure 6.11) highlights the large stability field of the mu-bi-g-pl-ksp-qtz (+H_2O or +liq) mineral assemblage for the studied Mn-rich bulk composition. To this extent, little constraint on P-T conditions can be provided by the mineral assemblage present in the metasedimentary enclaves.

Thermobarometry was undertaken using the program Thermocalc 3.2.6 (Powell and Holland, 1988) using the internally consistent dataset of Holland and Powell (1998, data set tcds55, file created 01/01/2004). Results of thermobarometric calculations for igneous mineral crystallisation and metasedimentary enclave metamorphic mineral crystallisation are shown in Table 6.7 (all uncertainties are 1σ). All calculations assumed an $aH_2O=1$, results were also tested for differing aH_2O to confirm the validity of this assumption. Average pressure calculations for sample 06-MNJ-05 yield pressures ranging from 5.2 ± 1.7 kbar at 600°C to 6.2 ± 1.8 kbar at 700°C. Given the peraluminous ms-bi-gt-bearing nature of the granite it is reasonable to assume a crystallisation temperature near the granite solidus of ~650°C (presence of zoned garnet suggests garnet crystallisation below

Table 6.5 - Representative major element mineral composition

Sample	06-MNJ-05	06-MNJ-05	06-MNJ-05	06-MNJ-05	06-MNJ-05	06-MNJ-11	06-MNJ-11	06-MNJ-11	06-MNJ-11	06-MNJ-11	06-MNJ-11	06-MNJ-32	06-MNJ-32	06-MNJ-32	06-MNJ-32
Mineral	Garnet	K-feldspar	Ilmenite	Biotite	Muscovite	Garnet	Garnet	Plagioclase	K-feldspar	Biotite	Muscovite	Garnet	Garnet	Plagioclase	Plagioclase
Analysis Location	Gt Interior		Inc. in Gt			Rim	Core					Rim	Core	Matrix	Rapakivi
SiO_2	36.38	65.27	0.02	37.27	46.65	37.28	36.16	65.23	64.44	36.31	45.35	36.60	35.44	67.27	68.17
TiO_2	0.15	0.01	46.12	1.92	0.66	0.07	0.13	0.01	0.03	2.19	0.79	0.17	0.18	0.02	0.00
Al_2O_3	20.36	18.13	0.00	17.36	31.08	21.05	20.32	21.08	17.97	16.70	32.10	19.78	19.68	20.01	19.89
$FeO_{(T)}$	15.55	0.05	42.58	19.18	3.81	11.94	18.27	0.00	0.01	19.00	3.85	10.29	12.73	0.05	0.04
MnO	24.66	0.00	6.88	1.04	0.13	23.15	22.11	0.00	0.00	1.03	0.06	25.64	29.01	0.00	0.00
MgO	1.35	0.00	0.00	7.34	1.57	0.26	1.55	0.00	0.03	7.57	1.08	0.09	0.29	0.00	0.00
CaO	0.42	0.00	0.01	0.00	0.00	6.82	0.36	2.35	0.00	0.00	0.00	5.62	1.19	1.10	0.35
NaO_2	0.00	0.57	0.00	0.06	0.24	0.00	0.00	10.19	0.43	0.01	0.45	0.00	0.00	11.04	10.71
K_2O	0.00	15.06	0.00	9.68	10.31	0.00	0.00	0.14	15.85	9.49	9.81	0.00	0.00	0.11	0.02
BaO	0.00	0.05	0.00	0.05	0.03	-	-	-	-	-	-	0.00	0.00	0.00	0.03
P_2O_5	0.00	0.00	0.00	0.00	0.00	-	-	-	-	-	-	0.00	0.00	0.00	0.00
Cr_2O_5	-	-	-	-	-	0.00	0.00	0.00	0.00	0.00	0.00	-	-	-	-
Total	98.87	99.14	95.61	93.90	94.47	100.57	98.90	99.00	98.76	92.30	93.48	98.20	98.51	99.60	99.18

Sample	06-MNJ-32	06-MNJ-32	06-MNJ-32	06-MNJ-32	06-MSMJ-1	06-MSMJ-1	06-MSMJ-1	06-MSMJ-4	06-MSMJ-4	06-MSMJ-4	06-MSMJ-6	06-MSMJ-6	06-MSMJ-6	06-MSMJ-6	06-MSMJ-6
Mineral	K-feldspar	K-feldspar	Muscovite	Muscovite	Garnet	Biotite	Muscovite	Garnet	Muscovite	Biotite	Garnet	Garnet	Muscovite	Biotite	Ilmenite
Analysis Location	Matrix	Rapakivi Core	Matrix	Rapakivi rim							Rim	Core			In Garnet
SiO_2	65.05	65.15	47.11	46.41	35.85	35.74	45.35	36.68	46.15	38.06	36.64	36.59	44.99	35.99	0.01
TiO_2	0.01	0.01	0.32	0.50	0.08	2.57	1.03	0.06	0.59	0.83	0.00	0.32	0.57	2.32	51.78
Al_2O_3	17.94	18.08	30.13	28.18	19.58	16.04	31.56	19.71	30.93	16.48	20.34	19.25	32.40	16.96	0.00
$FeO_{(T)}$	0.11	0.00	5.58	6.07	15.09	19.19	4.78	11.91	4.13	14.53	14.18	1.64	3.61	18.27	16.92
MnO	0.00	0.00	0.25	0.51	26.40	1.06	0.01	25.52	0.02	1.01	21.49	32.73	0.07	0.94	29.46
MgO	0.00	0.00	1.84	1.77	0.90	9.63	1.09	1.43	1.18	13.24	1.52	2.09	1.19	9.33	0.01
CaO	0.00	0.00	0.01	0.04	1.81	0.03	0.02	3.70	0.02	0.01	4.17	6.25	0.00	0.01	0.04
NaO_2	0.64	0.48	0.16	0.19	0.00	0.10	0.28	0.00	0.30	0.06	0.00	0.00	0.25	0.10	0.00
K_2O	15.89	16.06	10.20	10.73	0.00	9.47	10.71	0.00	10.56	9.89	0.00	0.00	10.70	9.33	0.00
BaO	0.12	0.15	0.13	0.02	-	-	-	-	-	-	-	-	-	-	-
P_2O_5	0.00	0.00	0.00	0.00	-	-	-	-	-	-	-	-	-	-	-
Cr_2O_5	-	-	-	-	0.00	0.09	0.00	0.01	0.06	0.00	0.06	0.04	0.02	0.08	0.00
Total	99.75	99.93	95.71	94.42	99.73	93.93	94.83	99.02	93.94	94.11	98.40	98.90	93.81	93.32	98.22

Table 6.6 - Trace and Rare Earth element data for garnet from Pt Bell and Pt James intrusions

Sample	06-MNJ-32	06-MNJ-32	06-MNJ-32	06-MNJ-32	06-MNJ-32	06-MNJ-32	06-MNJ-32	06-MNJ-11	06-MNJ-11	06-MNJ-11	06-MNJ-11	06-MNJ-11	06-MNJ-11	06-MNJ-11	06-MNJ-11	06-MNJ-11
Spot	32.gt.1	32.gt.2	32.gt.3	32.gt.4	32.gt.5	32.gt.6	32.gt.7	11.gt.1	11.gt.2	11.gt.3	11.gt.4	11.gt.5	11.gt.6	11.gt.7	11.gt.8	11.gt.9
Y	2664.3	2255.5	2189.6	2426.1	835.8	1348.8	2038.4	278.9	147.6	409.4	415.1	1555.9	65.5	80.1	152.4	1862.9
La	0.1053	0.0026	0.0828	3.7000	0.0566	0.4970	0.0144	0.0132	0.0052	<0.0041	0.0050	0.0041	0.0050	0.0028	<0.0030	0.1228
Ce	0.172	0.018	0.446	17.740	0.091	1.334	0.057	0.047	0.019	0.015	0.007	0.019	0.009	0.011	0.004	0.408
Pr	0.055	0.016	0.041	1.587	0.026	0.234	0.013	0.005	<0.0025	<0.0019	<0.0031	0.004	0.003	0.003	<0.0021	0.064
Nd	0.73	0.42	0.48	7.62	0.35	1.34	0.30	0.05	0.05	0.07	<0.016	0.06	0.05	0.03	0.04	0.49
Sm	5.51	4.25	3.39	6.07	3.36	2.65	3.53	0.42	0.29	0.46	0.23	1.04	0.22	0.29	0.43	1.75
Eu	0.44	0.30	0.30	0.52	0.40	0.32	0.34	0.16	0.14	0.17	0.08	0.27	0.12	0.10	0.13	0.45
Gd	37.02	31.15	25.33	29.15	27.22	17.95	28.26	3.21	2.77	4.64	3.17	15.06	2.26	2.51	4.02	21.79
Dy	286.59	244.82	205.19	189.46	82	144.27	220.91	31.96	17.61	47.14	50.39	189.14	8.95	9.92	21.1	233.38
Er	471.0	408.1	367.2	203.8	55.1	214.0	339.5	31.9	13.2	46.8	94.7	197.1	3.4	4.0	12.5	193.0
Yb	1268.7	1046.2	1020.1	358.2	87.3	521.2	876.1	42.5	14.0	61.1	162.4	254.3	1.9	2.7	13.5	214.0
Lu	216.8	178.6	178.7	49.4	12.4	85.2	150.7	5.1	1.6	7.8	27.3	32.9	0.2	0.2	1.7	24.8

~700°C, Dahlquist et al., 2007). Pressure calculations at this temperature give a pressure of 5.7 ± 1.8 kbar. Average temperature calculations yield a temperature range of 625 ± 14 - 662 ± 14°C for pressures from 4-8 Kbar. Average pressure calculations for sample06-MNJ-11 yield a pressure of 5.9 ± 0.9 kbar at 650°C. This pressure is effectively identical to that obtained from 06-MNJ-05. P-T conditions calculated from metasedimentary enclave samples 06-MJMS-1, 06-MJMS-4 and 06-MJMS-6 are shown in Table 6.7. In each sample, P-T constraints are interpreted to represent peak metamorphism as mineral assemblages do not appear to have undergone retrogression (Section 6.3). Sample 06-MJMS-1 yields conditions of 4.1 ± 1.0 kbar and 529 ± 28°C. Calculations for sample 06-MJMS-4 yield conditions of 5.1 ± 0.9 kbar and 614 ± 26°C. Calculations for sample 06-MJMS-6 yield results of 7.1 ± 1.0 kbar and 650 ± 27°C.

6.6 Discussion

6.6.1 Age of the Munjeela Suite

The set of intrusions collectively termed the Munjeela Suite are muscovite-biotite-garnet-bearing peraluminous granites with rare metasedimentary enclaves. U-Pb zircon ages obtained in this study are interpreted to be the age of granite crystallisation based upon concentric growth zoning evident in zircon grains yielding ages consistent with the mean age of the population. Metamictisation of zircon grains, most likely due to their U-rich nature, creates some age spread about the mean and results in excessive Pb-loss and age disturbance in some grains. The ages obtained in this study are 1591 ± 11 Ma and 1577 ± 9 Ma for the Sinclair/Bell intrusion and 1580 ± 15 Ma for the Pt James intrusion. These ages are all within error and support a coeval genesis of the Sinclair/Bell and Pt James intrusions. An age range of *c.* 1590-1580 Ma is suggested for the crystallisation age of the Munjeela Suite.

6.6.2 Petrogenesis of the Munjeela Suite

Although yielding indistinguishable crystallisation ages, the Sinclair/Bell and Pt James intrusions vary slightly in whole-rock chemistry and mineralogy. The Sinclair/Bell intrusion is highly peraluminous with SiO_2 values in the range of 71.7-

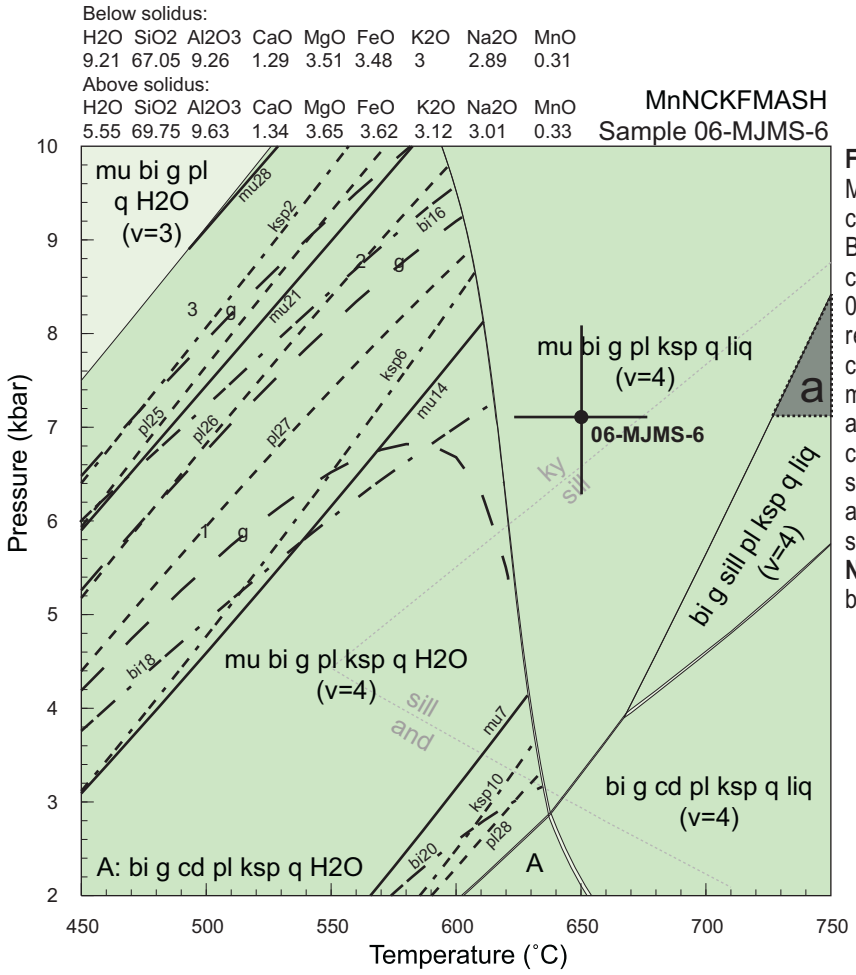

Figure 6.11 - P-T pseudosection in MnNCKFMASH space for bulk composition of sample 06-MJMS-6. Black dot with 1 error bars represents calculated P-T conditions for sample 06-MJMS-6. Gray-shaded field (a) represents minimum melt-formation conditions for granite based upon muscovite-dehydration melting reaction and pressure constraints for granite crystallisation and 06-MJMS-6. Bold solid and dashed lines represent modal abundance of mineral growth below the solidus.
Note: P-T pseudosection constructed by D. Kelsey.

74.7 wt%. In comparison the Pt James intrusion has a SiO_2 range of 74.7-75.7 wt%, is slightly less peraluminous (Figure 6.7), contains rapakivi feldspar textures and porphyritic phases. In addition the Pt James intrusion has elevated HREE levels as highlighted in Figure 6.7. This section addresses the petrogenesis of the granite and focuses on the mineralogical and chemical differences between the two Munjeela Suite intrusions to assess a co-genetic link.

6.6.2.1 Formation of rapakivi textures of the Pt James intrusion

The primary mineralogical difference between the two intrusions is the presence of rapakivi feldspar textures in the Pt James intrusion. Rapakivi feldspar textures represent a change in chemical composition or intensive physical parameters of crystallising granites such that plagioclase becomes stable at the expense of K-feldspar and quartz (Ramo and Haapala, 1995; Eklund and Shebanov, 1999; Haapala and Ramo, 1999). Two concepts are widely purported to explain the phase-stability change: an influx and mixing of a more mafic magma phase or near-isothermal decompression (Hibbard, 1981; Nekvasil, 1991; Stimac and Wark, 1992; Ramo and Haapala, 1995; Eklund and Shebanov, 1999). Given the leucogranitic composition of the Pt James intrusion and lack of associated mafic and intermediate magmas it appears unlikely that a composition change by mixing with a more mafic magma is the cause of plagioclase mantling around orthoclase.

A near-isothermal decompression mechanism for rapakivi texture formation is also consistent with other mineralogical textures from the Pt James intrusion. Porphyritic granite phases in which phenocrysts and matrix have similar mineralogy are suggestive of a change in physical conditions during crystallisation of the Pt James intrusion. Plagioclase mantles and large, zoned plagioclase crystals are observed to be fluid-inclusion rich in thin-section, particularly when compared to the inclusion poor K-feldspar cores of the rapakivi texture. The concentrated nature of fluid inclusions in rapakivi feldspar rims is consistent with a change

Table 6.7 - Thermobarometry results for selected granite and metasedimentary enclave samples

Calculations	Average-P Calculations				Average-T Calculations				Average P-T Calculations				
Sample	Press. (kbars)	1 s.d. (kbars)	*Temp. (°C)*	Sig. fit	*Press. (kbars)*	Temp. (°C)	1 s.d. (°C)	Sig. fit	Press. (kbars)	1 s.d. (kbars)	Temp. (°C)	1 s.d. (°C)	Sig. fit
06-MJMS-1	4.1	1.0	*530*	0.4	-	-	-	-	4.1	1.0	529	28	0.58
06-MJMS-4	5.4	0.5	*625*	1.2	*5.0*	609	14	1.3	5.1	0.9	614	26	1.32
06-MJMS-6	7.1	0.6	*650*	1.3	*7.0*	645	17	1.4	7.1	1.0	650	27	1.42
06-MNJ-05	5.7	1.8	*650*	0.7	*5.2*	639	14	0.8	-	-	-	-	-
06-MNJ-11	5.9	0.8	*650*	1.1	*6.0*	630	14	1	-	-	-	-	-

*Italics represent user input data

in physical conditions of crystallisation (Eklund and Shebanov, 1999).

6.6.2.2 Source of HREE enrichment and Sm/Nd disequilibrium in Pt James intrusion

The Pt James intrusion displays a number of geochemical differences compared to the Sinclair/Bell intrusion. This includes a slightly lower degree of peraluminousity, HREE-enrichment and garnet displaying significantly higher Mn-content. In addition, and correlated to the HREE-enrichment (Figure 6.7d), is the high-degree of fractionation between Sm and Nd indicated by anomalously high $^{147}Sm/^{144}Nd$ ratios (Table 6.4).

Fractionation of Sm and Nd is recognised to occur during crustal anatexis and has often been attributed to the role of REE-rich accessory mineral phases (eg. zircon, monazite and apatite) in melt generation (Watson and Harrison, 1983; Montel, 1993; Wolf and London, 1995; Ayres and Harris, 1997). Ayres and Harris (1997) attribute primary control of LREE and MREE to apatite and monazite and HREE to apatite and garnet. Their attempts to model elevated Sm/Nd ratios in Himalayan leucogranites using the contribution of apatite REE budget in the melt, failed to account for Sm/Nd ratios above 0.31. Sm/Nd ratios in the Pt James intrusion range from 0.29-0.52, with the majority above 0.31. This would seem to preclude apatite as a controlling phase in the observed Sm-Nd fractionation. This premise is further supported by the lack of correlation between Sm/Nd and low to below detection limit P_2O_5 concentrations. Removal of monazite from the melt, although potentially explaining low P_2O_5 concentrations, does not sufficiently fractionate Nd and Sm to create the observed high Sm/Nd values (Montel, 1993). The most efficient mechanism for creating high Sm/Nd ratios in the Pt James granite appears to be incorporation of restitic garnet into a melt that is otherwise relatively REE-poor. Figure 7.7g and 7.7h highlight the positive correlation of Sm/Nd, Sm and $La_{(n)}/Yb_{(n)}$ with Y.These trends are consistent with garnet controlling the distribution of REE element within the Pt James intrusion (typical garnet partition coefficients (K_d): Y = 35.0, Ce=0.35, Nd = 0.530, Sm = 2.66, Rollinson, 1993, and references therein). In contrast, REE distribution controlled by apatite would display positive correlations of Sm/Nd, Nd and Ce with Y (typical apatite partition coefficients (K_d): Y = 40.0, Ce=34.7, Nd = 57.1, Sm = 62.8, Rollinson, 1993, and references therein).

The interpretation of restitic garnet inheritance in the Pt James intrusion is consistent with petrological and major and trace element characteristics of the garnet from this intrusion. Garnet typically occurs as fragments with the appearance of dissolution of once larger grains (Figure 6.4d). In sample 06-MNJ-32 garnet is significantly enriched in spessartine content (Mn) and depleted in almandine (Fe) compared to that observed in the Sinclair/Bell intrusion. Given the Pt James intrusion has a slightly higher $Fe_2O_{3(T)}$ content and similar MnO content to the Sinclair/Bell intrusion, this is not attributable to bulk granite chemistry. REE concentrations from the core of garnet in sample 06-MNJ-32 display marked Sm, MREE and HREE enrichment compared to garnet from sample 06-MNJ-11 (Figure 6.9). This difference (up to 2 orders of magnitude) is consistent with garnet controlling Sm/Nd and HREE chemistry in the Pt James intrusion. REE distribution coefficients (D) between garnet and granite bulk chemistry (assumed to represent melt composition) are plotted in Figure 6.9d. Distribution coefficients in the garnet core have been calculated using the 06-MNJ-11 bulk composition. Experimental distribution coefficient data of Rubatto and Hermann (2007) is displayed for comparison in Figure 6.9d. Rubatto and Hermann (2007) used experimental conditions of

20 kbar with temperature runs between 800-1000°C. Increasing pressure tends to act in the negative sense to increasing temperature (Rollinson, 1993, and references therein), such that at 20 kbar the 1000°C experiment is the most appropriate for mica-dehydration melting reaction generated granite. Although limited by the approximated melt composition, D values for the garnet core are not typical of previously calculated values (Figure 6.9, Rubatto and Hermann, 2007). This suggests the garnet core did not grow in equilibrium with the surrounding bulk granite and instead represents restitic, metamorphic garnet. D values from the Ca-rich rim of the garnet are more typical of known D values and support the Ca-rich rim crystallising in equilibrium with the bulk composition of the host granite. The differences in observed major and RE element chemistry are consistent with garnet within the Pt James intrusion being restitic, metamorphic garnet while garnet within the Sinclair/Bell intrusion is magmatic in origin. The Ca-rich rim of the mapped garnet from 06-MNJ-32 (Figure 6.10), may however represent igneous garnet crystallisation.

6.6.2.3 Coeval or cogenetic origin of the Pt James intrusion?

Mineralogy and geochemistry of the Sinclair/Bell intrusion is typical of highly peraluminous, muscovite-biotite-bearing granite that occurs in many collisional orogenic belts worldwide (Ayres and Harris, 1997; Patino Douce and Harris, 1998; Barbarin, 1999; Patino Douce, 1999; Nabelek and Liu, 2004; Dahlquist et al., 2007). Highly peraluminous granites containing muscovite and biotite ± garnet, such as the Sinclair/Bell intrusion, are typically assigned a wholly crustally-derived origin generated by partial melting of metasedimentary lithologies (Barbarin, 1996; Ayres and Harris, 1997; Patino Douce and Harris, 1998; Nabelek and Liu, 2004). The alternative and less common mode of petrogenesis for a highly peraluminous granite is generation as an end product of fractional crystallisation/assimilation of a less peraluminous or metaluminous granitoid pluton (Barbarin, 1996, and references therein). Given the slightly less peraluminous character and inherited garnet of the Pt James pluton, generation through fractional crystallisation should also be considered.

The potential parent suite for a fractional crystallisation petrogenesis of the Pt James intrusion is the coeval, voluminous 1595-1575 Ma Hiltaba Suite which dominates the central and eastern Gawler Craton (Flint, 1993; Johnson and Cross, 1995; Stewart and Foden, 2001; Jagodzinski, 2005; Jagodzinski et al., 2006; Fanning et al., 2007). Although the Hiltaba Suite is temporally equivalent to the Munjeela Suite, the Pt James intrusion does not appear to be spatially related to any Hiltaba Suite intrusives (Figures 6.1 and 6.2, Fairclough et al., 2004). However, this may simply be due to current exposure levels in the region. Trace element data for the nearest Hiltaba Suite plutons (~150km W and NW) is plotted in Figure 6.7c. This demonstrates that even for the most felsic Hiltaba plutons (2 samples in field > 75 wt% SiO_2, outlier sample has 77.73 wt% SiO_2), the Hiltaba Suite is too trace and RE element-enriched to be a parent magma for the Pt James intrusion. In support of a cogenetic petrogenesis for the Sinclair/Bell and Pt James intrusions are the major and trace element composition and Nd-isotope characteristics. The major element composition of the Pt James intrusion typically falls upon the extension of fractional crystallisation trends defined by major element data for the Sinclair/Bell intrusion (Figure 6.7). The notable exception to this is $Fe_2O_{3(T)}$, which is slightly elevated in the Pt James intrusion. $\varepsilon_{Nd}(T)$ values for the Sinclair/Bell and Pt James intrusions are relatively juvenile compared to the pre-existing Gawler Craton lithologies (Figure 6.8), and are consistent with derivation from metasedimentary material such as that preserved in the enclaves within the granite (Figure 6.8, Section 6.6.3). The Sinclair/Bell and Pt James intrusion trace element patterns (with the exception of Y and HREE discussed above) are also highly similar and support a cogenetic petrogenesis for the two intrusions.

6.6.2.4 Petrogenesis of the Munjeela Suite

The Sinclair/Bell and Pt James intrusions are interpreted to be cogenetic based upon similarities in major and trace element geochemical criteria. The incorporation of xenocrystic garnet in the Pt James intrusion has altered the granite REE chemistry partially disguising the characteristics of the primary melt generated to form the Munjeela Suite. In the Sinclair/Bell intrusion relatively flat REE patterns with slight LREE-enrichment and negative Eu anomalies (Figure 6.7) are consistent with melt generation with a plagioclase-dominated

restite (as are elevated Rb/Sr ratios of the Munjeela Granite, eg. Harris and Inger, 1992; Prince et al., 2001). The lack of plagioclase melting at source suggests melt reactions were vapour-absent as significant plagioclase (+quartz) melting occurs in the presence of H_2O at similar P-T conditions to muscovite dehydration melting (eg. Conrad et al., 1988; Harris and Inger, 1992; Patino Douce and Harris, 1998). The mineralogy (ms-bi-gt-bearing) and major and RE element chemistry (highly peraluminous, high Rb/Sr, high alkali to ferromagnesian element ratios) of the Munjeela Suite is consistent with melt generation occurring through muscovite-dehydration melt reactions (eg. Harris and Inger, 1992; Nabelek et al., 1992; Patino Douce and Harris, 1998; Patino Douce, 1999; Nabelek and Liu, 2004).

Ms-bi-gt-bearing granites formed through vapour-absent, muscovite-dehydration melting are thought to be sourced from pelitic protoliths which contain muscovite as the dominant mica at near-solidus P-T conditions (Inger and Harris, 1993; Patino Douce and Harris, 1998). Given the similarity in isotopic characteristics, and Mn-rich composition of inherited garnet in the Pt James intrusion, it is reasonable to suggest that the Munjeela Suite is derived from melting of the same, or a similar, sedimentary sequence as represented by metasedimentary enclaves found at Pt Sinclair (Section 6.6.3). The similarity in granite protolith and metasedimentary enclaves allows the P-T pseudosection constructed for the bulk composition of sample 06MJMS-06 (Figure 6.11) to be applied to melting conditions of the granite protolith. The calculated pseudosection predicts that muscovite-dehydration melting occurs from 670°C at 4 kbar to 750°C at 8.4 kbar. Mineral equilibria calculations were not conducted for higher T conditions. The calculated granite crystallisation conditions of ~ 6 kbar at 650°C (Sinclair/Bell intrusion) and pressure of ~7 kbar obtained from P-T calculations for 06-MJMS-06 place minimum depth constraints on granite melt generation and restrict the apparent field of granite generation to greater than ~730°C and 7 kbar. This minimum temperature of granite generation is consistent with the temperature constraints of Harris et al. (1995) for Himalayan leucogranite generation.

6.6.3 Age and Significance of metasedimentary enclaves

Metasedimentary enclaves within the Munjeela Suite at Pt Sinclair are of two primary lithologies: Qtz-Ms-Bi (±Gt) psammo-pelites and Ms-Bi-Gt pelites. These two lithologies also have distinct Nd-isotope and detrital zircon characteristics. The psammo-pelitic lithologies have $\varepsilon_{Nd}(T)$ values of -0.1 and -0.6 while the pelitic lithologies have slightly more evolved $\varepsilon_{Nd}(T)$ values of -1.5 and -3.4. This difference in isotope signatures is consistent with the detrital zircon spectra obtained. Psammo-pelitic samples, MNJ-MS-1 and MNJ-MS-3, have maximum depositional ages of 1623.4 ± 3.6 Ma and 1638 ± 33 Ma. The majority of analyses for these two samples fall within the age range 1630-1730 Ma. By contrast the analysed pelitic sample, 06-MJMS-6, has an older maximum depositional age of 1678.7 ± 7 Ma with the majority of analyses falling between 1680 and 1770 Ma with a second peak at ~1820 Ma. The combination of more evolved $\varepsilon_{Nd}(T)$ values with older detrital zircon ages indicates differing provenance lithologies between the pelitic and psammo-pelitic lithologies and potentially a different age of deposition.

The obtained detrital zircon age spectra for both the pelitic and psammo-pelitic lithologies are consistent with derivation from the Gawler Craton. In the case of 06-MJMS-1 detritus in the age range of 1630 - 1650 Ma is broadly consistent with derivation from the nearby Nuyts Volcanics (1630 Ma) and volcanic lithologies intercalated with the Tarcoola Formation in the central Gawler Craton (Figure 6.1, Cowley and Martin, 1991; Fanning et al., 2007). The detritus in sample 06-MJMS-3 is consistent with derivation largely from Tunkillia Suite intrusives (1690-1670 Ma, Figure 6.1, *Chapter 5*, Ferris and Schwarz, 2004; Fanning et al., 2007), intercalated volcanics of the Labyrinth Formation (*c.* 1715 Ma, Fanning et al., 2007) and magmatic suites of the Kimban Orogeny (1730-1700 Ma, Fanning et al., 2007). The detritus in sample 06-MJMS-6 in the age range 1680-1770 Ma is consistent with derivation from the Tunkillia Suite, Labyrinth formation volcanics, Kimban Orogeny intrusives (Moody and Middlecamp Suites) and *c.* 1770 volcanics of the Wallaroo Group (Fanning et al., 2007). The age peak at *c.* 1820 Ma does not have any apparent source rocks within the Gawler Craton but is a common timeline within pre-Kimban Orogeny metasedimentary lithologies of the

northern Gawler Craton (Payne et al., 2006a) and eastern Gawler Craton (Szpunar et al., 2006). Given the timing of the Kimban Orogeny which exhumed metasedimentary lithologies older than 1730 Ma, recycling of older sedimentary packages is an acceptable source for the detritus. $\varepsilon_{Nd}(T)$ values for the pelitic samples are consistent with derivation from the Gawler Craton with characterised potential source lithologies yielding $\varepsilon_{Nd}(T)$ values of +0.1 - -2.3 and -1.4 - -7.6 for previously characterised Kimban Orogeny and Tunkillia Suite intrusives, respectively (Figure 6.9). Nd-isotope data has not been obtained for the younger volcanic suites thought to be represented in the psammo-pelitic samples.

The time frame for deposition of the protolith sedimentary lithologies ranges from *c.* 1680 -1590 Ma for 06-MJMS-6 to *c.* 1625 -1590 Ma for 06-MJMS-1. The enclaves represent one or more sedimentary sequences which do not otherwise outcrop and have not been characterised from drill core intersection. The revised interpretation of regional TMI data in Figure 6.2 suggests the Sinclair/Bell and Rockhole intrusions are surrounded by, and presumably intrude, deformed metasedimentary lithologies. These interpreted metasedimentary lithologies potentially represent the source of metasedimentary enclaves found within the granite. The only known temporal correlative with the metasedimentary enclaves within the Gawler Craton is the *c.* 1650 Ma Tarcoola Formation (Cowley and Martin, 1991; Fanning et al., 2007). Limited Nd-isotope data for Tarcoola Formation lithologies reports similar $\varepsilon_{Nd}(T)$ values of -1.4 and -2.4 (Turner et al., 1993), roughly correlating with the pelitic enclave samples. This Nd-isotope data is consistent with a similar provenance for the Tarcoola Formation and metasedimentary enclaves from Pt Sinclair. A basal conglomerate of the Tarcoola Formation yields detrital zircon ages in the range ~1740-1700 Ma (Budd, 2006).

6.6.4 Early Mesoproterozoic metamorphism and crustal thickening on the Gawler Craton

Recent work has suggested the Gawler Range Volcanics and Hiltaba Suite magmatism did not occur in an anorogenic setting as previously thought (Holm, 2004; Skirrow et al., 2006; Direen and Lyons, in press; Hand et al., in press). This is in contrast to previous work (Haynes et al., 1995) suggesting an anorogenic or extensional setting for Hiltaba Suite magmatism. As ms-bi-gt granites generated by muscovite-dehydration melting are typically restricted to medium- to high-grade metamorphic belts within orogens (Inger and Harris, 1993; Patino Douce and Harris, 1998; Harris et al., 2000; Nabelek and Liu, 2004), the formation of the Munjeela Suite is also circumstantial evidence for orogenesis during the early Mesoproterozoic.

As discussed in Section 6.6.2.5, granite emplacement occurred at 6 kbar, equivalent to a depth of approximately 18-20 km. The source of metasedimentary enclaves is likely to be from a similar or greater depth than the depth of granite intrusion. This suggests the pressure of ~4.1 kbar calculated for sample 06-MJMS-1 does not represent an accurate pressure for mineral growth. Given the small crystal size in the sample (garnet <300 μm) it is possible that the metasedimentary enclave, when entrained into the host granite, underwent thermal perturbation of sufficient duration to enable significant major element diffusion. Such mineral chemistry disruption would result in in-accurate thermobarometry calculations such as observed for pressure calculations. Enclave 06-MJMS-6 yields pressures of 7 kbar at ~650°C which is consistent with a source from greater structural depth than the emplacement depth of the granite. Granite emplacement depth and enclave P-T constraints require burial of the metasedimentary protolith to greater than 20 km depth within the timeframe *c.* 1625-1590 Ma. Possible mechanisms for burial are stratigraphic burial (eg. 15-20 km deep Belt-Purcell basin, Harrison, 1972, Petrel sub-basin, Baxter, 1998) combined with magmatic loading or crustal thickening during orogenesis.

The intrusion of the Munjeela Suite into the 1615-1608 Ma St Peter Suite east of the Koonibba Shear Zone indicates the presence of the metasedimentary protolith beneath the St Peter Suite. This implies the St Peter Suite, at least in part, intruded through and was emplaced above the protolith to the Munjeela Suite. Magmatic loading from the St Peter Suite may provide some burial of the metasedimentary protolith, although the thickness of the St Peter Suite and subsequent magnitude of magmatic loading are currently unknown. Typical estimates of maximum vertical thickness of intrusive plutons range from 5-10 km (Vigneresse, 2004, and references therein) requiring

a basin depth of 10-15 km to reach burial depths of ~20 km. For melting to occur through a simple stratigraphic burial mechanism, additional basin depth is required to reach P-T conditions suitable for melt generation (and sufficient fertile protolith material at melt conditions). As melting of the Munjeela Suite source protolith did not occur synchronously with the thermal pulse and magmatic loading of St Peter Suite magmatism, it would seem unlikely for melting to occur approximately 10-20 Myr afterwards through purely stratigraphic loading .

Evidence for two tectonic foliations within the metasedimentary enclaves suggests deformation occurred synchronously with metamorphic mineral growth. Folded inclusion trails within garnet (ilmenite, magnetite, chlorite, Figures 6.4b and 6.10) are overprinted by the matrix foliation which wraps around garnet porphyrblasts. The interpreted metasedimentary package in TMI data (Figure 6.12) also preserves evidence of two deformation events. Regional scale fold axes appear to be refolded by a later folding event, consistent with two deformation events (Figure 6.12). The petrographic correlation of deformation with metamorphism of up to 7kbar and 650°C strongly supports burial of the granite protolith during deformation. Given the presence of P-T conditions of 7 kbar at 650°C it appears most likely deformation was compressional which is consistent with the P-T conditions falling at or above the kyanite-sillimanite transition (Figure 6.11), generally considered representative of crustal thickening during orogeneis (Spear, 1993). Such a tectonic setting is consistent with the typical setting of muscovite-dehydration derived melts elsewhere (Inger and Harris, 1993; Patino Douce and Harris, 1998; Barbarin, 1999; Nabelek and Liu, 2004).

Evidence obtained within this study suggests orogenic crustal thickening occurred during the period 1625-1590 Ma. This is the first evidence for significant crustal thickening in the Gawler Craton during this time period. Previously obtained metamorphic constraints have only provided low-P, high-T metamorphic conditions (eg. 4.7 kbar and 765°C, Forbes and Giles, 2007) in the Mt Woods region (Figure 6.1).

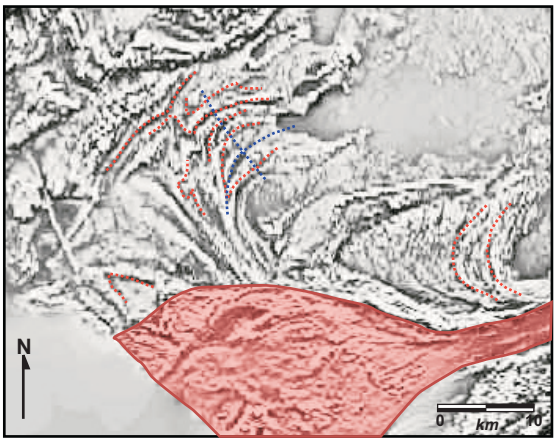

Figure 6.12 - Total Magnetic Intensity map of the region surrounding the Sinclair/Bell intrusion (red shading) with fold trace and axes marked. Red dashed line represents structural traces and blue dashed lines represent interpreted fold axes showing refolded folds.

6.7 Conclusions

New age data for the studied Munjeela Suite intrusions indicates they formed at *c.* 1590-1580 Ma, co-eval with the GRV/Hiltaba magmatic event. Geochemical and isotopic constraints indicate they were generated through muscovite dehydration melting reactions of a metasedimentary source similar to that preserved within enclaves in the Sinclair/Bell intrusion. The Pt James intrusion preserves evidence for syn-crystallisation, sub-isothermal decompression as indicated by the presence of rapakivi feldspar textures. The presence of xenocrystic garnet within the Pt James intrusion is demonstrated to account for HREE enrichment and Sm-Nd disequilibrium within this granite.

Metasedimentary enclaves within the Munjeela Suite granite provide evidence for a previously uncharacterised sedimentary sequence on the Gawler Craton deposited between approximately 1680 Ma and 1590 Ma. The apparent youngest sedimentary sample (max. dep. *c.* 1625 Ma) constrains the timing of metamorphism and deformation preserved within these enclaves to the period *c.* 1625-1590 Ma. Generation of the ms-bi-gt-bearing Munjeela Suite and recorded P-T conditions from metasedimentary enclaves provide the best evidence to date of significant crustal thickening and deformation within this time period for the Gawler Craton. This provides further evidence the voluminous Hiltaba Suite magmatism did not occur in an anorogenic setting.

References

Allen, S.R. and McPhie, J., 2002. The Eucarro Rhyolite, Gawler Range Volcanics, South Australia: A > 675 km^3, compositionally zoned lava of Mesoproterozoic age. Geological Society of America Bulletin, 114(12): 1592-1609.

Allen, S.R., Simpson, C.J., McPhie, J. and Daly, S.J., 2003. Stratigraphy, distribution and geochemistry of widespread felsic volcanic units in the Mesoproterozoic Gawler Range Volcanics, South Australia. Australian Journal of Earth Sciences, 50(1): 97-112.

Andersen, T., 2002. Correction of common lead in U-Pb analyses that do not report ^{204}Pb. Chemical Geology, 192(1-2): 59-79.

Ayres, M. and Harris, N., 1997. REE fractionation and Nd-isotope disequilibrium during crustal anatexis: Constraints from Himalayan leucogranites. Chemical Geology, 139(1-4): 249-269.

Barbarin, B., 1996. Genesis of the two main types of peraluminous granitoids. Geology, 24(4): 295-298.

Barbarin, B., 1999. A review of the relationships between granitoid types, their origins and their geodynamic environments. Lithos, 46(3): 605-626.

Baxter, K., 1998. The role of small-scale extensional faulting in the evolution of basin geometries. An example from the late Palaeozoic Petrel Sub-basin, northwest Australia. Tectonophysics 287 (1-4): 21-41.

Betts, P.G., Giles, D., Lister, G.S. and Frick, L.R., 2002. Evolution of the Australian lithosphere. Australian Journal of Earth Sciences, 49(4): 661-695.

Budd, A., 2006. The Tarcoola Goldfield of the Central Gawler Gold Province, and the Hiltaba association Granites, Gawler Craton, South Australia. Ph.D. Thesis, Australian National University, 365 pp.

Budd, A.R. and Fraser, G.L., 2004. Geological relationships and Ar-40/Ar-39 age constraints on gold mineralisation at Tarcoola, central Gawler gold province, South Australia. Australian Journal of Earth Sciences, 51(5): 685-699.

Coggon, R. and Holland, T.J.B., 2002. Mixing properties of phengitic micas and revised garnet-phengite thermobarometers. Journal of Metamorphic Geology, 20(7): 683-696.

Conor, C.H.H., 1995. An interpretation of the geology of the Maitland and Wallaroo 1:100 000 sheet areas. Env 8886, Department of Primary Industries and Resources South Australia, Adelaide.

Conrad, W.K., Nicholls, I.A. and Wall, V.J., 1988. Water-Saturated and Water-Undersaturated Melting of Metaluminous and Peraluminous Crustal Compositions at 10 Kb - Evidence for the Origin of Silicic Magmas in the Taupo Volcanic Zone, New-Zealand, and Other Occurrences. Journal of Petrology, 29(4): 765-803.

Cowley, W.M., Conor, C.H.H. and Zang, W., 2003. New and revised Proterozoic stratigraphic units on northern Yorke Peninsula. MESA Journal, 29: 46-58.

Cowley, W.M. and Martin, A.R., 1991. Kingoonya, 1:250 000 Geological Map Explanatory Notes, Department of Mines and Energy, South Australia, Adelaide.

Creaser, R.A., 1995. Neodymium Isotopic Constraints for the Origin of Mesoproterozoic Felsic Magmatism, Gawler-Craton, South Australia. Canadian Journal of Earth Sciences, 32(4): 460-471.

Creaser, R.A. and White, A.J.R., 1991. Yardea Dacite - Large-Volume, High-Temperature Felsic Volcanism from the Middle Proterozoic of South-Australia. Geology, 19(1): 48-51.

Dahlquist, J.A., Galindo, C., Pankhurst, R.J., Rapela, C.W., Alasino, P.H., Saavedra, J. and Fanning, C.M., 2007. Magmatic evolution of the Penon Rosado granite: Petrogenesis of garnet-bearing granitoids. Lithos, 95(3-4): 177-207.

Daly, S.J. and Fanning, C.M., 1993. Archaean. In: J.F. Drexel, W.V. Preiss and A.J. Parker (Editors), The geology of South Australia - The Precambrian, Bulletin 54. Mines and Energy, South Australia, Adelaide, pp. 242.

Daly, S.J., Fanning, C.M. and Fairclough, M.C., 1998. Tectonic evolution and exploration potential of the Gawler Craton, South Australia. In: I. Hodgson and B. Hince (Editors), Geology and mineral potential of major Australian mineral provinces. AGSO Journal of Australian Geology and Geophysics, pp. 145-168.

Direen, N.G. and Lyons, P., in press. Crustal setting of iron-oxide Cu-Au mineral systems of the Olympic dam region, South Australia: insights from potential fields data. Economic Geology.

Dutch, R., Hand, M. and Kinny, P.D., 2006. On the Kimban overprint: New geochronological constraints on high-grade metamorphism from Eyre Peninsula, southern Gawler Craton. In: D. Denham (Editor), Australian Earth Sciences Convention 2006. Geological Society of Australia, Melbourne.

Eklund, O. and Shebanov, A.D., 1999. The origin of rapakivi texture by sub-isothermal decompression. Precambrian Research, 95: 129-146.

England, P., Lefort, P., Molnar, P. and Pecher, A., 1992. Heat-Sources for Tertiary Metamorphism and Anatexis in the Annapurna-Manaslu Region Central Nepal.

Journal of Geophysical Research-Solid Earth, 97(B2): 2107-2128.

Fairclough, M.C., Schwarz, M. and Ferris, G.J., 2004. Interpreted crystalline basement geology of the Gawler Craton, South Australia. In: J. Mcphie and P. McGoldrick (Editors), 17th Australian Geological Conference. Geological Society of Australia, Hobart.

Fanning, C.M., Reid, A.J. and Teale, G.S., 2007. A geochronological framework for the Gawler Craton, South Australia. Bulletin 55, Geological Survey, Primary Industries and Resources South Australia.

Ferris, G.J. and Schwarz, M., 2004. Definition of the Tunkillia Suite, western Gawler Craton. MESA Journal, 34: 32-41.

Flint, R.B., 1993. Mesoproterozoic. In: J.F. Drexel, W.V. Preiss and A.J. Parker (Editors), The geology of South Australia - The Precambrian, Bulletin 54. Mines and Energy, South Australia, Adelaide, pp. 242.

Flint, R.B., Rankin, L.R. and Fanning, C.M., 1990. Definition: the Palaeoproterozoic St. Peter Suite of the western Gawler Craton. Quarterly Geological Notes, Geological Survey of South Australia.

Forbes, C.J. and Giles, D., 2007. Metamorphic analysis across the Southern Overthrust in the Prominent Hill region, Gawler Craton. In: A. Collins (Editor), Deformation in the Desert - SGTSG 2007. Geological Society of Australia Abstracts.

Foster, D.A. and Ehlers, K., 1998. Ar-40-Ar-39 thermochronology of the southern Gawler craton, Australia: Implications for Mesoproterozoic and Neoproterozoic tectonics of east Gondwana and Rodinia. Journal of Geophysical Research-Solid Earth, 103(B5): 10177-10193.

Fraser, G.L. and Lyons, P., 2006. Timing of Mesoproterozoic tectonic activity in the northwestern Gawler Craton constrained by $^{40}Ar/^{39}Ar$ geochronology. Precambrian Research, 151: 160-184.

Garner, A. and McPhie, J., 1999. Partially melted lithic megablocks in the Yardea Dacite, Gawler Range Volcanics, Australia: implications for eruption and emplacement mechanisms. Bulletin of Volcanology, 61(6): 396-410.

Haapala, I. and Ramo, O.T., 1999. Rapakivi granites and related rocks: an introduction. Precambrian Research, 95(1-2): 1-7.

Hand, M., Mawby, J., Kinny, P. and Foden, J., 1999. U-Pb ages from the Harts Range, central Australia: evidence for early Ordovician extension and constraints on Carboniferous metamorphism. Journal of the Geological Society, 156: 715-730.

Hand, M., Reid, A. and Jagodzinski, E.A., in press. Tectonic framework and evolution of the Gawler Craton, Southern Australia. Economic Geology.

Harris, N., Ayres, M. and Massey, J., 1995. Geochemistry of granitic melts produced during the incongruent melting of muscovite: implications for the extraction of Himalayan leucogranite magmas. Journal of Geophysical Research, 100: 15767-15777.

Harris, N., Vance, D. and Ayres, M., 2000. From sediment to granite: timescales of anatexis in the upper crust. Chemical Geology, 162(2): 155-167.

Harris, N.B.W. and Inger, S., 1992. Trace-Element Modeling of Pelite-Derived Granites. Contributions to Mineralogy and Petrology, 110(1): 46-56.

Harrison, J.E., 1972. Precambrian Belt basin of the northwestern United States, its geometry, sedimentation, and copper occurrences. Geological Society of America Bulletin 83, 1215–1240.

Haynes, D.W., Cross, K.C., Bills, R.T. and Reed, M.H., 1995. Olympic Dam ore genesis: a fluid mixing model. Economic Geology, 90, 281-307.

Hibbard, M.J., 1981. The Magma Mixing Origin of Mantled Feldspars. Contributions to Mineralogy and Petrology, 76(2): 158-170.

Holland, T. and Powell, R., 1992. Plagioclase Feldspars - Activity-Composition Relations Based Upon Darken Quadratic Formalism and Landau Theory. American Mineralogist, 77(1-2): 53-61.

Holland, T.J.B. and Powell, R., 1998. An internally consistent thermodynamic data set for phases of petrological interest. Journal of Metamorphic Geology, 16(3): 309-343.

Holm, O., 2004. New geochronology of the Mount Woods Inlier and Central Gawler Gold Province, Gawler Craton - State of Play Conference, abstract volume. RB 2004/18, Primary Industries and Resources South Australia, Adelaide.

Hopper, D.J., 2001. Crustal Evolution of Paleo- to Mesoproterozoic rocks in the Peake and Denison Ranges, South Australia. PhD Thesis, University of Queensland, Brisbane, 216 pp.

Howard, K.E., Reid, A.J., Hand, M., Barovich, K.M. and Belousova, E.A., 2007. Does the Kalinjala Shear Zone represent a palaeo-suture zone? Implications for distribution of styles of Mesoproterozoic mineralisation in the Gawler Craton. Minerals and Energy South Australia Journal, 43: 6-11.

Inger, S. and Harris, N., 1993. Geochemical Constraints on Leukogranite Magmatism in the Langtang Valley, Nepal Himalaya. Journal of Petrology, 34(2): 345-368.

Jackson, S.E., Pearson, N.J., Griffin, W.L. and Belousova, E.A., 2004. The application of laser ablation-inductively coupled plasma-mass spectrometry to in-situ U-Pb zircon geochronology. Chemical Geology, 211(1-2): 47-69.

Jagodzinski, E.A., 2005. Compilation of SHRIMP U-Pb geochronological data, Olympic Domain, Gawler Craton, 2001-2003, Geoscience Australia, Record 2005/20.

Jagodzinski, E.A., Black, L.P., Frew, R.A., Foudoulis, C., Reid, A., Payne, J.L., Zang, W. and Schwarz, M., 2006. Compilation of SHRIMP U-Pb geochronological data, for the Gawler Craton, South Australia 2005. Geochronology Series Report Book 2005-1. Geochronology Series Report Book 2005-1, Primary Industries and Resources South Australia, Report Book 2006/20.

Johnson, J.P. and Cross, K.C., 1995. U-Pb Geochronological Constraints on the Genesis of the Olympic Dam Cu-U-Au-Ag Deposit, South Australia. Economic Geology and the Bulletin of the Society of Economic Geologists, 90(5): 1046-1063.

Johnson, J.P. and McCulloch, M.T., 1995. Sources of Mineralizing Fluids for the Olympic Dam Deposit (South-Australia) - Sm-Nd Isotopic Constraints. Chemical Geology, 121(1-4): 177-199.

Kinny, P.D., Strachan, R.A., Kock, H. and Friend, C.R.L., 2003. U-Pb geochronology of late Neoproterozoic augen granites in the Moine Supergroup, NW Scotland: dating of rift-related, felsic magmatism during supercontinent break-up? Journal of the Geological Society, 160: 925-934.

Mahar, E.M., Baker, J.M., Powell, R., Holland, T.J.B. and Howell, N., 1997. The effect of Mn on mineral stability in metapelites. Journal of Metamorphic Geology, 15(2): 223-238.

Mawby, J., Hand, M. and Foden, J., 1999. Sm-Nd evidence for high-grade Ordovician metamorphism in the Arunta Block, central Australia. Journal of Metamorphic Geology, 17(6): 653-668.

McFarlane, C.R.M., 2006. Palaeoproterozoic evolution of the Challenger Au Deposit, South Australia, from monazite geochronology. Journal of Metamorphic Geology, 24(1): 75-87.

Miller, C.F. and Stoddard, E.F., 1981. The Role of Manganese in the Paragenesis of Magmatic Garnet - an Example from the Old Woman Piute Range, California. Journal of Geology, 89(2): 233-246.

Miller, C.F., Stoddard, E.F., Bradfish, L.J. and Dollase, W.A., 1981. Composition of plutonic muscovite: genetic implications. Canadian Mineralogist, 19: 25-34.

Montel, J.M., 1993. A Model for Monazite/Melt Equilibrium and Application to the Generation of Granitic Magmas. Chemical Geology, 110(1-3): 127-146.

Morrow, N. and McPhie, J., 2000. Mingled silicic lavas in the Mesoproterozoic Gawler Range Volcanics, South Australia. Journal of Volcanology and Geothermal Research, 96(1-2): 1-13.

Myers, J.S., Shaw, R.D. and Tyler, I.M., 1996. Tectonic evolution of Proterozoic Australia. Tectonics, 15(6): 1431-1446.

Nabelek, P.I. and Liu, M., 2004. Petrologic and thermal constraints on the origin of leucogranites in collisional orogens. Transactions of the Royal Society of Edinburgh-Earth Sciences, 95: 73-85.

Nabelek, P.I., Russ-Nabelek, C. and Denison, J.R., 1992. The generation and crystallization conditions of the Proterozoic Harney Peak Leucogranite, Black Hills, South Dakota, USA: Petrologic and geochemical constraints. Contributions to Mineralogy and Petrology, 110(2): 173-191.

Nekvasil, H., 1991. Ascent of Felsic Magmas and Formation of Rapakivi. American Mineralogist, 76(7-8): 1279-1290.

Patino Douce, A.E., 1999. What do experiments tell us about the relative contributions of crust and mantle to the origin of granitic magmas? In: A. Castro, C. Fernandez and J.L. Vigneresse (Editors), Understanding Granites: Integrating New and Classical Techniques. Geological Society, London, Special Publications, 168, pp. 55-75.

Patino Douce, A.E. and Harris, N., 1998. Experimental constraints on Himalayan anatexis. Journal of Petrology, 39(4): 689-710.

Payne, J.L., Barovich, K. and Hand, M., 2006a. Provenance of metasedimentary rocks in the northern Gawler Craton, Australia: Implications for palaeoproterozoic reconstructions. Precambrian Research, 148(3-4): 275-291. ***Chapter 3 of this thesis.***

Payne, J.L., Barovich, K.M. and Hand, M., 2006b. On the tectonic setting of the magmatic suite previously known as the 'Arc-like Tunkillia/Ifould'. In: D. Denham (Editor), Australian Earth Sciences Convention 2006. Geological Society of Australia, Melbourne. ***Chapter 5 of this thesis.***

Payne, J.L., Hand, M., Barovich, K. and Wade, B.P., 2008. Temporal constraints on the timing of high-grade metamorphism in the northern Gawler Craton: implications for construction of the Australian Proterozoic. Australian Journal of Earth Sciences, 55, in press. ***Chapter 4 of this thesis.***

Powell, R. and Holland, T., 1999. Relating formulations of the thermodynamics of mineral solid solutions: Activity modeling of pyroxenes, amphiboles, and

micas. American Mineralogist, 84(1-2): 1-14.

Powell, R. and Holland, T.J.B., 1988. An Internally Consistent Dataset with Uncertainties and Correlations .3. Applications to Geobarometry, Worked Examples and a Computer-Program. Journal of Metamorphic Geology, 6(2): 173-204.

Prince, C., Harris, N. and Vance, D., 2001. Fluid-enhanced melting during prograde metamorphism. Journal of the Geological Society, 158: 233-241.

Ramo, O.T. and Haapala, I., 1995. 100 Years of Rapakivi Granite. Mineralogy and Petrology, 52(3-4): 129-185.

Rankin, L.R., Flint, R.B. and Fanning, C.M., 1990. Palaeoproterozoic Nuyts Volcanics of the western Gawler Craton, South Australia, Department of Primary Industries and Resources South Australia, Report Book 90/60.

Reid, A., Hand, M., Jagodzinski, E.A., Kelsey, D. and Pearson, N.J., in press. Palaeoproterozoic orogenesis within the southeastern Gawler Craton, South Australia. Australian Journal of Earth Sciences.

Rollinson, H.R., 1993. Using Geochemical Data: Evaluation, Presentation, Interpretation. Longman, Harlow, 352 pp.

Rubatto, D. and Hermann, J., 2007. Experimental zircon/melt and zircon/garnet trace element partitioning and implications for the geochronology of crustal rocks. Chemical Geology, 241(1-2): 38-61.

Skirrow, R., Fairclough, M., Budd, A., Lyons, P., Raymond, O., Milligan, P., Bastrakov, E., Fraser, G., Highet, L., Holm, O. and Williams, N., 2006. Iron oxide Cu-Au (-U) potential map of the Gawler Craton, South Australia. (First Edition) 1:500 000 scale. Geoscience Australia, Canberra, ISBN: 1 920871 76 4.

Spear, F.S., 1993. Metamorphic Phase Equilibria and Pressure-Temperature-Time Paths. Mineralogical Society of America, Monograph.

Stewart, K. and Foden, J.D., 2001. Mesoproterozoic Granites of South Australia, Part 1 - The Gawler Craton, University of Adelaide.

Stimac, J.A. and Wark, D.A., 1992. Plagioclase Mantles on Sanidine in Silicic Lavas, Clear-Lake, California - Implications for the Origin of Rapakivi Texture. Geological Society of America Bulletin, 104(6): 728-744.

Stowell, H.H., Taylor, D.L., Tinkham, D.L., Goldberg, S.A. and Ouderkirk, K.A., 2001. Contact metamorphic P-T-t paths from Sm-Nd garnet ages, phase equilibria modelling and thermobarometry: Garnet Ledge, south-eastern Alaska, USA. Journal of Metamorphic Geology, 19(6): 645-660.

Sun, S.S. and McDonough, W.F., 1989. Chemical and isotopic systematics of oceanic basalts: implications for mantle composition and processes. Geological Society of London Special Publication, 42: 313-345.

Swain, G., Barovich, K., Hand, M. and Ferris, G.J., 2005a. Proterozoic magmatic arcs and oroclines: St Peter Suite, Gawler Craton, SA. In: M.D. Wingate and S.A. Pisarevsky (Editors), Supercontinents and Earth Evolution Symposium. Geological Society of Australia Inc. Abstracts 81, 177 p.

Swain, G., Woodhouse, A., Hand, M., Barovich, K., Schwarz, M. and Fanning, C.M., 2005b. Provenance and tectonic development of the late Archaean Gawler Craton, Australia; U-Pb zircon, geochemical and Sm-Nd isotopic implications. Precambrian Research, 141(3-4): 106-136.

Swain, G.M., Hand, M., Teasdale, J., Rutherford, L. and Clark, C., 2005c. Age constraints on terrane-scale shear zones in the Gawler Craton, southern Australia. Precambrian Research, 139(3-4): 164-180.

Szpunar, M., Hand, M. and Barovich, K.M., 2006. Insights into age and provenance of the Palaeoproterozoic Hutchison Group, southern Gawler Craton, South Australia. In: A. Reid (Editor), Primary Industries and Resources SA, University of Adelaide and Monash University, ARC Linkage Program: 2006 Reporting day. Primary Industries and Resources South Australia, RB 2007/01.

Taylor, S.R. and McLennan, S.M., 1985. The Continental Crust: its composition and Evolution. Blackwell, Oxford., 312 pp.

Teasdale, J., 1997. Methods for understanding poorly exposed terranes: The interpretive geology and tectonothermal evolution of the western Gawler Craton. PhD Thesis, University of Adelaide, Adelaide, 179 pp.

Turner, S., Foden, J., Sandiford, M. and Bruce, D., 1993. Sm-Nd Isotopic Evidence for the Provenance of Sediments from the Adelaide Fold Belt and Southeastern Australia with Implications for Episodic Crustal Addition. Geochimica Et Cosmochimica Acta, 57(8): 1837-1856.

Vance, D. and Holland, T., 1993. A Detailed Isotopic and Petrological Study of a Single Garnet from the Gassetts Schist, Vermont. Contributions to Mineralogy and Petrology, 114(1): 101-118.

Vigneresse, J.L., 2004. A new paradigm for granite generation. Transactions of the Royal Society of Edinburgh-Earth Sciences, 95: 11-22.

Wade, B.P., Barovich, K.M., Hand, M., Scrimgeour, I.R. and

Close, D.F., 2006. Evidence for early Mesoproterozoic arc magmatism in the Musgrave Block, central Australia: Implications for Proterozoic crustal growth and tectonic reconstructions of Australia. Journal of Geology, 114(1): 43-63.

Wade, B.P., Payne, J.L., Hand, M. and Barovich, K.M., 2007. Petrogenesis of ca 1.50 Ga granitic gneiss of the Coompana Block: filling the 'magmatic gap' of Mesoproterozoic Australia. Australian Journal of Earth Sciences, 54: 1089-1102.

Watson, E.B. and Harrison, T.M., 1983. Zircon Saturation Revisited - Temperature and Composition Effects in a Variety of Crustal Magma Types. Earth and Planetary Science Letters, 64(2): 295-304.

White, R.W., Powell, R. and Holland, T.J.B., 2001. Calculation of partial melting equilibria in the system Na2O-CaO-K2O-FeO-MgO-Al2O3-SiO2-H2O (NCKFMASH). Journal of Metamorphic Geology, 19(2): 139-153.

White, R.W., Powell, R. and Holland, T.J.B., 2007. Progress relating to calculation of partial melting equilibria for metapelites. Journal of Metamorphic Geology, 25(5): 511-527.

Wolf, M.B. and London, D., 1995. Incongruent Dissolution of Ree-Rich and Sr-Rich Apatite in Peraluminous Granitic Liquids - Differential Apatite, Monazite, and Xenotime Solubilities During Anatexis. American Mineralogist, 80(7-8): 765-775.

Chapter 7

A global context for the Palaeoproterozoic evolution of the Mawson Continent

In Review as: Payne, J.L., Hand, M., Barovich, K.M. and Reid, A.. A global context for the Palaeoproterozoic evolution of the Mawson Continent. Geological Society of London Special Publications, IGCP 509 Palaeoproterozoic Earth special volume.

Abstract

Continental crust formed and reworked during the Palaeoproterozoic era is a major component of pre-1070 Ma Australia and the East Antarctic Shield. Within this crust, the Mawson Continent encompasses the Gawler-Adélie Craton in southern Australia and Antarctica and crust of the Miller Range, Transantarctic Mountains, which are thought to have assembled during *c.* 1730-1690 Ma tectonism of the Kimban-Nimrod-Strangways Orogenies. Recent geochronology has strengthened correlations between the Mawson Continent and Shackleton Range, but the potential for later rifting and/or accretion events limit conclusive extension of the Mawson Continent to include the Shackleton Range.

New data and revised interpretations of pre-existing data indicate a number of models previously proposed for the evolution of the Mawson Continent and North Australian Craton are inconsistent with geological, geophysical and palaeomagnetic constraints. A new model proposed for the late Archaean to early Mesoproterozoic evolution of the Mawson Continent highlights important timelines in the tectonic evolution of the crust of Australia. The Gawler-Adélie Craton and North Australian Craton have comparable tectonothermal events at ~2.56-2.45 Ga, ~2.0 Ga, ~1.85 Ga, 1.8-1.69 Ga and 1.6-1.55 Ga. This is interpreted to indicate that the North Australian and Gawler-Adélie Cratons were part of a single continuous crustal block until their separation at *c.* 1.55 Ga.

The Archaean to earliest Palaeoproterozoic evolution of the North Australian-Gawler-Adélie crust is linked to that of the Sask Craton in the Trans-Hudson Orogen. This correlation is based upon co-eval magmatism and metamorphism in the late Archaean in both crustal blocks and the correlation of detrital zircon ages in the North Australian-Gawler-Adélie crust with magmatic and inherited zircon ages in the Sask Craton. Correlation between two now-disparate continental terrains highlights the dynamic nature of Palaeoproterozoic global tectonics and the need to consider a wide range of possible crustal geometries in attempting to reconstruct supercontinent assemblages during the Archaean and early Proterozoic.

Supplementary Appendix 1

U-Pb geochronology of age-constrained monazite from the Harts Range, Central Australia

SA1.1 Introduction

Incorporated into the setup of LA-ICP-MS U-Pb monazite geochronology at the University of Adelaide was analysis of a number of age-constrained monazite populations. This was undertaken primarily to test the accuracy of the method but in some cases also provided useful geological information. Reported in this supplementary appedix is U-Pb age data for a selected suite of samples which provide useful geological information on the timing of metamorphism in the Harts Range region of central Australia.

SA1.2 Geological Background

The Harts Range region of central Australia incorporates a complex sedimentary, megmatic and orogenic history spanning from the Palaeoproterozoic to the late Carboniferous (eg. Arnold et al., 1995; Foden et al., 1995; Miller and Cartwright, 1997; Miller et al., 1997; Hand et al., 1999; Mawby et al., 1999; Buick et al., 2001; Buick et al., 2005; Maidment et al., 2005; Maidment et al., 2007). In the past decade various research studies have recognised the presence of extensive Neoproterozoic to Palaeozoic metasedimentary and metaigneous lithologies that are affected by a complex sequence of metamorphic and deformation events associated with both extensional regimes and compressional regimes (Hand et al., 1999; Mawby et al., 1999; Buick et al., 2001). Extensional events are associated with a period of early Ordivician rapid sediment deposition and extension in the intracratonic Centralian Superbasin represented by the Amadeus and Georgina Basins in the central Australia region (Hand et al., 1999). Compressional events are associated with the intra-cratonic Alice Springs Orogeny (*c.* 400 - 300 Ma) which resulted in approximately 20 km of exhumation in the Arunta Region (Hand et al., 1999).

Hand et al. (1999) reported a series of SHRIMP U-Pb monazite ages constraining the age of two high-grade metamorphic events in the Ordovician and Carboniferous. The first event is recorded in the Harts Range Group from garnet-bearing leucosomes within a biotite-sillimanite-plagioclase-garnet-quartz metapelite (sample 94-222). Hand et al. report an $^{206}Pb/^{238}U$ age of 467 ± 4 Ma (95% confidence interval re-calculated using data in Table 3 of Hand et al. 1999) for monazite separated from within the matrix of the leucosome. The second event is represented by monazite growth in a kyanite-garnet-bearing metapelite with overprinting sillimanite-biotite-muscovite-chlorite-quartz-bearing shearbands (sample 94-91). In this sample, monazite records a $^{206}Pb/^{238}U$ age of 343 ± 4 Ma (95% confidence interval re-calculated using data in Table 3 of Hand et al. 1999).

Subsequent to the work of Hand et al. (1999), Maidment (2005) dated a monazite population separated from the same leucosome in the same outcrop as sample 94-222 of Hand et al. (1999). Monazite for this sample was separated from within garnet and recorded a $^{206}Pb/^{238}U$ age of450.2 ± 3.4 Ma (MSWD=1.5). As discussed by Maidment (2005) the difference in ages obtained by the two studies from the same leucosome is inconsistent with the geological interpretation of the mineral assemblage. Garnet within the leucosome is interpreted to record peak metamorphism (Hand et al., 1999). Hence, monazite growth within the garnet is likely to represent peak or prograde metamorphic mineral growth, assuming monazite is armoured within the garnet. That the age obtained from monazite within garnet is statistically and significantly younger than the age obtained from monazite in the leucosome matrix is inconsistent with this geological interpretation. If monazite within garnet was entirely reset during retrograde metamorphism then

NOTE:
This figure is included on page A2 of the print copy of the thesis held in the University of Adelaide Library.

Figure SA1.1 - Generalised geology of the Arunta Region and Harts Range region modified after Hand et al. (1999). a) Generalised structure of the Arunta Region showing location of Entia Dome and location of map in Figure SA1.1.b). Inset: location map of Arunta Region in Australia. b) Simplified geological map of the Harts Range region showing sample locations of Hand et al. (1999).

monazite within the matrix would also be reset, again inconsistent with the obtained ages of Hand et al. (1999) and Maidment (2005). The geologically irreconcilable difference in ages obtained from the same mineral system within the same leucosome calls into question the reliability of at least one set of the age data. Although not the initial intention when undertaking LA-ICP-MS geochronology on samples 94-222 and 94-91, the obtained LA-ICP-MS age data has allowed for some resolution of the differing ages for metamorphism.

SA1.3 Samples and Analytical Procedure

Four monazite samples are analysed in this study. For two samples, 94-222 and 94-91 (Hand et al., 1999), analyses were conducted on the same grain mount as that used for previous SHRIMP analysis, and in some case on the same grains as SHRIMP analyses. Monazite grains for sample Bruna-NW were taken from the same mineral separate as used for SHRIMP analysis in Maidment (2005). Sample 222-intra-gt, was taken from a mineral separate of sample 94-222 in which monazite grains were separated from within garnet. This means that monazite grains from samples Bruna-NW and 222-intra-gt represent the same tecxtural location for monazite grains, both from within peak metamorphic garnet from the same leucosome.

Mineral separation procedures are as discussed in Hand et al. (1999) and Maidment (2005), with only hand-picking and mounting of unmounted samples was undertaken as part of this study. LA-ICP-MS analytical procedures are the same as those described in Payne et al. (2007). Age calculations were done using Isoplot

SA1.4 Results

U-Pb age data is reported in Table SA1.1 and concordia diagrams are plotted in Figure SA1.2. All uncertainties for calculated ages are reported for 95% confidence interval. Representative BSE images for analysed monazite populations are shown in Figure SA1.3. No correlation between monazite compositional zoning and age was observed in any of the analyses monazite populations.

SA1.4.1 Sample 94-222

Six grains were targeted for a total of 20 analyses over two analytical sessions. The monazites range

from 5.52 to 10.41 wt% Th and 0.23 to 0.62 wt% U. No correlation was found between BSE compositional domains and recorded age (Figure SA1.2a). The $^{206}Pb/^{238}U$ weighted mean age is 449.7 ± 3.4 Ma (MSWD=1.14) and concordia age of 452.9 ± 3.5 Ma ($MSWD_{conc\&eqv}$=1.6). Both ages are significantly younger than the previously reported $^{206}Pb/^{238}U$ age of 467 ± 8 Ma (Hand et al., 1999).

SA1.4.2 Sample Bruna-NW

Eight grains were analysed for sample Bruna-Nw for a total of 24 analyses. Analysis of the SHRIMP separate was done on 8 grains and produced a $^{206}Pb/^{238}U$ age of 447.4 ± 2.8 Ma (MSWD=0.48) and a Terra-Wasserberg intercept age of 446.7 ± 3.9 Ma (MSWD =1.07). Minor common-Pb was evident in this sample and, together with small degrees of lead-loss, accounts for the minor dispersion of the data points in $^{207}Pb/^{206}Pb$ and $^{207}Pb/^{235}Pb$ space (not shown). The age obtained for this sample is within error of the age obtained in SHRIMP analysis of Maidment (2005).

SA1.4.3 Sample 222-intra-gt

Eight monazite grains were analysed from 222-intra-gt for a total of twenty seven analyses. All analyses yielded a weighted mean $^{206}Pb/^{238}U$ age of 449.5 ± 1.8 Ma (MSWD=0.68). Plotting upon a Terra-Wasserberg diagram yields an intercept age of 450.3 ± 2.5 (MSWD=0.61). This sample exhibits minor common-Pb, but greater Pb-loss than Bruna-NW which accounts for the obtained spread of data and anomalous slope of the constructed Terra-Wasserberg discord.

SA1.4.4 Sample 94-91

Thirteen monazite grains were analysed over three analytical sessions for a total of 24 analyses Th concentrations range from 2.23 - 3.9 wt% and U concentrations from 0.69 to 0.85 wt%. (MSWD=0.49) and a $^{206}Pb/^{238}U$ weighted mean age of 334.1 ± 1.8 Ma (MSWD=0.72) were obtained. The concordia age for this sample is 333.6 ± 2.3 Ma ($MSWD_{conc\&eqv}$=0.68, Figure SA1.2). All of these ages are significantly different (>10 Myr) from that reported in Hand et al. (1999).

SA1.5 Discussion

Age data obtained within this study is considered in the context of implications for previous geochronology and subsequent timing of metamorphism in the Harts Range region.

As outlined in secton SA1.2 previous studies have obtained monazite ages of 467 ± 4 Ma (Hand et al., 1999) and 450.2 ± 3.4 Ma (Maidment, 2005) from the same garnet-bearing leucosome in the Harts Range region. The LA-ICP-MS U-Pb monazite age obtained for Bruna-NW of 447.4 ± 3 Ma is within analytical uncertainty of the SHRIMP age obtained by Maidment (2005) for the same monazite population. A similarly statistically indistinguishable age of 449.5 ± 1.8 Ma is obtained for the texturally-equivalent monazite population of sample 222-intra-gt. In contrast, the age of 449.7 ± 3.4 Ma obtained for sample 94-222 is significantly different to the previously reported age of 467 ± 4 Ma for the same mineral grains. However, the age obtained for sample 94-222 is statistically indistinguishable from the SHRIMP and LA-ICP-MS ages of samples Bruna-NW and 222-intra-gt. Given the consistency of ages obtained using LA-ICP-MS and SHRIMP analysis of Maidment (2005) we suggest the previously reported age of 467 ± 4 Ma for metamorphic monazite growth is inaccurate. This revision in age of metamorphic monazite growth results in a geologically consistent scenario in which monazite in both the matrix and within garnet in the studied leucosome are suggested to record the growth of peak metamorphic mineral growth.

Difference in ages obtained for sample 94-91 with LA-ICP-MS and SHRIMP analysis cannot be resolved by direct comparison with other monazite U-Pb dating. The observed consistency of LA-ICP-MS ages and the SHRIMP age of Maidment (2005) suggests the LA-ICP-MS age for 94-91 may be the more reliable age. As the original Hand et al. (1999) SHRIMP analyses for 94-222 and 94-91 were conducted in the same analytical session the potential for a systematic analytical error exists. Assuming LA-ICP-MS age data for 94-91 are accurate an age over-estimation of ~2.7% is observed for the SHRIMP data of Hand et al. (1999). This compares to a calculate age over-estimation of ~3.78% for the Hand et al. (1999) SHRIMP data for sample 94-222. The difference between these two overestimations is within analytical uncertainty of the two methods and may simply be an artifact of analytical uncertainties. Supporting the younger monazite age obtained by

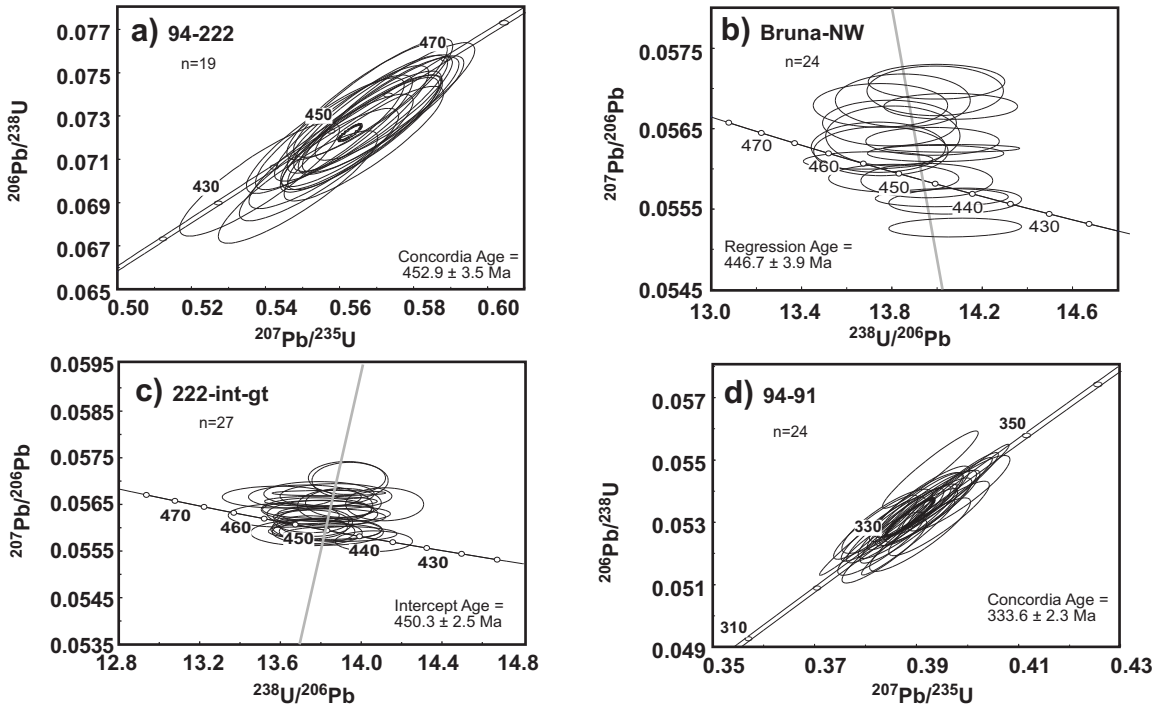

Figure SA1.2 - U-Pb concordia diagrams for monazite geochronology data. Samples are: a) 94-222, b) Bruna-NW, c) 222-intra-gt, and d) 94-91.

LA-ICP-MS, is metamorphic zircon age data obtained by Maidment (2005). For the same location as sample 94-91, Maidment (2005) reported a metamorphic zircon age of ~330 Ma. Metamorphic zircon is well documented to typically record an older U-Pb age than that recorded by metamorphic zircon (Rubatto et al., 2001; Kelsey et al., 2006), hence a significantly younger metamorphic zircon age (ie. ~330 Ma compared to 343± 4 Ma) is anomalous. By comparison the zircon and LA-ICP-MS ages are relatively similar and could be considered to both represent peak metamorphism. The limited data in the zircon age of Maidment (2005) prevents conclusive discussion on comparative zircon and monazite ages.

Given that: *a)* SHRIMP data of Hand et al. (1999) were collected within one analytical session, *b)* the Hand et al. SHRIMP analysis of 94-222 is demonstrated to report an old U-Pb age and *c)* metamorphic zircon ages from the locality of 94-91 are significantly younger than the previously reported SHRIMP age, we suggest the LA-ICP-MS age is the more accurate of the two ages obtained for monazite from sample 94-91. Further independent monazite geochronology is required to conclusively resolve the age of monazite in sample 94-91.

SA1.6 Conclusions

New LA-ICP-MS U-Pb monazite geochronology has been able to resolve monazite age differences between previously reported SHRIMP data. The leucosome sampled by samples 94-222 and Bruna-NW record metamorphic monazite growth at *c.* 450 Ma for monazite both within garnet and within the matrix. This age is interpreted to represent the age of peak metamorphism as per the discussion of Hand et al. (1999). The LA-ICP-MS age reported for sample 94-91 is also preferred to the age of Hand et al. (1999) but further work is required to resolve the age of metamorphism in this sample.

Acknowledgements

David Maidment, Jo Mawby and Martin Hand are thanked for supplying mineral separates and grain mounts used in this study.

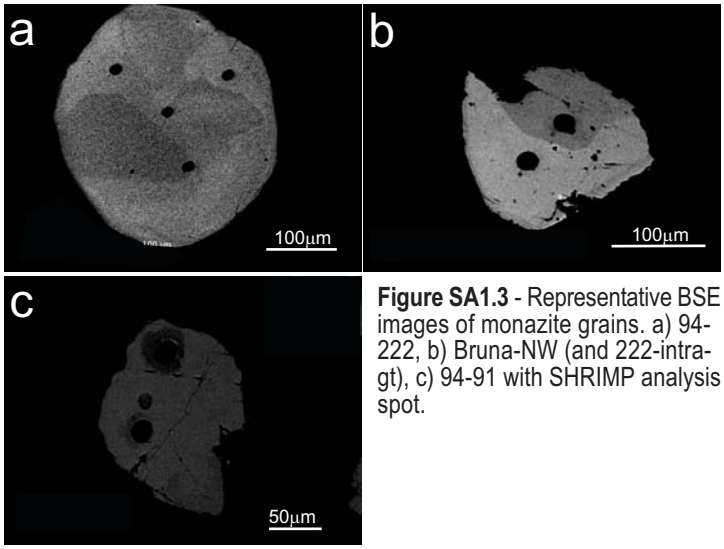

Figure SA1.3 - Representative BSE images of monazite grains. a) 94-222, b) Bruna-NW (and 222-intra-gt), c) 94-91 with SHRIMP analysis spot.

References

Arnold, J., Sandiford, M. and Wetherley, S., 1995. Metamorphic Events in the Eastern Arunta-Inlier .1. Metamorphic Petrology. Precambrian Research, 71(1-4): 183-205.

Buick, I.S., Hand, M., Williams, I.S., Mawby, J., Miller, J.A. and Nicoll, R.S., 2005. Detrital zircon provenance constraints on the evolution of the Harts Range Metamorphic Complex (central Australia): links to the Centralian Superbasin. Journal of the Geological Society, 162: 777-787.

Buick, I.S., Miller, J.A., Williams, I.S. and Cartwright, I., 2001. Ordovician high-grade metamorphism of a newly recognised late Neoproterozoic terrane in the northern Harts Range, central Australia. Journal of Metamorphic Geology, 19(4): 373-394.

Foden, J., Mawby, J., Kelley, S., Turner, S. and Bruce, D., 1995. Metamorphic Events in the Eastern Arunta-Inlier .2. Nd-Sr-Ar Isotopic Constraints. Precambrian Research, 71(1-4): 207-227.

Hand, M., Mawby, J., Kinny, P. and Foden, J., 1999. U-Pb ages from the Harts Range, central Australia: evidence for early Ordovician extension and constraints on Carboniferous metamorphism. Journal of the Geological Society, 156: 715-730.

Kelsey, D., Clark, C. and Hand, M., 2006. Integrating zircon and monazite saturation with metamorphism in Melt-bearing systems. Geochimica et Cosmichimica et acta, 70(18, Supplement 1).

Maidment, D.W., 2005. Palaeozoic high-grade metamorphism within the Centralian Superbasin, Harts Range region, central Australia. Ph.D. Thesis, Australian National University, Canberra, 422 pp.

Maidment, D.W., Hand, M. and Williams, I.S., 2005. Tectonic cycles in the Strangways Metamorphic Complex, Arunta Inlier, central Australia: geochronological evidence for exhumation and basin formation between two high-grade metamorphic events. Australian Journal of Earth Sciences, 52(2): 205-215.

Maidment, D.W., Williams, I.S. and Hand, M., 2007. Testing long-term patterns of basin sedimentation by detrital zircon geochronology, Centralian Superbasin, Australia. Basin Research, 19(3): 335-360.

Mawby, J., Hand, M. and Foden, J., 1999. Sm-Nd evidence for high-grade Ordovician metamorphism in the Arunta Block, central Australia. Journal of Metamorphic Geology, 17(6): 653-668.

Miller, J.A. and Cartwright, I., 1997. Early meteoric fluid flow in high-grade, low-O-18 gneisses from the Mallee Bore area, northern Harts Range, central Australia. Journal of the Geological Society, 154: 839-848.

Miller, J.A., Cartwright, I. and Buick, I.S., 1997. Granulite facies metamorphism in the Mallee Bore area, northern Harts Range: implications for the thermal evolution of the eastern Arunta Inlier, central Australia. Journal of Metamorphic Geology, 15(5): 613-629.

Rubatto, D., Williams, I.S. and Buick, I.S., 2001. Zircon and monazite response to prograde metamorphism in the Reynolds Range, central Australia. Contributions to Mineralogy and Petrology, 140(4): 458-468.

Table SA1.1 - LA-ICP-MS U-Pb monazite geochronology data

Spot No.	$^{206}Pb/^{238}U$	1σ	$^{207}Pb/^{235}U$	1σ	$^{207}Pb/^{206}Pb$	1σ	$^{206}Pb/^{238}U$ (Ma)	1σ	$^{207}Pb/^{235}U$ (Ma)	1σ	$^{207}Pb/^{206}Pb$ (Ma)	1σ
9491a	0.0534	68	0.39227	565	0.05319	67	335.3	4.2	336.0	4.1	336.8	28.1
9491b	0.05315	68	0.38855	544	0.05292	64	333.8	4.1	333.3	4.0	325.4	27.1
9491c	0.05356	68	0.39068	548	0.05281	64	336.3	4.2	334.9	4.0	320.5	27.1
9491d	0.05285	68	0.38198	545	0.05233	65	332.0	4.1	328.5	4.0	299.6	27.9
9491e	0.05356	69	0.39042	580	0.05277	69	336.3	4.2	334.7	4.2	318.8	29.5
9491f	0.05232	67	0.38306	562	0.05300	68	328.7	4.1	329.3	4.1	328.9	28.9
9491g	0.05304	68	0.38423	586	0.05244	71	333.1	4.2	330.1	4.3	304.8	30.6
9491h	0.05279	68	0.38348	545	0.05259	64	331.6	4.1	329.6	4.0	311.0	27.6
9491i	0.05207	67	0.38371	550	0.05334	66	327.2	4.1	329.8	4.0	343.4	27.8
9491k	0.05360	80	0.39058	649	0.05277	67	336.6	4.9	334.8	4.7	318.8	28.6
9491l	0.05289	79	0.38850	632	0.05318	65	332.2	4.8	333.3	4.6	336.6	27.4
9491m	0.05290	79	0.38583	630	0.05281	65	332.3	4.8	331.3	4.6	320.5	27.7
9491o	0.05347	80	0.39260	649	0.05315	67	335.8	4.9	336.3	4.7	335.3	28.0
9491p	0.05261	78	0.39069	653	0.05376	68	330.5	4.8	334.9	4.8	361.0	28.5
9491q	0.05304	79	0.38825	641	0.05299	66	333.2	4.8	333.1	4.7	328.1	28.0
9491r	0.05313	79	0.39441	651	0.05374	67	333.7	4.9	337.6	4.7	360.0	27.9
9491s	0.05394	80	0.39829	662	0.05345	67	338.7	4.9	340.4	4.8	347.7	28.2
9491t	0.05346	80	0.39186	655	0.05305	67	335.8	4.9	335.7	4.8	331.0	28.5
9491u	0.05470	82	0.39272	620	0.05198	61	343.3	5.0	336.4	4.5	284.5	26.4
9491v	0.05402	81	0.39663	623	0.05315	61	339.2	5.0	339.2	4.5	335.3	25.7
9491w	0.05386	81	0.39548	620	0.05315	61	338.2	5.0	338.4	4.5	335.4	25.6
9491y	0.05251	79	0.38836	604	0.05354	60	329.9	4.8	333.2	4.4	351.8	25.0
9491z	0.05427	82	0.39884	616	0.05320	59	340.7	5.0	340.8	4.5	337.3	24.7
9491a1	0.05250	79	0.37977	582	0.05236	57	329.9	4.8	326.9	4.3	301.2	24.6
94-222 1	0.07266	109	0.56324	851	0.05610	60	452.2	6.5	453.6	5.5	455.8	23.4
94-222 2	0.07225	108	0.56686	856	0.05678	61	449.7	6.5	456.0	5.6	482.3	23.8
94-222 3	0.07367	111	0.57496	880	0.05648	62	458.2	6.6	461.2	5.7	470.4	24.3
94-222 4	0.07369	111	0.56743	884	0.05572	63	458.4	6.7	456.4	5.7	440.8	24.7
94-222 5	0.07309	110	0.57174	892	0.05660	64	454.8	6.6	459.1	5.8	475.2	25.2
94-222 6	0.07308	111	0.56752	883	0.05619	63	454.7	6.6	456.4	5.7	459.0	24.9
94-222 7	0.07313	110	0.56903	875	0.05631	62	455.0	6.6	457.4	5.7	463.9	24.3
94-222 9	0.07302	111	0.57054	886	0.05653	63	454.3	6.7	458.4	5.7	472.5	24.5
94-222 10	0.07383	112	0.56907	878	0.05577	61	459.2	6.7	457.4	5.7	442.8	23.5
94-222 11	0.07225	108	0.56587	878	0.05670	65	449.7	6.5	455.3	5.7	479.2	25.3

Table SA1.1 - LA-ICP-MS U-Pb monazite geochronology data

Spot No.	$^{206}Pb/^{238}U$	1σ	$^{207}Pb/^{235}U$	1σ	$^{207}Pb/^{206}Pb$	1σ	$^{206}Pb/^{238}U$ (Ma)	1σ	$^{207}Pb/^{235}U$ (Ma)	1σ	$^{207}Pb/^{206}Pb$ (Ma)	1σ
94-222 12	0.07076	106	0.55444	878	0.05672	67	440.7	6.4	447.9	5.7	480.1	26.3
94-222 13	0.07172	108	0.56653	880	0.05718	65	446.5	6.5	455.8	5.7	498.1	25.3
94-222 14	0.07225	108	0.55848	867	0.05596	64	449.7	6.5	450.5	5.7	450.6	24.7
94-222 15	0.07213	108	0.56539	875	0.05675	64	449.0	6.5	455.0	5.7	481.1	25.0
94-222 16	0.07241	109	0.56581	889	0.05657	66	450.7	6.6	455.3	5.8	473.9	25.7
94-222 17	0.07137	108	0.55773	906	0.05657	70	444.4	6.5	450.1	5.9	474.1	27.5
94-222 18	0.07210	109	0.55615	871	0.05584	64	448.8	6.6	449.0	5.7	445.6	25.0
94-222 19	0.06972	106	0.54878	880	0.05699	69	434.4	6.4	444.2	5.8	490.5	26.7
94-222 20	0.07008	107	0.53840	883	0.05562	70	436.6	6.4	437.4	5.8	436.9	27.3
Bruna-NW 1	0.07242	100	0.55801	779	0.05578	59	450.7	6.0	450.2	5.1	443.1	22.9
Bruna-NW 2	0.07166	99	0.55187	775	0.05574	60	446.2	6.0	446.2	5.1	441.9	23.1
Bruna-NW 4	0.07102	98	0.54444	744	0.05550	56	442.3	5.9	441.3	4.9	432.0	22.3
Bruna-NW 5	0.07302	101	0.56487	778	0.05600	57	454.3	6.1	454.7	5.1	451.9	22.2
Bruna-NW 6	0.07132	99	0.54716	756	0.05553	57	444.1	6.0	443.1	5.0	433.4	22.7
Bruna-NW 7	0.07102	98	0.54122	743	0.05517	56	442.3	5.9	439.2	4.9	418.8	22.3
Bruna-NW 8	0.07112	99	0.55676	782	0.05667	60	442.9	6.0	449.4	5.1	478.0	23.4
Bruna-NW 9	0.07153	100	0.55569	785	0.05624	60	445.4	6.0	448.7	5.1	461.1	23.5
Bruna-NW 14	0.07272	104	0.56370	831	0.05612	62	452.5	6.2	453.9	5.4	456.7	24.1
Bruna-NW 15	0.07252	103	0.56565	825	0.05647	61	451.3	6.2	455.2	5.4	470.1	23.9
Bruna-NW 16	0.07146	102	0.55366	793	0.05610	58	444.9	6.1	447.4	5.2	455.8	22.6
Bruna-NW 17	0.07110	101	0.55149	784	0.05615	58	442.8	6.1	446.0	5.1	458.1	22.3
Bruna-NW 18	0.07273	104	0.56949	834	0.05668	62	452.6	6.2	457.7	5.4	478.2	24.2
Bruna-NW 20	0.07244	103	0.56342	838	0.05630	64	450.9	6.2	453.7	5.4	463.4	25.0
Bruna-NW 21	0.07278	104	0.56466	833	0.05617	62	452.9	6.2	454.6	5.4	458.6	24.1
Bruna-NW 22	0.07147	102	0.56141	826	0.05687	63	445.0	6.1	452.4	5.4	485.7	24.5
Bruna-NW 23	0.07221	103	0.56603	836	0.05674	63	449.5	6.2	455.4	5.4	480.9	24.7
Bruna-NW 24	0.07144	102	0.56229	815	0.05698	61	444.8	6.1	453.0	5.3	490.3	23.7
222-i-gt 1.01	0.07188	64	0.56028	539	0.05643	61	447.5	3.8	451.7	3.5	468.6	23.9
222-i-gt 1.02	0.07209	64	0.56133	547	0.05638	61	448.7	3.9	452.4	3.6	466.5	24.1
222-i-gt 1.03	0.07171	64	0.56372	563	0.05692	63	446.4	3.9	453.9	3.7	487.7	24.7
222-i-gt 1.04	0.07179	65	0.56487	561	0.05696	63	446.9	3.9	454.7	3.6	489.5	24.5
222-i-gt 1.05	0.07262	65	0.56193	542	0.05602	60	451.9	3.9	452.8	3.5	453.0	23.3
222-i-gt 2.06	0.07271	65	0.56279	528	0.05604	59	452.5	3.9	453.3	3.4	453.6	22.7

Table SA1.1 - LA-ICP-MS U-Pb monazite geochronology data

Spot No.	$^{206}Pb/^{238}U$	1σ	$^{207}Pb/^{235}U$	1σ	$^{207}Pb/^{206}Pb$	1σ	$^{206}Pb/^{238}U$ (Ma)	1σ	$^{207}Pb/^{235}U$ (Ma)	1σ	$^{207}Pb/^{206}Pb$ (Ma)	1σ
222-i-gt 2.07	0.07275	65	0.56180	528	0.05591	58	452.7	3.9	452.7	3.4	448.4	22.7
222-i-gt 2.08	0.07256	65	0.55946	530	0.05582	59	451.5	3.9	451.2	3.5	445.0	22.8
222-i-gt 3.09	0.07111	64	0.54622	512	0.05561	58	442.8	3.9	442.5	3.4	436.7	22.5
222-i-gt 3.11	0.07084	64	0.55189	548	0.05640	62	441.2	3.9	446.2	3.6	467.5	24.2
222-i-gt 4.28	0.07251	95	0.56713	763	0.05663	61	451.2	5.7	456.2	5.0	476.3	23.7
222-i-gt 4.29	0.07258	95	0.56433	757	0.05628	60	451.7	5.7	454.3	4.9	462.7	23.5
222-i-gt 5.30	0.07242	95	0.56215	762	0.05618	61	450.7	5.7	452.9	5.0	458.8	23.9
222-i-gt 5.31	0.07232	95	0.55805	750	0.05583	59	450.1	5.7	450.3	4.9	445.4	23.0
222-i-gt 6.32	0.07228	95	0.55720	756	0.05577	60	449.9	5.7	449.7	4.9	443.1	23.3
222-i-gt 6.33	0.07207	95	0.56320	763	0.05653	61	448.6	5.7	453.6	5.0	472.4	23.7
222-i-gt 6.34	0.07237	96	0.55801	749	0.05577	59	450.4	5.8	450.2	4.9	442.9	22.8
222-i-gt 6.35	0.07224	96	0.56009	753	0.05610	59	449.6	5.8	451.6	4.9	456.1	22.9
222-i-gt 6.36	0.07212	96	0.55984	754	0.05617	59	448.9	5.8	451.4	4.9	458.6	22.8
222-i-gt 7.37	0.07253	96	0.56395	757	0.05627	59	451.4	5.8	454.1	4.9	462.4	23.1
222-i-gt 7.38	0.07344	98	0.56973	779	0.05616	60	456.9	5.9	457.8	5.0	458.4	23.3
222-i-gt 8.39	0.07359	99	0.57488	789	0.05652	61	457.8	5.9	461.2	5.1	472.3	23.8
222-i-gt 8.40	0.07284	97	0.56133	770	0.05575	60	453.3	5.9	452.4	5.0	442.2	23.2
222-i-gt 8.41	0.07288	98	0.56937	784	0.05656	61	453.5	5.9	457.6	5.1	473.8	23.8
222-i-gt 8.42	0.07246	97	0.56513	76	0.05642	58	450.9	5.8	454.9	4.9	468.2	22.8
222-i-gt 8.43	0.07196	96	0.55430	747	0.05573	58	448.0	5.8	447.8	4.9	441.4	22.5
222-i-gt 8.44	0.07225	97	0.56527	758	0.05655	58	449.7	5.8	455.0	4.9	473.4	22.7

Supplementary Appendix 2

Co-authored Peer-reviewed publications

1. Wade, B.P., Payne, J.L., Hand, M. and Barovich, K.M., 2007. Petrogenesis of the ca. 1.50 Ga granitic gneiss of the Coompana Block: filling the 'magmatic gap' of Mesoproterozoic Australia. Australian Journal of Earth Sciences, 54: 1089-1102.

2. Reid, A., Payne, J.L., Wade, B.P., 2006. A new geochronological capability for South Australia - U-Pb zircon dating via LA-ICP-MS. MESA Journal, 42, 27-31.

Australian Journal of Earth Sciences (2007) **54**, (1089–1102)

Petrogenesis of *ca* 1.50 Ga granitic gneiss of the Coompana Block: filling the 'magmatic gap' of Mesoproterozoic Australia

B. P. WADE*, J. L. PAYNE, M. HAND AND K. M. BAROVICH

Continental Evolution Research Group, Geology and Geophysics, University of Adelaide, SA 5005, Australia.

The Coompana Block is an essentially unknown basement province that separates the Gawler Craton of South Australia from the Yilgarn Craton of Western Australia. Previously unstudied granitic gneiss intersected by deep drilling in the Coompana Block represents an important period of within-plate magmatism during a time of relative magmatic quiescence in the Australian Proterozoic. Granitic gneiss intersected at ~1500 m depth in Mallabie 1 diamond drillhole is metaluminous and dominantly granodioritic in composition. The granodiorites have distinctive A-type chemistry characterised by high contents of Zr, Nb, Y, Ga, LREE with low Mg#, Sr, CaO and HREE. U–Pb LA-ICPMS dating of magmatic zircons provides an age of 1505 ± 7 Ma, interpreted as the crystallisation age of the granite protolith. ε_{Nd} values are high with respect to exposed crust of the Musgrave Province and Gawler Craton, and range from +1.2 to +3.3 at 1.5 Ga. The granitic gneiss is interpreted to be a fractionated melt of a mantle-derived parental melt. The tectonic environment into which the precursor granite was emplaced is not clear. One possibility is emplacement within an extensional environment. Regardless, the granitic gneiss intersected in Mallabie 1 represents magmatic activity during the 'Australian Mesoproterozoic magmatic gap' of *ca* 1.50–1.35 Ga, and is a possible source for *ca* 1.50 detrital zircons found in sedimentary rocks of Tasmania and Antarctica, and metasedimentary rocks of the eastern Musgrave Province.

KEY WORDS: A-type granite, Coompana Block, geochemistry, neodymium isotopes, Proterozoic, South Australia.

Wade, B.P., Payne, J.L., Hand, M. & Barovich, K.M. (2007) Petrogenesis of ca 1.50 Ga granitic gneiss of the Coompana Block: filling the 'magmatic gap' of Mesoproterozoic Australia
Australian Journal of Earth Sciences, v. 54 (8), pp. 1089-1102

*Corresponding author: benjamin.wade@adelaide.edu.au

ISSN 0812-0099 print/ISSN 1440-0952 online © 2007 Geological Society of Australia
DOI: 10.1080/08120090701615733

Reid, A.J., Payne, J.L. & Wade, B.P. (2006) A new geochronological capability for South Australia: U–Pb zircon dating via LA-ICPMS.
MESA Journal, v. 42, pp.27-31